Fatigue Behavior of Ceramic Matrix Composites at Elevated Temperatures Under Cyclic Loading

by

Mehran Elahi

Dissertation Submitted to the Faculty of the

Virginia Polytechnic Institute and State University

in Partial fulfillment of the requirements for the degree of

Doctor of Philosophy

in

Engineering Mechanics

Kenneth L. Reifsnider, Chair

Jack C. Duke

Dean T. Mook

Ronald D. Kriz

Eric R. Johnson

Key Words: **ceramic matrix composites, fatigue, elevated temperature, life, remaining strength, life prediction, strength prediction**

December 19, 1996

Blacksburg, Virginia

FATIGUE BEHAVIOR OF CERAMIC MATRIX COMPOSITES AT ELEVATED TEMPERATURES UNDER CYCLIC LOADING

by

Mehran Elahi

Kenneth L. Reifsnider, Chairman

Engineering Mechanics

(ABSTRACT)

To achieve satisfactory levels of strength, fracture toughness, and reliability for man-rated systems such as jet engines, fiber reinforced ceramic matrix composites are needed. An elevated temperature axial testing system is developed to investigate and characterize fatigue behavior of Nicalon fiber reinforced enhanced silicon carbide matrix composites at 1800 °F under fully-reversed cyclic loading. Notch effect on quasi-static tensile response is also considered. Quasi-static and fatigue damage mechanisms and failure modes are examined using various specimen geometries, load levels, fatigue ratios, and laminates stacking sequences by employing a number of NDE techniques. Issues such as damage tolerance and durability are addressed by conducting interrupted fatigue tests at various stages of life for different load levels. Results are compared to the predictions of remaining strength and life, obtained using a performance simulation code. Initial results indicate existence of a threshold stress value which limits the use of the material system.

Dedication

This work is dedicated to Dr. Kenneth L. Reifsnider for whom I have immense admiration as my mentor and my very good friend. I am fortunate to know him, and I am eternally grateful for all he has thought me about science and life.

Acknowledgments

The author would like to thank the following people for their contributions to this work:

- Dr. Kenneth L. Reifsnider for providing the author the opportunity to perform this research, for his guidance and patience, and for his example of gentlemanly scholarship.
- Drs. John C. Duke, Dean T. Mook, Eric T. Johnson, and Ronald D. Kriz for serving on the author's committee.
- Late Dr. Wayne W. Stinchcomb for his help, guidance, and friendship.
- Dr. Thomas J. Dunyak and GE aircraft engine for providing testing material and financial support.
- Dr. Scott case for all the help during my graduate study and for being all around gentleman. Thanks again.
- Howard Halverson and Ahmad Razvan for writing the most of the data acquisition software and Dawn Trandel, Miguel Sisson, and Anil Tiwari for helping with the NDE tests.
- Dr. Kin Liao for his friendship and helping with the SPATE system.
- Shelia Collins, Paula Lee, Melba Morrozoff, and Cindy Hopkins for being so helpful all these years. Thanks again.
- Mr. Ali Rezai-Zadeh my roommate of many years. He is the best friend anybody can ever have.
- Mrs. June Cherry for her advice, encouragement and most of all her friendship.
- My parents (two of the funniest people I have ever known), my brothers and my sisters for their support and encouragement during my academic career.

Table of Contents

List of Figures

List of Tables

1. Introduction and Literature Review

1.1 Problem Statement:

The aircraft engine industry is facing a highly competitive future as we approach the 21st century. Materials development holds the key for the United States to maintain or even increase its share of the world engine market. One of the major contributors to this goal is the development of advanced engineering materials for engines that will be used as the propulsion system for subsonic and supersonic commercial aircraft.

In early 1950's the aircraft industry reached the consensus that any improvement in gas turbine engine performance requires further reduction in weight and an increase in combustion efficiency at higher temperatures. Light weight and potential high temperature capability of monolithic ceramics that are obtained by sintering process has resulted in small scale production of structural parts. One of the main factors in slow progress of these materials is the fact that ceramics are not suitable for environment which involves high thermal and mechanical shock resistance as well as thermomechanical cycling. The success of the past 25 years with polymeric composite materials (PMC) has opened up the possibility for successful use of continuous fiber reinforced ceramic matrix composites. Ceramic matrix composites (CMC) have been the subject of many investigations because of their high strength retention and toughness at elevated temperatures. The prevention of catastrophic brittle failure and improvement in damage tolerance is possible because of various energy dissipative processes. The first serious consideration of ceramic matrix composites as engineering materials

started in 1985 when US air force initiated a research program to support the integrated high performance turbine engine technology (IHPTET). This program was intended to address long-term material technology requirements in the ultra high temperature regime.

There has been concerted effort to develop the technology required to build a high speed civil transport aircraft (HSCT) which is capable of flying at speeds as high as Mach 3.5. The entry date into service is projected to be year 2005. Flying at these speeds in a commercial/civilian environment demands addressing two important issues: economics and environment. The later is translated into two engine components design considerations. First, to design a combustor with lower levels of nitrous oxide (NOx) emission than the current levels, and second, to design a light weight exhaust nozzle that meets the federal aviation regulation community noise standards. The effort to design and develop the combustor material which meets the required environmental, economic, thermal, structural, and durability standards (18000 hr life), is initiated under the enabling propulsion material program [1]. Reinforcements of ceramic materials with high modulus and high strength fibers result in tougher materials with improved strength, fracture resistance, fatigue resistance, creep resistance and thermal shock resistance. The use of continuous fiber reinforced ceramic matrix composites for propulsion applications (such as the next generation of commercial supersonic aircraft) requires performance and durability evaluation of these materials under static and cyclic fatigue loading at elevated temperatures (≥1800 °F).

Studies on fatigue, creep and creep rupture of ceramic matrix composites is relatively new. During the past decade material developers' and researchers' attention has been mainly focused on fabrication techniques and

cost as well as improvement of strength. Now there is great demand for information regarding long term deformation characteristic such as fatigue and creep. Extensive literature review indicates that the work done on static and cyclic fatigue of ceramic composites under the in-service condition is very limited and basically nonexistent for some of these material systems. The material system addressed in this study suffers from this limitation too. Material evaluation and analysis has shown that the properties of silicon carbide/silicon carbide composites are most promising for HSCT combustor liners. This study is intended to characterize the thermomechanical behavior of the model material. The material of choice is silicon carbide fiber (Nicalon[1]) reinforced enhanced silicon carbide matrix composite processed by a chemical vapor infiltration technique (CVI). This material system is simply referred to as Nicalon[1]/E-SiC. The emphasis is mainly on the cyclic fatigue behavior of Nicalon[1]/E-SiC at elevated temperatures. Thermomechanical behavior as well as potential damage modes and failure mechanisms of theses materials are to be examined under various load level, stacking sequence, specimen geometry, and testing temperature.

1.2 Objectives:

To understand mechanical behavior of advanced ceramic composites, one needs to experimentally observe and measure the long term behavior and predict the remaining strength and life under the service environment of the actual engineering component. To fulfill these objectives the following goals were established:

1. Design and develop a computer controlled elevated temperature (≥1800 °F) fully aligned testing system and testing methodology with capability to carry out long-term dynamic (cyclic) tests .
2. Characterize room and elevated temperature quasi-static tensile mechanical properties.
3. Characterize the notch effect on room and elevated temperature quasi-static tensile mechanical properties.
4. Notch effect on stress distribution and local elastic properties.
5. Characterize elevated temperature long term mechanical properties and performance under cyclic fatigue loading and investigate influence of the related parameters such as laminate geometry, laminate stacking sequence, loading type, and load level.
6. Investigate the influence of specimen geometry, stacking sequence, load level, and loading type on remaining strength and other related mechanical properties.
7. Investigate and apply nondestructive methods to detect manufacturing flaws and monitor initial damage initiation and subsequent damage progression upon short term and long term load application using a broad spectrum of nondestructive techniques.
8. Predictions of remaining life and strength of ceramic matrix composites using a mechanistic performance simulation model.

From here on a systematic approach which follows the natural progression of this study is considered to be beneficial to meet the above objectives.

1.3 Literature Review:

At low temperatures, the brittle fracture of monolithic ceramic materials is related to pre-existing flaws and defects (possibly induced in the course of fabrication), that serve as the nucleation sites for cracks which grow under load and propagate to a critical size resulting in fracture. Because there is typically a distribution of such flaws, there is a resulting scatter in material strength. Monolithic ceramics are linearly elastic, and their strength is controlled by the largest flaw present in the tested volume (e.g., the strength of hot-pressed Si_3N_4 decreases with increasing volume). These materials can exhibit the phenomenon of slow (subcritical) crack growth under load at high temperatures ($\geq$ 1830 °F), suggesting that the strength is time dependent. Above 1800 °F, these materials are statically unstable and show creep deformation [2,3]. The failure modes and failure strength of monolithic ceramics are known to be temperature dependent. For low temperature ranges ($\leq$ 3630 °F for SiC) where the failure is brittle, the strength is unaffected by temperature. At higher temperature ranges, due to intergranular phases or in association with the pores, a region of progressive decrease in strength is exhibited during the transition from brittle to ductile failure. Finally, at much higher temperatures a totally ductile failure occurs which is governed by the yielding stresses [2] (figure 1.1).

With the exception of a few materials, most ceramics appear to be marginal for use in jet engines at elevated temperatures, especially for man-rated systems. To achieve satisfactory levels of strength, fracture toughness, and reliability, fiber reinforced composites will be required [4]. Reinforcement of ceramic matrix materials with high modulus and high strength continuous

ceramic fibers results in tougher materials [5,6]. The strength properties do not depend on the largest pre-existing flaw formed during fabrication; but rather, depend on the complex interaction of local stress field around the flaws and their growth due to global stresses [3]. Ceramic matrix composites exhibit macroscopic fracture characteristics similar to those encountered with polymer matrix composites. However, the damage mechanisms involved and the micromechanics that represent the material behavior are substantially different. The macroscopic mechanical behavior involves well-defined mode I, mode II, and mixed-mode cracking response. The incidence of these responses depends on the particular composite. The toughness of reinforced ceramics which fracture in mode I as a result of a single dominant flaw, is increased by debonding (creation of new surfaces), fiber pull-out (frictional dissipation), and fiber failure (dissipation of elastic energy), and is decreased by matrix cracking (residual stress relaxation) [5,8] (figure 1.2). A comprehensive literature survey was conducted to identify potential damage modes and failure mechanisms in ceramic and glass-ceramic composites due to mechanical and thermal as well as environmental effects. This review has been broad in nature, however, it was limited to five material systems of interest. This review covered silicon carbide fiber reinforced silicon carbide (Nicalon[1]/SiC), silicon carbide fiber reinforced alumina (Nicalon[1]/Al_2O_3), silicon carbide fiber reinforced silicon nitride ((SCS-6[2]/Si_3N_4), and silicon carbide fiber) reinforced alkaline earth aluminosilicate ((Nicalon[1]/1723[3]) as well as silicon carbide fiber reinforced calcium aluminosilicate ((Nicalon[1]/CAS) material systems. A complete review of this survey may be

[1] Nicalon, Nippon Carbon, Tokyo, Japan.
[2] Textron Specialty Materials, Lowell, MA, USA.
[3] Corning Glass Works, Corning, NY, USA.

found in reference [9]. For the sake completeness of this report a portion of the review dealing with Nicalon[1]/SiC material system is presented in the following paragraphs. To better understand the material behavior under various testing conditions the processes involved in production of Nicalon[1] fibers and the Nicalon[1]/SiC composites are described in the following few paragraphs. Finally published literature concerning the material response under variety of testing situations are reviewed.

1.3.1 Fiber processing:

High strength, high elastic modulus along with high-temperature capabilities of continuous ceramic fibers have made very attractive as a reinforcing material. The are various methods of fabricating ceramic fibers which may be categorized as polymer pyrolysis ,chemical vapor deposition, and sol-gel techniques. The first two methods are used in production of SiC fibers. To get an insight into the nature and microstructure of Nicalon[1] fibers, the following few paragraphs explain the manufacturing process involved in production of Nicalon[1] fibers via polymer pyrolysis technique [10] (figure 1.3).

Production of ceramic fibers via polymer pyrolysis process is considered to be a great break through in development of ceramic fibers. This process traditionally have been used to produce carbon fibers from carbon-based polymers. However demand for materials with better thermal stability, higher oxidation resistance and superior mechanical properties has resulted in production of ceramic fibers and coatings such as B_4C, BN, SiC and Si_3N_4 from polymers containing C, B, Si, and N_2 under very controlled conditions. The steps involved in this production may be identified as finding a suitable starting polymer and an economical polymer

preparation method, polymer characterization, melt spin the polymer to a fiber precursor, curing the fiber precursor to cross-link the molecular chains (making it infusible during the subsequent pyrolysis), and finally pyrolyze to obtain the ceramic fiber. Nicalon[1] fiber is one those ceramic fibers that was developed through polymer pyrolysis. Development of SiC fiber through polymer pyrolysis was first made possible in mid 70's by professor Yajima and his colleagues in Japan and is commercially being produced by the Nippon Carbon Company under the trade name of Nicalon[1].

This particular process uses dichlorodimethylsilanne as the starting material which is upon reaction with sodium is dichlorinated to solid polydimethylsilanne. The thermal decomposition and polymerization (under high pressure autoclave at 880 °F in an argon atmosphere for 8-14 hours followed by vacuum distillation at 540 °F) of the latter yields what is known as polycarbosilane (with an average molecular weight of 1500). Then the polycarbosillane is melt spun from a 500 hole nozzle at 660 °F under N_2 gas resulting in the formation precursor fiber with a extremely low tensile strength (≈1.45 Ksi). This continuous pre-ceramic fiber is evolved into an inorganic SiC fiber by curing in air followed by thermal exposure in N_2 gas at 1832 °F and 2370 °F (under tensile load) respectively. Currently Nicalon[1] fibers are being produced commercially with various grades. Some of the available material properties are presented in the following table along with the SCS-6[2] SiC monofilament fiber [11].

Table 1.1: Material properties of commercially available SiC fibers.

Fiber (Microstructure)	Grade (name)	fiber sizing	Elemental Composition (wt%)	Dia. (μm)	Density (lb/in^3)	Young's Modulus (Msi)	Tensile Strength (Ksi)
SiC Nicalon[1] (amorphous)	Standard NLP-102	Epoxy (P)	β-SiC, SiO_2, 56% Si, 30% C ,14%O	10-20	0.0925	29	405
SiC Nicalon[1] (amorphous)	Ceramic NLM-202	polyvinyl-aetate (M)	β-SiC, SiO_2 53% Si, 31% C ,10% O	10-20	0.0925	29	405
SiC Monofilament	SCS-6[2]	-------	β-SiC	140	0.1192	63	508

1.3.2 Material Processing:

Ceramic composite processing via CVI technique has gained lot of attention in the past few years. This processing method is one of the few processes which is known not to damage fibers either chemically, thermally or mechanically upon processing as well as being able to produce near net shape composites. In general a CVI processing system is composed of reactor in which the fiber preform is held at high temperatures inside a furnace. From the reactant gases supply the reacting gases are entered into the furnace and pass through the preform which upon exposure to high temperature react and in which a layer of coating in form of solid gets deposited on fibers [figures 1.4-1.5]. As this process continues the fiber coating gets larger and finally interlock with the neighboring fiber coatings causing fibers to hold together in form of a bundle.

Depending on preform processing temperature profile and the way the reactant gases are introduced to the preform, the CVI process may be divided into five categories of isothermal, thermal gradient, pulse flow, isothermal-forced flow, and thermal gradient-forced flow (figure 1.6).

Isothermal processing (figure 1.6I) which is the most commercially used CVI technique for processing various preform shapes and sizes, requires the preform to be held at a constant temperature (isothermal) inside a furnace. Reaction gases are entered into the furnace, and using chemical diffusion they infiltrate into the preform which upon chemical reaction they form the matrix inside the preform. The major shortcoming using this technique is that deposition of matrix on of the preform blocks further infiltration of reactants gases into the preform. This results in a preferential degree of infiltration on the outside of preform and produces substantial degree of porosity in these materials. Since the technique requires diffusion of gases into the preform, numerous number of infiltration is required which may last for several weeks.

Thermal gradient processing (figure 1.6II) as the name implies is based on the thermal gradient along the thickness of the preform. The hot gases are entered from the cold side and are diffused into the preform through the thickness which upon reaction form the matrix which gets deposited on the hot side. Matrix deposition increases the density which in turn improves thermal conductivity causing uniform temperature distribution from the hot side. This further improves the matrix deposition from the hot side to the cold side.

Isothermal forced flow processing (figure 1.6III) uses the same technique as the isothermal processing except that the reacting gases are forced flow through the preform which is heated uniformly. The process continues until the preform becomes impermeable or the desired density is reached whichever comes first. Again like the previous processes this

process suffers from preferential densification where the preform has higher density at the entrance side of the preform.

Thermal gradient forced flow processing (figure 1.6IV) employs the same processing technique as the thermal gradient processing except the reactant gases are forced flow through the cold side of the preform which has a steep thermal gradient across its thickness. It is reported that change of direction of flow path could be used in obtaining higher degree of infiltration resulting in less porosity.

Pulsed flow processing (figure 1.6V) requires cyclic flow of reagents in and out of the preform inside the reacting chamber in a pulsative manner. The evacuated gases are collected and fed back into the reaction chamber. Due to small size of the furnace this technique has not yet recognized as a viable commercial alternative to the processes described earlier.

Beside being a simpler manufacturing process, forced flow technique is found to result in reduction in infiltration time (could be in order of 10-24 hours), and resulting in higher and uniform infiltration in comparison to other processes.

1.3.3 Material Behavior:

Nicalon[1]/SiC composites, have shown different behavior depending on the testing temperature, atmospheric condition, and testing duration. Tensile or flexural response of these materials is represented by stress-strain (load-deflection) curves which indicate linear elastic behavior up to a point where matrix cracking is very much saturated (proportional limit strength). Further loading initiates further matrix microcracking and partial fiber-matrix debonding, resulting in a nonlinear region which is probably controlled by

fiber pull-out, crack deflection, and fiber bridging mechanisms [13-22] (figure 1.7) .

The performance of continuous fiber reinforced ceramic matrix composites is significantly influenced by processing techniques and processing parameters as well as fiber architecture [23-25]. In cases where woven fiber preform is used, the matrix is introduced by infiltration or deposition techniques. Stress-strain behavior is directly related to the degree of infiltration and porosity created due to the differences in the infiltration processes. Fiber architecture will not only affect the infiltration of the matrix, but also the mechanical porosity and failure behavior by influencing the pore size, pore geometry, and pore distribution of the fibrous preform. These pores act as points of crack initiation and the strength decreases significantly as the void fraction increases [17,25-27] (figures 1.8-1.9).

Investigations of the failure behavior of continuous fiber reinforced ceramic composites have reported the presence of an increase in the fracture resistance of Nicalon[1]/SiC composites with crack extension at ambient temperatures using slow crack growth tests. The increase in the fracture energy to propagate the crack is related to the multiple branching of the crack, wherein the number of cracks increases along with the energy to propagate them. The rising R-curve effect is also related to the presence of toughening mechanisms, such as fiber bridging and microcracking in the crack wake of the newly created crack as well as microcracking in the crack front process zone. The frontal process zone is not the primary contributor to this toughening process, but rather it is the wake region behind the advancing crack front which is the critical feature. This is quite reasonable, for as the crack propagates the frontal process zone is actually decreasing as

it encounters the specimen back surface, but the wake region is increasing in size. However, fiber pull-out and crack bridging are significantly reduced at higher temperatures. Temperature is reported to influence the fiber-matrix interface bond strength through interface modification and fiber degradation [17,28-31].

At elevated temperatures, SiC_f/SiC composites show different behavior depending on the testing atmosphere. Elevated temperature is found to weaken the fiber-matrix interface which in turn results in delamination crack growth. The weakening of the fiber-matrix interface is due to the relaxation of residual stresses caused by the mismatch in the coefficient of thermal expansion between the fiber and the matrix, resulting in crack branching [28]. Thermal treatments may also result in modification of residual stresses such that the strength of the system is still maintained, and does not show any significant difference after various treatments [18,32-33]. Testing under vacuum, an increase in strength as a function of temperature is reported for temperatures up to 2200 °F [13,16,33] (figure 1.10). Ar-H_2 atmospheric testing does not cause any significant change in strength up to 2000 °F [34]. These behaviors are all followed by a continuous drop in strength as a result of thermal degradation of the Nicalon[1] fibers. Test temperature and oxidation treatment cause a decrease in initial elastic modulus. This is thought to be due to a reduction in the interfacial sliding stresses [35]. Thermal shock treatments of these materials result in a slight decrease in strength for temperatures higher than 570 °F as well as a decrease in strain to failure[13,18]. These treatments cause the interface to crack, thereby reducing the amount of fiber pull-out.

Thermal exposure results in fiber strength degradation. Nicalon[1] fibers lose strength above 1832 °F [36-38], which in turn may modify the fiber-matrix interface. Also it is reported that Nicalon[1] fiber is susceptible to decomposition, oxidation, accelerated grain boundary growth, and creep at elevated temperatures [39-40]. Exposure of Nicalon[1] fibers at elevated temperatures in an oxidizing environment for a long period of time causes the crystallization of the amorphous silica layer which is associated with volume decrease [41-45].

An oxidizing environment is found to have a detrimental effect on the fracture behavior of unprotected specimens; i.e., fiber pull-out and toughness. These effects are reported to be progressive. Oxidation at 1832 °F for a short period of time results in a loss of ultimate strength and proportional limit strength; however, the failure of these composites is associated with significant fiber pull-out. As the exposure time increases, the degree of fiber pull-out decreases, which ultimately results in brittle fracture [46] (figure1.11). This progressive weakening and embrittlement of the material is believed to be the direct result of removal of the initial carbon interface and growth of a silica layer. This fiber-matrix interface evolution causes a strong and brittle bond between the fibers and the matrix. Air testing results in an evolution in the failure mode with test temperature [22]. From room temperature to 1300 °F, the fracture sequence is controlled by the fiber-matrix interface, and the strength increases while the elastic modulus is unchanged. Above 1300 °F, the flexural strength increases monotonically with the specimen thickness and the failure mode changes to exhibit a brittle rupture of the fiber [16]. Oxidation is reported to have a significant effect on the microstructure of SiC composites in the temperature range of 1740 °F to

2730 °F. This phenomenon is categorized in three stages. First, oxidation of the carbon interface results in gaps or cavities on the fiber. This is then followed by gaseous diffusion of oxygen in these cavities. Subsequently, oxidation of the SiC matrix and fibers results in formation of a silica layer at the fiber-matrix interface. This reduces the oxygen diffusion into these cavities. It is also reported that the difference in the oxidation rate of the fibers and the matrix results in a distinct boundary or gap in the amorphous silica layer. Nicalon[1] fiber is composed of SiC, SiO_2, and C; therefore it oxidizes more rapidly, producing a thicker SiO_2 layer at the fiber surface than at the matrix surface. Cavity closure is shown to occur at a faster rate as the temperature increases, whereas lower temperature causes severe oxidation in the bulk [46-50] (figure 1.12). Carbon coating is deposited on the fiber prior to infiltration to protect ceramic fibers from chemical attack during processing or developed during the processing [51-53]. It is known to influence the interfacial bonding and friction, and therefore the matrix cracking, and to alter the fracture behavior and mechanical properties of composites[18,54-55]. However, the poor oxidation resistance of carbon has limited the use of this material above certain temperatures. Oxidation of the carbon layer is reported to start at 800 °F where the rate increases significantly at higher temperatures in air. Pyrolytic graphite is known to oxidize at 1832 °F in air at rate of 0.2 in/min [56]. Although the sintered α-SiC exhibits much superior creep resistance at elevated temperatures than does the SiC_f/SiC composite [57-59], the low toughness and low strength make this material vulnerable to thermal shock and particle impact failures [60]. The relatively high steady-state creep rate of the composite may be a consequence of the high porosity content of the SiC matrix or poor chemical stability of the

Nicalon[1] fibers at high temperatures [59]. Once above the matrix cracking stress, the creep behavior is mainly due to SiC fibers. Different SiC fibers exhibit various creep strains at similar test conditions. The chemical vapor deposited silicon carbide (CVD-SiC) fiber has a creep strain that is almost an order of magnitude lower than the polymer-derived Nicalon[1] fibers [61,62]. This is believed to be a result of the lower viscosity silicon-oxide phase which is formed in the Nicalon[1] fibers during the development process [63]. The predominant mechanisms which govern the creep behavior might be related to the stress exponent (the slope of strain rate-log stress curve). Investigation of tensile and compressive creep resistance has shown that once above the proportional limit strength, the stress exponent increases from 1.4 to 4 due to change in the modes of deformation [64,65]. This is also witnessed in the elevated temperature creep tests under vacuum, for which different stress exponents corresponding to various modes of failure are observed. The operative mechanisms might be crack growth in the matrix, sliding of the fiber within the matrix, and structural evolution of the fiber in terms of temperature. Matrix microcracking and fiber pull-out were observed at 2200 °F with a stress exponent of 1.7, where fiber fracture occurs within the matrix at a fiber flaw. At a higher temperature, 2550 °F, the fibers play a smaller role where the reduction in the fiber pull-out is related to the structural evolution of the Nicalon[1] fibers [36,41] resulting in a stress exponent of 2.4.

Creep resistance and environment are two of the main limiting factors for the application of SiC_f/SiC composites. Thermal degradation of the Nicalon[1] fibers may be delayed to at least 2200 °F by application of a layer of CVD-SiC oxidizing resistant coating [14]. This resistant coating may not be

resistant to long term exposure to sodium at elevated temperatures. Sodium weakens the composite by reacting with the ceramic component to form a soda-glass corrosion product. Although the exposure to the combustion products of natural gas and air at 1830 °F produces similar results in strength, the embrittlement of the composite is more rapid [46]. Oxidation of SiC is found to occur at a faster rate in the presence of water vapor and sulfur [66,67]. Room temperature fatigue behavior CMC's with various matrix material indicate SiC_f/SiC composites as one of the most durable material systems. Fatigue response of CMC's indicate the existence of a endurance limit. Cyclic tests conducted at or below the proportional strength limit results in run-out condition [68]. Tension-compression cyclic fatigue (R=-1, f=10 Hz, 1hz for the first 1000 cycles) of 2-D woven quasi-isotropic SiC/SiC indicates a endurance limit of 63% of ultimate tensile strength. Compression is found not to be a factor in fatigue life subjected to tension-compression loading (R=-1). Tension-tension tests (R=0.1) have resulted in a very similar damage initiation, damage progression, S-N curve, and endurance limit as when compared with R=-1 tests. Composite shows damage in the form of matrix cracking [69]. Fiber architecture appears to be a factor in crack growth. Fully-reversed cyclic fatigue (R=-1, f=10 Hz, 1 Hz for the first 1000 cycles) of 3-D braided SiC_f/SiC indicate an endurance limit as high as 95% [70]. All measurable stiffness losses occur in the first cycle resulting in a large hysteresis loop. This indicates damage occurs mainly in the form of matrix cracking and manifest as residual strain accumulation.

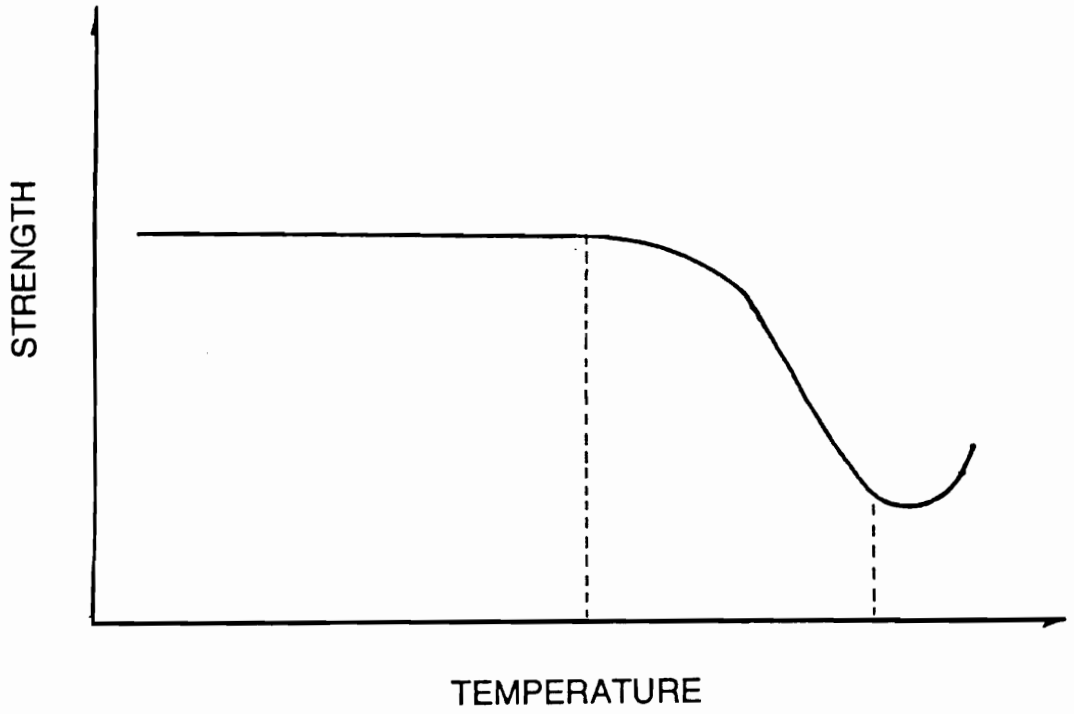

Figure 1.1: Strength of monolithic ceramics (fine polycrystaline) as a function of temperature.

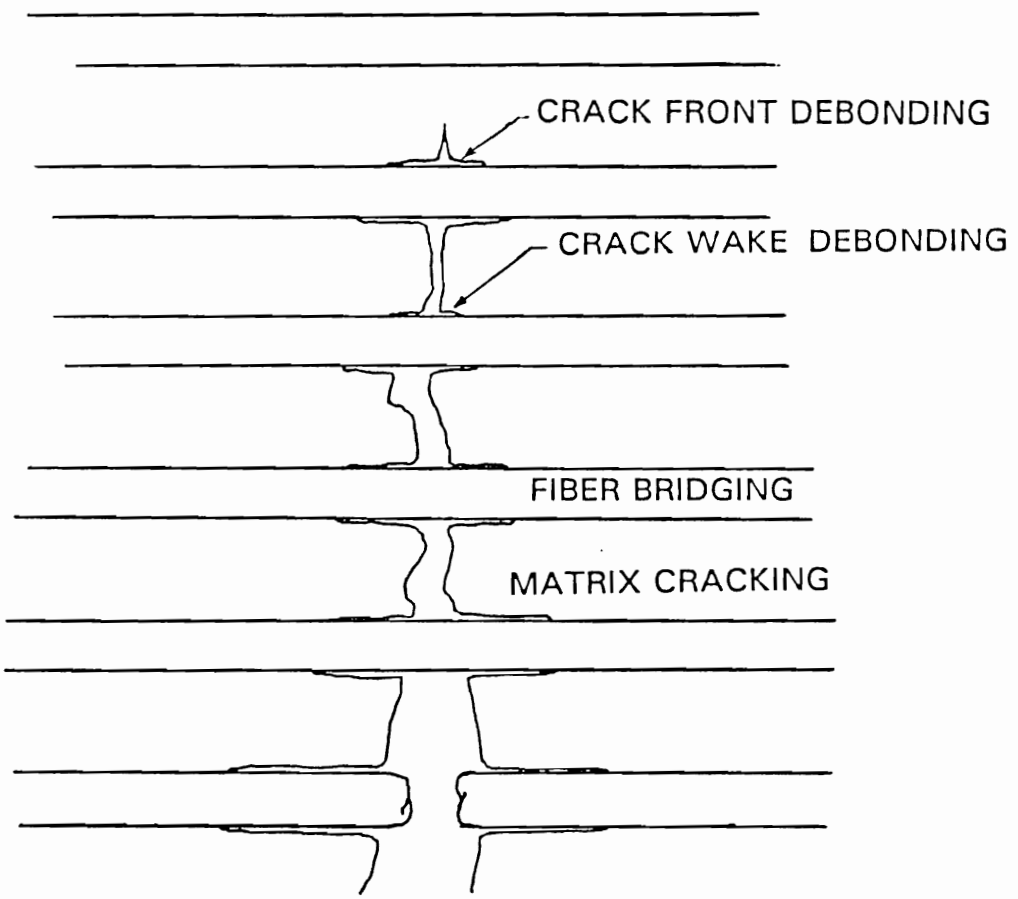

Figure 1.2: Various toughening mechanisms in fiber reinforced ceramic matrix composites.

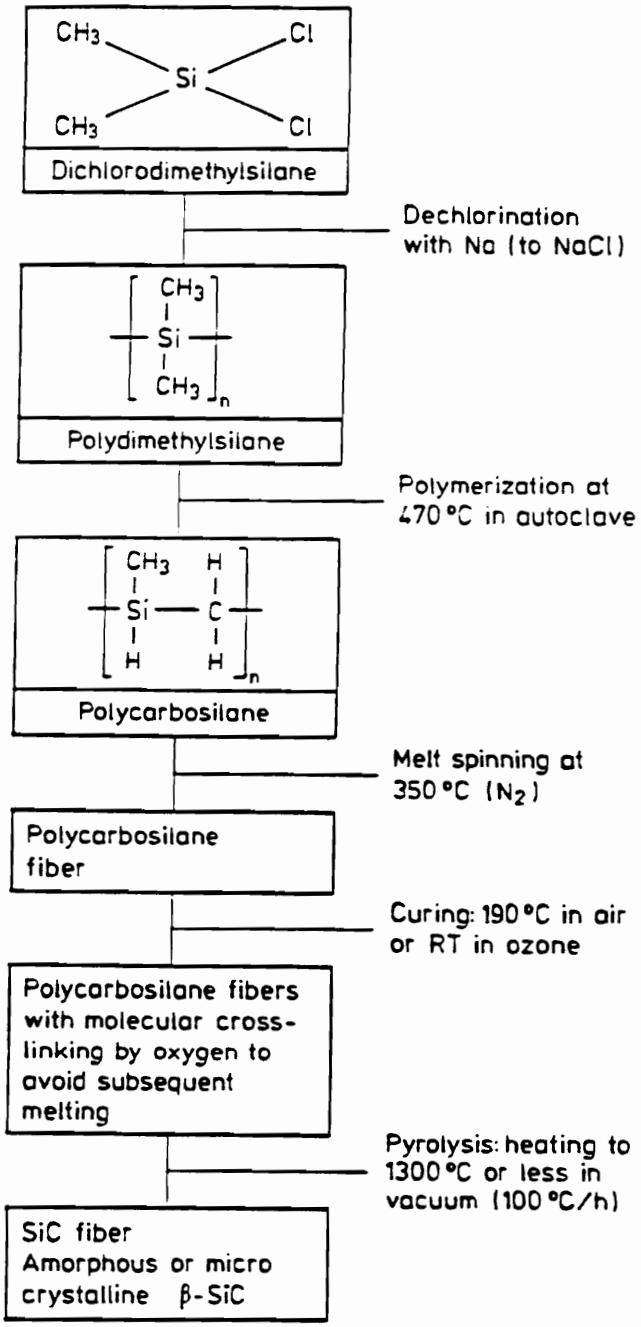

Figure 1.3: Schematic diagram showing the processes involved in production of Nicalon fibers (adapted from ref. 10).

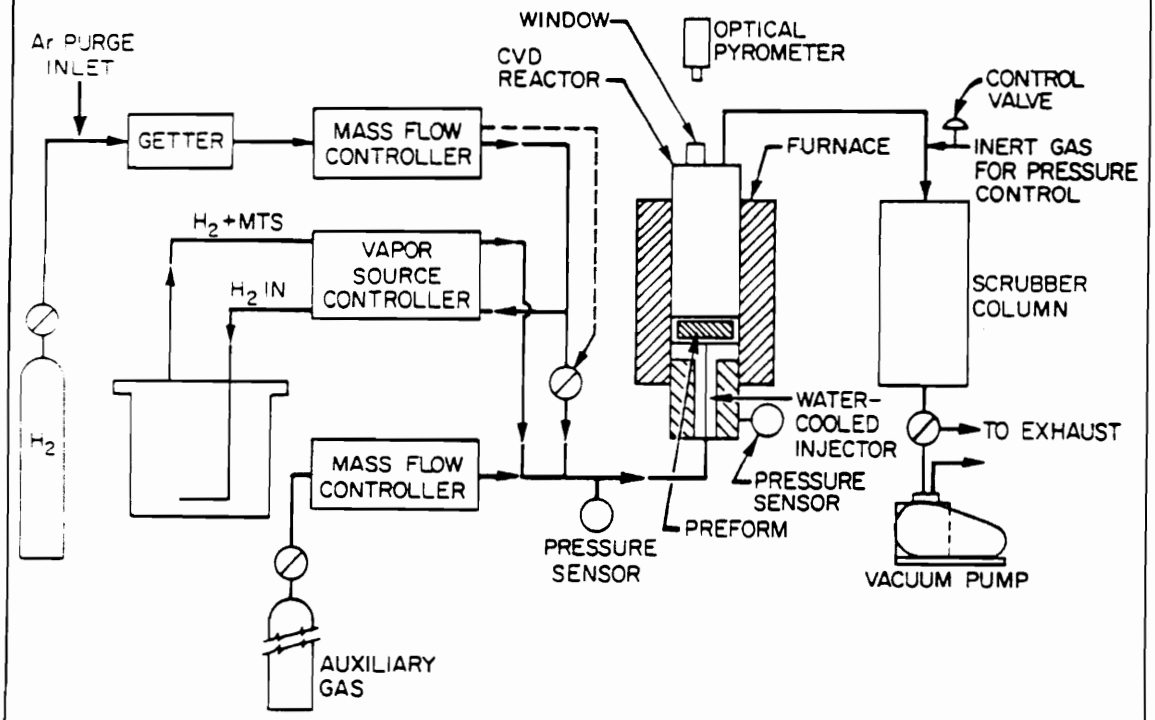

Figure 1.4: Various components of a CVI system (reactant gases, furnace, effluent gas handeling systems, adapted from ref. 12).

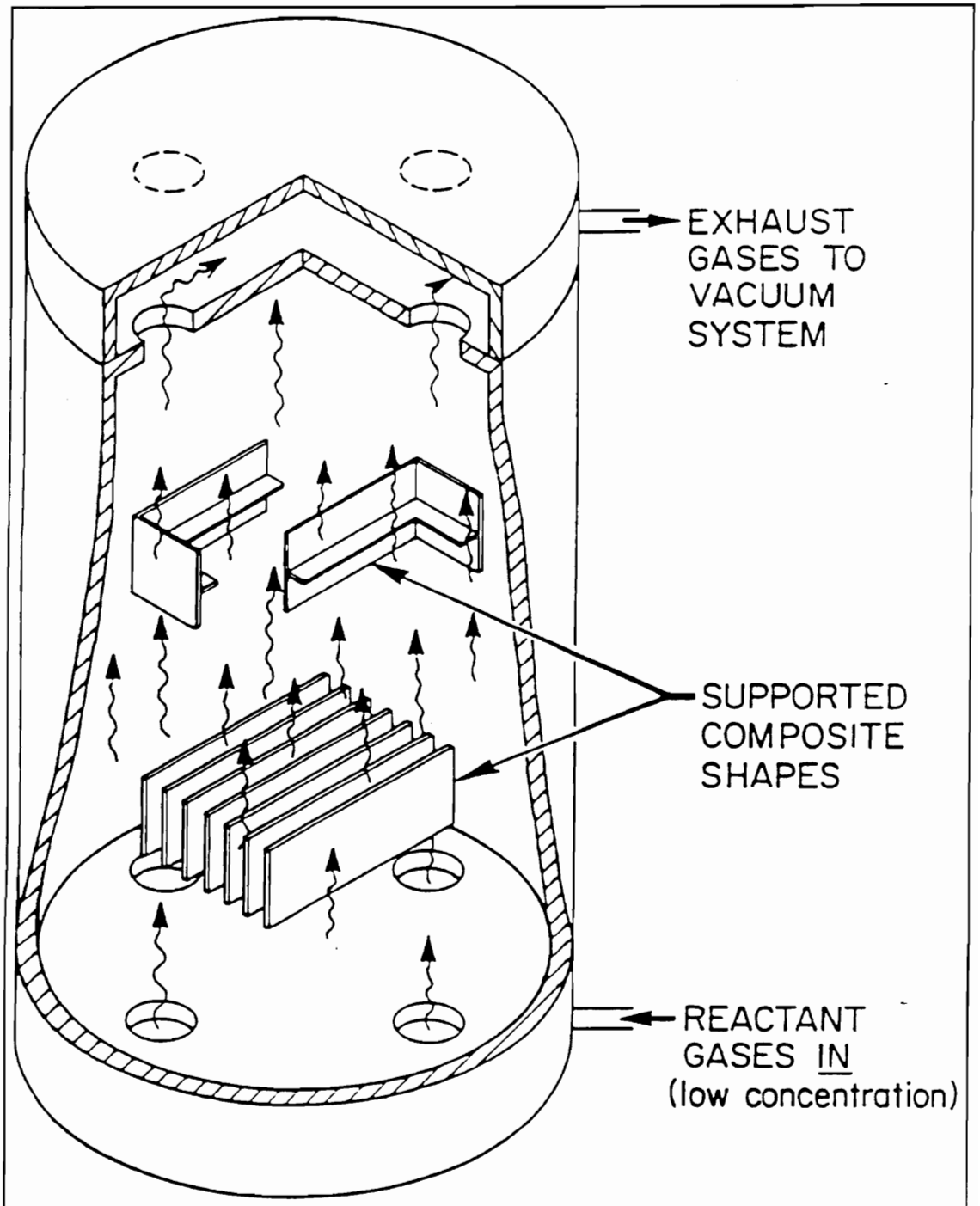

Figure 1.5: A CVI furnace where reactant gases diffuse into the preform (adapted from ref. 12).

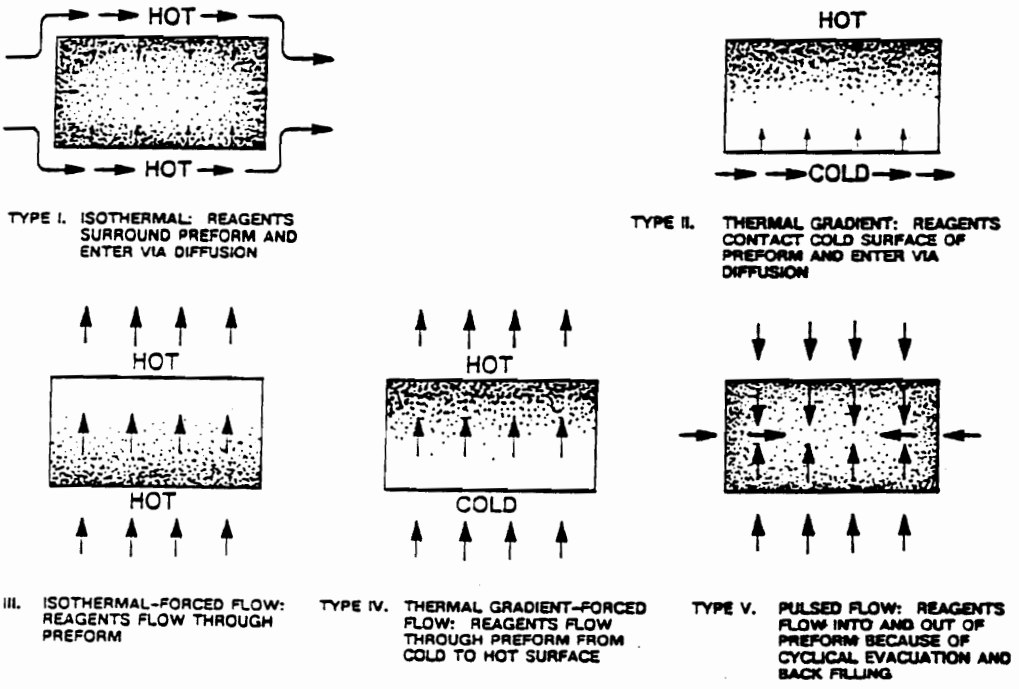

Figure 1.6: Various CVI processes based on preform temperature uniformity and flow of reactant gases (adapted from ref. 12).

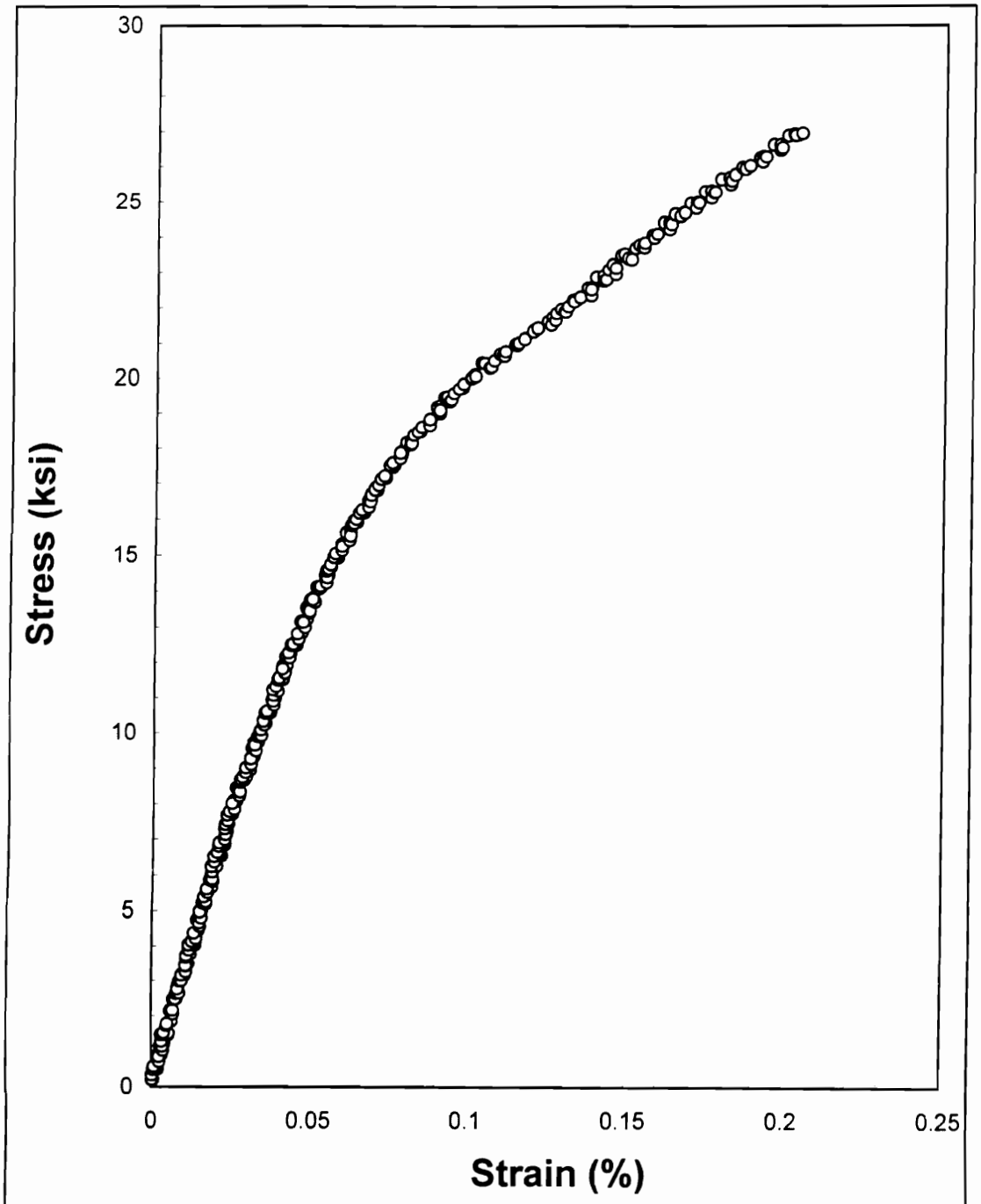

Figure 1.7: Room temperature tensile behavior of a 2-D woven Nicalon/SiC laminate.

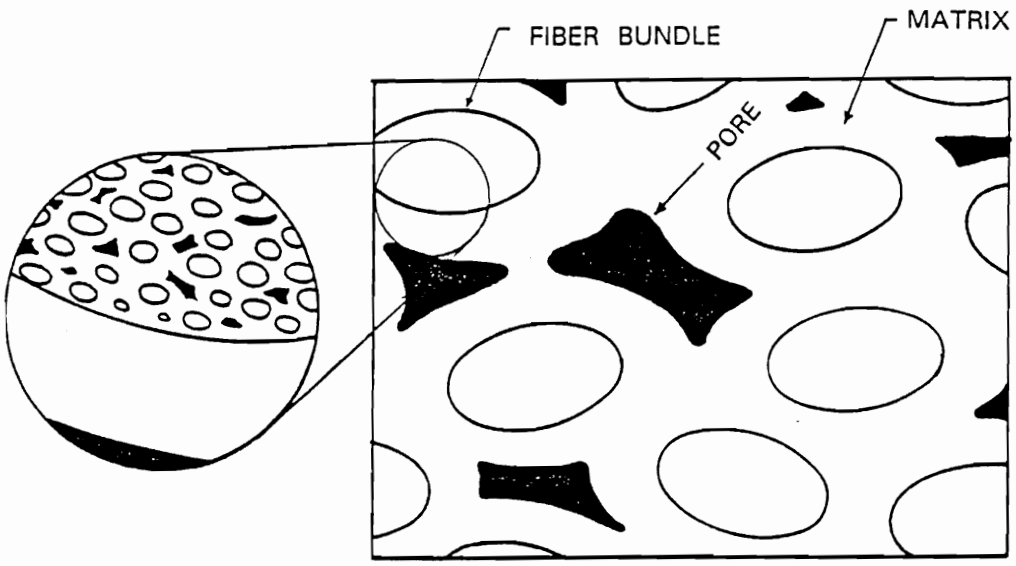

Figure 1.8: Porosity induced in fiber bundle and composite by CVI processing technique.

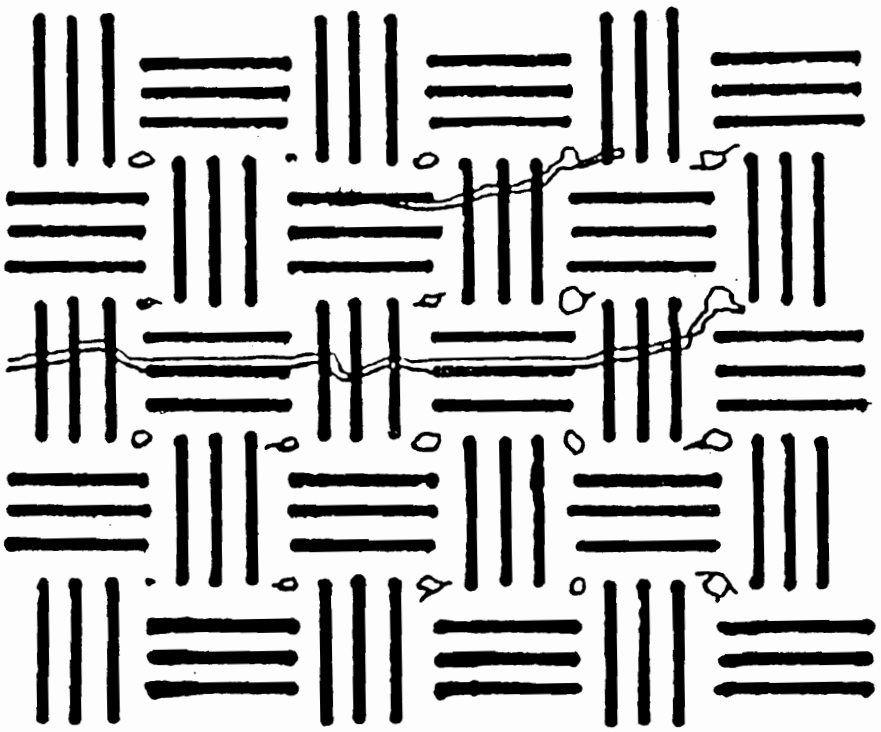

Figure 1.9: Pores acting as the point of crack initiation in a 2-D woven composite.

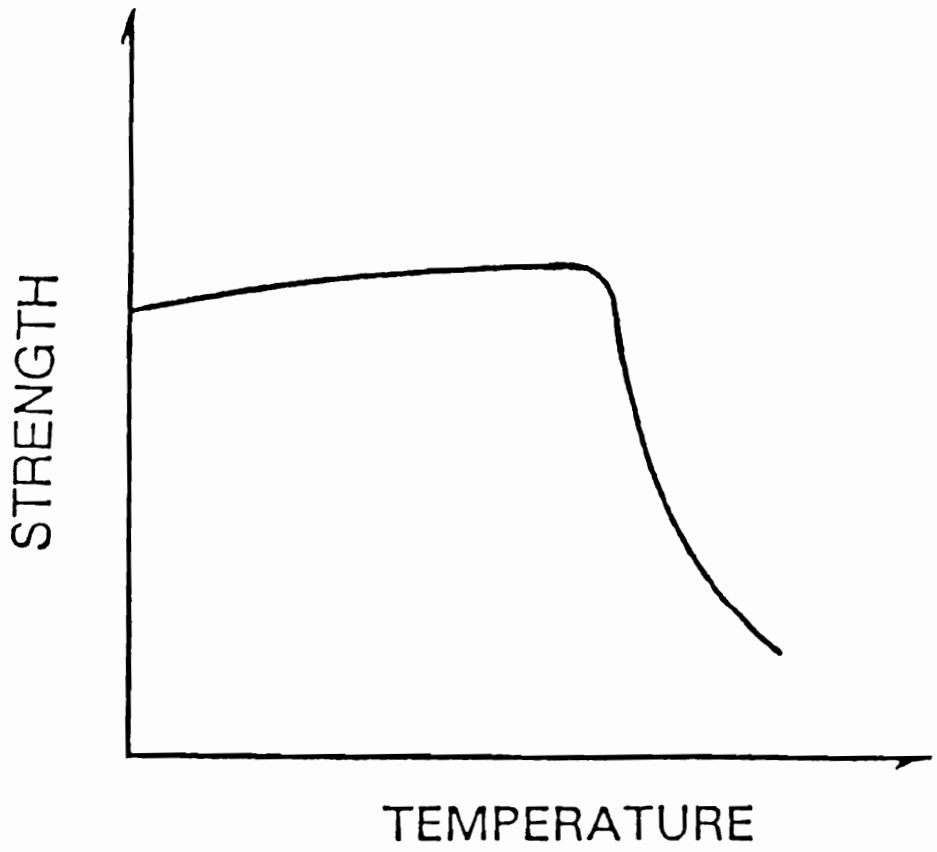

Figure 1.10: Strength of 2-D woven Nicalon /SiC composites as a function of temperature.

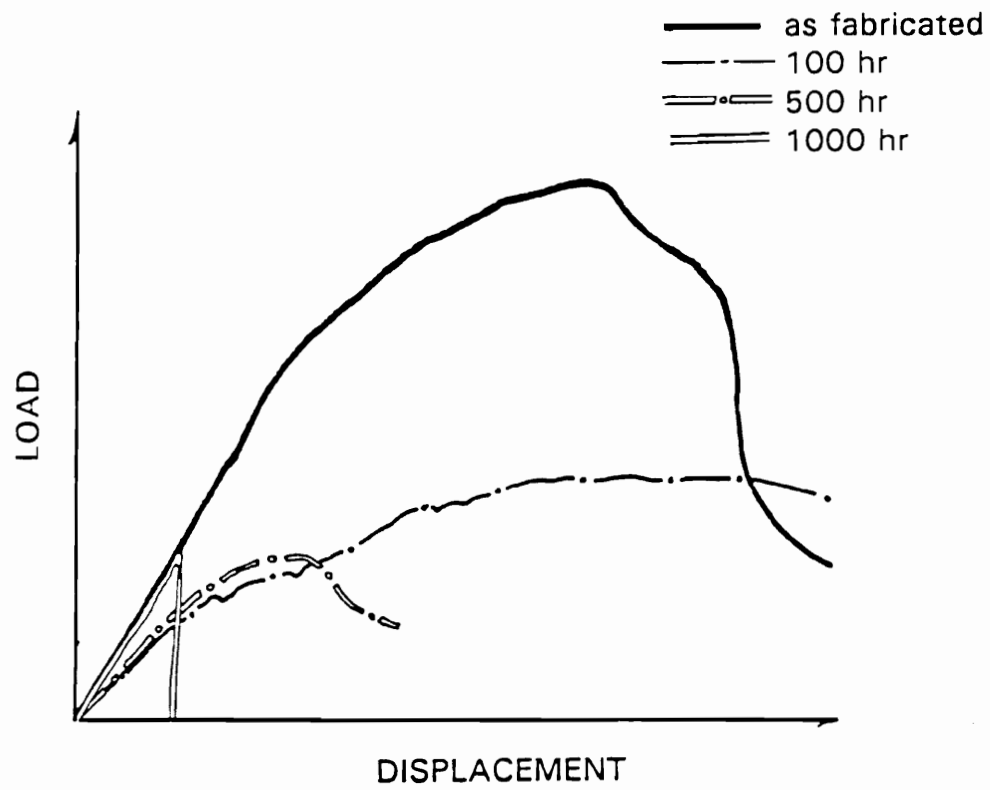

Figure 1.11: Influence of heat treatments on tensile response and fracture behavior of Nicalon /SiC composites.

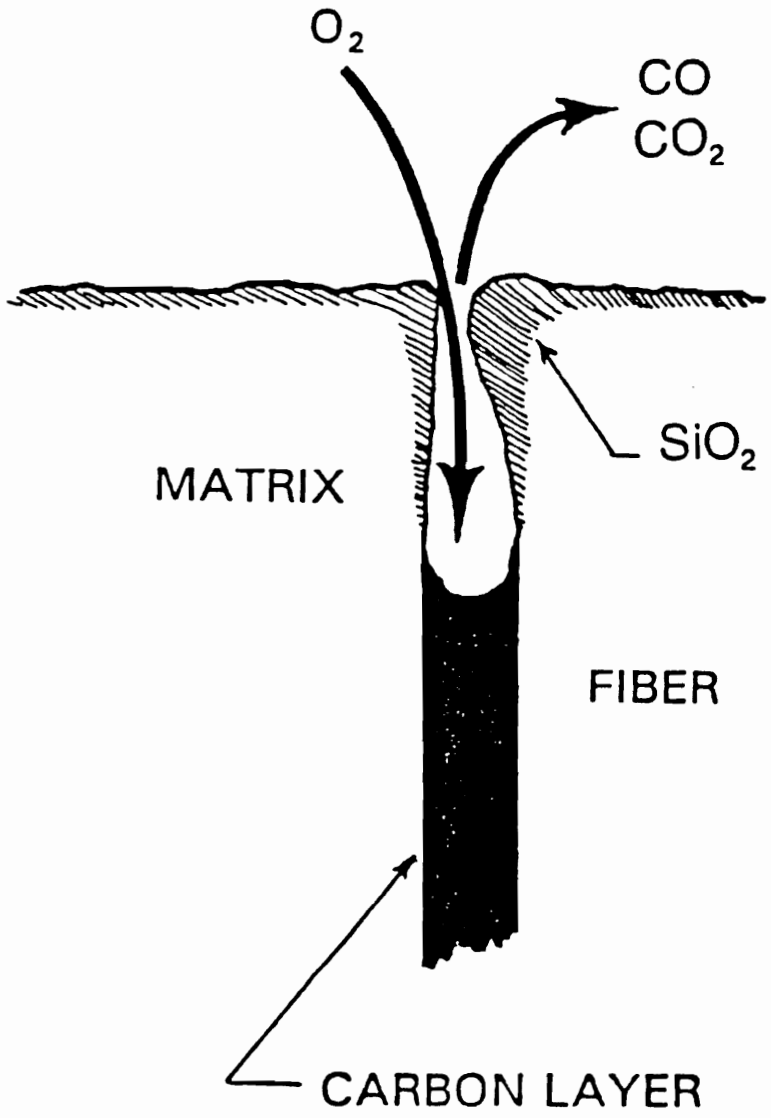

Figure 1.12: Evolution of Nicalon /SiC fiber-matrix interface (pyrolitic carbon) in an oxidizing environment.

2. Investigative Approach

2.1 Tests Specimens and Testing System:

In this investigation 2-D woven flat coupons made of SiC fiber (Nicalon[1]) reinforced enhanced silicon carbide matrix composite (SiC/E-SiC) were chosen as the test specimens. The material is processed by an isothermal chemical vapor infiltration technique (ICVI) and is manufactured by Du Pont Lanxide Composites Inc. The fiber is of ceramic grade Nicalon[1], 1800 denier, 500 filaments per tow, balanced plain weave cloth (0/90 plain weave cloth), with 17 tows per inch and cloth areal weight of 8.24 oz/yd^2. The matrix material is enhanced SiC (enhanced with respect to previous version) which contains boron based particles for protection of fibers against oxidation. Each ply has a thickness of 0.0105 inch (0.0105"), density of 0.83 lbs/in^3, fiber volume fraction of 40%, and porosity of 12%. This new version is developed based on the same manufacturing techniques as with the original Nicalon[1]/SiC and is believed to have superior stress rupture behavior [71]. The final product is in form of square panels (12"x12"). For this study the coupons were cut from the panels and were put back into the furnace where a layer of SiC (80-100 μm) was chemically vapor deposited on their outer surface for further protection against oxidation.

2.1.1 Specimens Geometry:

Based on the chosen test matrices which will shortly follow, two types of specimen geometries were selected, notched and unnotched. The

unnotched specimens with stacking sequences of $[(0,90)/(0,90)]_{2s}$ (cross-ply) and $[(0,90)/(+45,-45)]_{2s}$ (quasi-isotropic) were cut in a bow-tie shape from the panels. Based on their width, they were further divided into two categories. The wide specimens with an average thickness of 0.09", gage section width of 0.75", grip section width of 0.85", and length of 6.0", and the narrow ones with an average thickness of 0.09", gage section width of 0.40", grip section width of 0.50", and length of 6.0". The notched specimens were cut from the $[(0,90)/(0,90)]_{2s}$ panels in a straight edge rectangular shape. They were measured to have an average thickness of 0.09", width of 1.50", length of 6.0" with a 0.25" diameter hole drilled through at their geometric center (figure 2.1). Specimen thickness and width numbers represent average values of three measurements that were made inside the one-inch extensometer gage length located at the center of the specimen. Visual inspection of specimens indicated large variations on surface uniformity and texture. There were mainly due to existence of patches of excess seal coating material on the surface of specimens. These variations were found to be a function of panel numbers which may be explained by the fact that the panels were processed at different times. It is believed poor job in CVD of SiC layer on the outside surface of each panel created this non uniformity.

2.1.2 High Temperature Testing System:

In elevated temperature mechanical testing of ultra-high temperature materials such as ceramic matrix composites many factors such as load train, load train alignment, gripping, heating system and heating process, and strain measurement process and device may influence the test results. To be able to characterize long-term mechanical behavior of

CMCs under in-service environment, an axial testing system with high temperature testing capability was developed. This testing system included a hydraulic testing frame, a furnace, cooling system, an extensometer with high temperature application, and a data acquisition/controller computer system (figure 2.2). This system can be used for long-term mechanical tests such as creep and high cycle fatigue for temperatures up to 2200 °F. The various parts of this test system along with the related issues are briefly explained in the following paragraphs.

Mechanical tests were performed by a servo controlled, hydraulically actuated, MTS load frame with a load capacity of 22 Kips. Since ceramic matrix composites generally exhibit failure to strains of less than 1.5%, machine alignment also becomes one of the primary concerns in any quasi-static or cyclic testing where small amounts of bending could cause premature matrix cracking and influencing the material response. The alignment of testing frame was determined per HSCT standards [72]. The alignment instrument used in this study was a rectangular shaped accurately ground steel bar. The bar was equipped with four resistance foil strain gages at perpendicular planes on either side of the bar's mid-section (total of 8 gages). Test system exhibited a maximum bending strain (face to face) of 12.5 micro strain upon gripping the specimen at zero applied load and a maximum bending of 7.8% at each plane (face to face or edge to edge) for an applied load of 1000 pounds.

Due to versatility and ease of use, a cold gripping system was chosen among the existing gripping systems. This system employed two sets of water cooled hydraulic wedge grips which were essential for through-zero loading of the flat coupon-type specimens. The recent research has proven

that acceptable temperature gradients can be achieved with this technique up to 4200 °F [73]. In all the tests flat friction loaded specimens were gripped under a grip line pressure of 400-450 psi and using three layers of 60 aluminum grid sand paper. Due to size of the furnace and the need for insulating the furnace, only one inch at each ends of a 6" long specimen was gripped. The upper grip temperature did not exceed a maximum of 170 °F for a test specimen temperature of 1832 °F. The cooling of the whole system was achieved by sending cold water through hydraulic wedge grips, high temperature extensometer, and extensometer heat shield. The cooling system included a solenoid valve, water filter, inlet flow meter and outlet flow meter. These features were placed in the cooling network so that in future the cooling process could be monitored via a computer controlled environment. The system safety net was designed so that the heating process and water pressure could be terminated upon triggering the alarms which were to be set based on inlet water flow, inlet and outlet flow differential, grip temperature, furnace temperature, load level, and operation of hydraulic testing frame. These features are necessary in any long-term elevated temperature testing (figure 2.2).

A convection/radiation heating method was used via a splitting face, box type furnace (3.25"x3.25"x3.25") with a series of heating elements. In process of setting up the heating system which included numerous dry run tests to further smooth the heating process, few points were discovered. Originally, furnace was equipped with three sets of heating elements (three on each side). But it was learned (by trial and error) for better temperature control, the middle heating elements should not make any contribution therefore they were disconnected (not removed). The furnace operation was

controlled by a microprocessor based temperature and process controller (master and slave type) via monitoring the specimen temperature using two R-type thermocouples positioned 2.5" apart on the thickness side of the specimen. Also, for optimum temperature control, the master controller should be connected to thermocouple closest to the top heating elements and the slave controller to the thermocouple closest to the bottom heating elements. The smooth operation of extensometer was best achieved when the power outputs (not the temperature) by the master and slave controllers were reasonably stable (not necessarily equal). This may be explained by the fact that thermocouples have slower response than extensometers. The heating process was accomplished according to HSCT standards [74] which required monotonically increasing the test temperature to the target value within a period of 15-20 minutes. Reaching a test temperature of 1800 °F in 20 minutes requires a heating rate of 90 °F per minute. Achieving this heating rate, overall operation of the furnace and ultimately specimen temperature profile were influenced greatly by how well the heating system was insulated. Except for the access ports for extensometer rods (two 0.25" dia holes), thermocouples (three 0.2" dia. holes), and the specimen (two 0.2"x1.5" slits in case of notched specimens), furnace was completely insulated by one-inch thick insulation blanket. This configuration guaranteed smooth operation of heating system for heating rate as high as 120 °F. Although the temperature overshoot did not exceed 1% for test temperature of 1832 °F, the heat up ramp was always followed by a 20 minutes soak time to further stabilize the specimen temperature prior to any load application (figure 2.3). The temperature uniformity of the test specimen 1.0 inch gage section was monitored by readings of three

thermocouples. One was placed at the middle of gage section and the other two were placed approximately 0.25" outside and away from either end of the gage section. Variations in test temperature along the length of specimen were less than 0.1% (figure 2.4).

In elevated temperature testing, specimens were gripped and heated up to the desired temperature in load control mode. This mode of control prevented risk of any possible damage to the specimens, as a result of thermal expansion, prior to mechanical testing. For quasi-static tensile testing, once the prescribed temperature was reached, control mode was switched from load to stroke. This was not possible with the controller 448 MTS controller and a 458 MTS controller was used instead. To be consistent in all of the tensile testing, same procedure was followed for room temperature testing also.

Room temperature strain measurements a MTS extensometer with 1" gage length with maximum operating temperature of 350 °F, 15% maximum range, and 1.5% calibrated operating range, was placed at the geometric center of the specimens. The knife edges of extensometer were securely placed in V-notched aluminum tabs via rubber bands. Aluminum tabs were bounded to specimen using silicon rubber adhesive. Elevated temperature strain measurement was made possible via a one-inch gage length MTS extensometer designed for high temperature applications (maximum operating temperature of 2200 °F) with 15% linear operating range capability. In this study an extensometer calibrated range of 1.5% was used. This is a water cooled unit (requires certain water flow rate for maximum cooling and smooth operation) which comes in contact with specimen via two alumina rods (6" long). Rods were loaded (0.25 pound) by

the leaf springs mounted on the heat shield bracket. Due to surface roughness of specimens alumina rods with conical ends were used as opposed to the rods with straight knife edge. Alumina rods with recommended maximum operating temperature of 2200 °F, are the main limiting factor in using the extensometer unit at higher temperatures.

2.2 Quasi-Static Tensile Tests:

Room and elevated temperature (1800 °F) quasi-static tensile tests are required to understand tensile response, corresponding mechanical properties and the possible temperature effects on tensile behavior. Ultimately, the test results are used in defining fatigue load limits and as baseline data for comparison with remaining properties for various loading situations. These tests were carried out according to the HSCT standards for quasi-static tensile testing of ceramic matrix composites [73]. This required monotonic tensile tests under stroke control for a pre determined stroke rate of 0.02 in/min (obtained by trial and error) in atmospheric air. These tests were performed at another testing laboratory and the results were used in cyclic fatigue testing.

Bow-tie shaped specimens with stacking sequences of $[(0,90)/(0,90)]_{2s}$ and $[(0,90)/(+45,-45)]_{2s}$ were chosen for this stage of testing. Material manufacturer has reported few tensile test data for cross-ply laminates (a total 80 tests at room temperature and 11 tests at 1830 °F). Due to need and limited availability of specimens only one cross ply specimen was dedicated to room temperature testing. This test was useful in verifying material behavior as reported by the manufacturer, and checking the existing testing system

and material system. This data could always be complemented by the room temperature data provided by material manufacturer. The other three specimen were tested at 1800 °F. The quasi-isotropic specimens were evenly distributed for each test temperature. Quasi-static tensile test matrix of unnotched cross-ply and unnotched quasi-isotropic laminates are presented in table 2.1.

Table 2.1: Test matrix for quasi-static tensile tests of $[(0,90)/(0,90)]_{2s}$ and $[(0,90)/(+45,-45)]_{2s}$ laminates.

Number of Tests	Stacking Sequence	Loading Mode	Atmosphere	Test Temperature (°F)
1	$[(0,90)/(0,90)]_{2s}$	Stroke	air	74
3	$[(0,90)/(0,90)]_{2s}$	Stroke	air	1800
2	$[(0,90)/(+45,-45)]_{2s}$	Stroke	air	74
2	$[(0,90)/(+45,-45)]_{2s}$	Stroke	air	1800

2.3 Notch Effect:

Notched specimens were used to study influence of notches on material response, damage initiation, damage growth and state stress in the material. Notch effect on material response was investigated by testing quasi-static tensile tests at 75 °F and 1800 °F in air. The results were examined and compared to the corresponding unnotched specimens. Notch effect on state of stress in the material was studied by application of strip strain gages around at the hole and conducting room temperature tensile test. Room temperature material response at incremental distances from the hole were recorded upon application of load. Full field, non contact, real

time stress patterns measurement at room temperature was attempted using an adiabatic infrared-based thermoelastic technique known as SPATE. Table 2.2 lists the complete test matrix for the notched specimens.

Table 2.2: Test matrix for center notched $[(0,90)/(0,90)]_{2s}$ laminates.

Number of Tests	Type of Test	Loading Mode	Test Temperature (°F)	Atmosphere
2	Quasi-Static Tensile	Stroke	75	air
2	Quasi-Static Tensile	Stroke	1800	air
1	Strip Gage	Load	75	air
2	SPATE	Load	75	air

2.4 Cyclic Fatigue to Failure Tests:

Fully reversed cyclic loads are considered by many to be the most detrimental to fiber composites because of activation of both tensile and compressive damage modes. Depending on the relative competition of these damage modes, either tensile or compressive failure mode ensue. Hence the fully-reversed loading regime provides a good opportunity to observe different damage mechanisms in composite laminates. In a load controlled mode, specimens were subjected to sinusoidal waveform at a frequency of 1 Hz, and a fatigue ratio of R=-1 under atmospheric air at 1800 °F. Cyclic fatigue to failure tests were performed at three different stress levels (σ_1, σ_2, and σ_3) for both cross-ply and quasi-isotropic laminates. These stresses represent three different damage states stress levels. They correspond to well below, right at,

and well above the proportional limit strength (matrix cracking saturation stress level). They were obtained from examination of material response under quasi-static tensile tests at temperature. Based on availability of specimens, at least two specimens were tested at each stress level. Following the HSCT standards on cyclic fatigue of CMC's [75], run-out was set at 10^5 cycles. Run-out specimens were subjected to quasi-static tensile test under stroke control at temperature. Test matrices for fatigue to failure tests of cross-ply and quasi-isotropic laminates are presented in tables 2.3 and 2.4 respectively.

Table 2.3: Test matrix for cyclic fatigue to failure tests of $[(0,90)/(0,90)]_{2s}$ laminates.

Number of Specimens	Loading Mode	Maximum Stress Level	Percent Life Cycled (%)	Fatigue Ratio R	Cyclic Frequency (Hz)	Test Atmosphere	Test Temperature (°F)
2	Load	σ_1	100	-1	1	air	1800
2	Load	σ_2	100	-1	1	air	1800
3	Load	σ_3	100	-1	1	air	1800

Table 2.4: Test matrix for cyclic fatigue to failure tests of $[(0,90)/(+45,-45)]_{2s}$ laminates.

Number of Specimens	Loading Mode	Maximum Stress Level	Percent Life Cycled (%)	Fatigue Ratio R	Cyclic Frequency (Hz)	Test Atmosphere	Test Temperature (°F)
2	Load	σ_1	100	-1	1	air	1800
2	Load	σ_2	100	-1	1	air	1800
2	Load	σ_3	100	-1	1	air	1800

2.5 Interrupted Cyclic Fatigue Tests:

Using the fatigue to failure test results from the previous section, influence of cyclic loading on response and mechanical properties of $[(0,90)/(0,90)]_{2s}$ and $[(0,90)/(+45,-45)]_{2s}$ laminates were investigated. This was accomplished by performing interrupted fatigue tests at three stages of life which correspond to "early", "middle", and "late" stages of fatigue damage development. These regimes represented 10%, 50%, and 90% of average life of two specimens cycled to failure for various load levels and stacking sequences. Stress levels σ_2 and σ_3 which were believed to induce the most damage and not result in any run outs, were chosen as the designated stress levels. Loading type, loading frequency and fatigue ratio were kept the same as the previous case. Tests were performed by cycling specimens under atmospheric air at 1800 °F to a predetermined number of cycles. Test interruptions were followed by quasi-static tensile test at temperature to determine the remaining strength and other related material properties. Results were compared to the as received quasi-static tensile properties intended with the expectation they would reveal some information on damage due to cycling effect as well as exposure time to temperature. The related test matrices for this part of the investigation are presented in the following tables. A total of three tests were performed at each stage of life for each load level.

Table 2.5: Test matrix for interrupted fatigue (tension-compression)/ remaining strength tests of $[(0,90)/(0,90)]_{2s}$ laminates.

Number of Specimens	Loading Mode	Maximum Stress Level	Percent Life Cycled (%)	Fatigue Ratio R	Cyclic Frequency (Hz)	Test Atmosphere	Test Temperature (°F)
3	Load	σ_2	10	-1	1	air	1800
3	Load	σ_2	50	-1	1	air	1800
3	Load	σ_2	90	-1	1	air	1800
3	Load	σ_3	10	-1	1	air	1800
3	Load	σ_3	50	-1	1	air	1800
3	Load	σ_3	90	-1	1	air	1800

Table 2.6: Test matrix for interrupted fatigue (tension-compression)/ remaining strength tests of $[(0,90)/(+45,-45)]_{2s}$ laminates.

Number of Specimens	Loading Mode	Maximum Stress Level	Percent Life Cycled (%)	Fatigue Ratio R	Cyclic Frequency (Hz)	Test Atmosphere	Test Temperature (°F)
3	Load	σ_2	10	-1	1	air	1800
3	Load	σ_2	50	-1	1	air	1800
3	Load	σ_2	90	-1	1	air	1800
3	Load	σ_3	10	-1	1	air	1800
3	Load	σ_3	50	-1	1	air	1800
3	Load	σ_3	90	-1	1	air	1800

To isolate the influence of tension loading on remaining material properties, a series of interrupted tension-tension cyclic fatigue tests were conducted. Material availability allowed testing only quasi-isotropic specimens. These tests were performed under the same conditions as the

previous interrupted tests except that the fatigue ratio which was modified to R=0.05 to represent tensile fatigue testing only. One specimen was dedicated for each load level and its stage of life as represented in table 2.7.

Table 2.7: Test matrix for interrupted fatigue (tension-tension)/remaining strength tests of $[(0,90)/(+45,-45)]_{2s}$ laminates.

Number of Specimens	Loading Mode	Maximum Stress Level	Percent Life Cycled (%)	Fatigue Ratio R	Cyclic Frequency (Hz)	Test Atmosphere	Test Temperature (°F)
1	Load	σ_2	10	0.05	1	air	1800
1	Load	σ_2	50	0.05	1	air	1800
1	Load	σ_2	90	0.05	1	air	1800
1	Load	σ_3	10	0.05	1	air	1800
1	Load	σ_3	50	0.05	1	air	1800
1	Load	σ_3	90	0.05	1	air	1800

2.6 Damage Detection and Damage Monitoring Techniques

One of the challenging issues associated with CMC's is ability to detect and monitor damage and be able to make distinction between defects and performance limiting defects. Non destructive evaluation techniques (NDE) for use with CMC's are not fully developed and what is available, with one exception, is applicable only at room temperature [76]. Depending on the test matrix, and test condition some of the NDE techniques available at Virginia Tech were employed. These methods are presented and explained in the following paragraphs and are explained in details whenever needed.

2.6.1 X-ray Radiography and Die Peneterant:

Standard X-ray radiography have long used in medical and industrial communities as a valuable NDE method. This technique has revealed valuable information regarding as received condition of specimens and may be helpful in identifying possible relationship between the manufacturing damage development and possible failure of CMC materials. In this technique, the target (CMC coupon in this case) is placed on a X-ray film (Kodak Industrex M5 film) as a collection plate. The incoming X-ray photons generated by the X-ray unit (HP Faxitron series) are passed through target. Depending on initial energy of photons, density of the target, the distance photons travel to get to the target (to have uniform incoming rays, specimens are usually placed as far as possible from the X-ray source), the distance photons travel inside the material (specimen thickness), and the time of exposure (as a safety precaution try to minimize time of exposure as much as possible), specific amount of energy carried by X-ray photons is absorbed by target and the rest collected by the film. Presence of any crack on the specimen allow more energy to get absorbed by the film thus presenting the crack as a thin dark line on the film. With composite materials this method works best with uniform planar specimens in detecting damage or irregularities such as density variation, porosity variation, and possibly cracks. This method along with liquid die peneterant technique has proven to be a valuable tool in detection of damage in polymeric composites. Die peneterant which is, highly corrosive, and contains high density material (Zinc), is applied to the specimen. The carrier fluid will seep and carry the zinc into the cracks, pores and crevices. Upon X-raying these regions will show up with a lighter contrast.

2.6.2 C-Scan:

Ultrasonic C-scans are used routinely to inspect for void, variation in density or porosity or any other irregularities associated with components. During C-scanning, the acoustic waves are passed through the material by a sweeping transducer. Non uniformity such as density variation tend to change the speed and result in attenuation and porosity or cracks cause scatter and result in dispersion of the transmitted sound waves. C-scans are found to be specially effective in detecting defects which lie in planes perpendicular to the direction of wave propagation in plane such as delamination. But it is not as effective for defects with lie in planes parallel to the direction of wave propagation.

Depending on the number of transducers used, C-scanning is divided into pitch-pitch and pitch-catch modes. In a pitch-catch mode, one transducers will serve both as a sender and receiver of the acoustic signals. Generated stress waves enter (through a medium which is usually water) from one side and travel through material. Transmitted signals get reflected of a glass placed underneath the material. The reflected waves travel back through the material and finally out of the material where it gets collected by the transducer. In a pitch-pitch mode, there are two transducers being used, one for generation of sound waves and the other for collecting transmitted signals. A data acquisition system constantly collects the transmitted signals and the available software record and maps the change in attenuation and speed of the waves indicating change in material structure.

The C-Scan system used in this investigation (Sonotek-Sonix) composed of an ultrasonic analyzer (Model 50520), 25 MHz transducer (0.25" Dia, 0.5" f.l.), pinducer (to receive transmitted signals) and signal conditioner. Data

acquisition/Imaging unit consists of a 100 MHz digitizer board to capture and store signals received by the pinducer, C-Scan Program (Sonix_Ultrasonic v.3.1), and a Image processing enhancement program(C-VUE v.3.1).

2.6.3 Scanning Acoustic Microscope (SAM) :

SAM systems are widely used as NDE tools to gain more in-depth information about state of material on a localized region. It is known to detect voids as small as twenty microns in sintered ceramics. The full capability of this technique was somewhat compromised, because for through penetration and detection of micro cracks (in order of 100 microns) transducers with capability of generating sound waves at or above 100 MHz are needed. The unit used in this study was limited to a transducer with capability of 30 MHz.

2.6.4 Acoustic Emission (AE):

Initiation and damage progression may be monitored using acoustic emission technique. Acoustic emission signal generated by stress waves which may be produced by some type of yielding or failure within the material (matrix cracking or fiber fracture) are monitored and collected by an acoustic sensor. This technique is one of the few in situ damage monitoring techniques which may be used during quasi-static and cyclic tests. The application of this method is limited to the temperature capability of the transducers. Also this technique could only be used with in situ damage progression where energy is transferred in the form of sound waves. It can not detect the previously existing damage in the material.

Emissions were monitored via a Spartan AT System with an IBM compatible 386 for data acquisition, a software package (SA-LOC v.1.1,

marketed by Physical Acoustic Corporation) for parameter setting and data analysis. A resonant sensor (5/16" dia.) with peak frequencies at 30 kHz and 500 kHz was used for collection of stress waves and subsequent conversion into electrical signal.

2.6.5 Acousto-Ultrasonics (AU):

This technique much like the AE technique may be used as an in situ damage monitoring technique at room temperature for quasi-static tests. Unlike the acoustic emission, stress waves are generated by transducers and propagated through the specimen. Voids and irregularities will change speed and attenuates the incoming stress wave. Monitoring and analysis the speed and attenuation of the acoustic wave are used as means of monitoring the state of damage in material.

2.6.6 Stiffness Degradation:

Measuring change in specimen stiffness as a function of cycles is known to be a well established and effective means of quantifying damage and monitoring damage growth. As damage initiate and grow in the material, the laminates global stiffness decreases due to internal load distributions. The change in stiffness is used in prediction of residual strength and life.

2.6.7 Energy Dissipation:

Monitoring energy dissipation, due to viscous damping and/or Coulomb frictional damping, is commonly used in cyclic fatigue tests as a mean to monitor the state of material. Hysteresis loops are recorded and measured as

a function of cycles. This technique could be useful tool in analysis of the results obtained by some of the other NDE techniques.

2.6.8 Dynamic Signal Analysis (DSA):

Damage and its progression may be monitored based on the new experimental technique developed by Elahi, et al. [77] This technique which uses the signal analysis as a means of investigating damage in fatigue process was developed primarily for elevated temperature testing. It involves the analysis of load and stroke signals output from a conventional serve-hydraulic systems. Using the functions such as cross-spectrum and frequency-response, parameters such as gain factor and phase factor can be measured and related to the state of damage or possibly damage rate in material. Schematic diagram of the experimental set up is presented in figure 2.5. Dynamic data acquisition is performed using an HP9000/PC-315 computer in-line with an HP-3852A/HP-3853A data acquisition control unit as well as an HP 3562-A dynamic signal analyzer. A software routine was developed for real time dynamic response analysis. Phase factor and gain factor from load/stroke signals from the hydraulic testing frame were plotted in conjunction with load, stroke, and temperature data. To avoid disk storage overflow, data were recorded according to their change with respect to the previous events.

In HP 3562-A signal analyzer, the signal on channel 1 was taken as the system's input (load) and the signal on channel 2 was assumed to be its output (stroke). Working in the frequency domain, all the measurements were made at the system's excitation frequency in a linear resolution mode. Initially, using the cross-spectrum function, the system's fundamental

frequency was determined. Finally, using the frequency response function, phase factor and gain factor measurements were made at this frequency (figure 4.7). A complete background and formulation of signal analysis part of the problem from mathematical and application (dynamic signal analyzers) points of view problem are presented in the following few paragraphs.

System response y(t) of any dynamical system may be expressed in terms of impulse (systems dynamic characteristic in time domain t, using the convolution integral

$$y(t) = \int_0^t x(\tau)h(t-\tau)d\tau \tag{2.1}$$

At times engineering application requires expressing system dynamical characteristics in terms of frequency domain, *f*. Consider *transfer function* which is defined as the *Laplace transform* of the system impulse response:

$$H(p) = \int_0^\infty h(t)e^{-pt}dt \quad \text{where p=a+jb} \tag{2.2}$$

For the special case where a=0 and p=$2\pi f$ (along the imaginary axis), the above integral results in *frequency response function* H(*f*):

$$H(f) = \int_0^\infty h(t)e^{-j2\pi ft}dt \tag{2.3}$$

which is simply the *Fourier integral* of the impulse response function. Furthermore H(*f*) may be expressed as

$$\begin{aligned} H(f) &= H_R(f) - jH_I(f) \\ &= \left|H(f)\right| e^{-j\theta(f)} \end{aligned} \tag{2.4}$$

where

$$H_R(f) = \int_0^\infty h(\tau)Cos(2\pi f\tau)d\tau \quad \text{is the real part} \tag{2.5}$$

$H_I(f) = \int_0^\infty h(\tau) Sin(2\pi f\tau) d\tau$ is the imaginary part (2.6)

$|H(f)| = \sqrt{H_R^2(f) + H_I^2(f)}$ is the gain factor (2.7)

and

$\theta(f) = \tan^{-1}\left[\frac{H_I(f)}{H_R(f)}\right]$ is the phase factor [78]. (2.8)

Dynamic signal analyzers measure frequency response function via spectral density functions which they may be obtained using finite Fourier transforms. *Fourier transform* of a signal is defined as:

$$X(f) = \int_{-\infty}^{\infty} x(t) e^{-j2\pi ft} dt \tag{2.9}$$

which is usually referred to as *forward transform*. It is possible to go from frequency domain f, back to the time domain t, via the following transformation

$$x(t) = \int_{-\infty}^{\infty} X(f) e^{j2\pi ft} dt \tag{2.10}$$

which is referred to as the *inverse transform*. These two integrals form what is traditionally known as *Fourier transform pair.*

To evaluate the Fourier transform integral using digital computers, a numerical procedure known as *Discrete Fourier Transform* (DFT) is employed. This requires digital processing of the data at discrete frequencies. First the signal or the variable $x(t)$ is sampled at Δt intervals apart, resulting in a discrete data sequence of $x_n = x(n\Delta t); n = 1,2,\ldots,N$ with period of $T = N\Delta t$ where N is the sample size. Also a fundamental frequency of $f_1 = \frac{1}{T}$, discrete frequency of $\Delta f = f_1$ and the corresponding Nyquist cut-off

frequency $f_c = \frac{1}{2\Delta t}$ are obtained. Then the continuous Fourier transform may be replaced by $X_m = X(m\Delta f); m = 1,2,\ldots,N$ where

$$X_m = X_m(m\Delta f) = \Delta t \sum_{n=1}^{N} x_n(n\Delta t)\, e^{-j2\pi mn/N}; m = 1,2,\ldots,N \qquad (2.11)$$

Assuming that the number of samples N is of multiples of 2, the number of computations in evaluating the above equation is drastically reduced giving rise to what is known as the *Fast Fourier Transform* (FFT) [79].

Spectral density functions (SDF) although a product of engineers (may be evaluated using the FFT of signals), but historically have evolved from correlation functions. Therefore, it is appropriate to say few sentences about correlation functions before covering the SDF. Correlation functions which are time-domain analysis, are mainly used as an indication of a measure of the similarity between two quantities. It is helpful in detection of hidden periodic signals buried in measurement noise. Mathematically *cross-correlation function* $R_{xy}(\tau)$, is comparison between two signals x(t) and y(t) as a function of time shift τ between them, and is defined as followings:

$$R_{xy}(\tau) = \lim_{T\to\infty} \frac{1}{T} \int_0^T x(t)y(t+\tau)dt \qquad (2.12)$$

where $R_{xy}(\tau)$ is always real-valued function which may be positive or negative. It is evident that the correlation function is largest when the two time records are similar or identical. Similarly the *autocorrelation function* may be defined as a special case of cross-correlation function where y(t)=x(t),

$$R_{xx}(\tau) = \lim_{T\to\infty} \frac{1}{T} \int_0^T x(t)x(t+\tau)dt \qquad (2.13)$$

which provides information regarding the general influence of the value of a variable at any time over the value of the variable at a future time. It is worthwhile to mention that, signal analyzers evaluate the correlation functions by direct use of Fourier transforms as followings:

$$R_{xx}(\tau) = F^{-1}\left[X(f)X^{*}(f) \right] = F^{-1}\left[G_{xx}(f) \right] \tag{2.14}$$

and

$$R_{xy}(\tau) = F^{-1}\left[X(f)Y^{*}(f) \right] = F^{-1}\left[G_{xy}(f) \right] \tag{2.15}$$

where F^{-1} is the *inverse Fourier transform* and the functions $G_{xy}(f)$ and $G_{xx}(f)$ are cross spectrum and power spectrum respectively and will be discussed in the following few paragraphs.

Cross spectral density function (also called cross spectrum) measurement is made for applications such as frequency response function measurements and measurement of time delays to name a few. The concept has evolved directly from the cross-correlation function and may be used to describe certain common or joint properties of different data from two or more random processes. Traditionally cross spectrum of a pair of variables x(t) and y(t) is defined as the Fourier transform of the cross-correlation function between those time variables. The two sided (both positive and negative frequencies) form of this function is represented by:

$$S_{xy}(f) = \int_{-\infty}^{\infty} R_{xy}(t)\, e^{-j2\pi ft}\, dt \tag{2.16}$$

However, for practical purposes it is more convenient to work with positive frequencies ($f \geq 0$). This gives rise to the one sided *spectral density function* which is defined as

$$G_{xy}(f) = 2\int_{-\infty}^{\infty} R_{xy}(t)\, e^{-j2\pi ft}\, dt \tag{2.17}$$

where $G_{xy}(f)$ is generally a complex number (because cross-correlation function is not an even function)

$$\begin{aligned} G_{xy}(f) &= C_{xy}(f) - jQ_{xy}(f) \\ &= \left|G_{xy}(f)\right| e^{-j\theta_{xy}(f)} \end{aligned} \tag{2.18}$$

where the real part, $C_{xy}(f)$, is called the coincident spectral density function

$$C_{xy}(f) = 2\int_{-\infty}^{\infty} R_{xy}(t) Cos(2\pi ft) dt \tag{2.19}$$

and the imaginary part, $Q_{xy}(f)$, is called the quadrature spectral density function

$$Q_{xy}(f) = 2\int_{-\infty}^{\infty} R_{xy}(t) Sin(2\pi ft) dt \tag{2.20}$$

Moreover

$$\left|G_{xy}(f)\right| = \left[C_{xy}^2(f) + Q_{xy}^2(f)\right]^{\frac{1}{2}} \tag{2.21}$$

and

$$\theta_{xy}(f) = \tan^{-1}\left[\frac{Q_{xy}(f)}{C_{xy}(f)}\right] \tag{2.22}$$

Auto-spectral density function (also called auto spectrum, power spectrum and power spectral density function) is usually applied to obtain the frequency composition of the physical data. It is an special case of cross-spectral density function where y(t)=x(t),

$$S_{xx}(f) = \int_{-\infty}^{\infty} R_{xx}(t)\, e^{-j2\pi ft}\, dt \tag{2.23}$$

and its one sided spectral density function is

$$G_{xx}(f) = 2\int_{-\infty}^{\infty} R_{xx}(t)\, e^{-j2\pi ft}\, dt \tag{2.24}$$

By the definition the autocorrelation functions is always an even functions of t which means the power spectral density function may be written as the real part of the Fourier transform

$$G_{xy}(f) = 2\int_{-\infty}^{\infty} R_{xx}(t)Cos(2\pi ft)dt$$

$$= 4\int_{0}^{\infty} R_{xx}(t)Cos(2\pi ft)dt \qquad (2.25)$$

Dynamic signal analyzers estimate spectral density functions via finite Fourier transforms of the signals. Then *cross spectrum* may be estimated by

$$G_{xy}(f) = X(f)Y^{*}(f) \qquad (2.26)$$

and *power spectrum* by

$$G_{xx}(f) = X(f)X^{*}(f) \qquad (2.27)$$

where * indicates the complex conjugate of the function[78].

The popular belief is that transfer function is defined as the ratio of a systems output to its input and may be obtained by taking the ratio of averaged measurement of power spectrum of two single channels, as following

$$|H(f)|^2 = \frac{\overline{G_{yy}(f)}}{\overline{G_{xx}(f)}} \qquad (2.28)$$

As may be seen, this definition does not provide any phase information. Also it can be shown that the magnitude obtained from the above relationship is high by the signal to noise ratio [80]. The transfer function may be obtained correctly using the dual channel technique. To obtain a correct relationship between the transfer function and the input-output signals let's consider a case where some noise, n(t), is introduced in the output signal. Then from

the definition of transfer function, the system response would be in the frequency domain is:

$$Y_y(f) = X_x(f)H(f) + N_n(f) \tag{2.29}$$

Recall the relationship between cross spectrum and the Fourier transform of the signals:

$$\begin{aligned}\overline{G_{yx}}(f) &= \overline{Y_y X_x^*} \\ &= \overline{(X_x H + N_n) X_x^*} \\ &= \overline{X_x X_x^* H} + \overline{N_n X_x^*} \\ &= \overline{G_{xx} H} + \overline{N_n X_x^*}\end{aligned} \tag{2.30}$$

or

$$H(f) = \frac{\overline{G_{yx}}(f)}{\overline{G_{xx}}(f)} + \overline{N_n X_x^*} \tag{2.31}$$

where — indicates the average value of the function. But N_n and X_x^* are uncorrelated therefore the $N_n X_x^*$ term will average to zero. Then the frequency response function is best obtained from the following relationship:

$$H(f) = |H(f)|e^{-j\theta(f)} = \frac{\overline{G_{yx}}(f)}{\overline{G_{xx}}(f)} \tag{2.32}$$

2.6.9 Stress Pattern Analysis by Thermal Emission (SPATE):

Based on the principal of thermoelastic effects in elastic solids, dilitational deformation of the material results in reversible temperature change under adiabatic conditions. Under cyclic loading, the material's temperature is found to have the same waveform type and waveform frequency as the applied load. Local temperature changes on the surface of

the specimen can be related to local stress and ultimately to the damage and damage progression. Infrared radiometers with high sensitivity and response time are used to measure temperature change on the surface of a dynamically-stressed material. This non-contact technique can provide full field, real time stress patterns of structures with complex geometry which may explain its popularity in the past few years. The theory was developed by Lord Kelvin based on laws of thermodynamics he proposed that when homogeneous, isotropic, linear elastic materials are subjected to cyclic loading under adiabatic conditions, the change in material principle stresses result in a change in material temperature

$$\Delta t = -\frac{\alpha}{\rho c_\sigma} T_o(\Delta\sigma_1 + \Delta\sigma_2 + \Delta\sigma_3) \tag{2.33}$$

where $\Delta t, \alpha, \rho, c_\sigma, T_o,$ *and* $\Delta\sigma$ represent material temperature change, thermal expansion coefficient, density, volumetric specific heat at constant stress, initial temperature, and change in principle stresses respectively. The system used in this study, SPATE 9000 is manufactured by Ometron Co., consists of a scanner equipped with an infrared photon detector linked to a correlator (lock-in amplifier) and two computers. According to above materials with positive thermal expansion coefficient a negative dilatation results in an increase in its temperature where state of pure shear does not cause any change in temperature. This technique is intended to provide a correlation between real time stress redistribution patterns, representing of damage evolution, and the measurable remaining parameters such as strength and stiffness.

The detector temperature changes in order of 0.001 °F according to Stefan-Boltzmann law, in which the change in specimen surface temperature is related to infrared radiation photon emittance, $\Delta\Phi$, as

$$\Delta\Phi = 3eBT_o^2\Delta T \tag{2.34}$$

where *e and B* are material's emissivity and Boltzmann constant.

The camera scans the marked surface area of the specimen point by point and raster like. Scanning time is function of scanning resolution (as small as 0.02" dia circles) and the time spent on scanning of each point (known as time constant).

To maintain an adiabatic deformations an excitation frequency of 5 Hz was used which in turn will be used by the lock in amplifier to ensure only collection of temperature variation of the same frequency by the detector. A detailed review of the literature on this technique was done by Bakis [81].

2.6.10 Environmental Scanning Electron Microscopy (ESEM):

An ESEM unit was used to visually investigate micro details of the fractured surfaces of the failed specimens as well as in-situ monitoring of possible changes in dimensions of fiber bundle, fiber, interface, and matrix due to exposure to 1800 °F test temperature. This method is believed to give valuable information such as failure mode, and fiber matrix bond strength. For example a strong fiber matrix bond results in less fiber pull out ("brittle" fracture) and a weak fiber-matrix bond is translated into a clean and long fiber pull out.

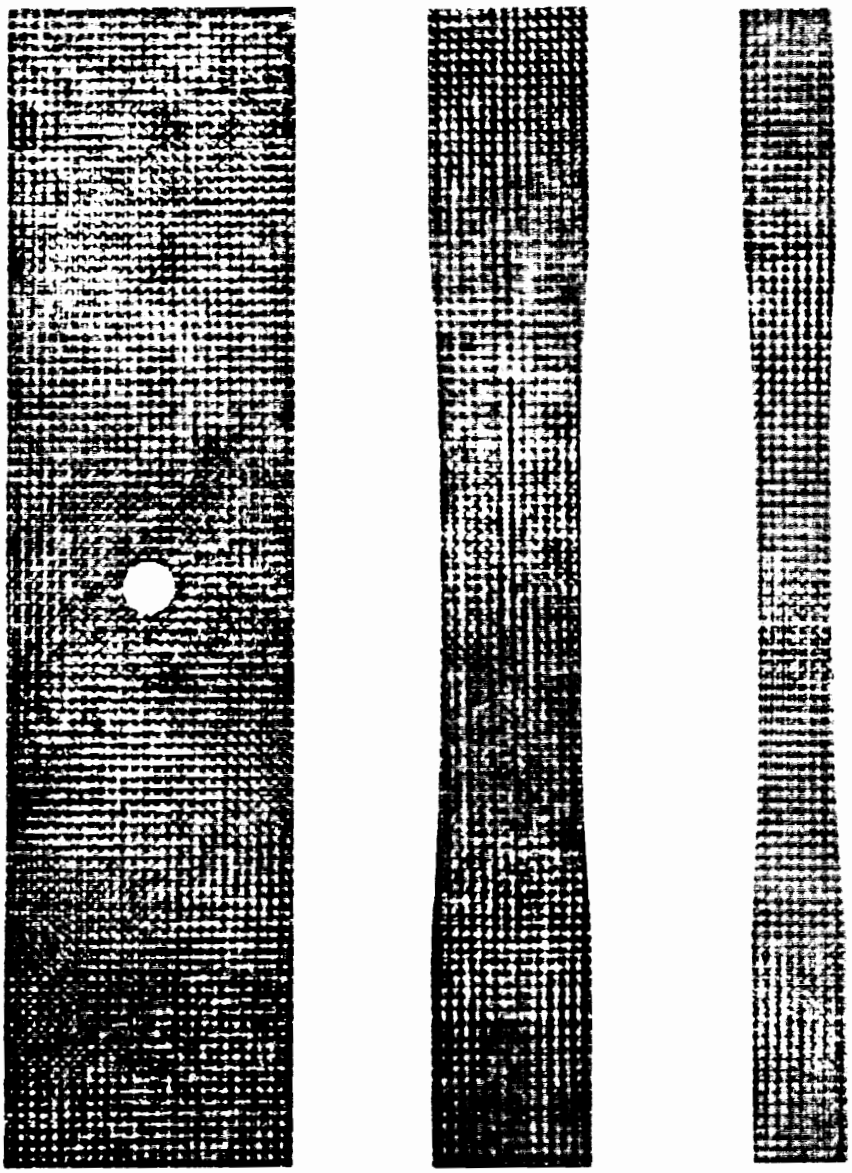

Figure 2.1: X-ray radiographs of test specimens.

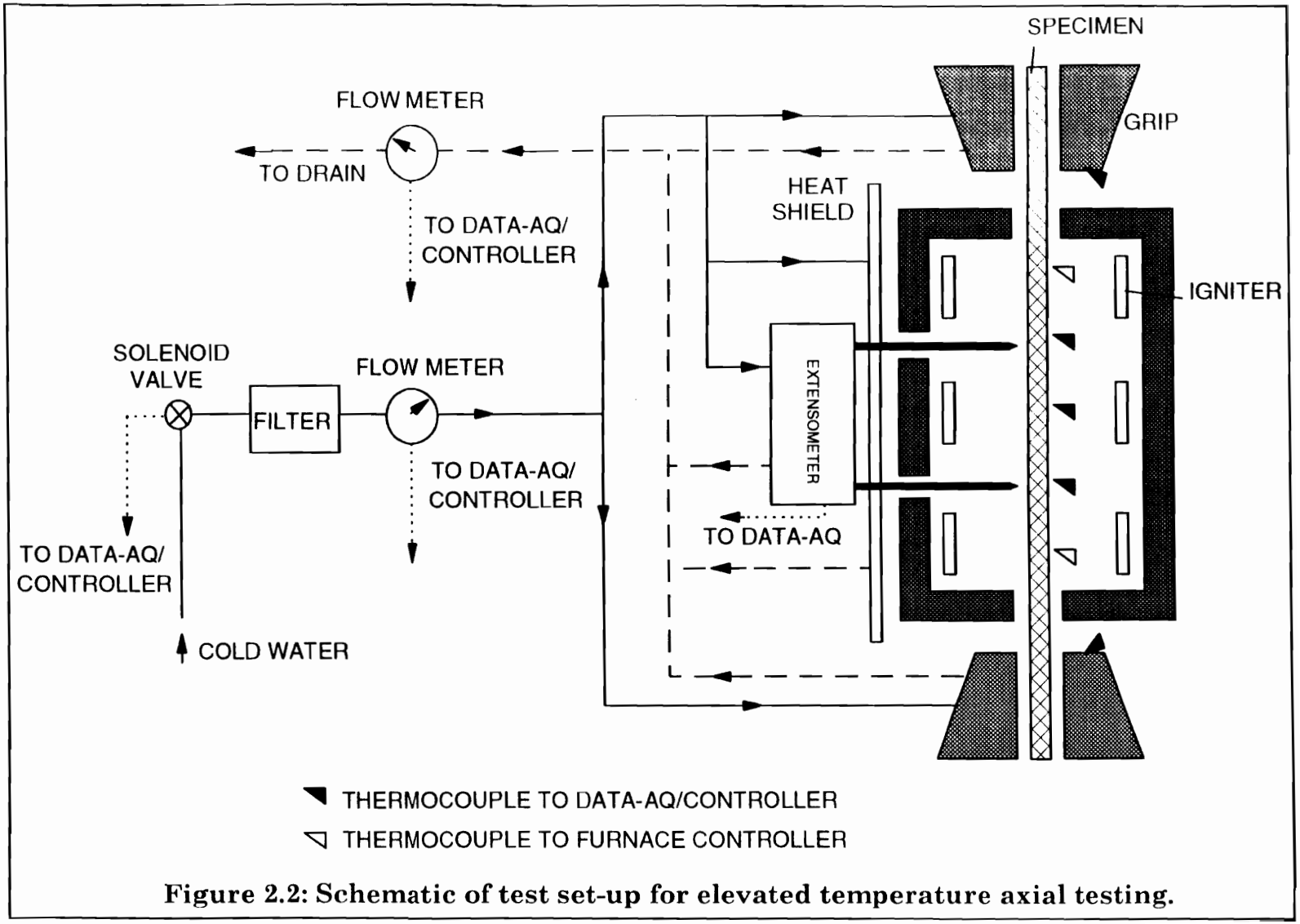

Figure 2.2: Schematic of test set-up for elevated temperature axial testing.

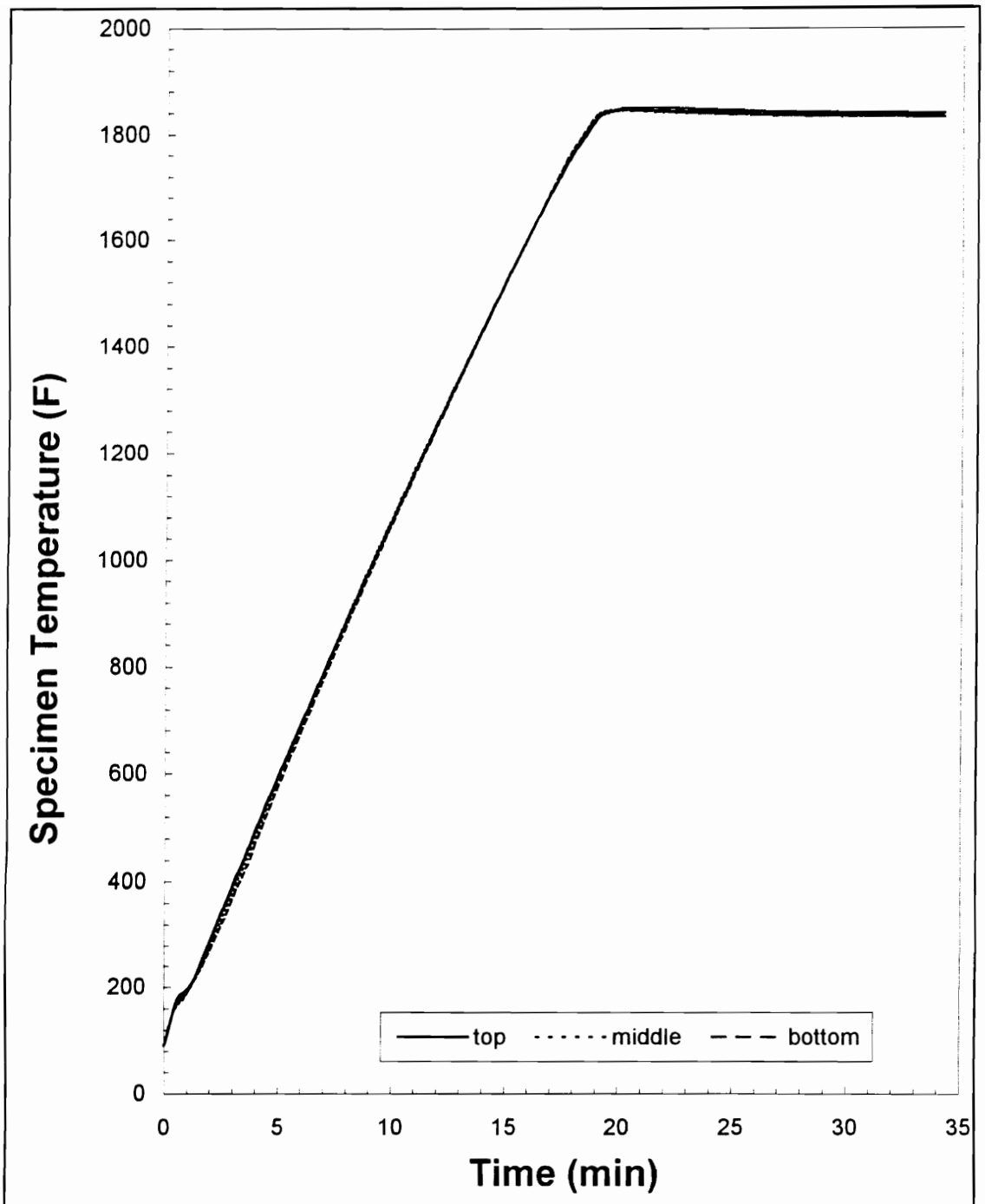

Figure 2.3: Typical heating cycle for an elevated temperature testing.

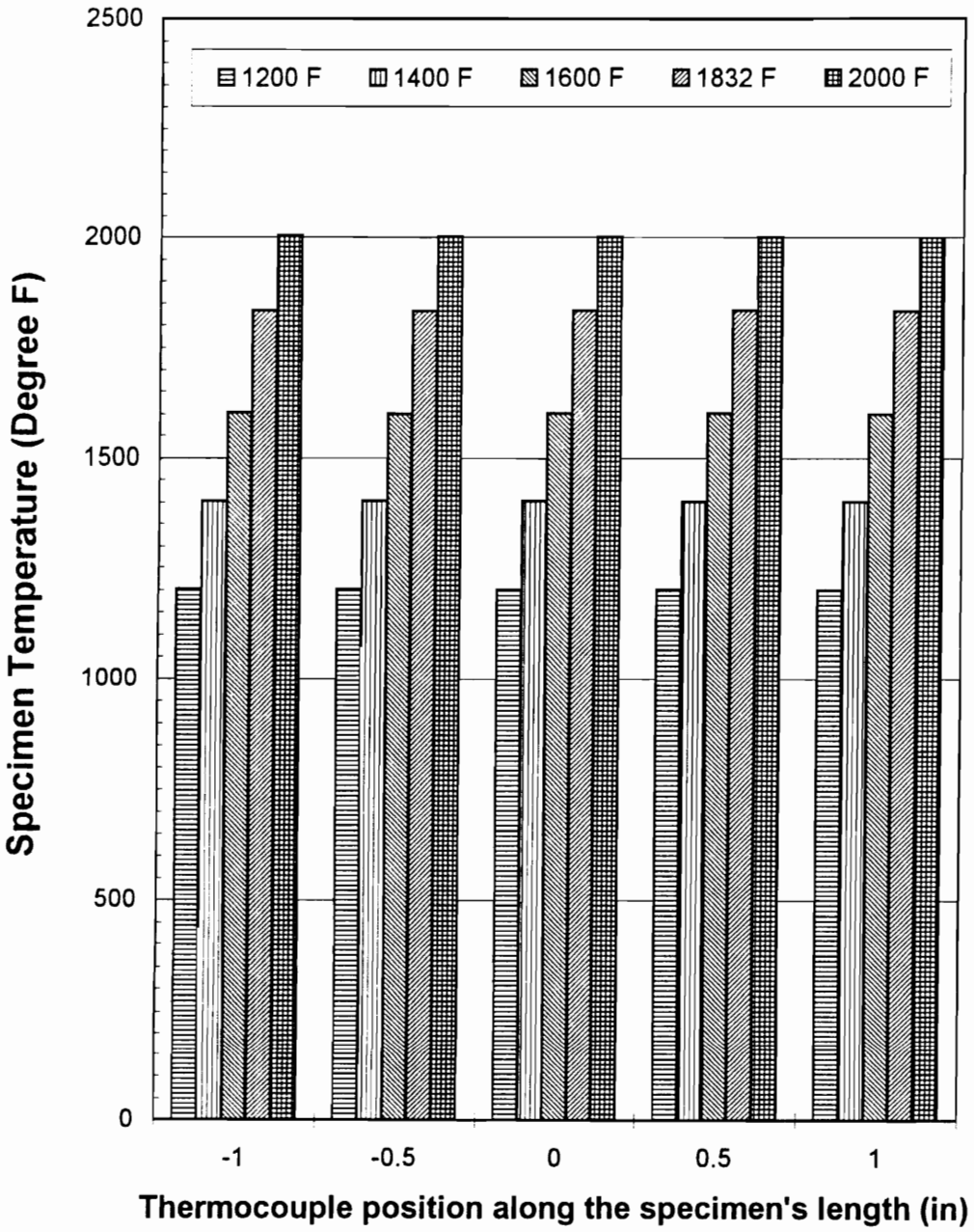

Figure 2.4: Specimen temperature profile for various furnace temperature settings.

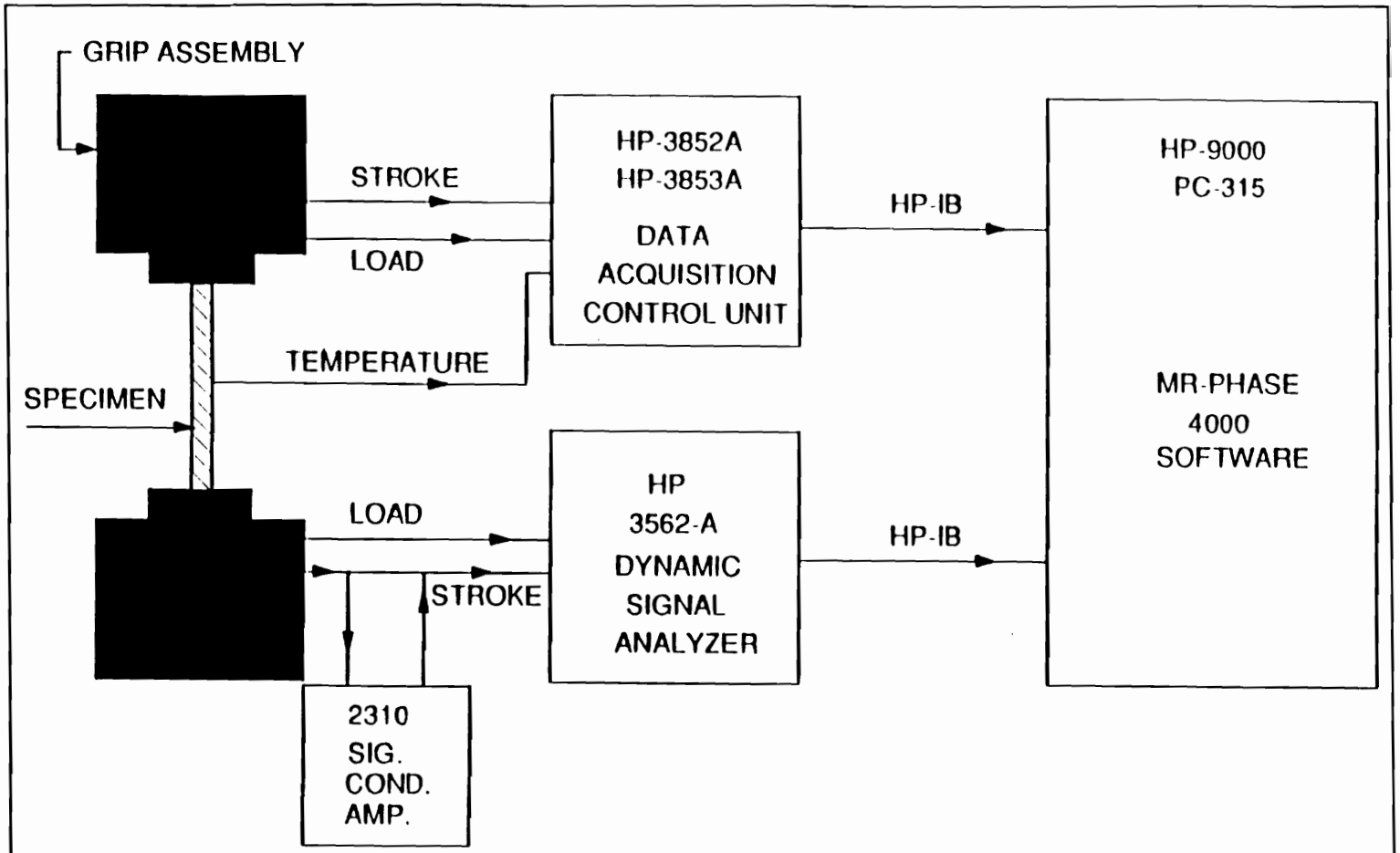

Figure 2.5: Experimental set-up for Dynamic Analysis Technique.

3. Quasi-Static Tensile Behavior

Quasi-static tensile tests of the unnotched specimens were not part of the test plan to be carried out at VPI. The following room and elevated temperature tensile responses and properties were obtained from Pratt & Whitney corporation (P&W). Test results of unnotched $[(0,90)/(0,90)]_{2s}$ laminates, unnotched $[(0,90)/(+45,-45)]_{2s}$ laminates, and center-notched $[(0,90)/(0,90)]_{2s}$ laminates are presented in the following sections. Each table lists individual test results along with their average values. The average values of test results of unnotched specimens with stacking sequences of $[(0,90)/(0,90)]_{2s}$ and $[(0,90)/(+45,-45)]_{2s}$ will be used as the baseline data for comparison purposes and setting the fatigue load limits.

3.1 Unnotched $[(0,90)/(0,90)]_{2s}$ Laminates:

A total of four specimens, one at 75 °F and three at 1800 °F, were pulled to failure quasi-statically. Tensile responses are presented in figure 3.1. Stress-strain curves indicate typical response of fiber reinforced ceramic matrix composites in which upon application of load, material deforms elastically in linear manner with a Young's elastic modulus of Ei. This region although linear but it is associated with some micro cracks, fiber matrix debonding and fiber breaks. This regime extends up to the start of a second region which is highly nonlinear. In this region the existing matrix micro cracks transform into major cracks causing large amount of fiber breaks and subsequent fiber pull-outs which bridge the cracks. The stress associated with this region marks a definite transition from the linear elastic region to a nonlinear region, is referred to as

the proportional limit strength (PLS). Following the HSCT/EPM standards [74], This point was obtained by locating the point of intersection between the stress-strain curve and a line drawn parallel to slope of initial Young's elastic modulus with 0.005% offset strain. Following this transition region, further application of load causes appearance of a second nonlinear region which is associated with large amount of fiber breaks, fiber pull-out and fiber bridging. In this region fibers are the main load carriers. More loading causes statistically enough fiber breakage in which the material can not sustain any further loading resulting in failure of the specimen. This point marks the ultimate tensile strength (UTS) of the material.

Measured material properties for both test temperatures are presented in table 3.1. From room temperature response, average values of 22.0 Msi for Ei, 29.5 Ksi for UTS and strain to failure of 0.32% were obtained. The PLS was measured to be 12.3 Ksi with a corresponding strain to of 0.06%. It should be noted that Du Pont Lanxide PLS of 8.0 Ksi with a corresponding strain of 0.045%, was not measured with any offset strain. This may explain the lower PLS value reported by Du Pont Lanxide. In general, the obtained UTS and strain to failure data were significantly lower than the Du Pont Lanxide data. Based on the fracture location, the 1800 °F test results have shown large variations in material response specially in strain to failure values. Therefore, it was decided to use tests results with highest strain to failure values (specimens i.d.'s 007-01-022-03 and 0007-001-025-03) for averaging purposes. This resulted in average values of 20.5 Msi for Ei, 35.8 Ksi for UTS, and 0.52% for strain to failure, 12.35 Ksi for PLS, and 0.07% for its corresponding strain.

The above test results have revealed significant temperature influence on material properties. On average the 1800 °F tests have resulted in a

decrease of 7% in Ei, an increase of 21% and 62% in UTS and strain to failure respectively. The increase in ultimate stress and strain can be related to relaxation in residual stresses and ultimately disappearance of interface. Although the increase in PLS was not significant but its corresponding strain showed an increase of 16%.

Table 3.1: Quasi-static tensile test* results of $[(0,90)/(0,90)]_{2s}$ laminates.

Specimen I.D.	Gage Width (in)	Test Temperature (°F)	Elastic Modulus (Msi)	PL Stress @ 0.005% offset Ksi)	PL Strain @ 0.005% offset (%)	Ultimate Strength (Ksi)	Ultimate Strain (%)	Fracture Location
007-01-017-02	0.75	74	22.00	12.30	0.060	29.50	0.320	OX
Ave. Value	—	***74***	***22.00***	***12.30***	***0.060***	***29.50***	***0.320***	—
Du Pont*	—	***73***	***20.50***	***8.00***	***0.045***	***33.00***	***0.410***	—
007-01-018-04	0.75	1800	20.00	12.10	0.070	32.20	0.440	OX
007-01-022-03	0.40	1800	21.00	12.00	0.070	35.00	0.530	IX
007-01-025-03	0.40	1800	20.00	12.70	0.070	36.60	0.510	IX
Ave. Value	—	***1800***	***20.50***	***12.35***	***0.070***	***35.80***	***0.520***	—

* Tests were performed by Cincinnati Testing Laboratory (CTL) for Pratt &Whitney.

* Ave. values of 81 room temperature tests performed by Du Pont Lanxide Composites, Inc.

3.2 Unnotched $[(0,90)/(+45,-45)]_{2s}$ Laminates:

A total of four specimens with $[(0,90)/(+45,-45)]_{2s}$ stacking sequence were equally distributed for 74 °F and 1800 °F tests. In general tensile responses were similar to the previous case (figure 3.2). Room temperature tests resulted in an average initial elastic modulus of 19.0 Msi, ultimate strength of 29.35 Ksi and strain to failure of 0.35%. Proportional limit strength of 11.35 Ksi with its corresponding strain of 0.065% were also obtained. Elevated temperature tests resulted in a decrease of 16% in Ei, an increase of 12% in

UTS and an increase of 31% in strain to failure from their corresponding room temperature values. The PLS basically remained unchanged but the corresponding strain showed an increase of 23%.

In comparison to cross-ply laminates, most of the room temperature properties of quasi-isotropic laminates remained the same except elastic modulus which showed a drop of 14%. The influence of off-axis lamination on material properties was more obvious for 1800 °F tests. A decrease of 22%, 8% and 12% for Ei, UTS and strain to failure were recorded respectively. The change in PLS was not significant but its strain decreased by 14%.

Table 3.2: Quasi-static tensile test* results of $[(0,90)/(+45,-45)]_{2s}$ laminates.

Specimen I.D.	Gage Width (in)	Test Temperature (°F)	Elastic Modulus (Msi)	PL Stress @ 0.005% offset (Ksi)	PL Strain @ 0.005% offset (%)	Ultimate Strength (Ksi)	Ultimate Strain (%)	Fracture Location
007-01-012-01	0.75	74	20.00	10.70	0.060	31.20	0.390	OX
007-01-012-07	0.75	74	18.0	12.00	0.070	27.50	0.310	OX
Ave. Value	**—**	***74***	***19.00***	***11.35***	***0.0650***	***29.35***	***0.350***	**----**
007-01-012-02	0.75	1800	16.00	12.40	0.080	32.30	0.430	OX
007-01-012-04	0.75	1800	16.00	11.00	0.080	33.60	0.490	IX
Ave. Value	**—**	***1800***	***16.00***	***11.70***	***0.080***	***32.95***	***0.460***	**----**

*Tests were performed by Cincinnati Testing Laboratory (CTL) for Pratt & Whitney.

3.3 Center-Notched $[(0,90)/(0,90)]_{2s}$ Laminates:

Room and elevated temperatures tensile tests of center notched cross-ply laminates were conducted by measuring the strain across the hole in direction of load application. Stress-strain responses and material properties for both test

temperatures are presented in figure 3.3 and table 3.3 respectively. Notch influence preceded the temperature effect therefore resulting in similar mechanical properties for both temperatures. The notch influenced the 75 °F tests by decreasing UTS and strain to failure by 35% and 38% from their corresponding unnotched values. As expected, initial elastic modulus remained basically unchanged at 20.41 Msi. Similarly, the 1800 °F tests indicated a decrease of 42% and 64% in UTS and failure strain from their corresponding unnotched values. In all of these tests, presence of notch guaranteed a fracture location inside the one inch extensometer gage length (figure 3.4).

In general, higher temperature did not result in a significant change in material response of notched specimens. The most noticeable differences were occurred in UTS, PLS and its corresponding strain in which temperature resulted in an increase of 8%, 12% and 17% from their corresponding room temperature values respectively.

Table 3.3: Quasi-static tensile test results of center notched $[(0,90)/(0,90)]_{2s}$ laminates.

Specimen I.D.	Test Temperature (°F)	Elastic Modulus (Msi)	PL Stress 0.005% offset (Ksi)	PL Strain 0.005% offset (%)	Ultimate Strength (Ksi)	Ultimate Strain (%)	Fracture Location
0007-001-008-01	75	19.33	9.25	0.053	19.55	0.197	IX
0007-001-008-04	75	21.49	10.25	0.055	18.98	0.199	IX
Ave. Value	***75***	***20.41***	***9.75***	***0.054***	***19.27***	***0.198***	------
0007-001-008-02	1800	21.14	11.25	0.063	20.96	0.188	IX
0007-001-009-02	1800	19.10	10.50	0.063	20.75	0.185	IX
Ave. Value	***1800***	***20.12***	***10.88***	***0.063***	***20.86***	***0.187***	------

3.4 Damage Detection:

Center-notched specimens were also chosen to investigate the application and success rate of some of the NDE techniques such as X-ray, C-scan, SAM, AE, AU, and SPATE. The results obtained from application of these techniques along with a stress distribution study are presented in the following few paragraphs.

During the course of this investigation, specimens were always X-rayed (40 kv for 2 minutes) prior to any mechanical testing in hope to reveal any possible processing defects. The technique was capable of revealing weave patterns and density variation in specimens due to various degree of matrix infiltration during a CVI process. Low density regions were shown with darker contrast than the high density regions in the positive (print figure 2.1). To detect damage caused by any mechanical loading, specimens were X-rayed before and after exposure to stress levels higher than PLS (to insure presence of major cracks). The technique was not sensitive enough to detect any change in material structure on meso and micro levels. Applicability of die penetrate which is a mixed solution consisting of 60 grams of Zinc Iodine, ZnI_2, 10 ml of Kodak Photo-Flo 200, 10 ml of isopropyl alcohol, and 10 ml of distilled water, was also investigated. It was noticed that unlike polymeric composites the die did not penetrate into holes, cracks and crevices. This was believed to be due to incompatibility of die carrier (Photo-Flo) with the matrix material. Use of another carrier fluid is recommended instead. Damage in CMC's occur in a much smaller scale than the PMC's and are usually in form of matrix cracks, fiber matrix debonding, and fiber fracture. To detect such a small scale damage, X-rays units with micro-focus capability are needed. With CMC's, upon removal of load cracks tend to close up. The suggested micro focus X-ray

unit should have the capability to X-ray the specimen in-situ. If not, construction of load application jig is needed to open the cracks while specimen is placed in a X-ray machine (cabinet type) with a micro focus unit. This jig could be in form of horizontal screw type machine equipped with a LVDT, and a small load cell (or a stiff spring with known spring constant).

Specimens were always C-scanned prior to any mechanical loading (figure 3.5). The colored scale represents the degree of signal attenuation as it goes through the specimen. Darker colors correspond to less attenuation (black color for the hole) than the lighter colors. Followings are the factors which prevented obtaining images with better quality and more details. Detection of small cracks (in order of 100 microns) requires high frequency transducers (in order of 100 MHz). Very high surface roughness of these specimens translated into oblique surface angles which in turn reflected and weakened the signal prematurely and resulting in some distortion in the signal. In the case of CMCs, attenuation by the matrix material is very high therefore not giving the fiber/matrix weak interface to transfer the signal as clearly.

The results obtained from SAM technique is shown in figure 3.6 as the unit was able to scan the sub surface area (-2 mm). Surface non uniformity seemed to influence the results greatly. White circles on the scan represents fiber bundle cross-over which is usually accompanied with large voids around them. One the problems encountered in use of SAM is difficulty in scanning the exact location before and after loading.

Application of acoustic emissions technique was possible only with room temperature tensile testing of notched specimens. Once the system gain and threshold were set, vacuum grease was applied (as a coupling) between

the sensor and the specimen. Sensor was clamped to the specimen, above the notch (outside the extensometer gage length), via a C clamp. Under stroke control, specimen was loaded monotonically in tension (at a rate of 0.02 in/min) and AE activities were collected [figures 3.7-3.8]. The AE activities may be best related to the rate of damage as is depicted in figure 3.9. For the time interval 0-5 seconds, there was not any AE activity and secant modulus basically stayed constant. During the 5-15 seconds time interval, number hits increased almost monotonically and secant modulus decreased. This time interval is associated with large amount of matrix cracking causing a drop from initial elastic modulus. At the end of this interval AE activities were stabilized indicating saturation of matrix cracks. Further loading caused more fiber breaks and more degradation of modulus but at a slower rate. Finally, the number of fiber fracture reached a critical mass resulting in failure of laminate. In general, interpretation of results are extremely difficult. Determination and contribution of each damage mechanisms (such as matrix cracking, fiber fracture, interface debonding,..) involved in generation of AE signals requires numerous amount of signal profiling and signal processing.

The results obtained from AU measurements are represented by time variation of parameters such as Mo which is the first moment, and M_1 the second moment of the received signal in figures 3.10-3.11. Value of Mo (energy of signal) and M_1 decrease with time. Degradation of M_1 resembles that of secant modulus which starts with a plateau (elastic region) lasting for almost 8 seconds followed by a decrease because of major matrix cracking.

Adiabatic Themography technique was applied using the SPATE system. First, system operation was validated by an area scan of a center notched aluminum specimen under $\sigma_{max} = 0.7\ S_y$ at a frequency of 1 Hz (figure

3.12). Darker color correspond to higher stressed areas with the highest values at either side of the hole on an axis transverse direction to the load. Then a notched composite specimen was subjected to maximum cyclic loading of 11 Ksi, fatigue ratio of R=0.05 and frequency of f=5 Hz under atmospheric air at room temperature. An area of 1.5"x1.5" at the geometric center of specimen was marked for scanning. The results of an area scan and a line scan are presented in figures 3.13-3.14. The line scan indicated extremely noisy signal. It was believed that non uniformity of surface area and small strain levels may have contributed to getting a distorted scan. To smooth the specimen surface and enhance the deformation signal, few layers of compliant adhesive (0.025"thick) were applied. This was followed by applying a thin layer opaque paint (can even be white color contrary to common belief). For the same loading conditions, new scans did not show any improvement in the signal. Therefore the idea was shelved for the time being.

In the SPATE line scan, the expectation was to see a signal with a large amplitude at the crack tip which decreases asymptotically toward the edge of specimen. Not being able to get such a signal, it was decided to measure stress concentration and stress distribution around the hole. To do so, strip strain gages (Micro Measurement brand, EP-08-045pg-120) were placed adjacent to the hole along the axis perpendicular to the load direction as shown in figure 3.15. To accommodate the strain gages on the specimen which had a rough surface texture, smoothing was made possible by application of a layer of epoxy (0.035" thick). Gages were then bonded to the specimen via adhesive (M-bond 200). Specimen was loaded quasi-statically to a stress level of 4.3 Ksi and unloaded back to zero. Results are presented in figure 3.16 in form of maximum strain as a function distance to the hole. The

data indicates a definite trend which was not the case for SPATE line signal. It is recommended to check the calibration of camera detector for the SPATE system.

An SEM unit was used to investigate the fracture surfaces of 75 °F and 1800 °F tensile test specimens. Fractured surface were cut and gold sputtered for SEM observation. Surfaces showed torturous fracture path with large amount fiber pull-out for both test temperatures (figures 3.17-3.18). In general, one expects an elevated temperature test result in more fiber pull-outs, longer pull-out lengths, and larger strain to failure than the room temperature tests such those shown in figures 3.19-3.20 for regular Nicalon[1]/SiC. But, in the case of notched specimen, the tensile behavior of center-notched specimens were mainly dominated by the presence of the notch such that the strain to failure were stayed almost the same for both test temperatures. Therefore, the notched specimens showed similar amount of fiber pull-out and pull-out lengths at both test temperatures. However, the 1800 °F tests resulted in clean fiber pull-outs and the 75 °F tests did not (figures 3.21-3.22). This is believed to be related to disappearance of fiber matrix interface (figure 3.23) and relieve of residual stresses at elevated temperatures. As it was mentioned earlier, in order to protect the fibers against oxidizing environment, the matrix material included boron-based particles. At high temperatures they melt and react with oxygen to form a sealant glass around the fibers [82]. Due to proprietary nature of the material processing, the details regarding the amount, distribution, required melting temperature and time for these inhibitors are not known at the moment. Comparison of 75 °F and 1800 °F tests specimens indicated that at 1800 °F these particle melt on to the adjacent fibers (figure 3.24), resulting in a new

layer of coating on the fibers. Close observation of the matrix material where the fibers were pulled out of, revealed the structural transformation matrix went through at higher temperature. Setting aside the porosity issue for the time being, matrix was found to be a relatively dense at room temperature whereas exposure to 1800 °F resulted in a highly porous matrix material (3.25-3.26).

A ESEM unit was used to investigate the possible mechanical effect of temperature on matrix, fiber, interface, and the fiber bundle. To make measurement at the interface level with a thickness as high as 1 micron, elaborate polishing of sample specimens are required. Using an automatic polishing unit along with a polishing procedure which included using 45 micron, 30 micron, 15 micron, 6 micron, 3 micron, 1 micron and 0.25 micron diamond paste polisher, sample specimens were polished and cleaned with acetone. The ESEM unit unlike regular SEM does not require high vacuum chamber therefore making it possible to operate with specimens at elevated temperatures. The unit does not require any gold sputtering of the specimen. A water cooled high temperature stage was used for both 75 °F and 1800 °F temperatures. Room temperature measurements of fixed locations on fiber bundle, fiber, interface, and matrix were made. The heating element which was located beneath the specimen was brought to 1800 °F in 30 minutes using an on/off temperature controller. To ensure equilibrium, the specimen was held at this temperature for 20 more minutes before any measurements were made. The same exact location on the fiber bundle, fiber, interface, and matrix were measured again and results were compared to room measurements made earlier (figures 3.27-3.34). Results revealed the following temperature effect on the composite constituents. Fiber bundle thickness was not changed, fiber

diameter (17.6 micron originally) was increased by 2%-3%, interface thickness (849 nm originally) was decreased by 12%, and matrix thickness was increased by 30%. It is believed that the interface is not present at these temperatures therefore the recorded change in interface thickness may have been the expansion of fiber and matrix into the space left by the original interface material.

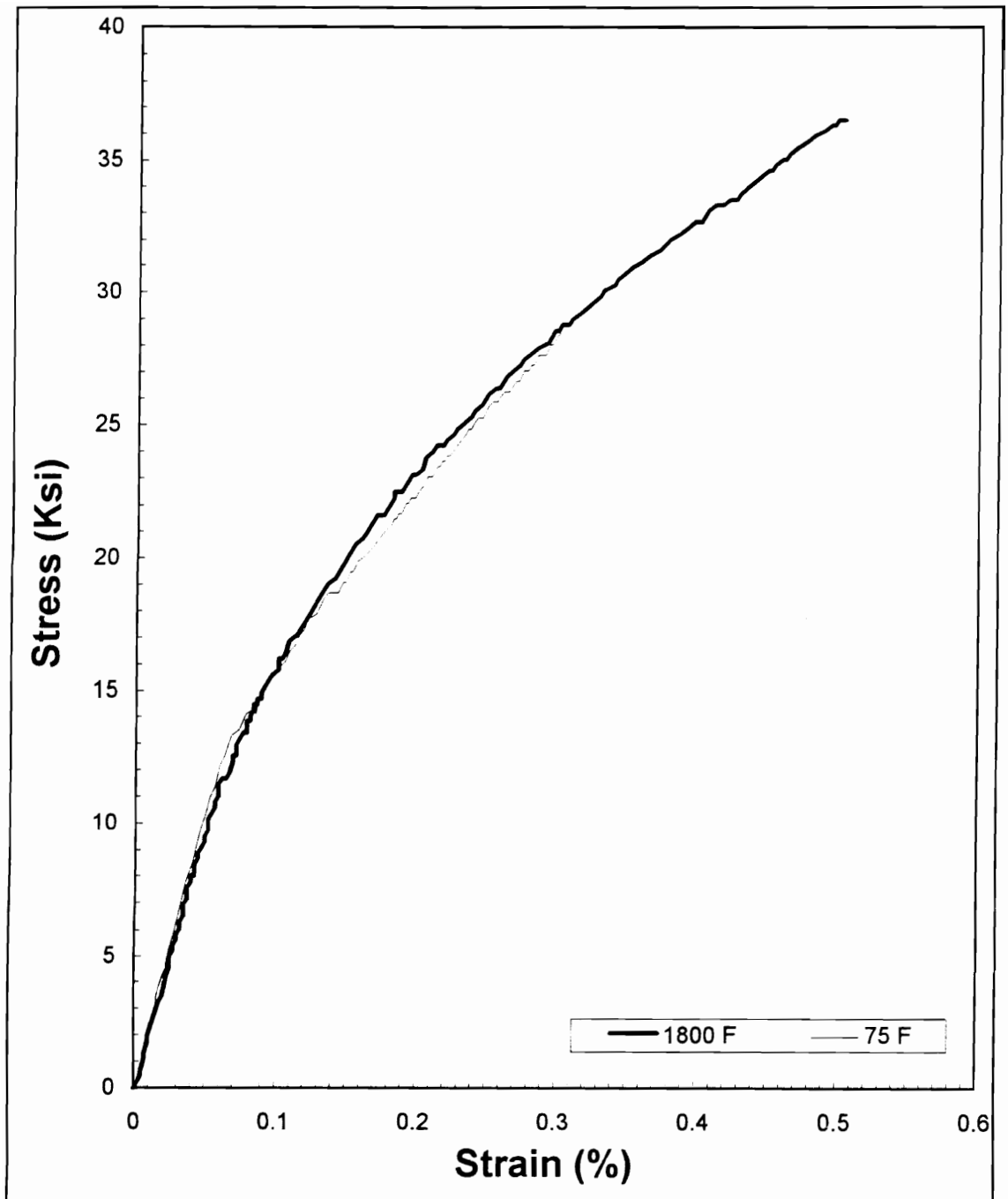

Figure 3.1: Room and elevated temperature quasi-static tensile responses of $[(0,90)/(0,90)]_{2s}$ laminates in atm. air.

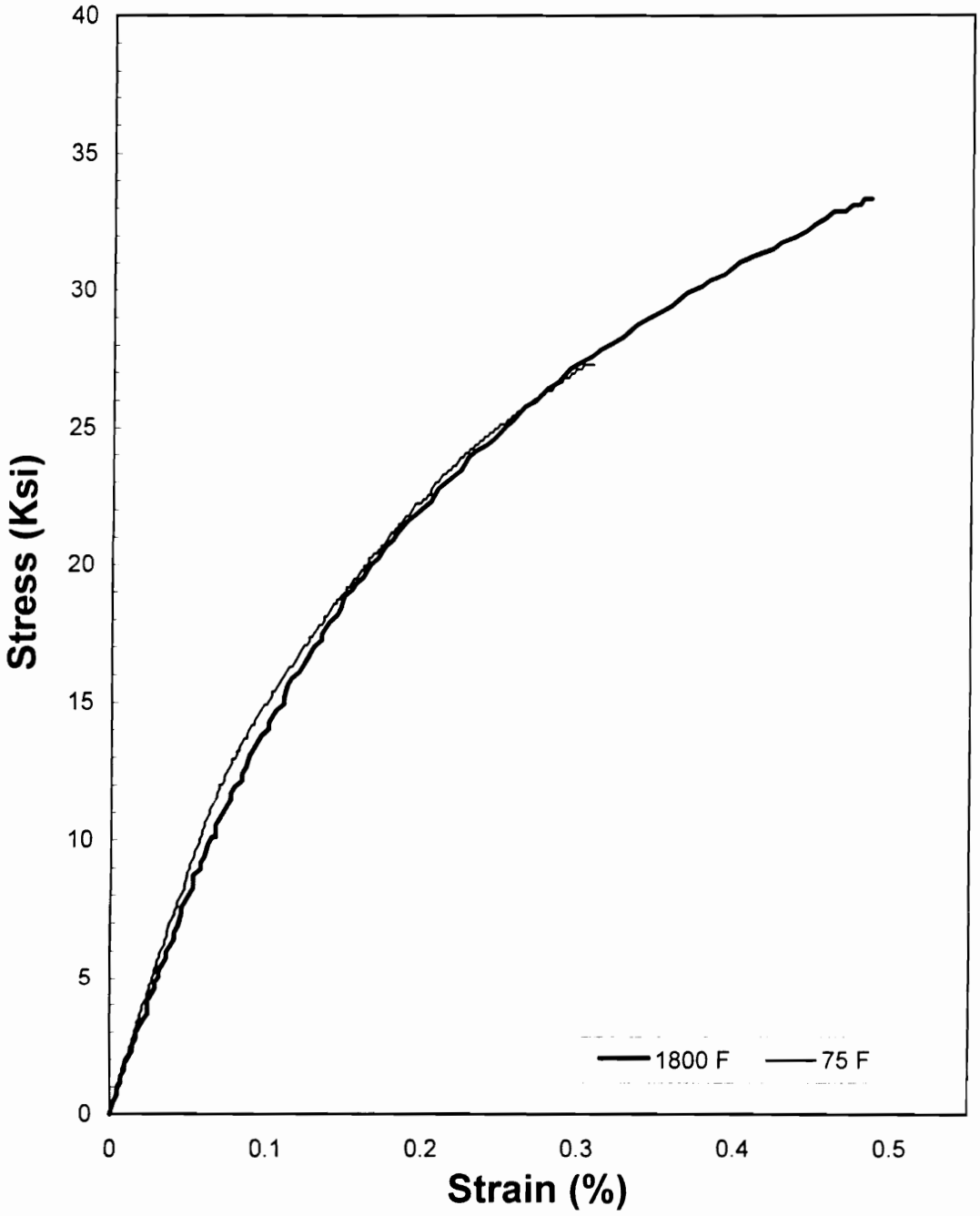

Figure 3.2: Room and elevated temperature quasi-static tensile responses of $[(0,90)/(+45,-45)]_{2s}$ laminates in atm. air.

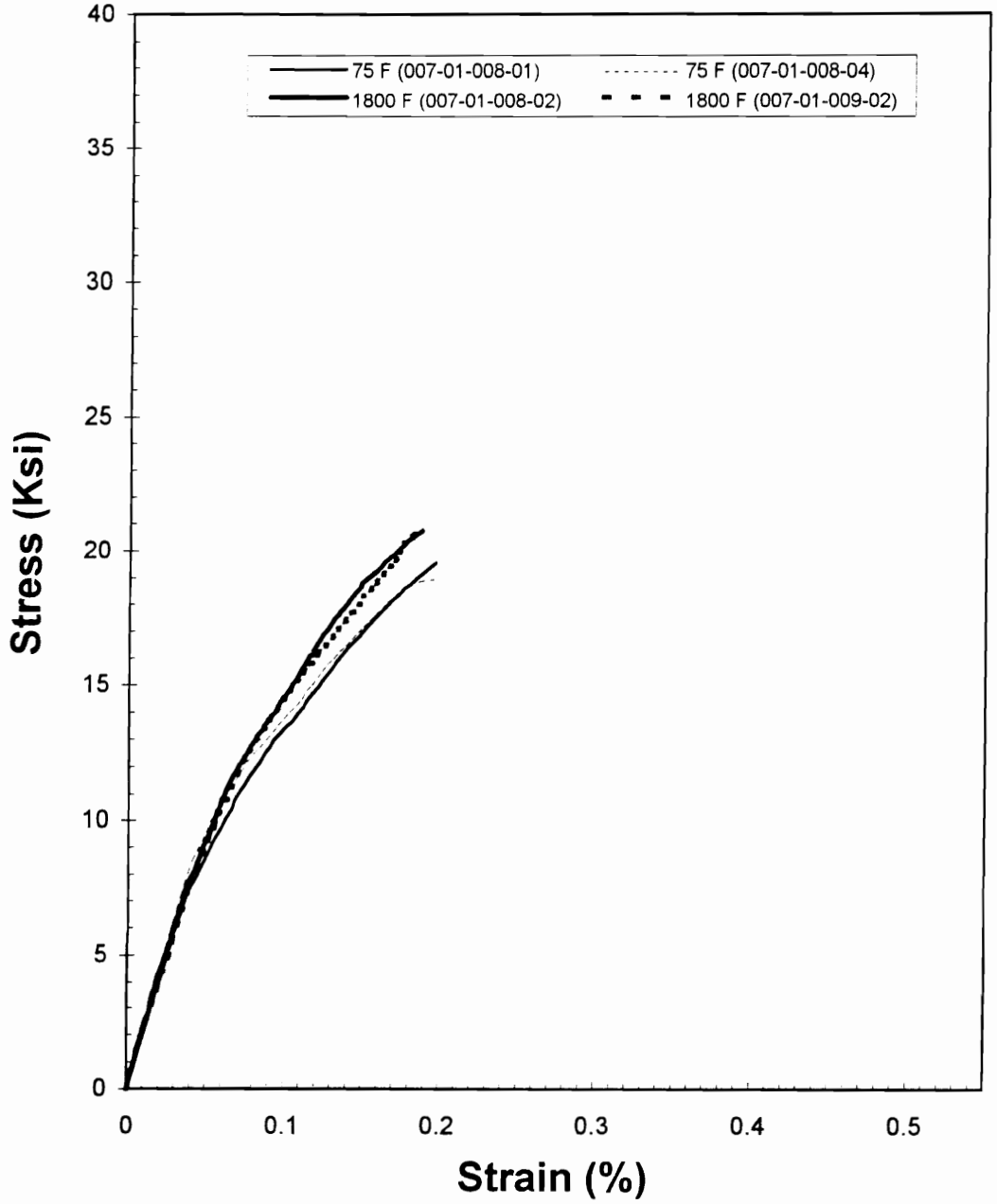

Figure 3.3: Room and elevated temperature quasi-static tensile responses of center-notched $[(0,90)/(0,90)]_{2s}$ laminates in atmospheric air.

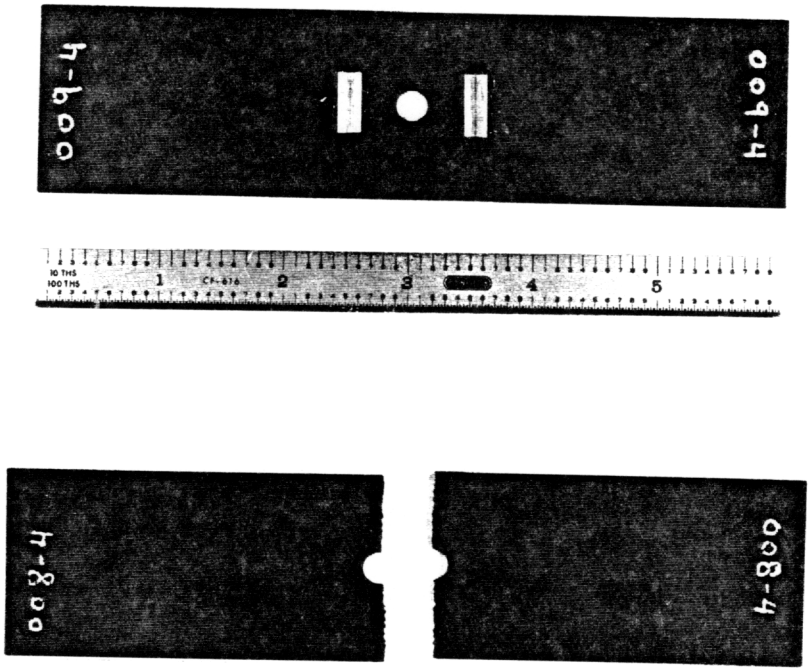

C.N.,0/90,Q-S,75

Figure 3.4: Fractured center-notched specimen from a quasi-static tensile test at 75 F.

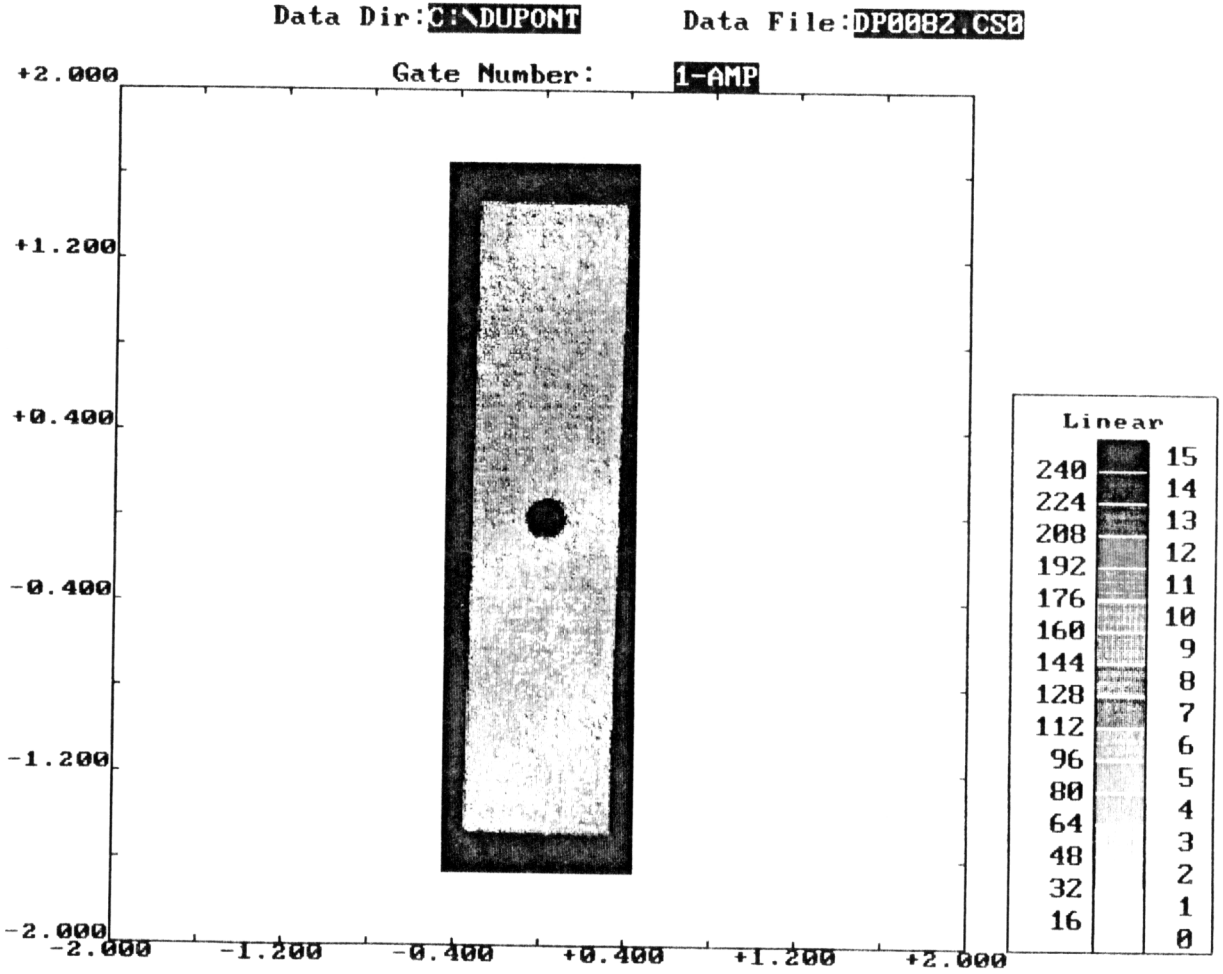

Figure 3.5: C-scan image of a center-notched specimen.

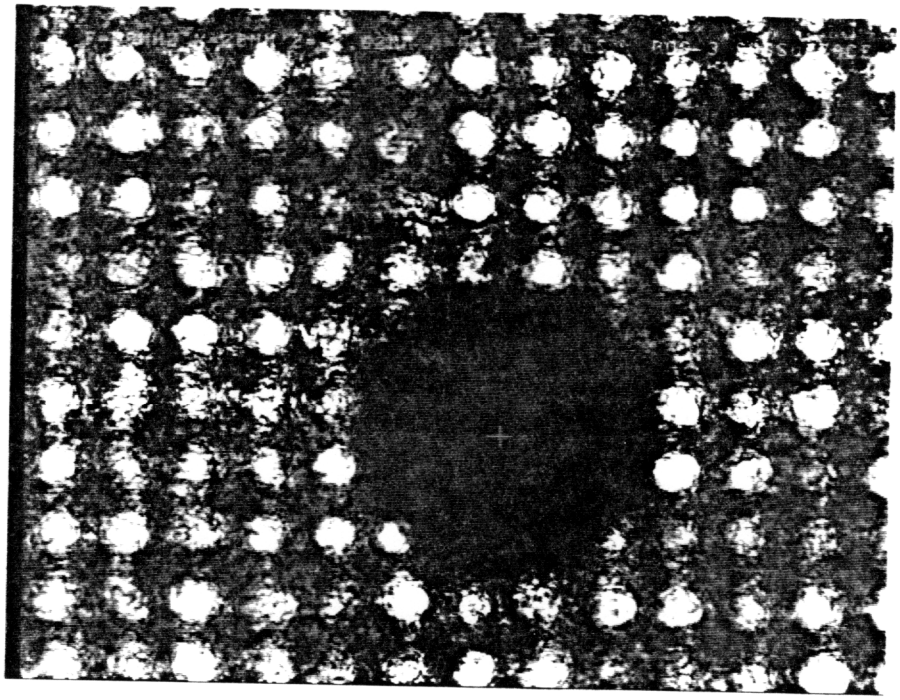

Figure 3.6: SAM image of a center-notched specimen.

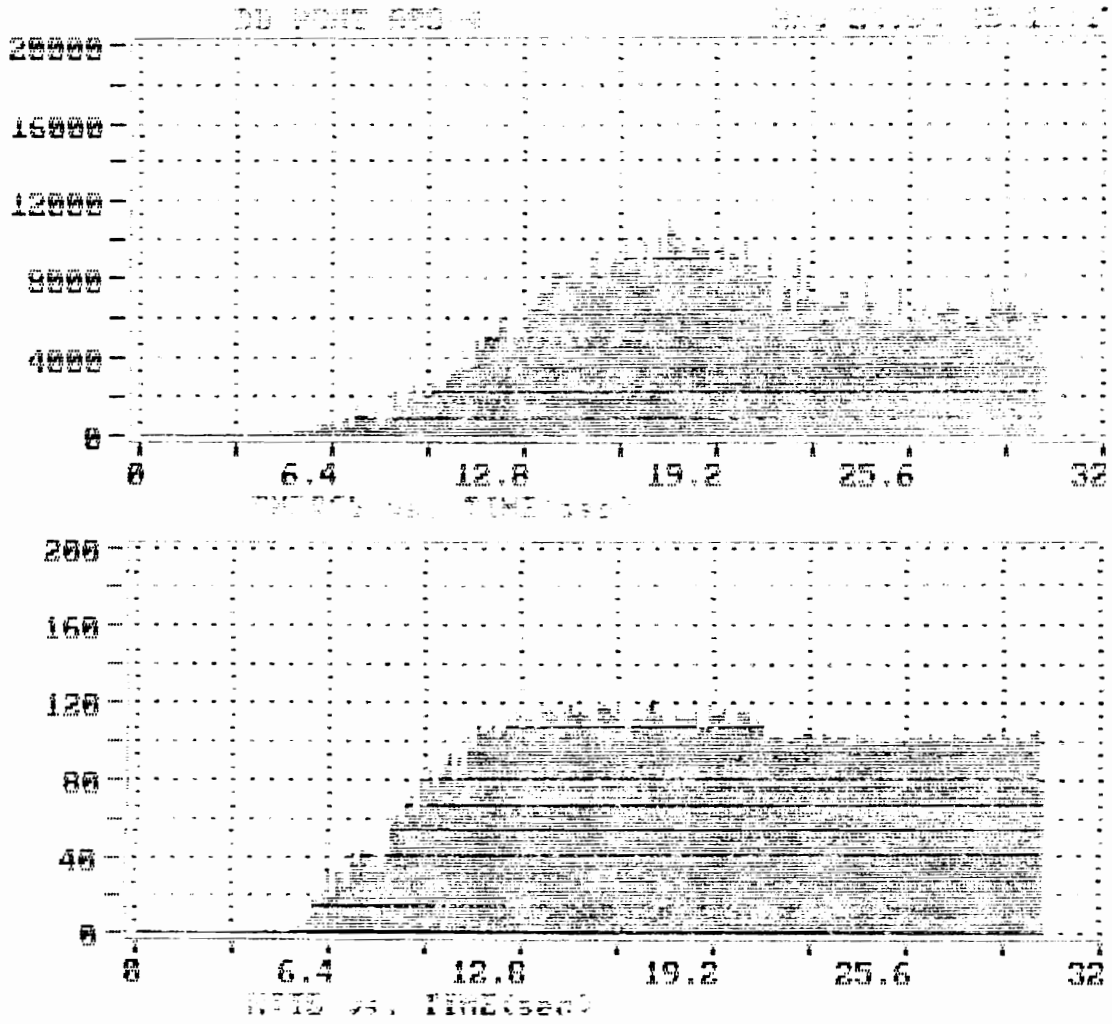

Figure 3.7: AE activities representing energy and number of hits as function of time for a center-notched specimen.

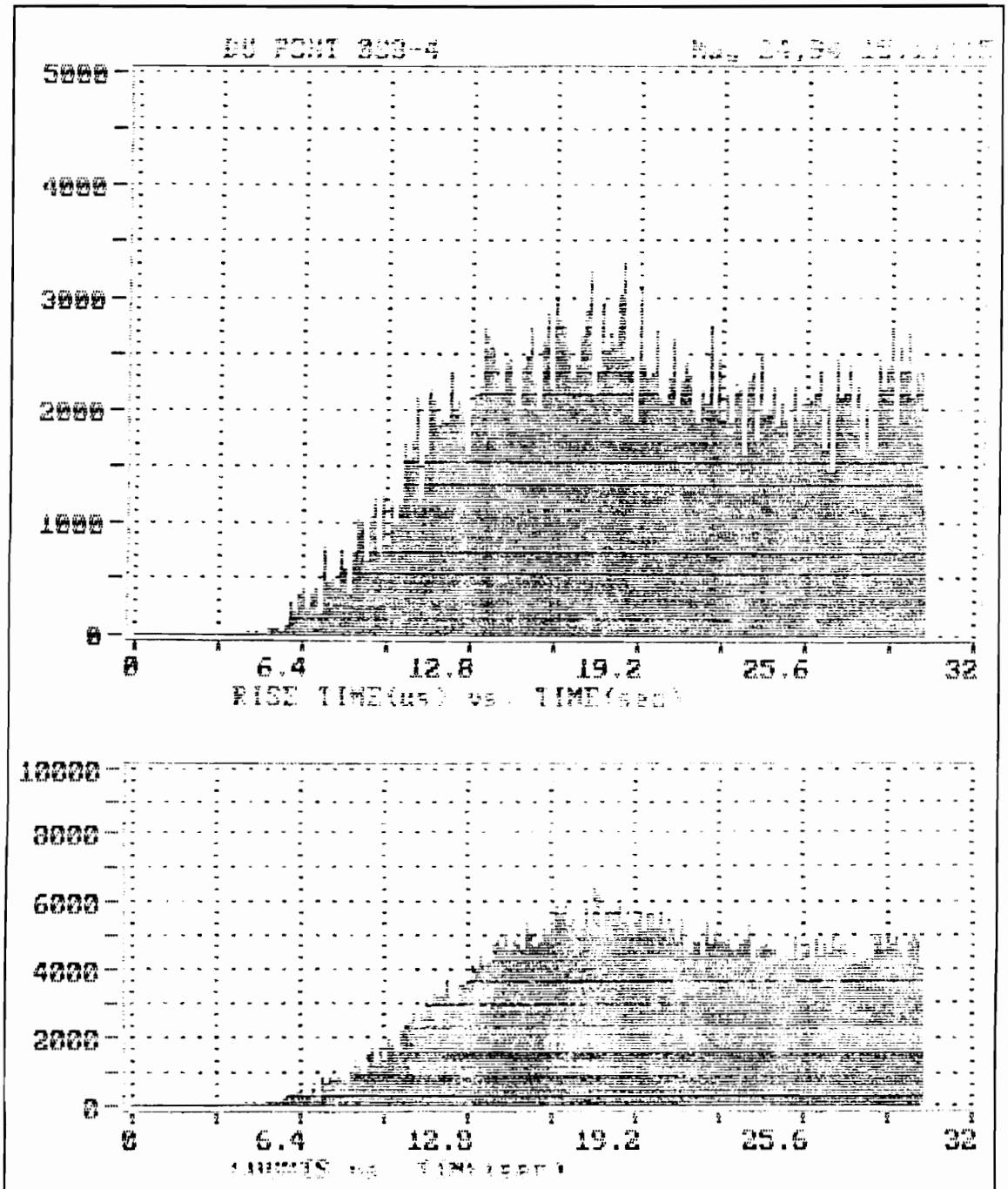

Figure 3.8: AE activities representing rise time and number of counts as function of time for a center-notched specimen.

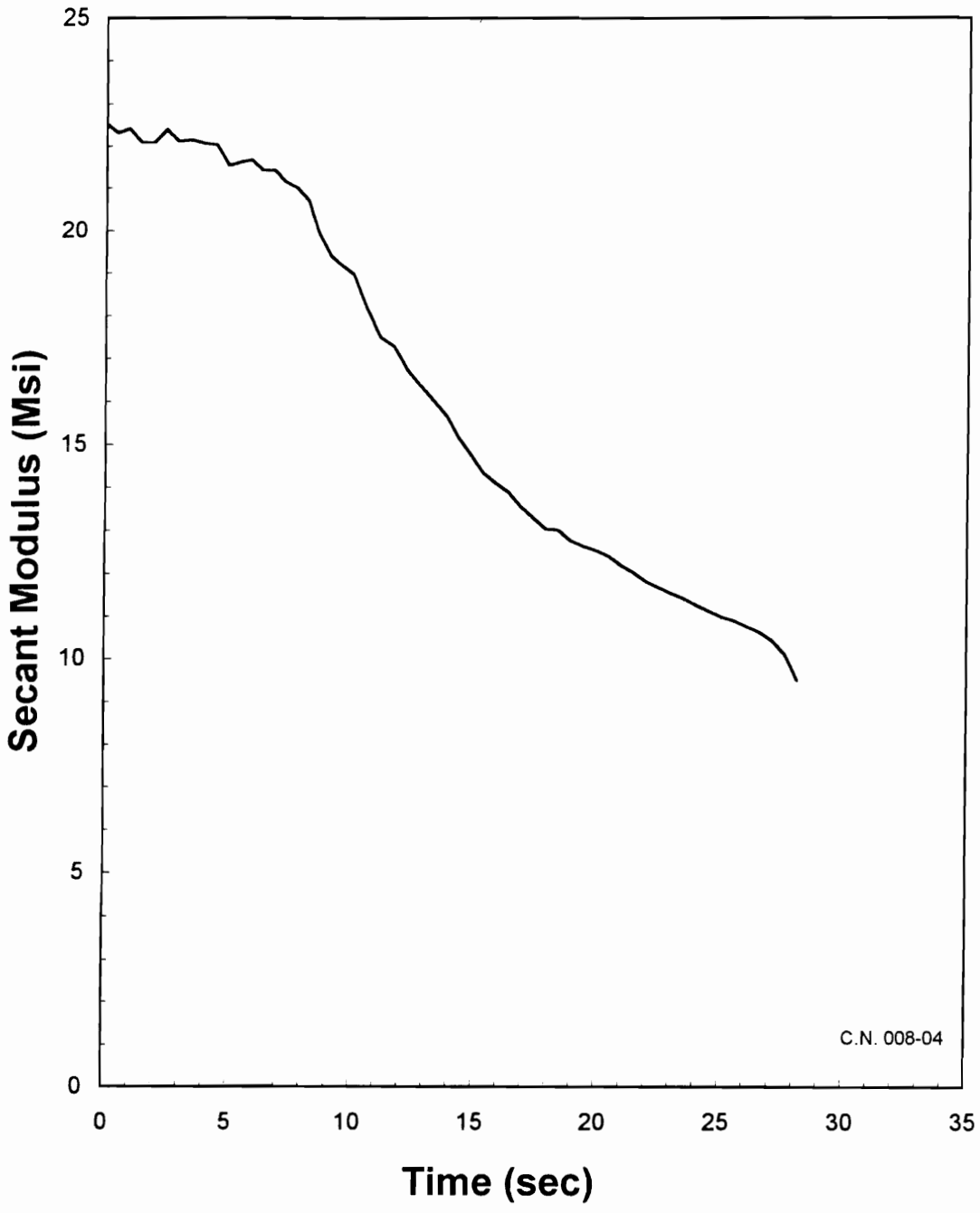

Figure 3.9: Evolution of secant modulus during tensile loading of a center-notched $[(0,90)/(0,90)]_{2s}$ specimen.

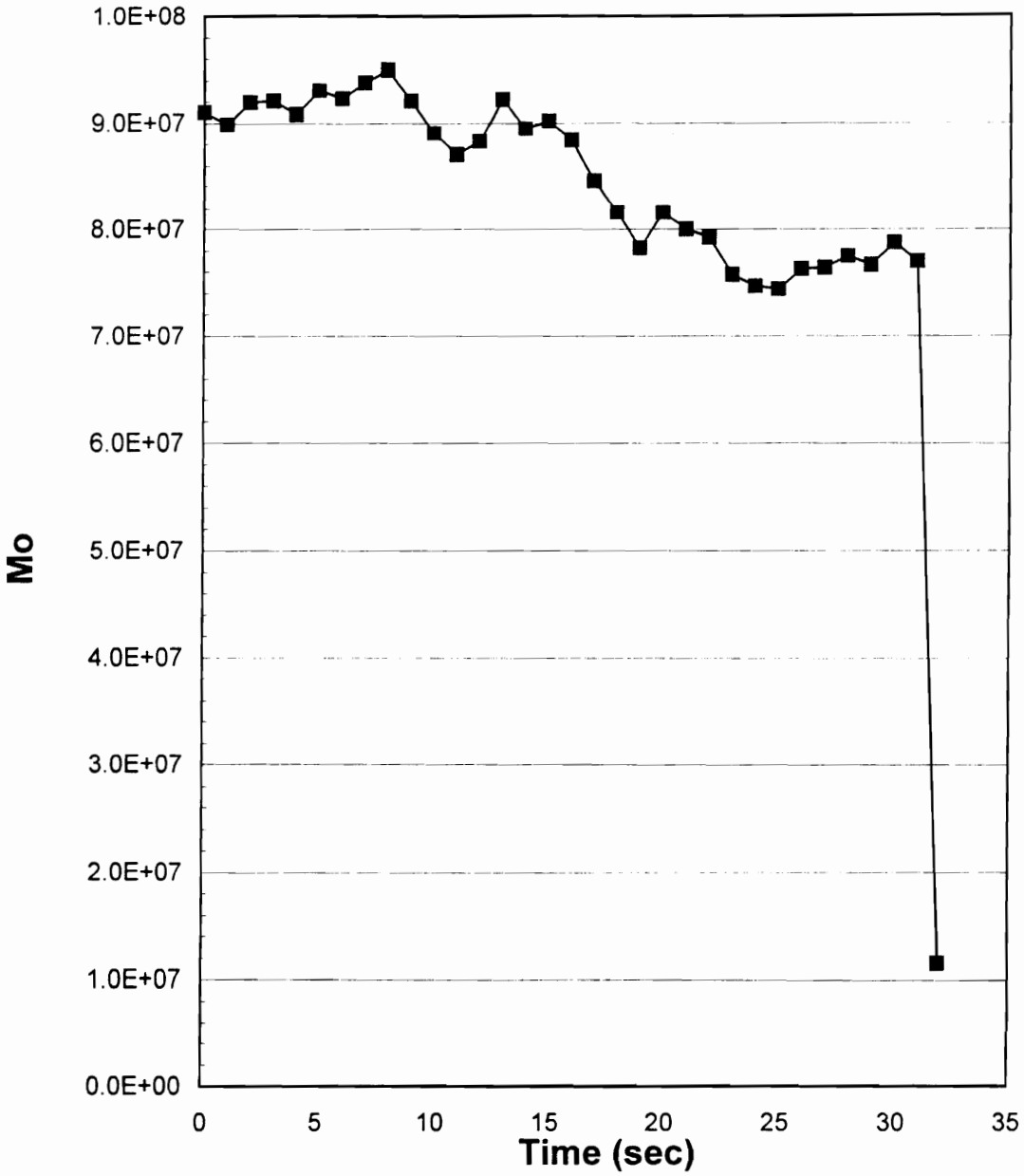

Figure 3.10 : Degradation of Mo with time for a center-notched $[(0,90)/(0,90)]_{2s}$ laminate subjected to quasi-static tensile loading at room temperature.

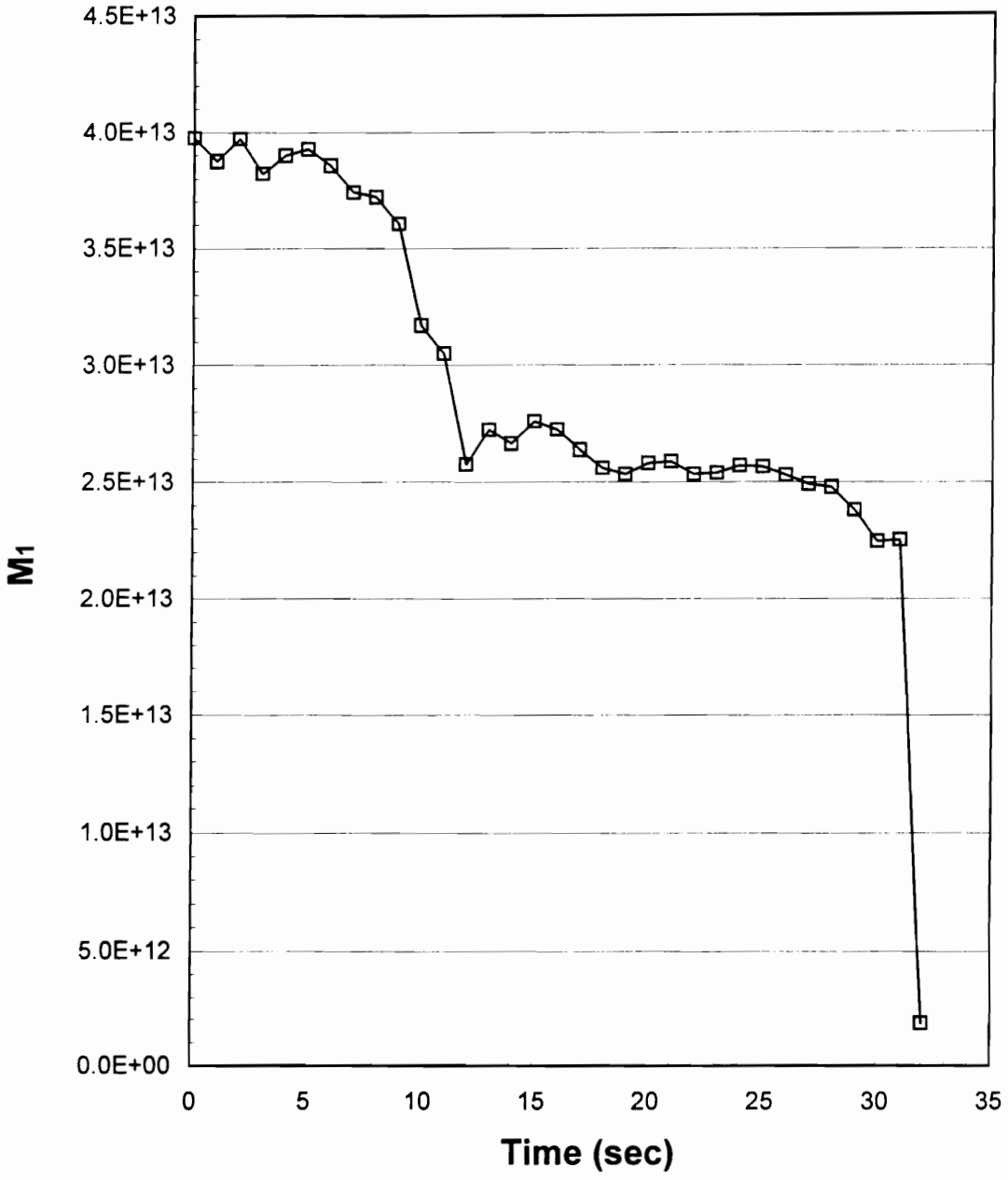

Figure 3.11: Degradation of M_1 with time for a center-notched [(0,90)/(0,90)]2s laminate subjected to quasi-static tensile loading at room temperature.

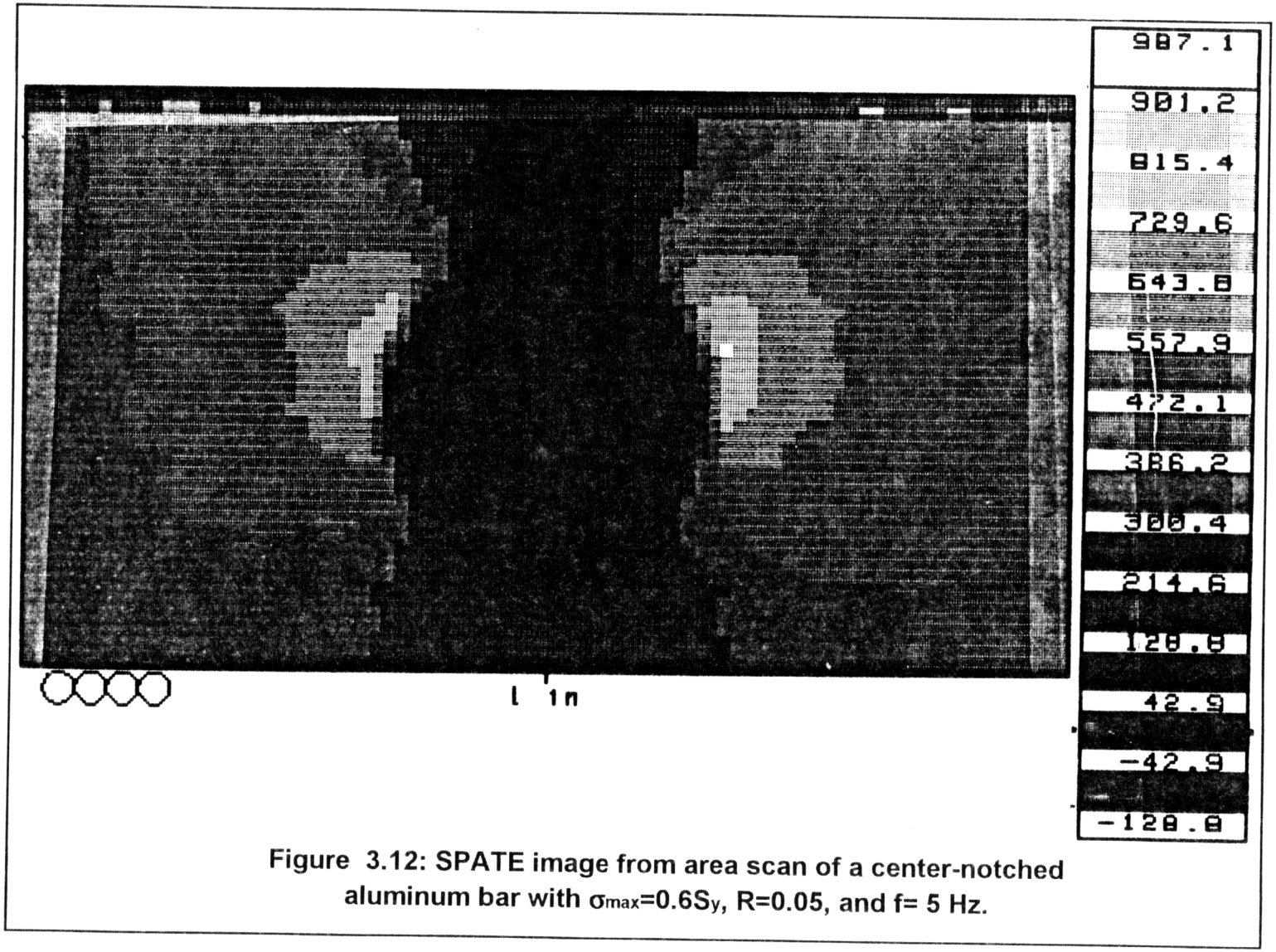

Figure 3.12: SPATE image from area scan of a center-notched aluminum bar with $\sigma_{max}=0.6S_y$, R=0.05, and f= 5 Hz.

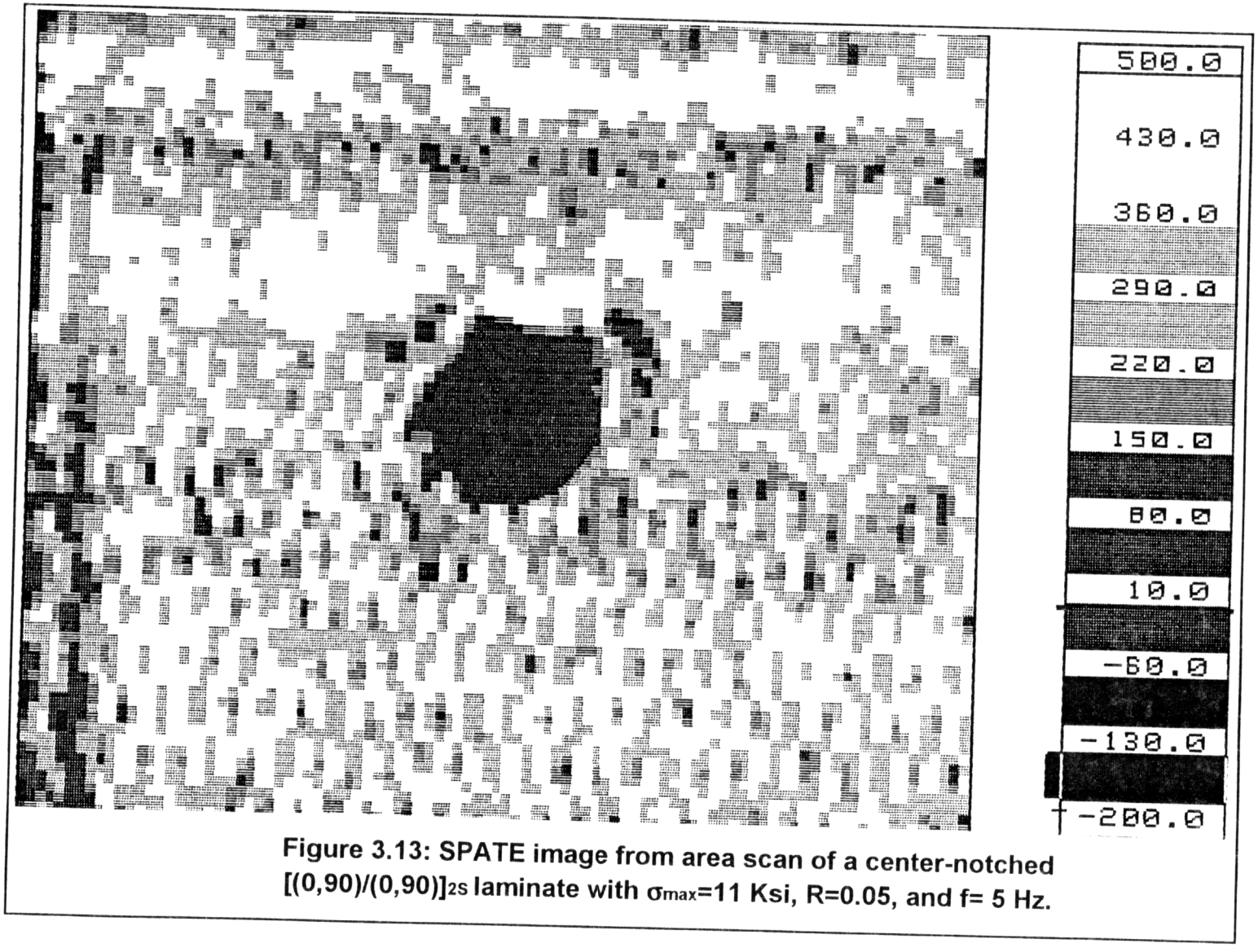

Figure 3.13: SPATE image from area scan of a center-notched $[(0,90)/(0,90)]_{2S}$ laminate with σ_{max}=11 Ksi, R=0.05, and f= 5 Hz.

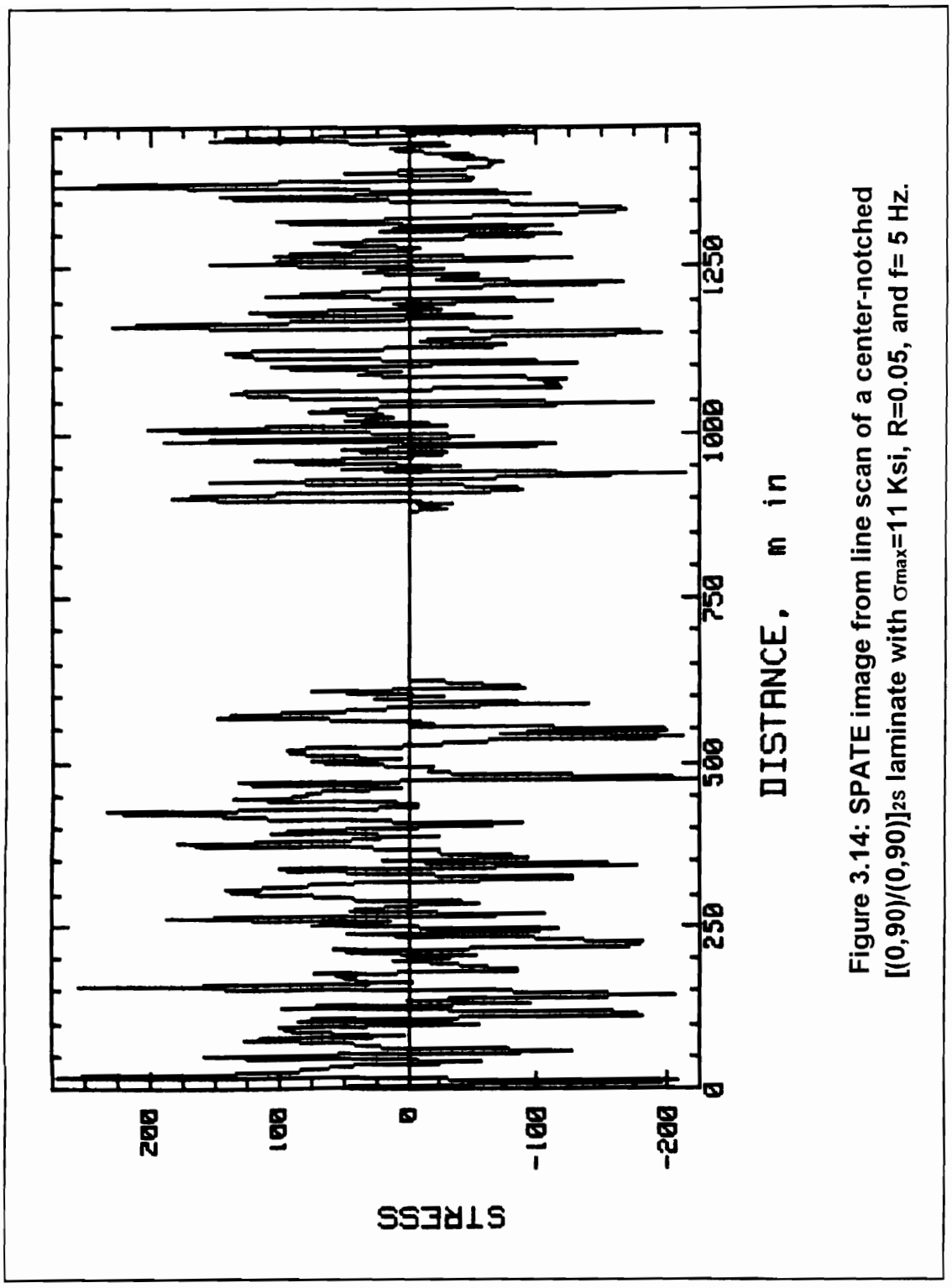

Figure 3.14: SPATE image from line scan of a center-notched $[(0,90)/(0,90)]_{2S}$ laminate with σ_{max}=11 Ksi, R=0.05, and f= 5 Hz.

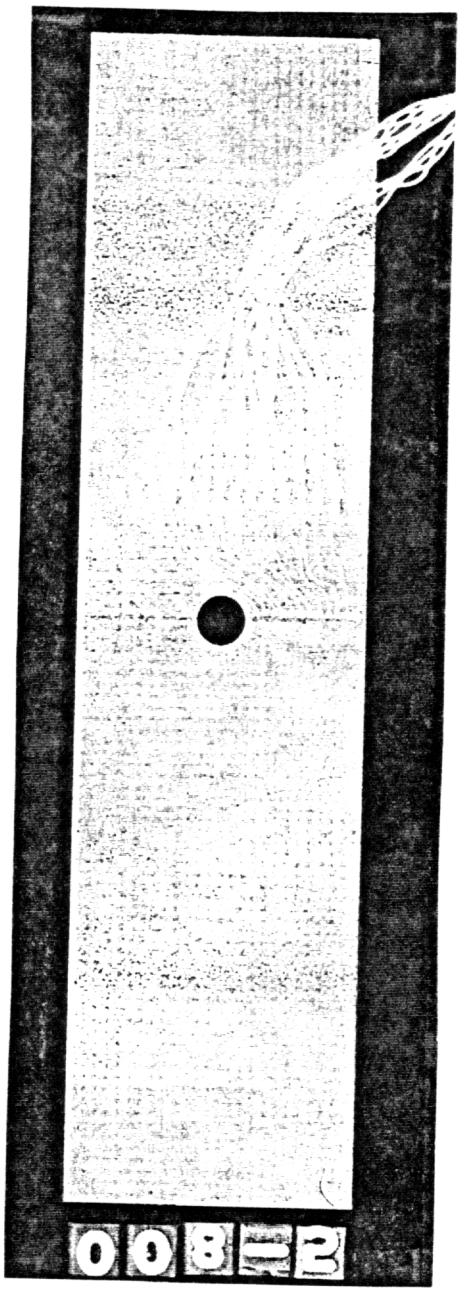

Figure 3.15: Placement of a strip-strain gage on a center-notched specimen.

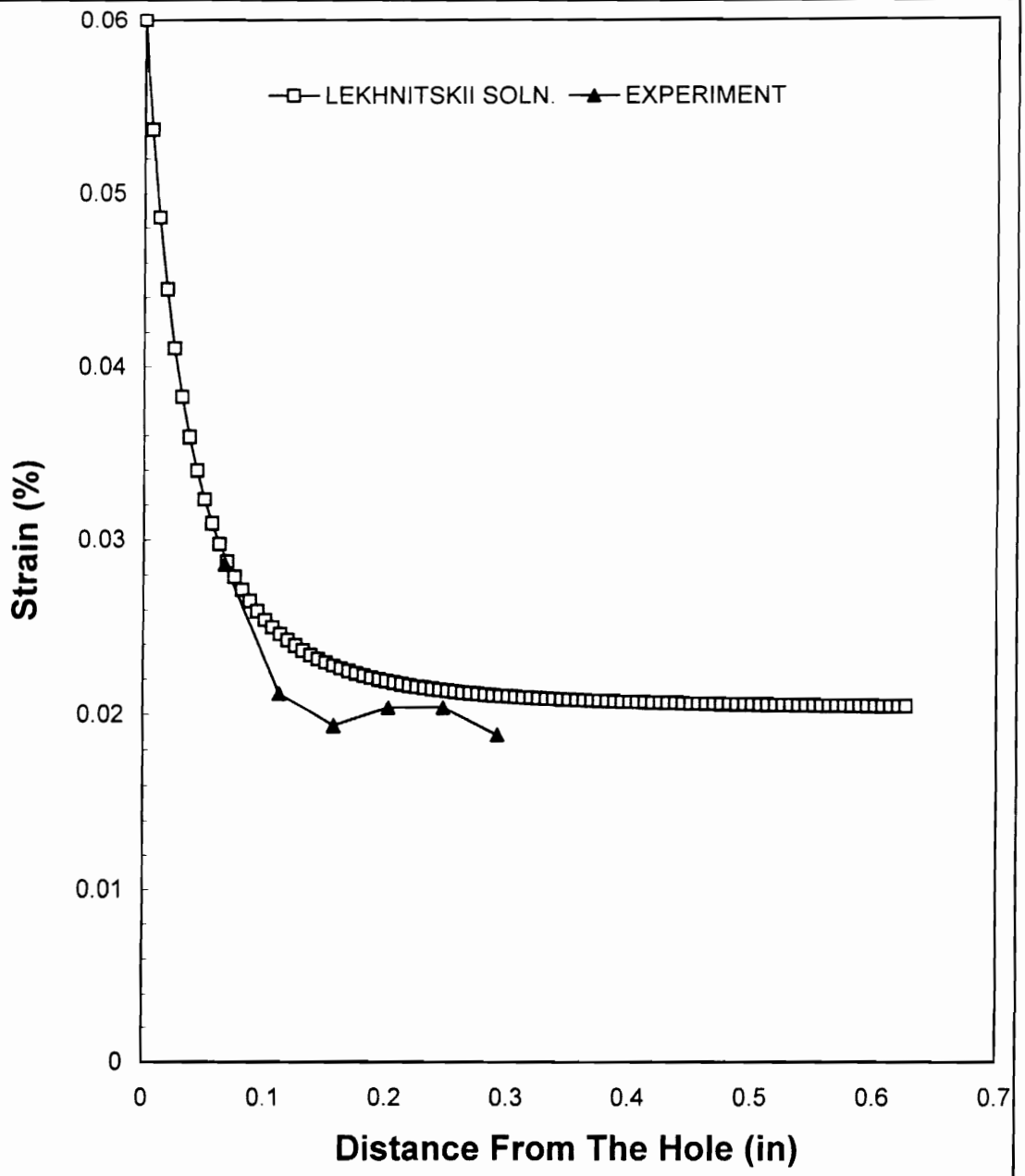

Figure 3.16 :Comparison between the strip-strain gage measurments and the predictions for a center-notched $[(0,90)/(0,90)]_{2s}$ laminate with σ_{max}= 4.257 Ksi.

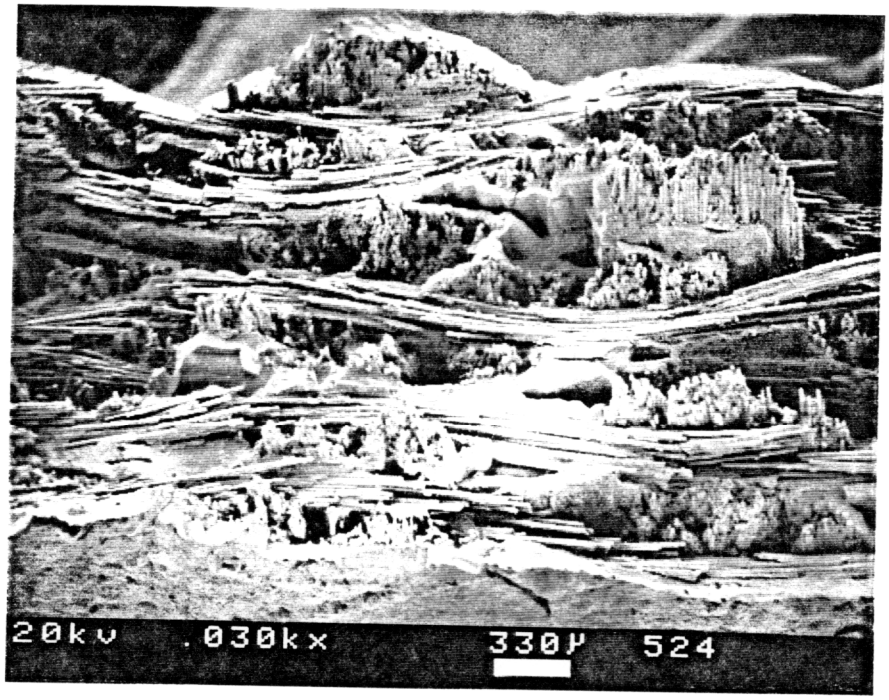

C.N.,0/90,Q-S,75

Figure 3.17: Fractured surface of a center-notched $[(0,90)/(0,90)]_{2S}$ laminate after quasi-static tensile test at 75 F.

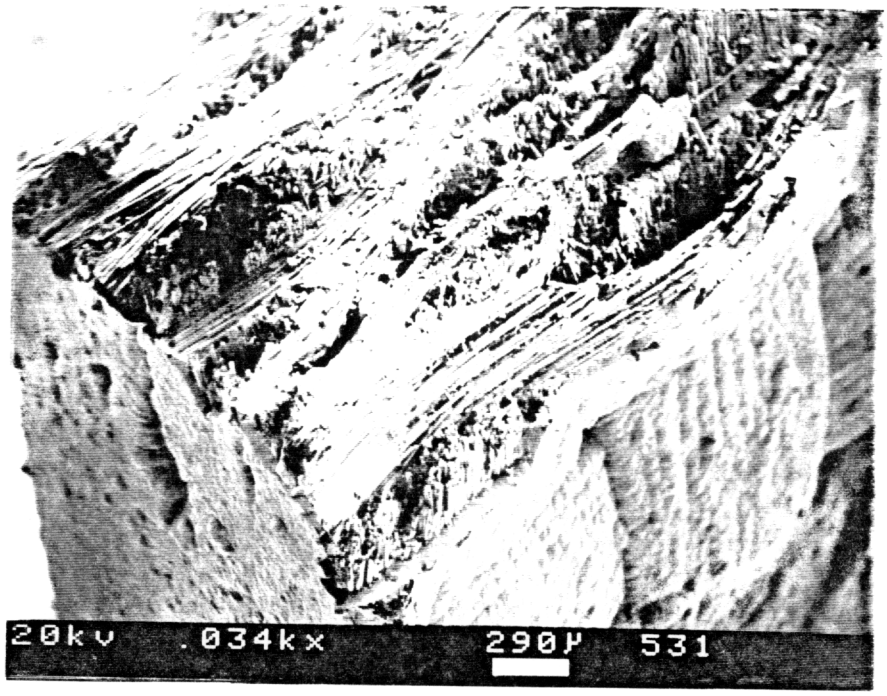

C.N..0/90,Q-S,1800

Figure 3.18: Fractured surface of a center-notched $[(0,90)/(0,90)]_{2S}$ laminate after quasi-static tensile test at 1800 F.

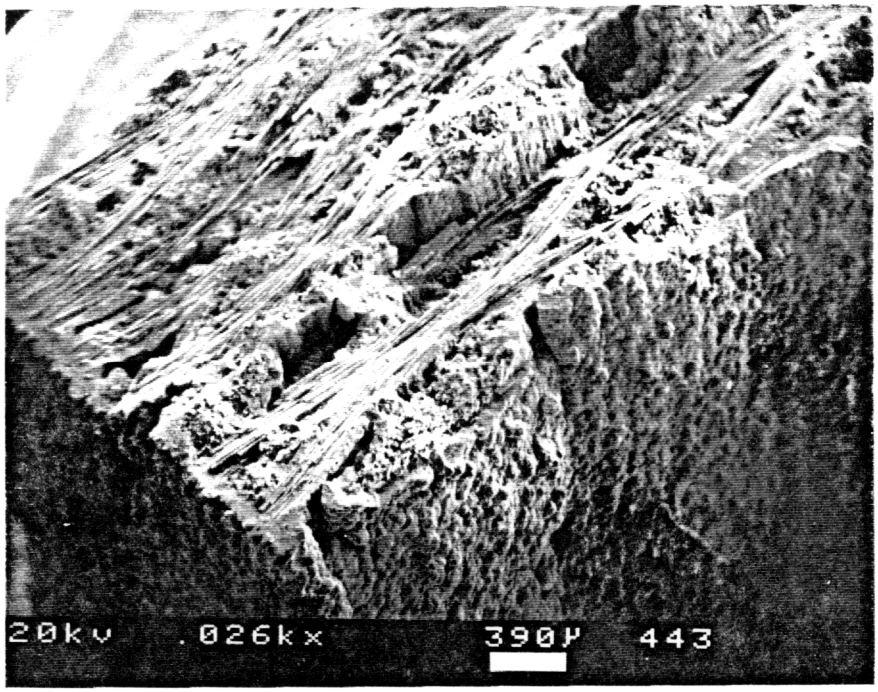

Figure 3.19: Fractured surface of a 2-D woven regular Nicalon/SiC laminate after quasi-static tensile test (ε_{ult}=0.205%) at 75 F.

Figure 3.20: Fractured surface of a 2-D woven regular Nicalon/SiC laminate after quasi-static tensile test (ε_{ult}=0.405%) at 1800 F.

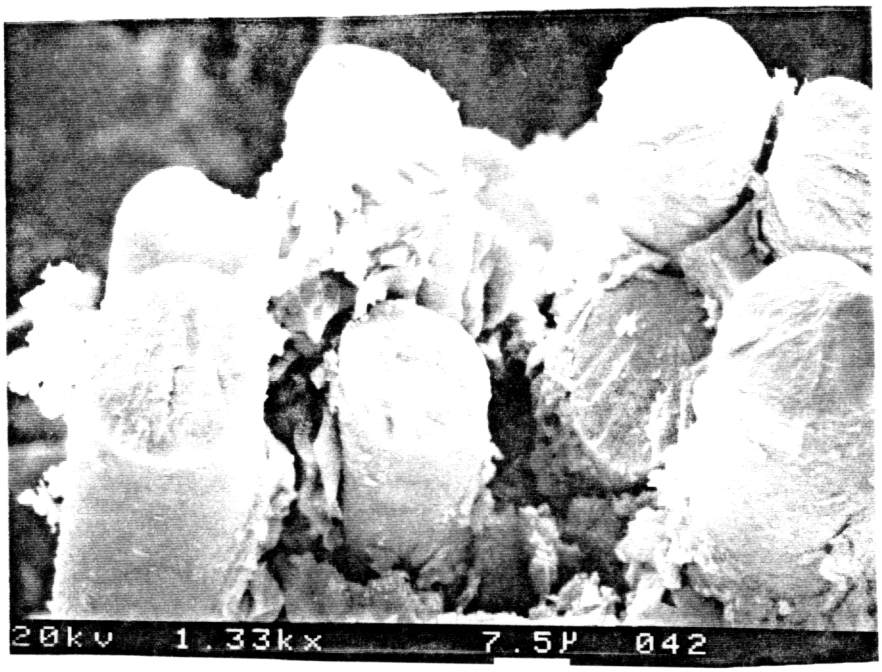

Figure 3.21: Not so clean fiber pull-outs in quasi-static tensile test at 75 F of a center-notched $[(0,90)/(0,90)]_{2S}$ laminate.

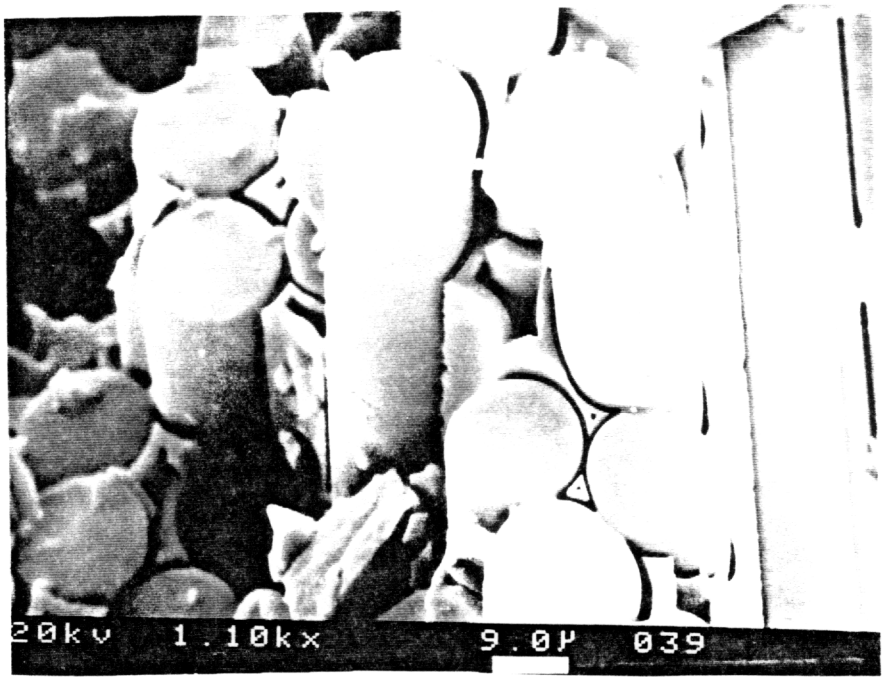

Figure 3.22: Clean fiber pull-outs in quasi-static tensile test at 1800 F of a center-notched $[(0,90)/(0,90)]_{2S}$ laminate.

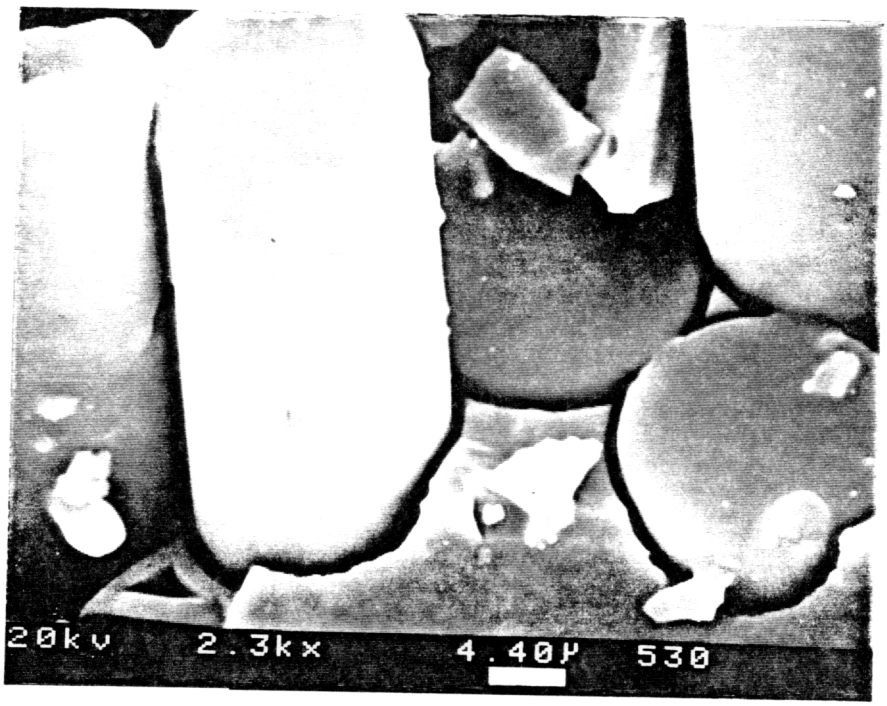

C.N.,0/90,Q-S,1800

Figure 3.23: Removal of interface in quasi-static tensile test at 1800 F of a center-notched $[(0,90)/(0,90)]_{2S}$ laminate.

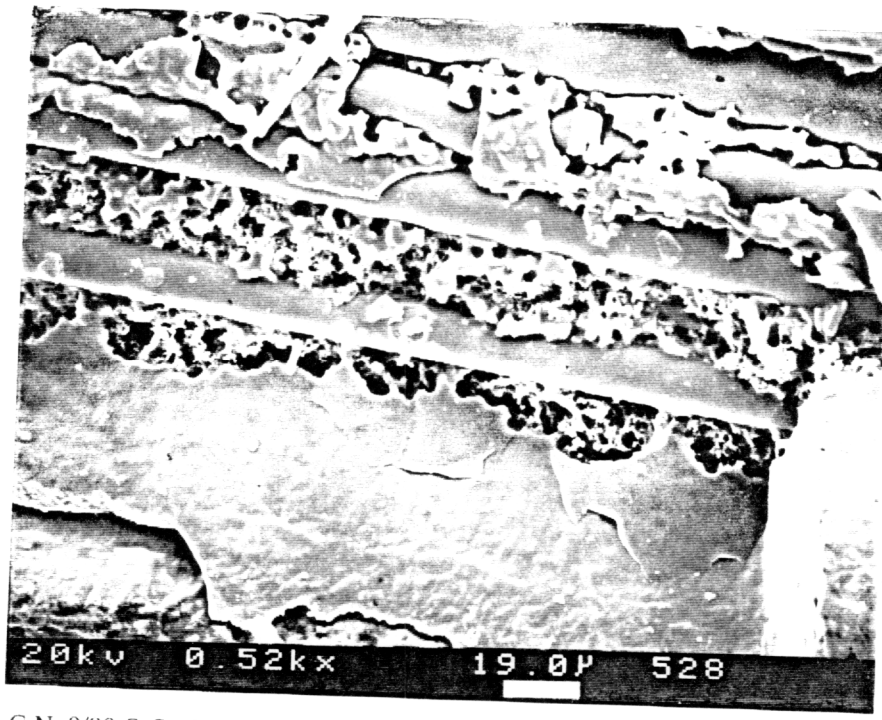

C.N..0/90.Q-S.1800

Figure 3.24: Boron-based patricles melt and coat the fibers at 1800 F.

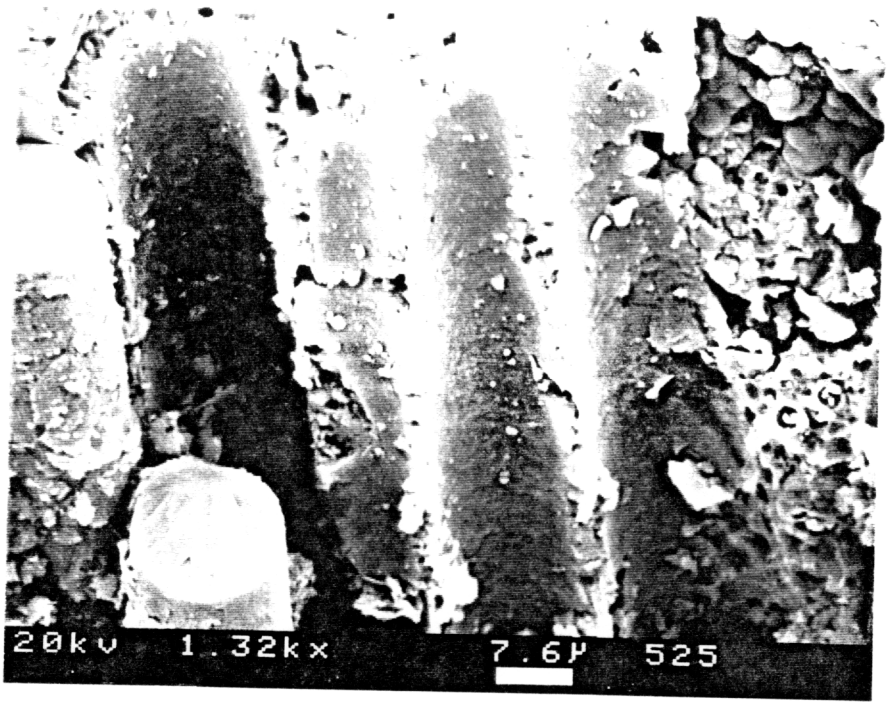

C.N.,0/90,Q-S,75

Figure 3.25: Matrix material before exposure to 1800 F.

C.N.,0/90,Q-S.1800

Figure 3.26: Matrix material after exposure to 1800 F.

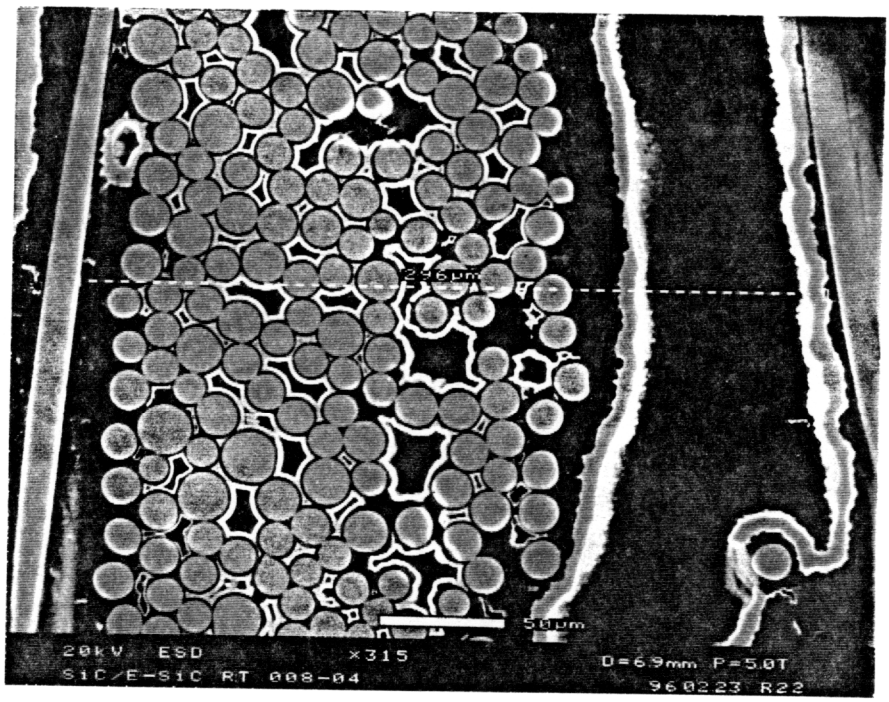

Figure 3.27: Cross-section of a fiber bundle at 75 F.

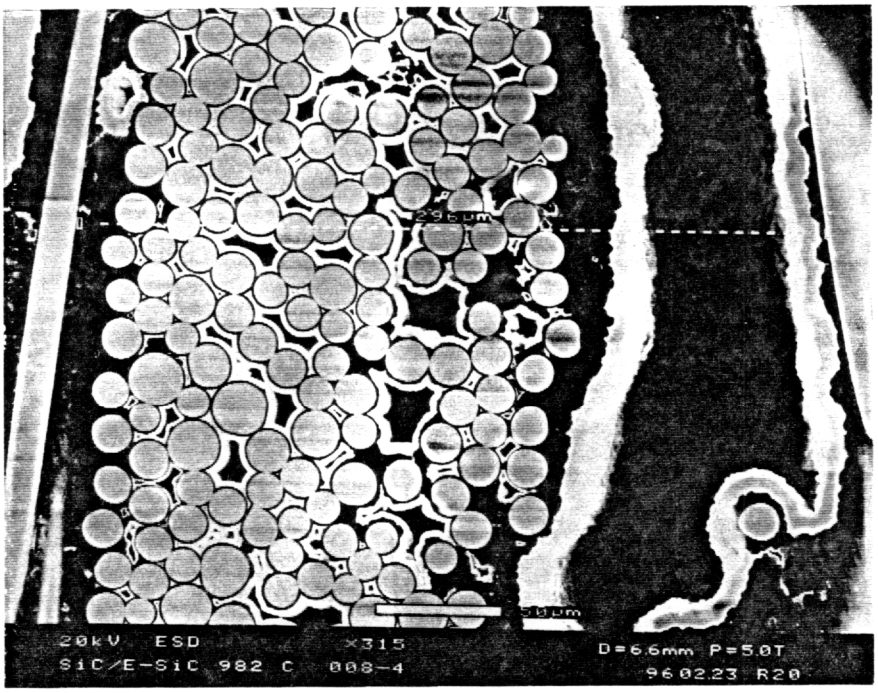

Figure 3.28: Cross-section of a fiber bundle at 1800 F.

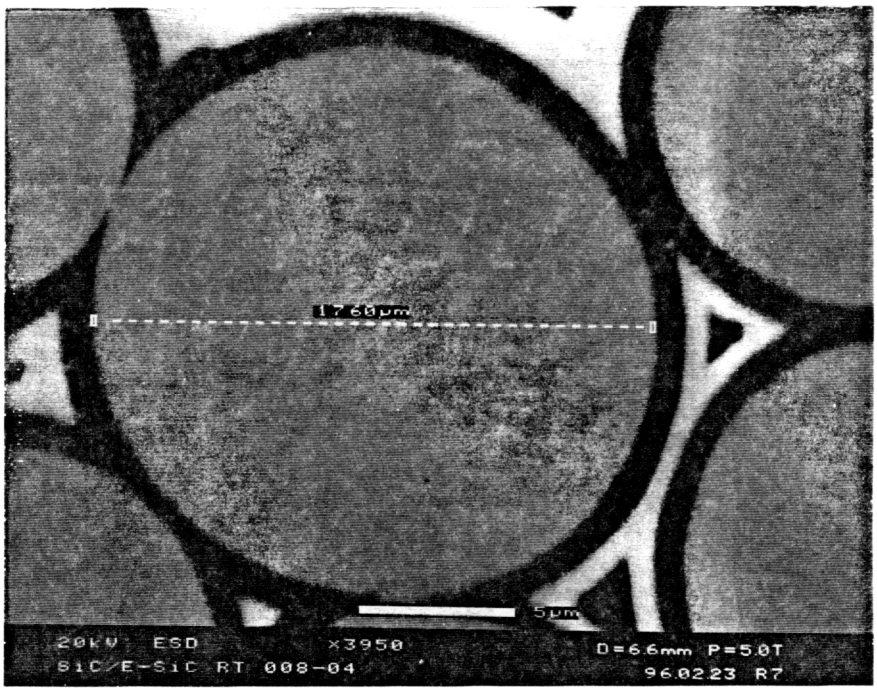

Figure 3.29: Cross-section of a Nicalon fiber at 75 F.

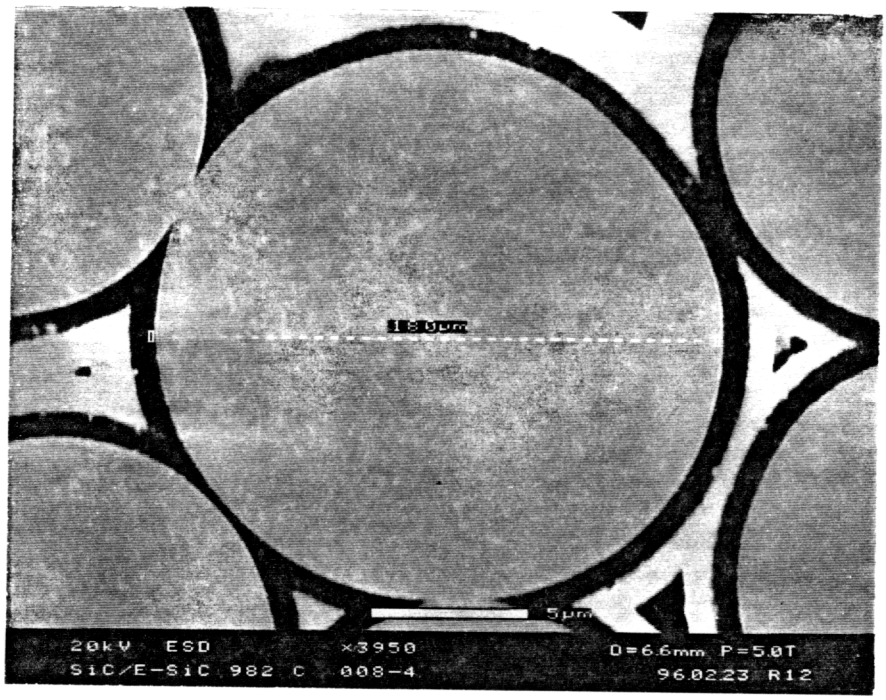

Figure 3.30: Cross-section of a Nicalon fiber at 1800 F.

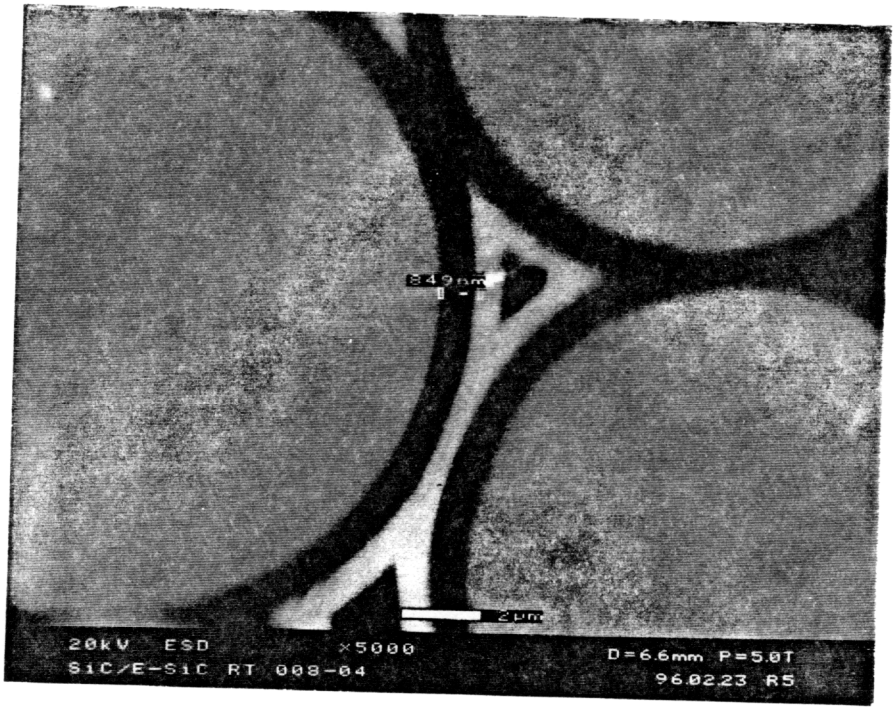

Figure 3.31: Fiber-matrix interface at 75 F.

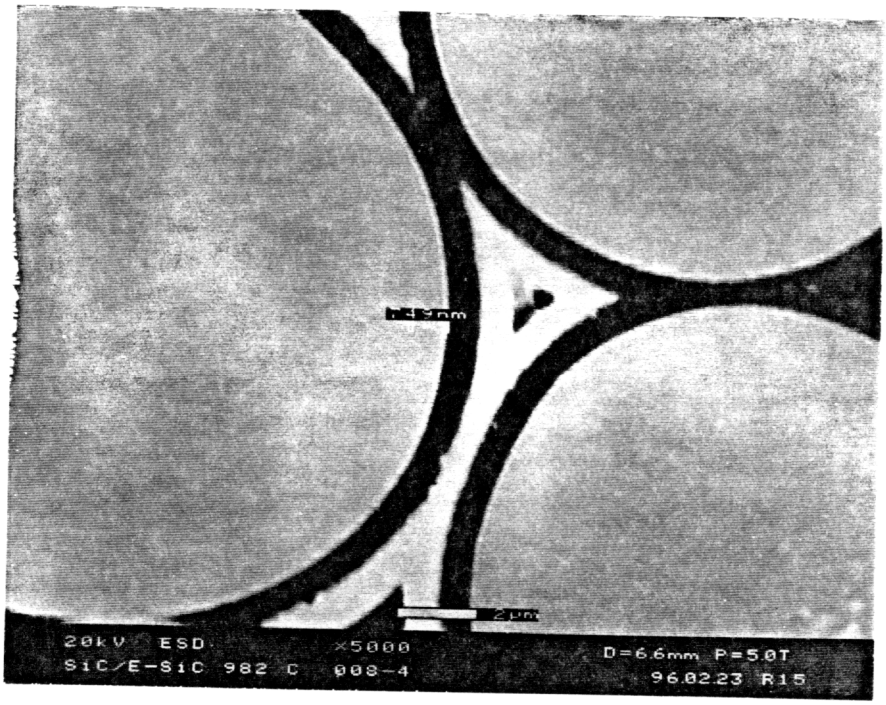

Figure 3.32: Fiber-matrix interface at 1800 F.

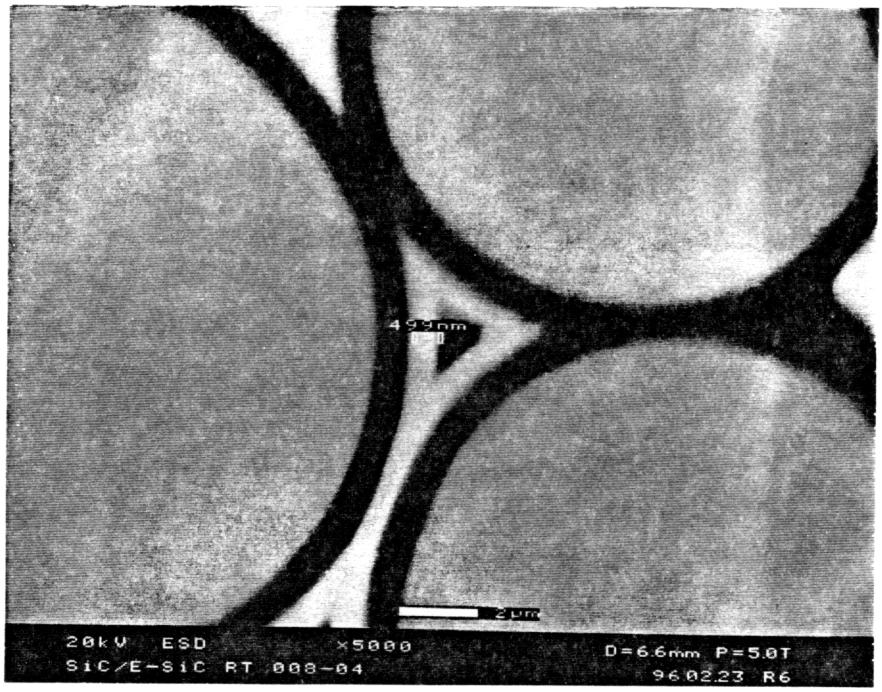

Figure 3.33: Matrix material around the fiber at 75 F.

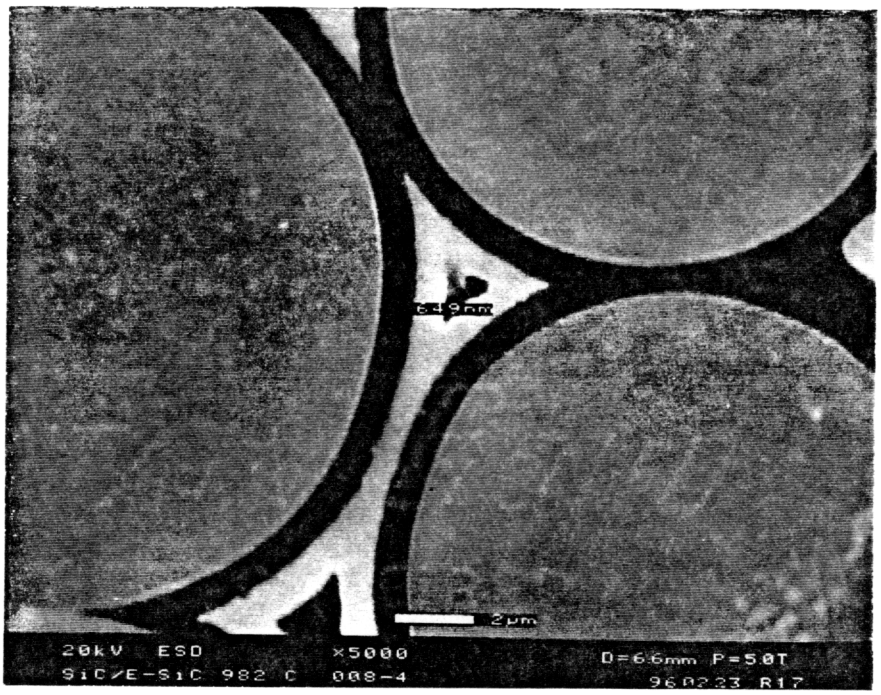

Figure 3.34: Matrix material around the fiber at 1800 F.

4. Fatigue Behavior and Damage Tolerance

4.1 Cyclic Fatigue to Failure Tests:

Using the quasi-static tensile test results of cross-ply and quasi-isotropic laminates at 1800 °F, fully-reversed cyclic fatigue tests were carried out at 1800 °F under three different stress levels representing three damage states of material. These stress levels corresponded to locations of well below, right at, and well above the proportional limit strength (PLS) in a tensile stress-strain curve. Based on PLS of 12.7 Ksi, stresses of 10 Ksi, 13 Ksi, and 15 Ksi were chosen as the maximum applied stresses. The 10 Ksi stress level is located within the linear elastic range, 13 Ksi stress level is located in a region where material is going through the transition from linear elastic regime to non-linear regime, and the 15 Ksi stress level is located in a non linear regime past the transition region (figures 3.1-3.2). Under a cyclic frequency of 1 Hz, related information were collected and results are presented in the following sections.

4.1.1 Fatigue Response of $[(0,90)/(0,90)]_{2s}$ Laminates:

From a total of seven specimens designated for this testing category, two were tested at 10 Ksi, two at 13 Ksi and three at 15 Ksi stress levels. At least one 0.75" width specimen was included at each stress level test. All the 10 Ksi tests lasted more than 10^5 cycles (representing an exposure time of 28 hours at temperature) and were considered as run-outs. Typical stress-strain loops are presented in figure 4.1. Application of the first loading cycle

induced small amount of hysteresis in tensile side of loading curve which lasted almost up to $5x10^4$ cycles and gradually disappeared upon further cycling. This hysteresis is believed to be associated with the presence of matrix micro-cracks at this load level. The small magnitude of the hysteresis area did not permit an accurate measurement but stiffness measurements were made and results will be presented. During these tests any activity regarding damage and damage evolution was confined to the tensile side of loading (figure 4.1). This was expected because the ultimate compression strength, UCS, of these materials were reported to be almost twice as large as the UTS [71]. Run-out specimens were pulled to failure in quasi-static tests under stroke control at 1800 °F. Large scatters in initial elastic modulus values (Young's elastic modulus before cycling) were present which might have contributed to variation in material response (specially in strain to failure). The scatter in initial elastic modulus values is believed to be directly related to the degree of porosity in specimens (nominal values of 10%-12% are reported. In the initial elastic region, the matrix contributes substantially to the modulus of composite. The fiber content of panels is fixed. Therefore, higher porosity translates into lower matrix material value. The contribution of the "lost" matrix material gets replaced with that of air, causing a reduction in the composite modulus. This explains the reason for larger scatter in elastic modulus than tensile strength. Initial elastic modulus, which is the only material property representing the virgin state of material, was always measured and recorded. Measured remaining properties for 10 Ksi tests indicated an average final elastic modulus (Young's elastic modulus after cycling) of 16.13 Msi, remaining strength of 26.16 Ksi, and remaining strain to failure

of 0.278% (Table 4.1). These values represented a decrease of 7%, 27%, and 47% from the corresponding average values from the quasi-static tensile tests of the uncycled specimens at 1800 °F. Due to presence of large scatter in initial elastic modulus, the percent reduction in modulus was based on the average initial elastic modulus of the same (17.38 Msi in case of the 10 Ksi test specimens, which is much smaller than 20.50 Msi reported by P&W). The proportional limit strength (PLS) and its strain remained basically unchanged. Specimen with wider gage width resulted in higher remaining properties.

The 13 Ksi tests resulted in very close lives where an average life of 26000 cycles were recorded (representing an exposure time of 8 hours). Typical loops were collected and results are presented in figure 4.2. The stress-strain hysteresis loops indicated significant amount of damage which were generated upon application of the first loading cycle. This is expected as the 13 Ksi stress causes significant matrix cracking. Initial elastic modulus values were averaged to 18.37 Msi. Similar to 10 Ksi tests, damage were initiated on the tensile side of loading. Upon further cycling they evolved and crept slowly into the compression side. Presence of small hysteresis on the compression side in part may be explained as following. This load level was large enough to produce fiber matrix debonding, matrix crack, fiber fracture, and fiber pull-out. Depending on the position of broken fibers and the large matrix cracks, upon unloading, some of these broken fibers do not go back to where there pulled out of. Therefore they break "into" the cracks, preventing full crack closure. This argument was supported by the absence of any stiffness degradation on the compression side of the loops where the unloading compressive modulus has the same

value as loading compressive modulus. Putting the first cycle aside, the hysteresis area started increasing steadily from the second cycle with the highest hysteresis occurring on the last cycle before final failure. It was not possible to capture the last few cycles before final failure without running the risk of storage overflow. The specimen with larger gage width lasted longer.

Depending on the gage width, the 15 Ksi tests showed large scatter in cycles to failure values. The wider specimen lasted almost twice as long as the narrow specimens. Narrow specimen lives were very close together averaging at 12350 cycles (representing an exposure time of almost 3.75 hours). It was decided to discard the life of the wide specimen and use the average life of narrow specimens as the reference life. This life is almost half of the life for 13 Ksi tests. The measured initial elastic modulus values were very close averaging at 18.03 Msi. Typical hysteresis loops were collected and are presented in figure 4.3. As is indicated by the size of the hysteresis loops, the 15 Ksi stress level generated more damage in the material than the previous two load levels. Similar to the previous two stress levels, damage was initially confined to the tensile loading side (at least for the first 100 cycles). Upon further cycling, hysteresis crept into the compression side. The same argument as the 13 Ksi tests may be applied here as to the nature of hysteresis on the compression side.

It should be noted that in all these tests tensile failure was the dominant mode of failure and failure always occurred in the specimen's discoloration zone. Normalizing the applied stresses with respect to UTS, the stress-cycle diagram (S-N diagram), resembled a straight line when plotted with a semi-log axis (figure 4.4). This line may be best be

represented by (Sa/Su)= 1.0008-0.0624 Log(N) where Sa ,Su, and N represent the applied stress level, ultimate tensile strength at 1800 °F, and number of applied loading cycles respectively.

These results have shown that matrix cracking played the most important role. With stress levels at or above the PLS, the composite has a short life. Also porosity seem to influence the fatigue response as well where fractured surfaces were associated with large porosity. Moschelle et al. [69] have reported similar observations based on room temperature fatigue test results of regular Nicalon[1]/SiC.

Table 4.1: Fatigue to failure test results of $[(0,90)/(0,90)]_{2s}$ laminates subjected to cyclic loads with R=-1, and f=1 Hz, at 1800 °F.

Specimen I.D. & Gage Width (in)	Max. Stress (Ksi)	Cycles to Failure (Fracture Location)	Initial Elastic Modulus (Msi)	Final Elastic Modulus (Msi)	PL Stress @ 0.005% offset (Ksi)	PL Strain @ 0.005% offset (%)	Remaining Strength (Ksi)	Remaining Strain (%)
0007-001-025-09 (0.40)	10.0	Run Out (OX)	16.41	14.99	11.70	0.075	24.85	0.263
0007-001-020-09 (0.75)	10.0	Run Out (IX)	18.34	17.26	13.59	0.079	27.51	0.293
Ave. Value	***10.0***	***Run Out***	***17.38***	***16.13***	***12.65***	***0.077***	***26.18***	***0.278***
0007-001-024-07 (0.40)	13.0	23515 (OX)	18.11	------	------	------	------	------
0007-001-020-08 (0.75)	13.0	28486 (OX)	18.63	------	------	------	------	------
Ave. Value	***13.0***	***26000***	***18.37***	------	------	------	------	------
0007-001-021-08 (0.40)	15.0	12679 (OX)	18.12	------	------	------	------	------
0007-001-023-10 (0.40)	15.0	12022 (OX)	17.93	------	------	------	------	------
0007-001-018-10♣ (0.75)	15.0	21825 (IX)	NA	------	------	------	------	------
Ave. Value	***15.0***	***12350***	***18.03***	------	------	------	------	------

♣ Fatigue test result of this particular specimen was not used for average life determination.

4.1.2 Fatigue Response of $[(0,90)/(+45,-45)]_{2s}$ Laminates:

The six specimens tested in this category, were equally distributed among the various stress level tests in which all included a specimen with narrow gage width. Similar to cross-ply laminates, the 10 Ksi tests resulted in run-outs. The stress-strain loops indicated similar characteristics as the cross-ply laminates (figure 4.5) with an average initial elastic modulus of 17.76 Msi. Based on quasi-static tensile tests at 1800 °F, average final elastic modulus of 16.35 Msi, remaining strength of 25.56 Ksi, and remaining strain to failure of 0.289% were recorded (Table 4.2). Comparison of average remaining properties of cycled specimens with the corresponding uncycled values, indicated a reduction of 8%, 23% and 37% in elastic modulus, UTS and strain to failure respectively. With an offset strain of 0.005%, a PLS of 12.36 Ksi with a corresponding strain of 0.079% were also obtained. Comparison between of remaining strength and remaining strain values of cross-ply and quasi-isotropic laminates does not indicate any significant difference in property degradation as a function of stacking sequence (figure 4.6).

The 13 Ksi stress level tests resulted in very close cycles to failure which were averaged to 25140 cycles representing an exposure time of 7.25 hours. This was slightly lower than the cross-ply laminates. An average initial elastic modulus of 18.26 Msi was obtained. The typical stress-strain loops are presented in figure 4.7. The evolution of hysteresis resembled those of cross-ply specimens. As to the nature of hysteresis in these curves, same argument at the cross-ply laminates may be applied.

The 15 Ksi stress level tests resulted in average life of 14800 cycles which translates to 4.36 hours exposure time. Similar to cross-ply laminates, this life was almost half of the life achieved by 13 Ksi tests. Unlike the life for 13 Ksi tests, the life for 15 Ksi tests was slightly higher than its cross-ply counterpart. An average value of 16.97 Msi was recorded. Typical stress-strain hysteresis loops are presented in figure 4.8.

In general, the off-axis lamination did not influence fatigue response significantly. The S-N diagram showed similar characteristics as the cross-ply laminates as well. The fatigue S-N data may be best represented by a straight line such as (Sa/Su)= +1.0032-0.0595 Log(N) (figure 4.9). The slope of this line was slightly lower than the one for the cross-ply case.

Table 4.2: Fatigue to failure test results of $[(0,90)/(+45,-45)]_{2s}$ laminates subjected to cyclic loads with R=-1, and f=1 Hz, at 1800 °F.

Specimen I.D. & Gage Width (in)	Max. Stress (Ksi)	Cycles to Failure (Fracture Location)	Initial Elastic Modulus (Msi)	Final Elastic Modulus (Msi)	PL Stress @ 0.005% offset (Ksi)	PL Strain @ 0.005% offset (%)	Remaining Strength (Ksi)	Remaining Strain (%)
0101-021-009-09 (0.40)	10.0	Run Out (IX)	18.63	16.82	12.36	0.077	26.38	0.300
0101-021-009-10 (0.40)	10.0	Run Out (IX)	16.89	15.87	12.36	0.082	24.73	0.277
Ave. Value	***10.0***	***Run Out***	***17.76***	***16.35***	***12.36***	***0.079***	***25.56***	***0.289***
0007-001-030-01 (0.40)	13.0	24300 (OX)	18.01	------	------	------	------	------
0007-001-030-02 (0.40)	13.0	25980 (OX)	18.51	------	------	------	------	------
Ave. Value	***13.0***	***25140***	***18.26***	------	------	------	------	------
0007-001-030-03 (0.40)	15.0	15614 (OX)	17.56	------	------	------	------	------
0007-001-030-04 (0.40)	15.0	13986 (OX)	16.37	------	------	------	------	------
Ave. Value	***15.0***	***14800***	***16.97***	------	------	------	------	------

4.1.3 Fatigue Induced Damage in $[(0,90)/(0,90)]_{2s}$ Laminates:

To monitor damage and damage accumulation as a function of applied number of load cycles, stiffness measurements were made. Initial unloading tensile modulus, E_i^{ul}, representing best the damaged state of material was obtained from the stress-strain curves. To be consistent in measuring E_i^{ul}, values were obtained within a predefined stress range. These stress intervals were defined as (6.5 Ksi-9.5 Ksi), (6.5-12.5 Ksi), and (6.5Ksi-14.5 Ksi) for 10 Ksi, 13 Ksi, and 15 Ksi tests respectively. To scale E_i^{ul} values with respect to the undamaged state of material, they were normalized by their initial elastic modulus. Stiffness degradation curves are presented in figures 4.10-4.12. For 10 Ksi tests, stiffness dropped by 7% upon the application of first cycle. It remained at this value basically unchanged up to around $5x10^4$ cycles. Then it started to increase slowly where at 10^5 cycles stiffness was build up back to 96% of its original value. This observation may be validated by inspection of hysteresis in stress-strain curves. Hysteresis loops tend to close up midway through cycling. There was hardly any noticeable hysteresis associated with the stress-strain curves around 10^5 (figure 4.1). This observation may be explained as following. The 10 Ksi stress level is large enough to induce micro-cracks, as evident by small initial drop in stiffness as well as appearance of small hysteresis upon the application first cycle. As time goes on, at the fiber-matrix interface the SiO_2 layer starts to form [82] (the extent of it is not known) therefore giving the material a new stiff character. The 13 Ksi and 15 Ksi tests show stiffness degradation as high as 30% and 32% upon the application of the first cycle respectively. This is mainly due to large matrix cracks which are known to increase laminate compliance and also modify the residual stress distribution, resulting in permanent strain.

Further cycling resulted in moderate decrease in stiffness which was more pronounced for the 15 Ksi tests than the 13 Ksi tests. Setting aside the loss in the first cycle for these two stress levels, stiffness degradation seemed to be represented best by a linear fit with a negative slope.

Having large enough hysteresis for 13 Ksi and 15 Ksi tests, hysteresis areas were successfully measured. To get a better sense of evolution of these loops, measured values were normalized with respect to value of the first loop. Results are plotted against cycles and are presented in figures 4.13-4.14. The hysteresis area as a function cycles, showed three distinct regions. The first region showed decaying trend which lasted up to cycle 10 for 13 Ksi tests and cycle 1 for the 15 Ksi tests. This was followed by a second region indicating almost a linear increase in hysteresis area. After 3000 cycles for 13 Ksi tests and 1000 cycles for 15 Ksi tests, the third region starts in which the increase in area may be represented by a power law fit. These curve are believed to contain important information regarding the evolution of bond at the interface. In the first region, highest area is associated with first loading cycle where the energy dissipation is very high mainly due to major matrix cracking. In 13 Ksi tests cracking gets saturated around cycle 10 where as the 15 Ksi test shows saturation is almost complete at the end of the first cycle. Further cycling is believed to cause interfacial wear causing a decrease in interfacial shear stress and an increase in hysteresis area. Reynaud et al. [83] have reported similar findings for various material systems as function of test temperatures. In case of regular Nicalon[1]/SiC material system which inherits compressive thermal residual stresses, similar responses were observed. Higher temperatures decreased the interfacial shear stress. Evans et al. [84-85] have suggested that interfacial shear stress decays exponentially with the

number of cycles and Rouby et al. [86] presented a power law decay. Both representations require initial and steady state values of interfacial shear stress and Lamon et al.[87] have suggested a relationship between the width of a hysteresis loop and the interfacial shear stress.

Employing the DSA technique, gain factor and phase factor were measured for 13 Ksi and 15 Ksi tests. To enhance their representation, they were normalized with respect to their highest value collected which occurs on the first cycle for gain factor and on the last cycle for the phase factor (figures 4.15-4.16). It take dynamic signal analyzer 17 cycles to calculate the first value for gain and phase. From here on, data were collected every 50 cycles. Using a much faster software and hardware (did not include any signal conditioning such as filtering, averaging,...), it is known that gain factor and phase factor curves resemble stiffness degradation and hysteresis are evolution curves respectively. Notice that the two of the three regions are very well defined. For both stress level, even though the last few cycles prior to failure were not collected, but the variations of phase factor from "beginning" to "end" were so large showing the final nonlinear region actually started around cycle 1000.

4.1.4 Fatigue Induced Damage in $[(0,90)/(45,-45)]_{2s}$ Laminates:

For 10 Ksi tests, stiffness degradation was similar to the cross ply case. On average, application of first, second and third loading cycles resulted in decrease of 5%, 8%, and 10% in E_1^{ul} respectively. Stiffness basically remained unchanged for almost the next 800 cycles. This was followed by an increasing trend in stiffness where at 10^5 cycles it was build up back to 96% of its original values (figure 4.17). Regarding the nature of

this behavior, same argument as the cross ply case may be applied here. For the 13 Ksi tests, upon tensile unloading of the first cycle, E_t^{ul} was dropped to 77% of its original value. This was followed by a region where stiffness decreased almost linearly with a small slope. Around 6000 cycles, the third region starts where stiffness degradation took a nonlinear form up to the failure (figure 4.18). The 15 Ksi tests shoed a similar behavior as the 13 Ksi tests including almost the same initial drop in E_t^{ul} . The linear region had more slope to it and the nonlinear part started at 3000 cycles (figure 4.19). Results of the measured hysteresis area as a function of cycles for the 13 Ksi and 15 Ksi tests are presented in figures 4.20-4.21. The measured hysteresis areas showed similar characteristics as the cross-ply specimen where the 15 Ksi tests are found to be dissipate energy at a much faster rate than the 13 Ksi tests. The DSA measurements for the applied stress level are presented in figures 4.22-4.23. They posses similar characteristics as the cross-ply laminates.

4.2 Interrupted Fatigue/Remaining Strength Test:

Results of fatigue to failure tests indicated that among the chosen three stress levels, only 13 Ksi and 15 Ksi were the most damaging ones. These two stresses were chosen for further investigation of cross-ply and quasi-isotropic laminates by performing interrupted tension-compression and tension-tension fatigue tests 1800 °F. Interruptions occurred at three different stages of life followed by quasi-static tensile tests at 1800 °F to determine remaining properties. Tension-tension fatigue tests were conducted for quasi-isotropic laminates only. Average values of measured remaining properties (except the elastic modulus) were compared to the corresponding

average values of quasi-static tensile test results of the as-received specimens at 1800 °F. Average remaining elastic modulus was compared to the measured average value of initial elastic modulus of the same specimens. Results are presented in the following sections.

4.2.1 Tension-Compression Fatigue of $[(0,90)/(0,90)]_{2s}$ Laminates:

With a maximum stress level of 13 Ksi, interrupted cyclic fatigue tests of cross-ply laminates were conducted for 10% of life (2600 cycles), 50% of life (13000 cycles) and 90% of life (24300 cycles). Cycling to 10% of life resulted in a reduction of 8%, 6%, 17%, and 7% in ultimate tensile strength, strain to failure, proportional limit strength and its corresponding strain respectively. Elastic modulus suffered 13% reduction. Cycling to 50% of life reduced tensile strength, strain to failure, PLS and its strain by 25%, 38%, 21%, and 14% respectively. Elastic modulus surprisingly suffered only 9% reduction. Cycling to 90% of life caused more degradation in which reductions of 32%, 44%, 38% and 23% were recorded for UTS, strain to failure, PLS and its strain respectively. Elastic modulus was decreased by 13%. Complete test results are presented in table 4.3.

One of the 90% life tests (specimen i.d.: 0007-001-020-07) failed prematurely because of hydraulic system malfunction (due to lightening). The strength and strain to failure values of this particular specimen were not included in calculation of averages. Average values remaining strength and remaining strain along with their upper and lower limits are presented in figures 4.24-4.25. Results indicated rates of degradation of ultimate strength and strain to failure were highest during the life interval of 10%-50% where they were reduced by as much as 17% and 32% respectively.

However, the highest reduction for elastic modulus occurred at 10% and 90% of life.

Table 4.3: Interrupted cyclic fatigue test results at various stages of life for $[(0,90)/(0,90)]_{2s}$ laminates subjected to σ_{max}=13 Ksi, with R=-1, and f=1 Hz at 1800 °F.

Specimen I.D. & Gage Width (in)	Applied Cycles (% Life), Fracture Location	Initial Elastic Modulus (Msi)	Final Elastic Modulus (Msi)	PL Stress @ 0.005% offset (Ksi)	PL Strain @ 0.005% offset (%)	Remaining Strength (Ksi)	Remaining Strain (%)
0007-001-018-09 (0.75)	2600 (10), [OX]	18.98	16.28	10.68	0.064	31.66	0.424
0101-021-004-04 (0.40)	2600 (10), [OX]	16.93	15.39	10.39	0.068	36.11	0.536
0101-021-003-06 (0.40)	2600(10), [IX]	18.38	15.73	9.71	0.064	31.23	0.509
Ave. Value	***-----***	***18.10***	***15.80***	***10.26***	***0.065***	***33.00***	***0.490***
0007-001-024-08 (0.40)	13000 (50), [IX]	18.94	17.33	10.23	0.060	22.82	0.218
0101-021-004-05 (0.40)	13000 (50), [IX]	19.10	17.09	9.32	0.060	28.76	0.362
0101-021-003-07 (0.40)	13000(50), [OX]	18.65	17.07	9.73	0.060	28.94	0.394
Ave. Value	***-----***	***18.90***	***17.16***	***9.76***	***0.060***	***26.84***	***0.325***
0007-001-020-07♣ (0.75)	23400 (90), [IX]	17.66	15.54	8.01	0.056	18.43	0.150
0101-021-004-06 (0.40)	23400 (90), [OX]	16.12	14.39	7.77	0.056	26.94	0.332
0101-021-003-08 (0.40)	23400(90), [IX]	18.10	15.30	7.32	0.051	22.02	0.252
Ave. Value	***-----***	***17.29***	***15.08***	***7.70***	***0.054***	***24.48***	***0.292***

♣Specimen premature failure system malfunction. Remaining strength and strain data are not reliable.

Test results at 15 Ksi stress level for 10% of life (1235 cycles), 50% of life (6175 cycles) and 90% of life (11115 cycles) are presented in table 4.4. Cycling to 10% of life reduced strength, strain, modulus, PLS and its

corresponding strain by 9%, 7%, 12%, 35% and 20% respectively. Cycling to 50% of life caused more severe degradation where a reductions of 24%, 33%, 14%, 37% and 24% were recorded. Finally, at 90% of life reductions of 27%, 37%, 12%, 37%, and 26% were recorded. Ultimate strength and strain to failure suffered the highest reduction during (10%-50%) life interval (figures 4.24-4.25).

Table 4.4: Interrupted cyclic fatigue test results at various stages of life for $[(0,90)/(0,90)]_{2s}$ laminates subjected to σ_{max}=15 Ksi, with R=-1, and f=1 Hz at 1800 °F.

Specimen I.D. & Gage Width (in)	Applied Cycles (% Life), Fracture Location	Initial Elastic Modulus (Msi)	Final Elastic Modulus (Msi)	PL Stress @ 0.005% offset (Ksi)	PL Strain @ 0.005% offset (%)	Remaining Strength (Ksi)	Remaining Strain (%)
0007-001-022-12 (0.40)	1235 (10), [IX]	19.53	17.23	8.86	0.06	30.79	0.470
0101-021-004-03 (0.40)	1235 (10), [IX]	18.13	16.08	7.89	0.056	33.18	0.458
0101-021-003-11 (0.40)	1235 (10), [OX]	19.33	17.21	7.43	0.052	33.95	0.529
Ave. Value	***1235 (10)***	***19.00***	***16.84***	***8.06***	***0.056***	***32.64***	***0.486***
0007-001-024-18 (0.40)	6175 (50), [IX]	18.84	17.13	8.09	0.053	24.71	0.281
0101-021-004-02 (0.40)	6175 (50), [OX]	17.14	14.84	7.71	0.053	28.79	0.353
0101-021-003-10 (0.40)	6175 (50), [OX]	18.61	15.19	7.27	0.52	28.26	0.407
Ave. Value	***6175 (50)***	***18.20***	***15.72***	***7.69***	***0.053***	***27.25***	***0.347***
0007-001-025-12 (0.40)	11115 (90), [IX]	16.19	13.99	6.99	0.053	23.17	0.270
0101-021-004-01 (0.40)	11115 (90), [OX]	16.34	14.62	7.81	0.053	30.47	0.398
0101-021-003-09 (0.40)	11115 (90), [IX]	18.30	16.41	8.52	0.053	25.19	0.319
Ave. Value	***11115 (90)***	***16.94***	***15.00***	***7.77***	***0.053***	***26.27***	***0.329***

At 10% of life, reduction in strength, strain to failure and initial elastic modulus basically remained unchanged for both stress levels. However, the 15 Ksi stress level reduced proportional limit strength twice as much and the associated strain three times as much as the 13 Ksi stress level. At 50% of life at 13 Ksi stress level, the most drastic change occurred in proportional limit strength and its strain. Largest reduction of strength and failure strain occurred during the 10%-50% interval for both stress levels.

4.2.2 Tension-Compression Fatigue of $[(0,90)/(+45,-45)]_{2s}$ Laminates:

Interrupted cyclic fatigue tests of quasi-isotropic laminates were carried out under a maximum stress level of 13 Ksi for 10% (2514 cycles), 50% (12570 cycles) and 90% of life (22626 cycles). Results are tabulated in table 4.5. Cycling to 10% of life, strength, strain to failure, modulus, PLS and its corresponding strain were reduced by 9%, 5%, 11%, 20% and 21% respectively. Cycling to 50% of life, this reduction increase to 25%, 31%, 13%, 29%, and 25%. The above indicates during the cycling interval of 10%-50%, remaining strength and remaining strain decrease significantly. At 90% of life reduction of 23%, 38%, 13%, 22%, and 26% were obtained. Fatigue degradation of ultimate tensile strength and ultimate tensile strain as a function of cycles are plotted in figures 4.26-4.27.

Table 4.5: Interrupted cyclic fatigue test results at various stages of life for $[(0,90)/(+45,-45)]_{2s}$ laminates subjected to σ_{max}=13 Ksi, with R=-1, and f=1 Hz at 1800 °F.

Specimen I.D. & Gage Width (in)	Applied Cycles (% Life), Fracture Location	Initial Elastic Modulus (Msi)	Final Elastic Modulus (Msi)	PL Stress @ 0.005% offset (Ksi)	PL Strain @ 0.005% offset (%)	Remaining Strength (Ksi)	Remaining Strain (%)
0007-001-030-06 (0.40)	2514 (10), [IX]	17.14	15.16	9.19	0.064	29.95	0.450
0007-001-030-16 (0.40)	2514 (10), [IX]	18.12	16.06	9.14	0.060	29.46	0.424
0101-021-009-01 (0.40)	2514 (10), [IX]	19.05	17.07	9.72	0.064	31.11	0.434
Ave. Value	***2514 (10)***	***18.10***	***16.09***	***9.35***	***0.063***	***30.17***	***0.436***
0007-001-030-07 (0.40)	12570 (50), [OX]	17.05	14.46	7.76	0.056	26.45	0.383
0007-001-030-14 (0.40)	12570 (50), [IX]	16.89	14.77	7.76	0.056	21.46	0.237
0101-021-009-03 (0.40)	12570 (50), [IX]	16.64	14.61	9.59	0.068	26.71	0.338
Ave. Value	***12570 (50)***	***16.86***	***14.61***	***8.37***	***0.060***	***24.87***	***0.319***
0007-001-011-08 (0.40)	22626 (90), [OX]	18.39	16.56	8.33	0.056	26.61	0.327
0101-021-009-07 (0.40)	22626 (90), [OX]	17.96	15.30	9.51	0.060	25.27	0.281
0101-021-009-08 (0.40)	22626 (90), [IX]	17.35	15.09	9.46	0.060	24.26	0.254
Ave. Value	***22626 (90)***	***17.90***	***15.65***	***9.10***	***0.059***	***25.38***	***0.287***

Results of 15 Ksi tests at 10% of life (1480 cycles), 50% of life (7400 cycles) and 90% of life (13320 cycles) are presented in table 4.6. At 10% of life tensile strength, strain to failure, elastic modulus, PLS and the strain associated with it were decreased by as much as 11%, 10%, 17%, 35%, and 20% respectively. Cyclic loading for 50% of life resulted in reduction of 21%,

29%, 14%, 25%, and 25%. At 90% of life, these reductions were as high as 33%, 43%, 12%, 39%, and 33% respectively.

Table 4.6: Interrupted cyclic fatigue test results at various stages of life for $[(0,90)/(+45,-45)]_{2s}$ laminates subjected to σ_{max}=15 Ksi, with R=-1, and f=1 Hz at 1800 °F.

Specimen I.D. & Gage Width (in)	Applied Cycles (% Life), Fracture Location	Initial Elastic Modulus (Msi)	Final Elastic Modulus (Msi)	PL Stress @ 0.005% offset (Ksi)	PL Strain @ 0.005% offset (%)	Remaining Strength (Ksi)	Remaining Strain (%)
0007-001-030-05 (0.40)	1480 (10), [OX]	17.07	13.92	8.40	0.064	27.59	0.375
0007-001-030-10 (0.40)	1480 (10), [OX]	17.29	13.76	6.67	0.067	28.95	0.409
0101-021-009-02 (0.40)	1480 (10), [OX]	16.34	14.28	7.79	0.060	31.06	0.461
Ave. Value	***1480 (10)***	***16.90***	***13.99***	***7.62***	***0.064***	***29.20***	***0.415***
0007-001-030-08 (0.40)	7400 (50), [OX]	16.91	14.25	7.78	0.060	25.14	0.317
0007-001-030-12 (0.40)	7400 (50), [IX]	17.78	15.74	8.86	0.060	25.04	0.323
0101-021-009-04 (0.40)	7400 (50), [IX]	17.74	15.42	9.62	0.060	27.61	0.341
Ave. Value	***7400 (50)***	***17.48***	***15.14***	***8.75***	***0.060***	***25.93***	***0.327***
0007-001-030-19 (0.40)	13320 (90), [IX]	NA	11.97	4.99	0.049	17.21	0.237
0101-021-009-05 (0.40)	13320 (90), [OX]	17.75	15.63	8.15	0.056	23.64	0.266
0101-021-009-06 (0.40)	13320 (90), [IX]	16.96	14.78	8.18	0.056	24.93	0.289
Ave. Value	***13320 (90)***	***17.35***	***15.21***	***7.11***	***0.054***	***21.93***	***0.264***

4.2.3 Tension-Tension Fatigue of $[(0,90)/(+45,-45)]_{2s}$ Laminates:

Interrupted tension-tension cyclic fatigue of quasi-isotropic laminates under maximum stress levels of 13 Ksi and 15 Ksi, fatigue ratio of 0.05, frequency of 1 Hz, and test temperature of 1800 °F were conducted. Not having any data on average lives of quasi-isotropic laminates for tension-tension loading, average lives of tension-compression tests results (section 4.1.2) were used instead. Specimens were cycled to 10%, 50%, and 90% of these lives. To gain more insight into tension-tension fatigue behavior of the laminates, stress-strain curves were collected during these tests and the results are presented in figures 4.28-4.29. In the 15 Ksi tests the specimen were fully cracked upon the application of the first cycle. This was translated to a more developed hysteresis in the stress-strain curves. Fatigue tests were followed by stroke control quasi-static tensile tests at 1800 °F and the results of remaining properties are presented in table 4.7. There were great variability in initial elastic modulus this batch of specimens which ultimately translated into large variations in remaining strength and remaining strain to failure data (figures 4.30-4.31). From table 4.7 it is evident that the values of initial elastic modulus are dependent on the panel number. Specimens subjected to 15 Ksi had higher remaining strength and remaining strain than those tested at 13 Ksi. There is no scientific explanation for these observations. Possibility of mistakes made in labeling the specimens or during manufacturing processing always exists. The stiffness measurement as a function of cycles were made. Evolution of unloading tensile modulus, normalized with respect to the initial tensile modulus, for two stress levels are presented in figures 4.32-4.33.

Table 4.7: Interrupted cyclic fatigue test results at various stages of life for $[(0,90)/(+45,-45)]_{2s}$ laminates subjected to σ_{max}=13 Ksi and σ_{max}=15 Ksi with R=0.05, f=1 Hz, at 1800 °F.

Specimen I.D. & Gage Width (in)	Max. Stress (Ksi)	Cycles (% Life) [Fracture Location]	Initial Elastic Modulus (Msi)	Final Elastic Modulus (Msi)	PL Stress @ 0.005% offset (Ksi)	PL Strain @ 0.005% offset (%)	Remaining Strength (Ksi)	Remaining Strain (%)
0007-001-034-07 (0.40)	13	2514 (10), [IX]	23.37	21.11	13.49	0.071	21.19	0.195
0007-001-034-01 (0.40)	13	12570 (50), [IX]	23.89	20.25	13.92	0.075	23.44	0.238
0007-001-034-02 (0.40)	13	22626 (90), [OX]	21.56	18.92	12.66	0.075	21.97	0.250
0007-001-011-06 (0.40)	15	1480 (10), [IX]	17.63	15.71	8.43	0.060	31.21	0.435
0007-001-007-20 (0.40)	15	7400 (50), [OX]	17.43	15.78	9.75	0.064	27.93	0.335
0101-001-007-18 (0.40)	15	13320 (90), [IX]	17.31	15.18	8.91	0.060	28.01	0.401

Similar to the tension-compression tests, the initial degradation of 13 Ksi tests occurred in the first three cycles where stiffness dropped to 80% of its original value. For the 15 Ksi tests same reduction in modulus occurred upon the application of first cycle. Because these data were collected for 90% tests, the final nonlinear part of the curves where stiffness degrades rapidly are missing.

4.3 SEM Observations

Close examination of a fiber bundle cross section (fig4.34) indicates that fibers (gray color), in general, are in close contact with the boron based particles (black ring around the fiber). The white color material is the SiC matrix, and the hexagon shapes represent the porosity between the fibers.

For stress levels higher than PLS, the oxidation protective coating and the matrix lying underneath it crack (figure 4.35), exposing the fibers to the oxygen. The boron-based particles react with the oxygen at 1800 °F and form a liquid glass which flows around the fibers and solidifies (figure 3.36). Under cyclic loading damage appears in form of, fiber fracture occurring at locations of fiber imperfection (figures 4.37-4.38) and frictional wear. Not all the fibers have the new glass coating. But for those that do, glass coatings begin to crack (figures 4.39-4.40). This may be caused by frictional wear, buckling due to compression part of the loading cycle or both. Damage by wear mechanism is operating on the fibers (figures 4.41-4.42) resulting in interfacial shear stress degradation. When the number of fiber fractures reaches a characteristic state, failure of the composite is immanent starting by fiber bundle failure (figure 4.43). Fracture surfaces of fatigued specimens were investigated indicating a torturous fracture path (figure 4.44) along with extensive fiber pull-outs for both stacking sequences The final fracture is more likely to occur at locations of high porosity (figure 4.45). There was not a noticeable difference in fracture behavior of cross-ply and quasi-isotropic laminates. The 0 degree and 45 degree plies showed the regular wear and tear caused by cyclic loading (figures 4.46-4.47).

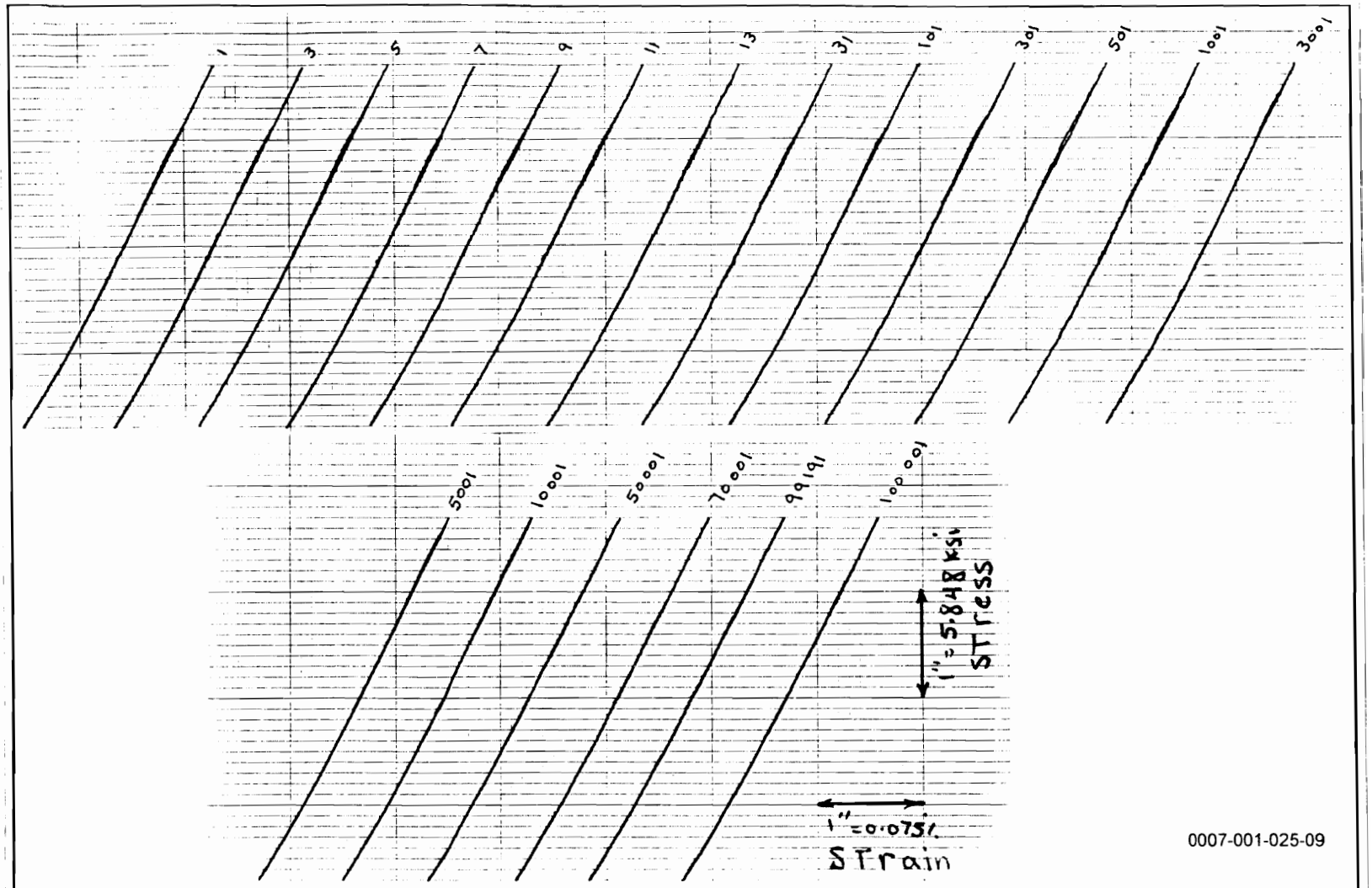

Figure 4.1: Stress-strain loops for a $[(0,90)/(0,90)]_{2s}$ laminate for σ_{max}=10 Ksi, R=-1, and f=1 Hz at 1800 F.

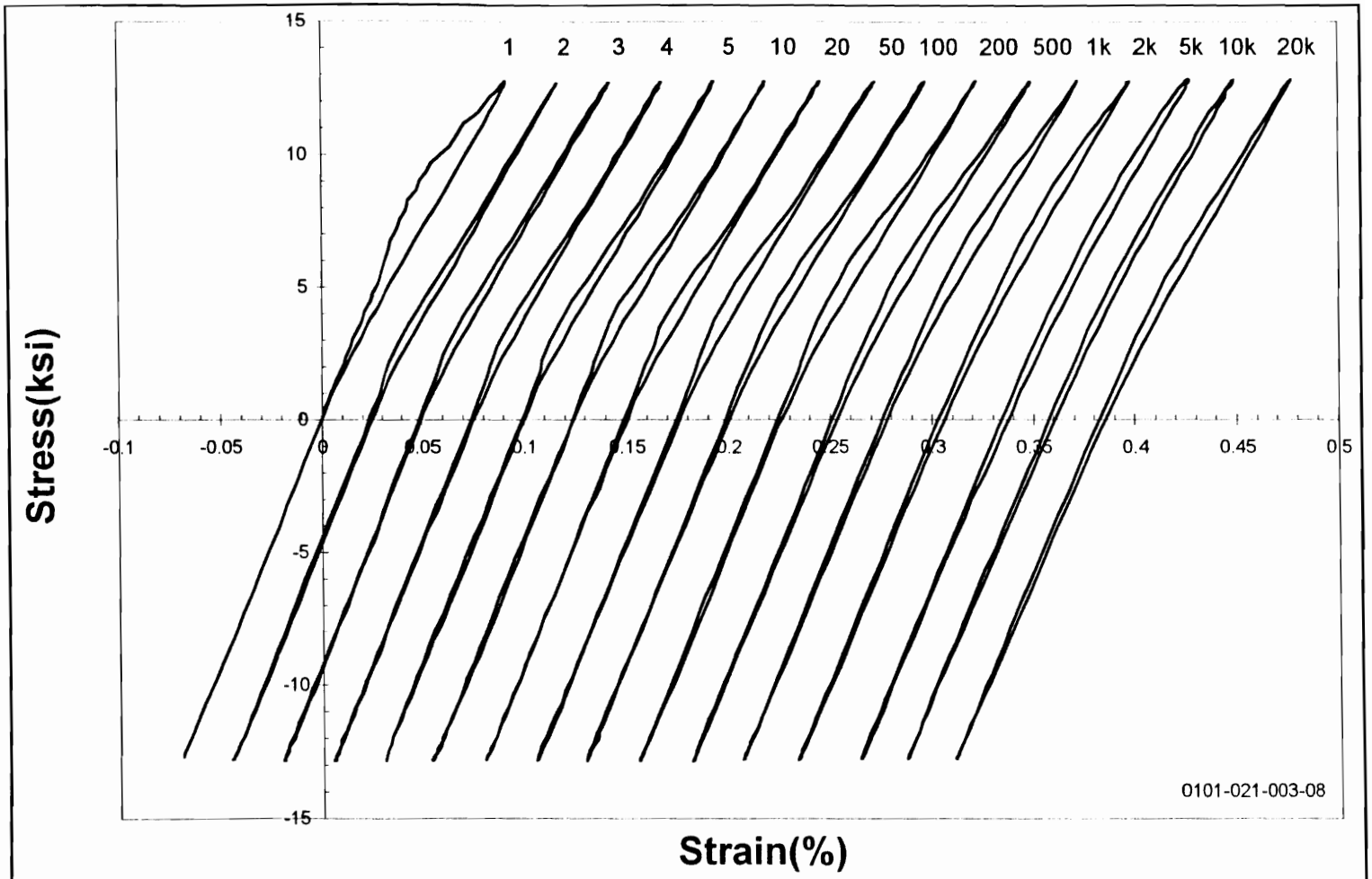

Figure 4.2: Evolution of stress-strain loops for a $[(0,90)/(0,90)]_{2s}$ laminate subjected to σ_{max}=13 Ksi, R=-1, f=1 Hz, at 1800 F.

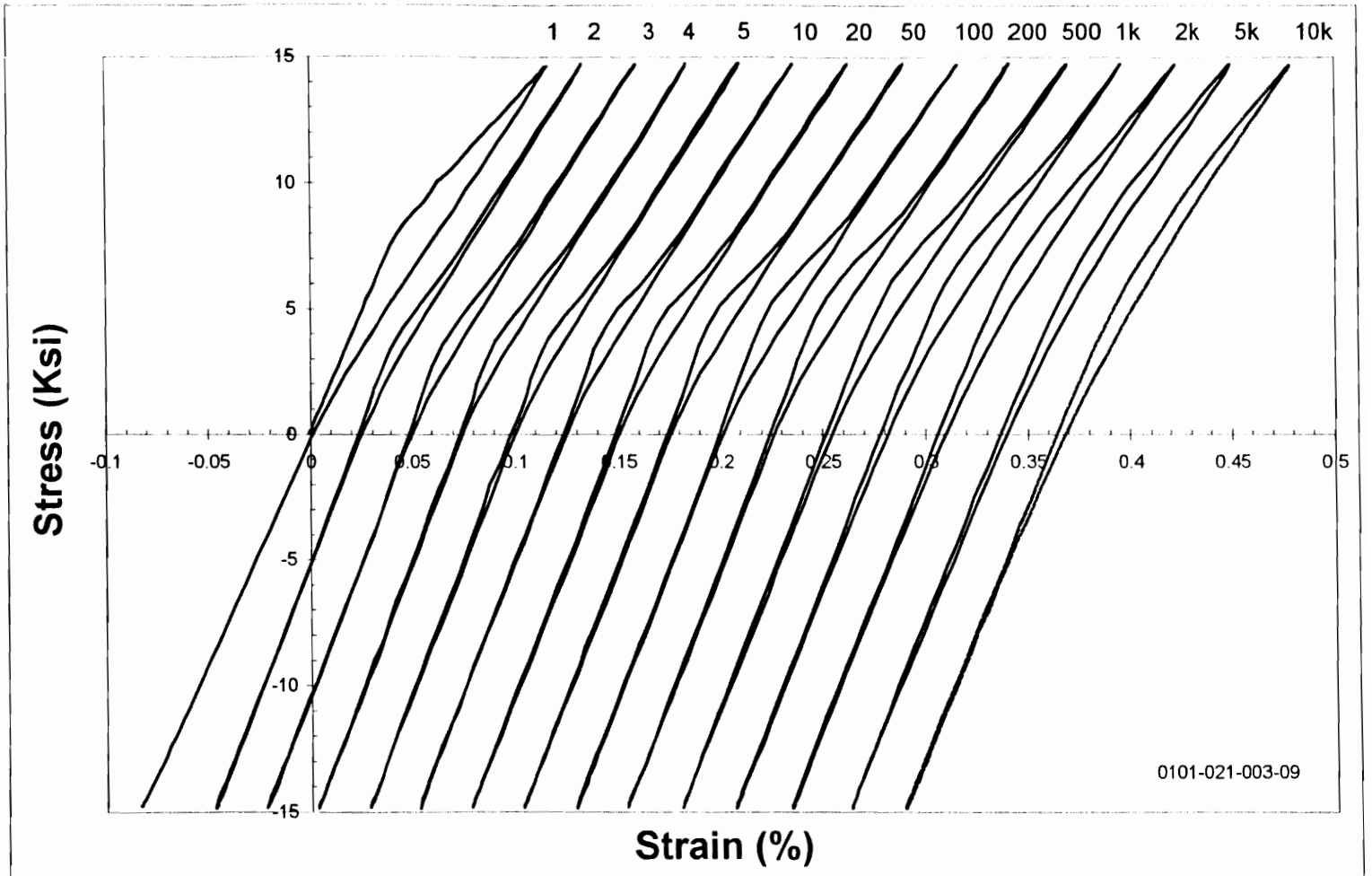

Figure 4.3: Evolution of stress-strain loops for a $[(0,90)/(0,90)]_{2s}$ laminate subjected to σ_{max}=15 Ksi, R=-1, and f=1 Hz, at 1800 F.

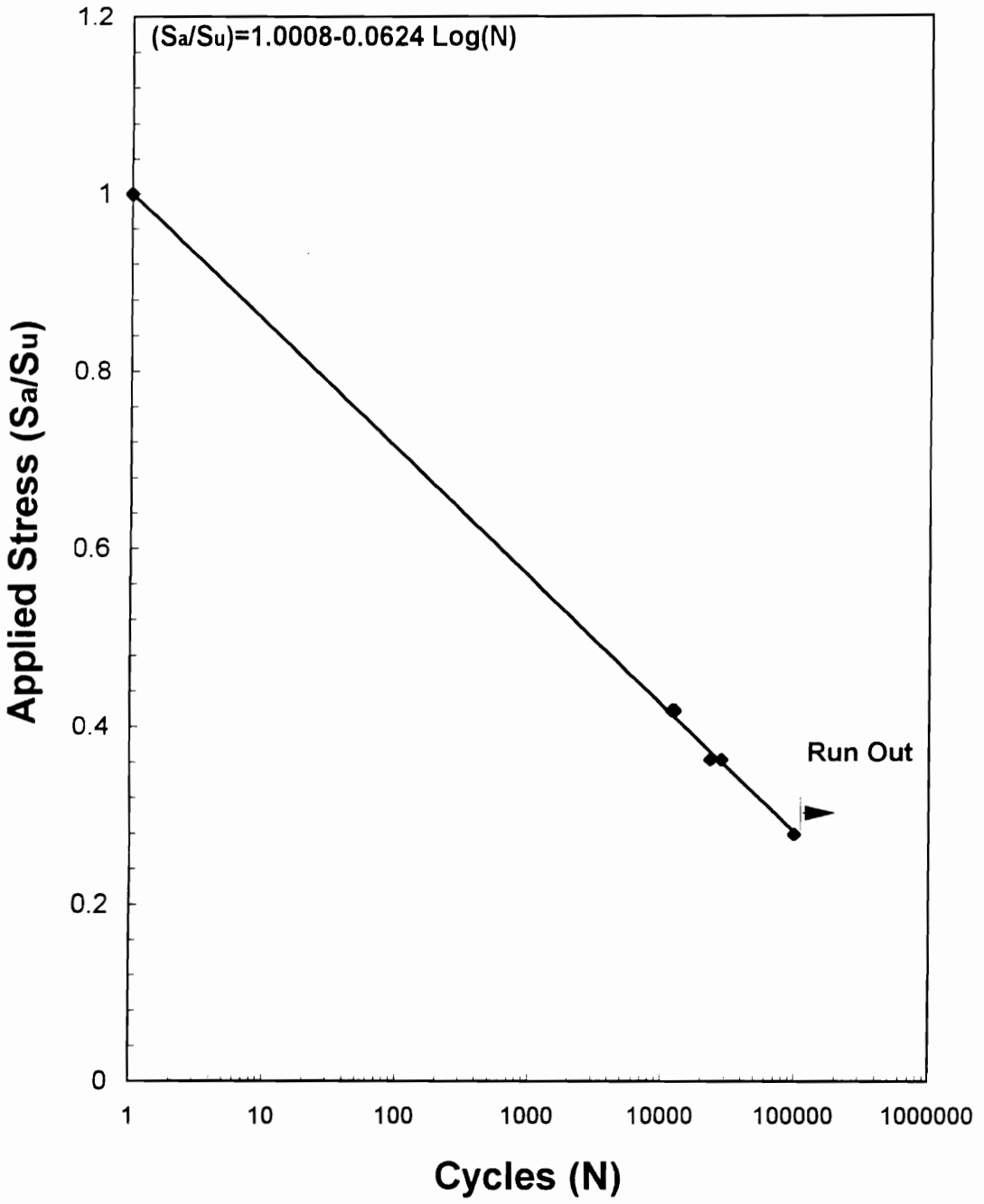

Figure 4.4: Fatigue response of $[(0,90)/(0,90)]_{2s}$ laminates for cyclic loading with R=-1, f=1 Hz at 1800 F.

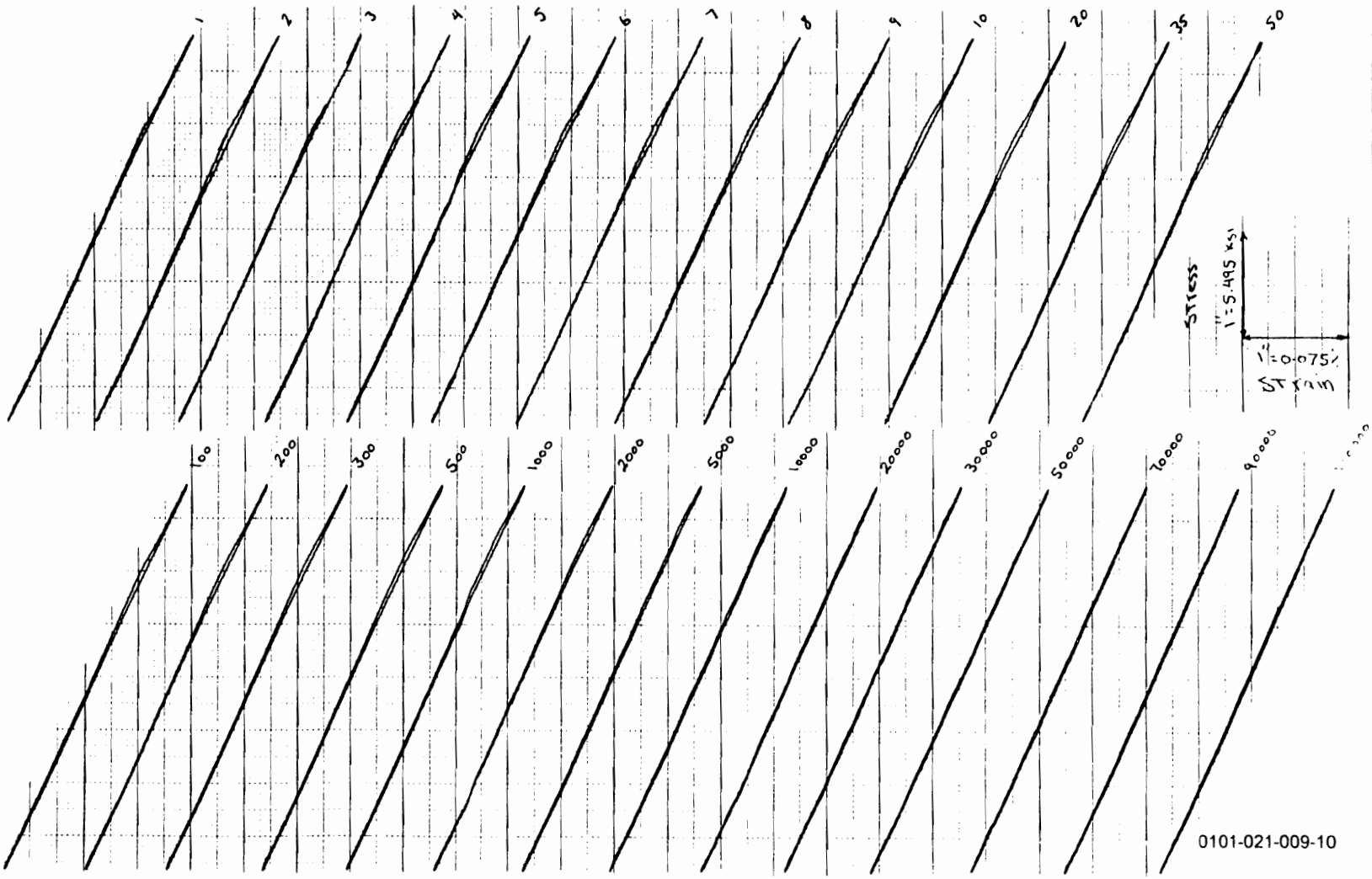

Figure 4.5: Stress-strain loops for a $[(0,90)/(45,-45)]_{2s}$ laminate for σ_{max}=10 Ksi, R=-1, f=1 Hz at 1800 F.

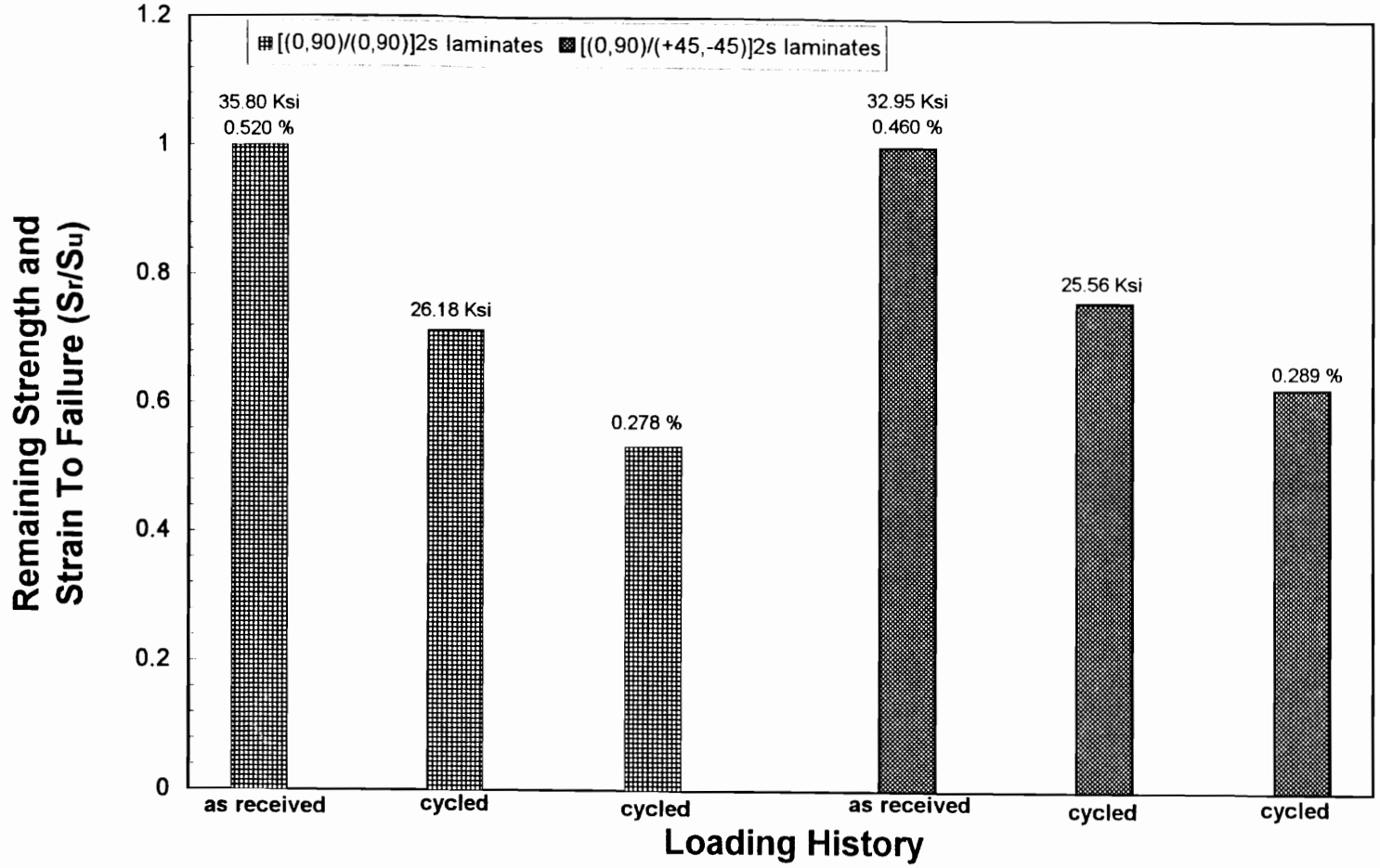

Figure 4.6: Remaining strength and strain of $[(0,90)/(0,90)]_{2s}$ and $[(0,90)/(+45/-45)]_{2s}$ laminates after 100 K cyclying under σ_{max}=10 Ksi with R=-1, and f=1 Hz at 1800 F.

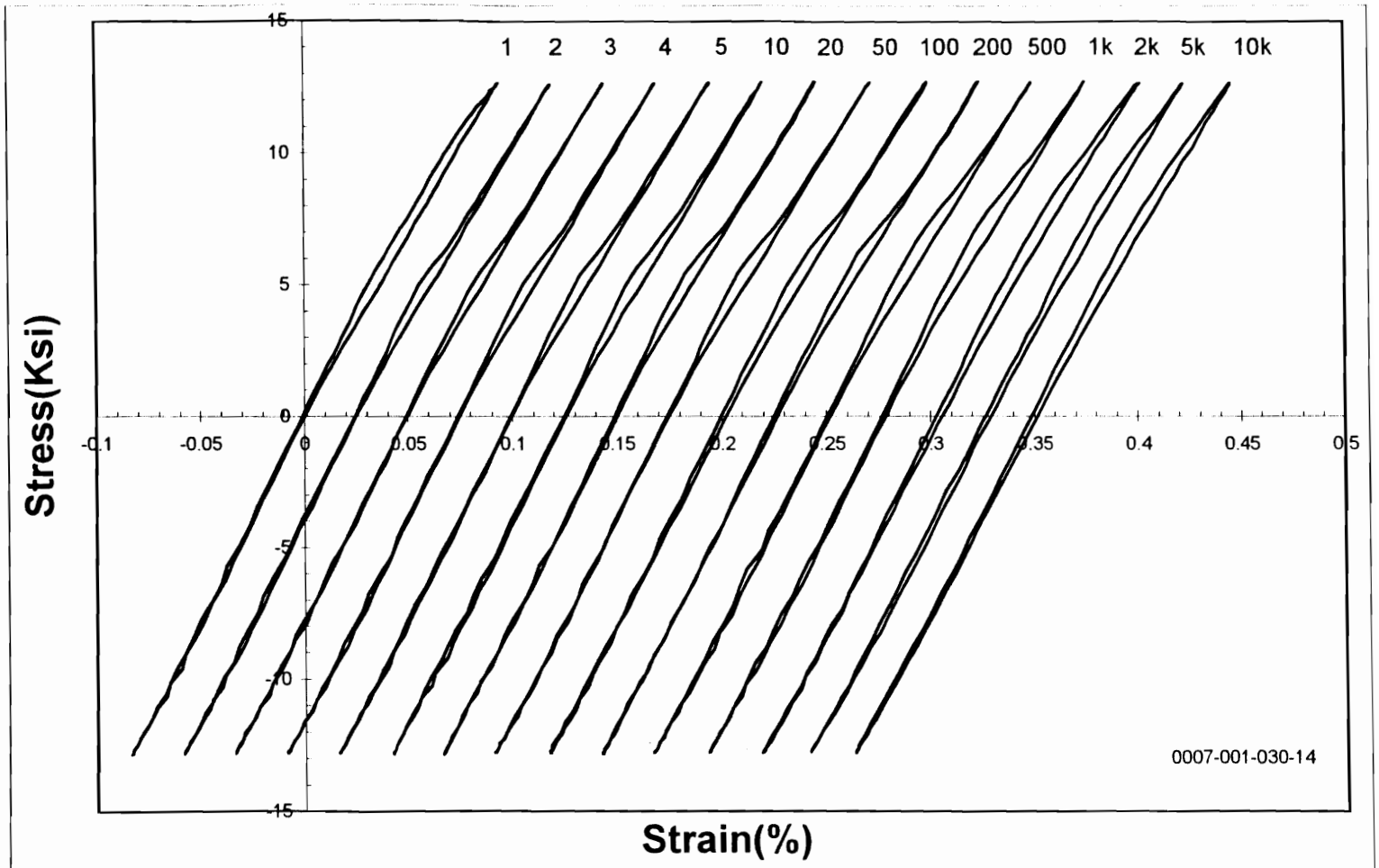

Figure 4.7: Evolution of stress-strain loops for a $[(0,90)/(+45,-45)]_{2s}$ laminate subjected to σ_{max}=13 Ksi, R=-1, and f=1 Hz at 1800 F.

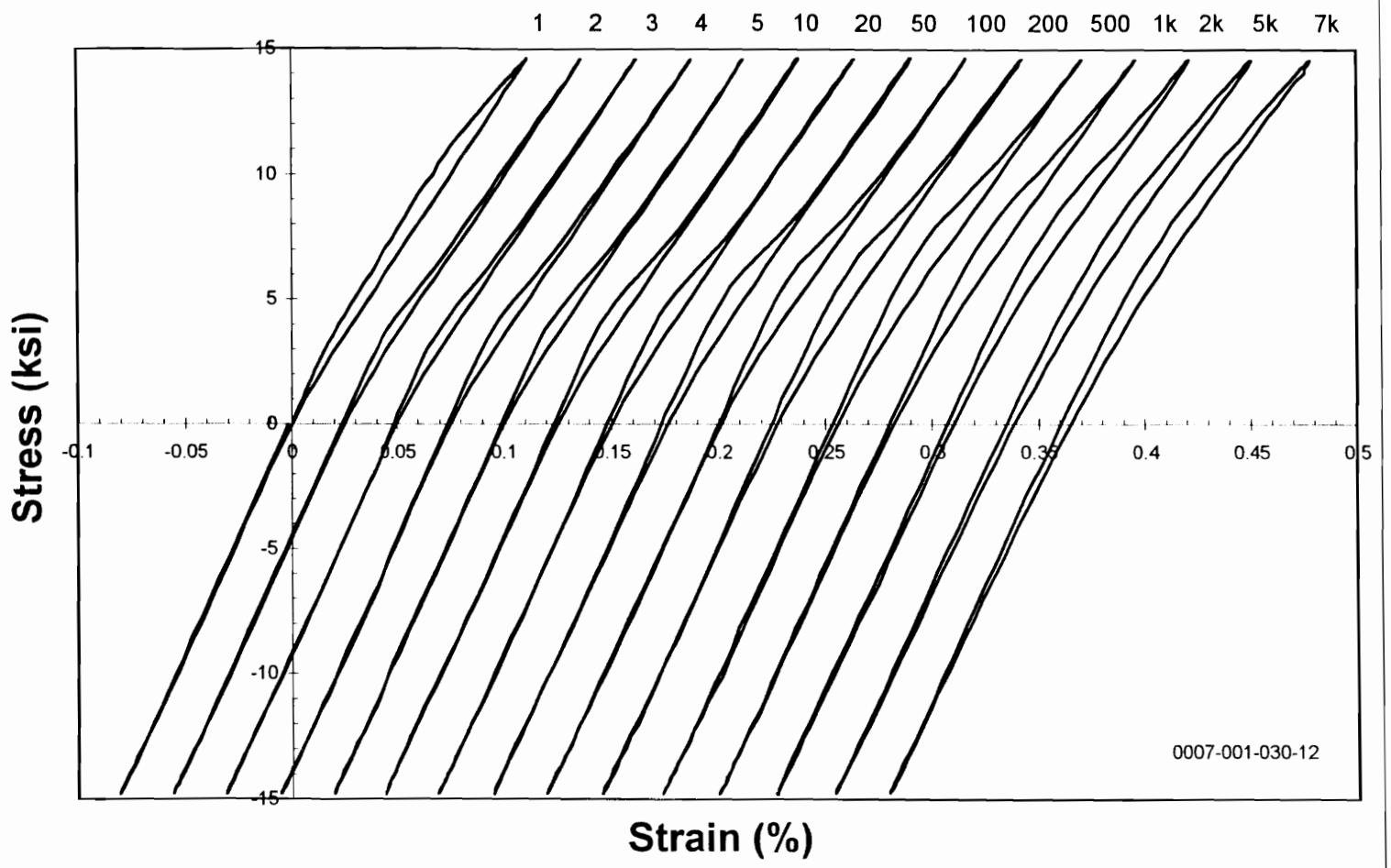

Figure 4.8: Evolution of stress-strain loops for a $[(0,90)/(+45,-45)]_{2s}$ laminate subjected to σ_{max}=15 Ksi, R=-1, and f=1 Hz at 1800 F.

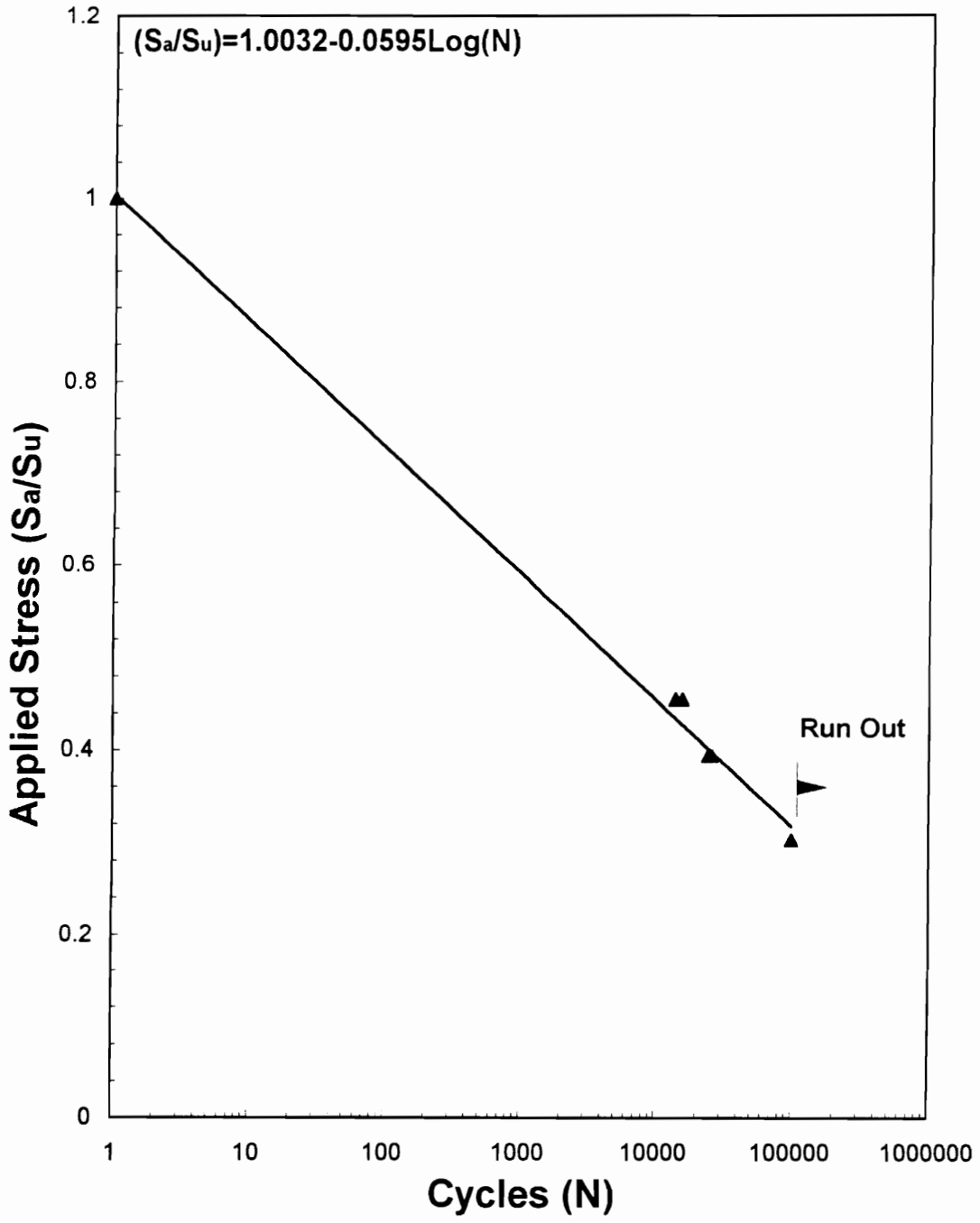

Figure 4.9: Fatigue response of $[(0,90)/(45,-45)]_{2s}$ laminates for cyclic loading with R=-1, f=1 Hz at 1800 F.

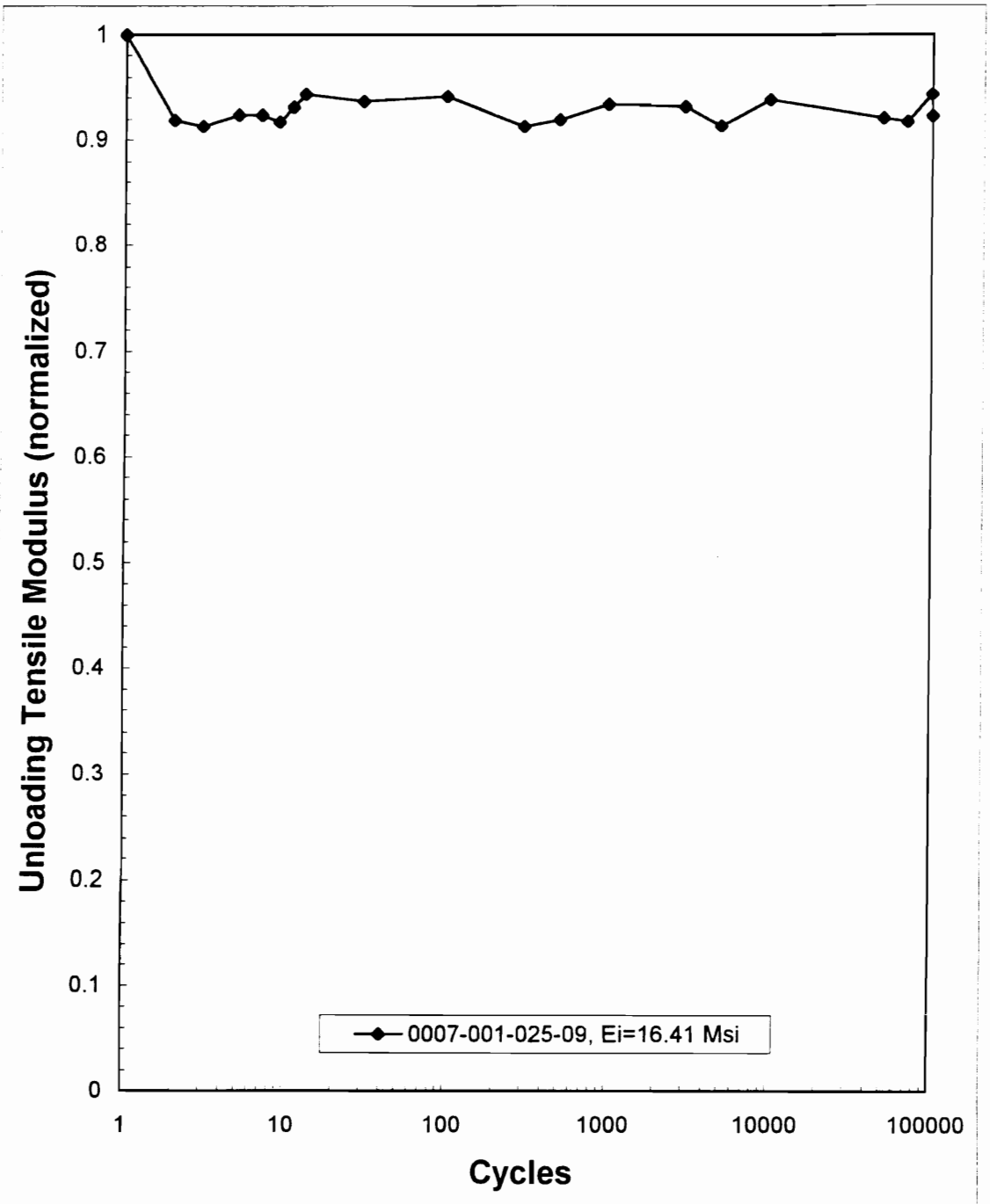

Figure 4.10:Stiffness degradation for a $[(0,90)/(0,90)]_{2s}$ laminate for σ_{max}=10 Ksi with R=-1, f=1 Hz at 1800 F.

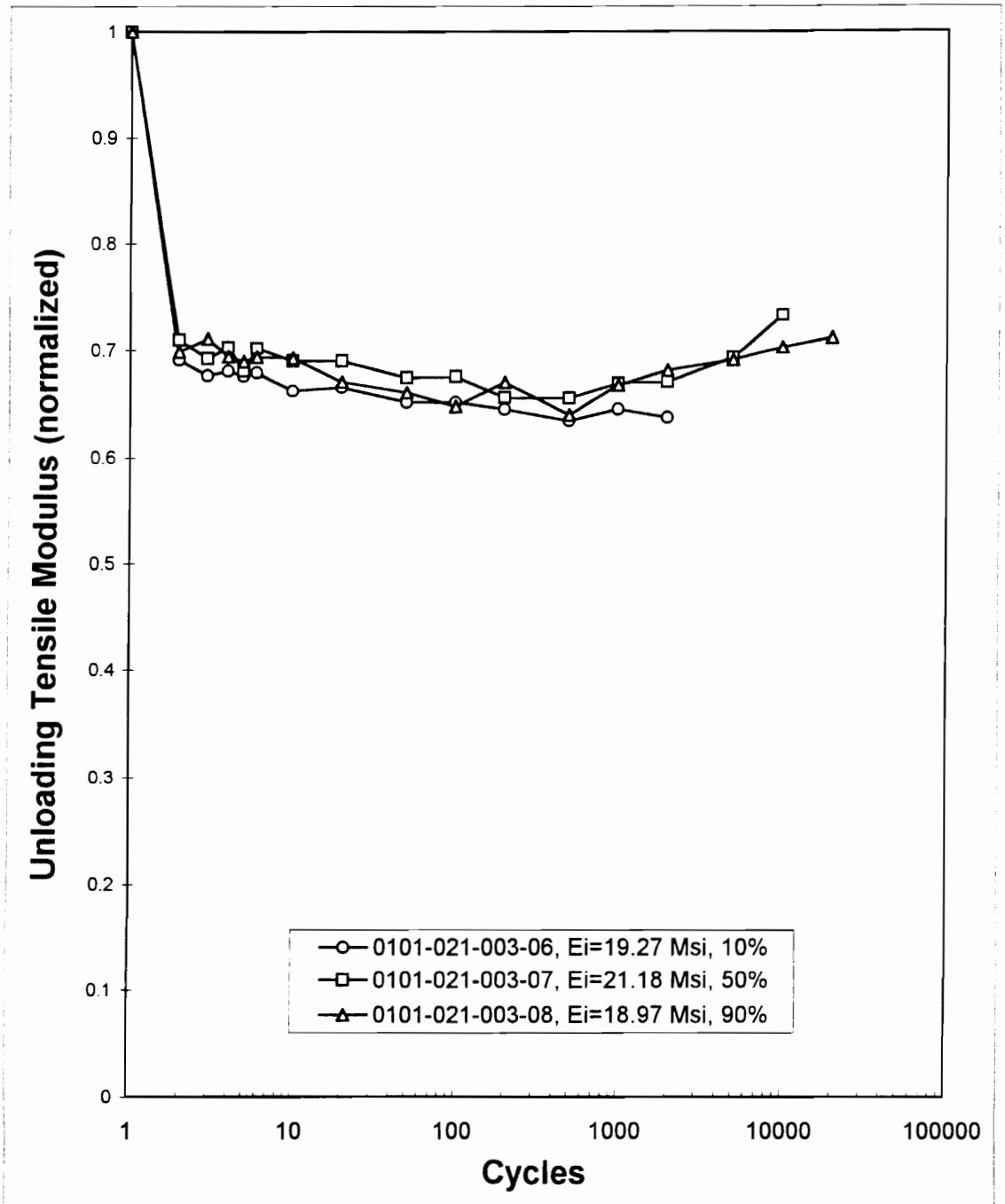

Figure 4.11: Stiffness degradation for a $[(0,90)/(0,90)]_{2s}$ laminate for σ_{max}=13 Ksi with R=-1, f=1 Hz at 1800 F.

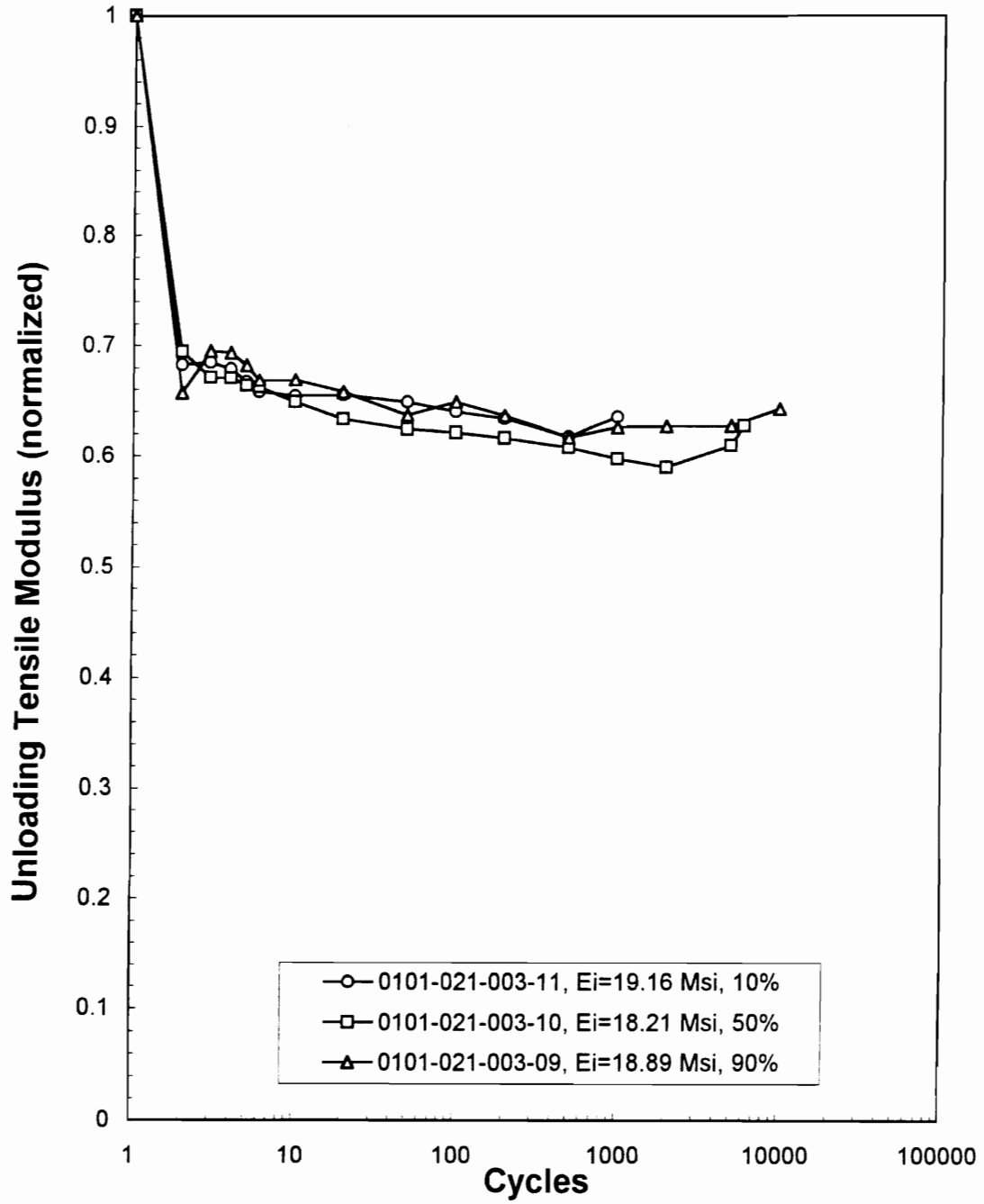

Figure 4.12: Stiffness degradation for a $[(0,90)/(0,90)]_{2s}$ laminate for σ_{max}=15 Ksi with R=-1, f=1 Hz at 1800 F.

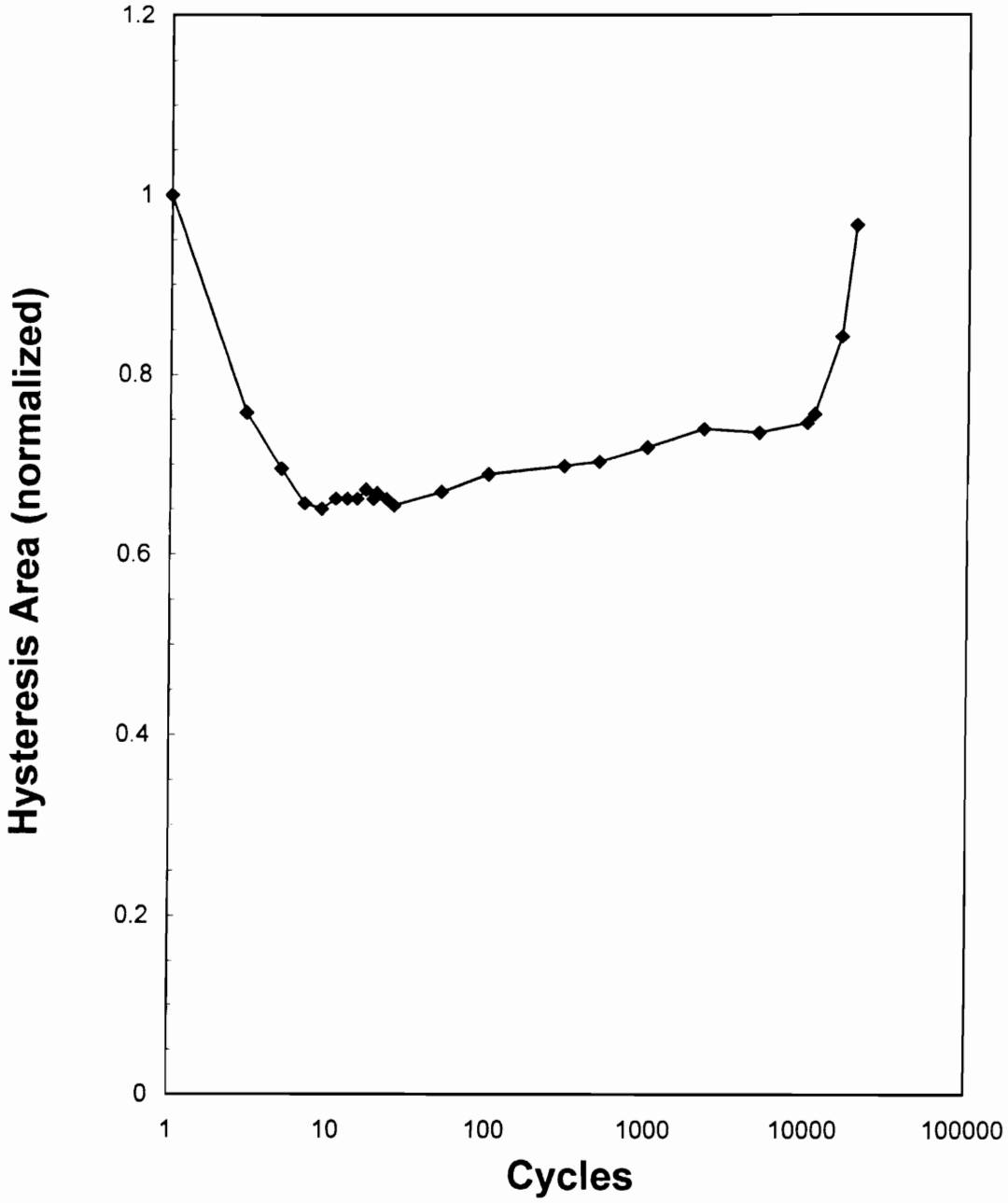

Figure 4.13: Evolution of hysteresis area for a $[(0,90)/(0,90)]_{2s}$ laminate for σ_{max}=13 Ksi with R=-1, f=1 Hz at 1800 F.

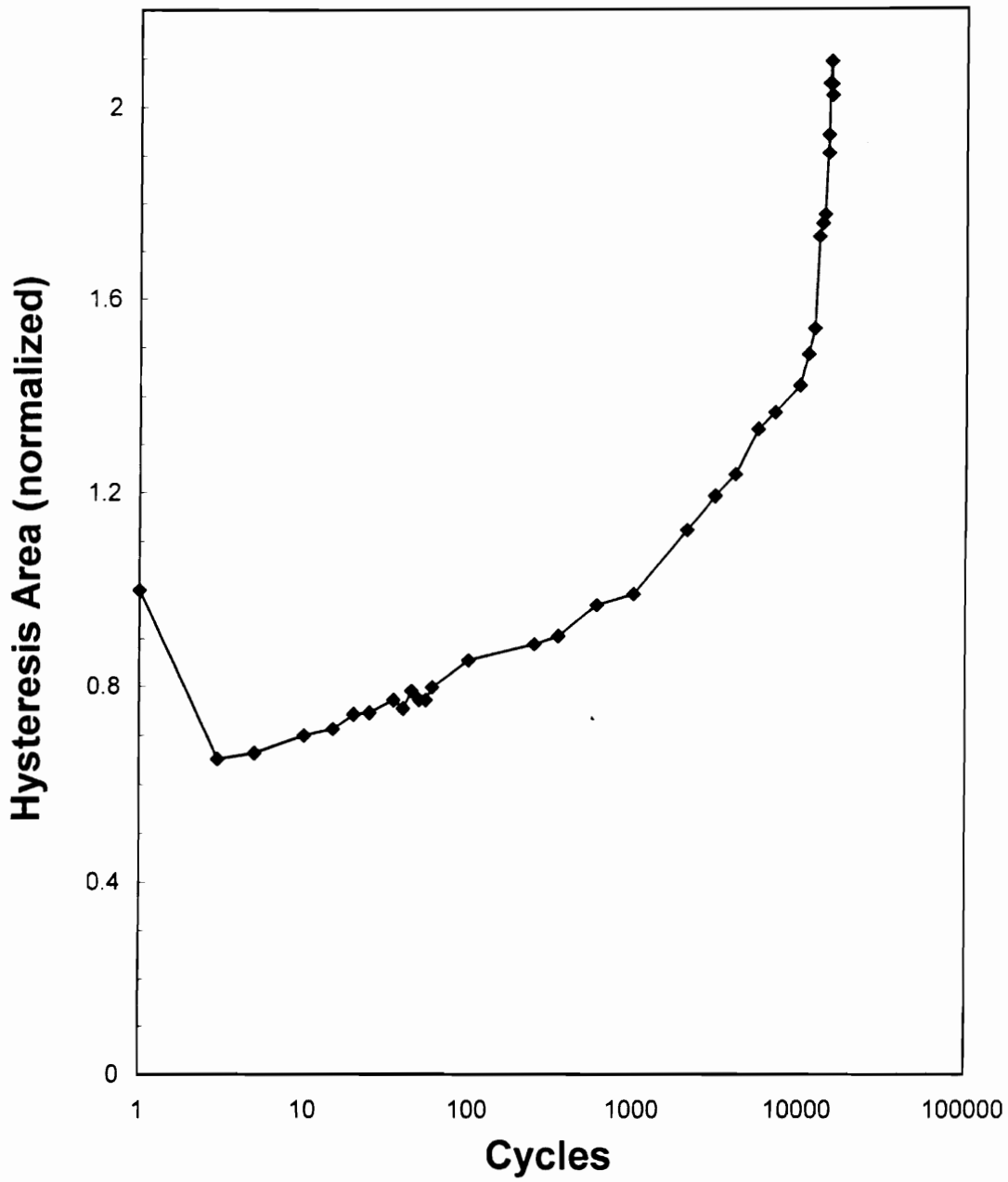

Figure 4.14: Evolution of hysteresis area for a $[(0,90)/(0,90)]_{2s}$ laminate for σ_{max}=15 Ksi, R=-1, f=1 Hz at 1800 F.

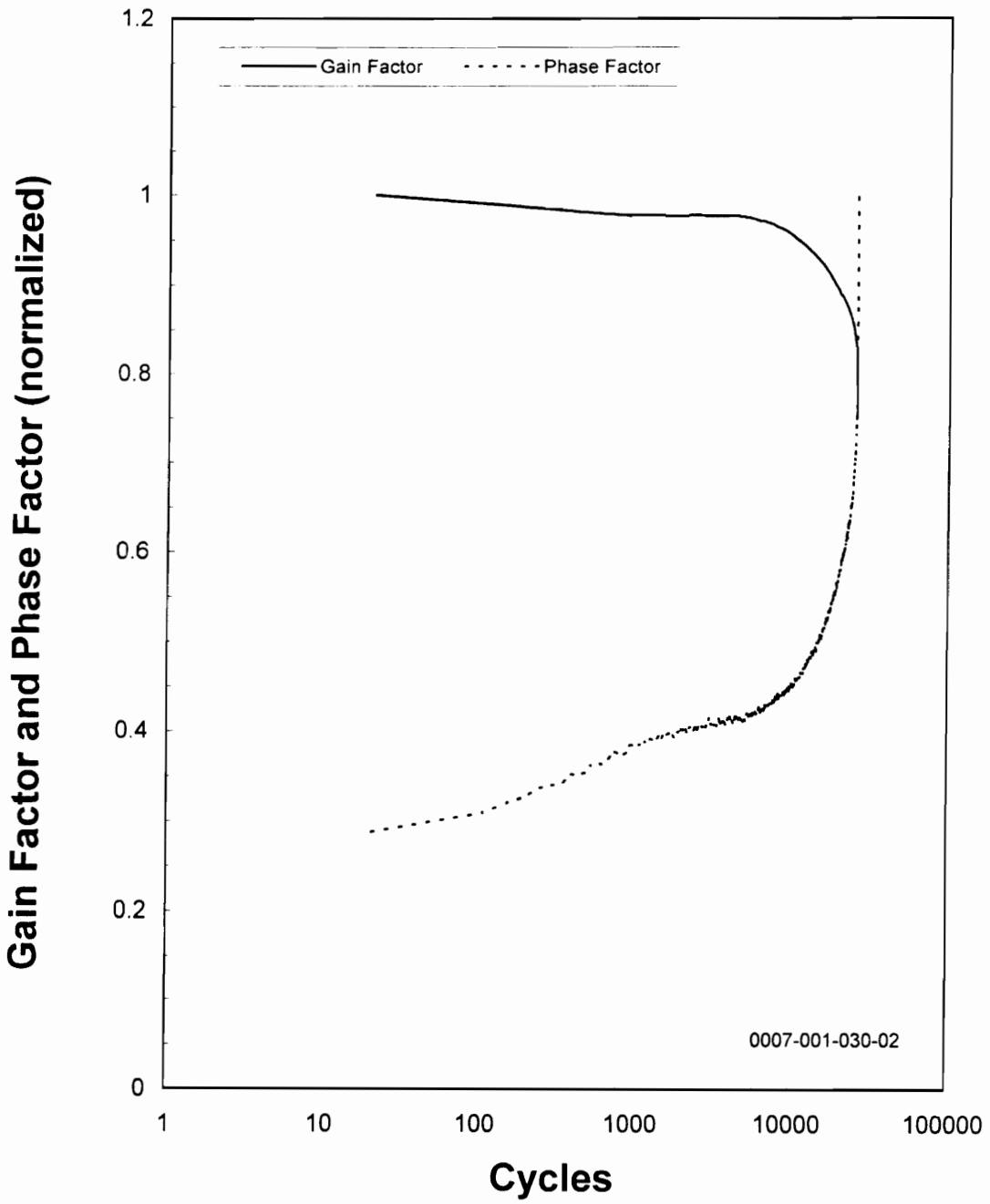

Figure 4.15: Dynamic response of a $[(0,90)/(0,90)]_{2s}$ laminate for σ_{max}=13 Ksi with R=-1, f=1 Hz at 1800 F.

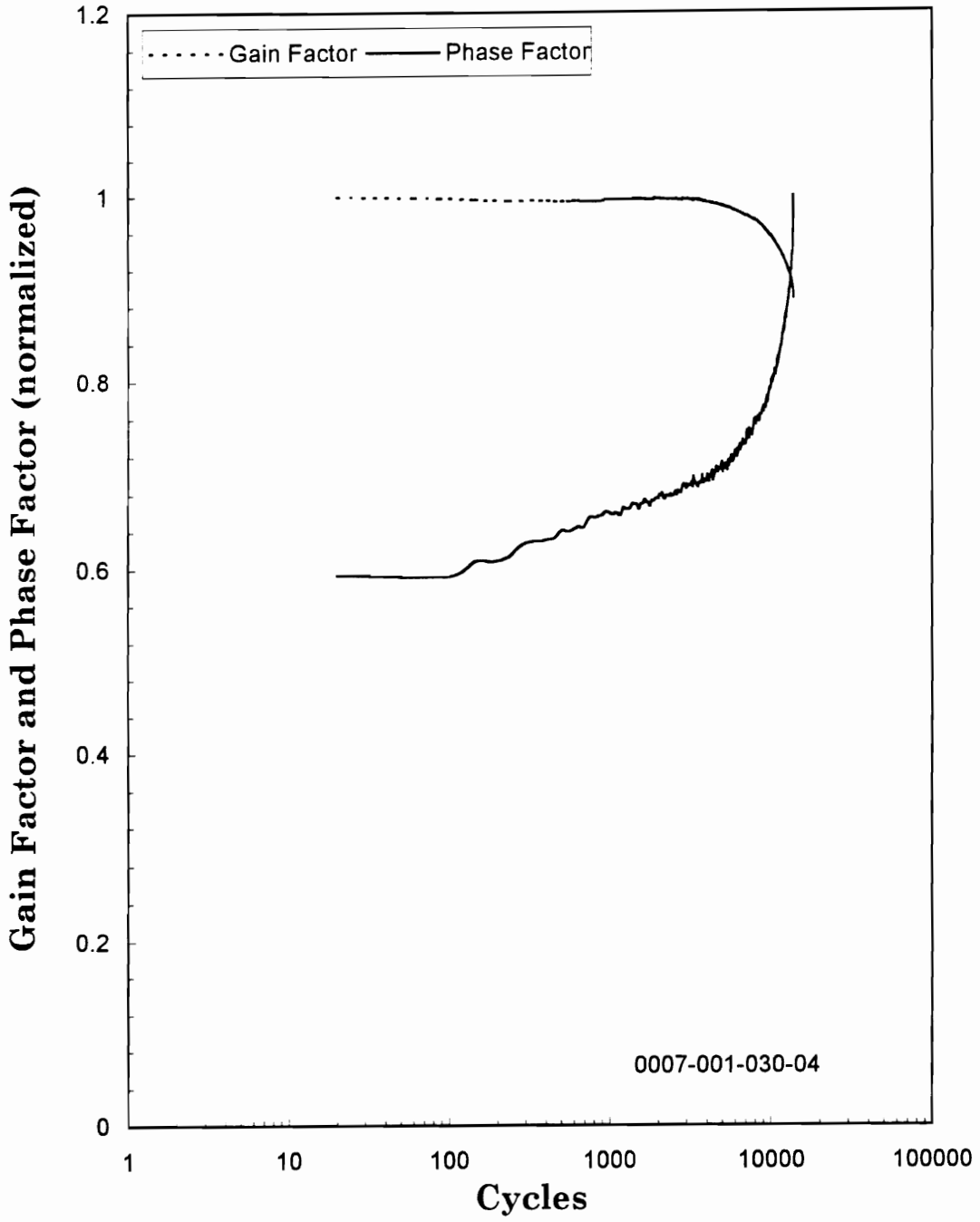

Figure 4.16: Dynamic response of a $[(0,90)/(0,90)]_{2s}$ laminate for σ_{max}=15 Ksi, R=-1, f=1 Hz, at 1800 F.

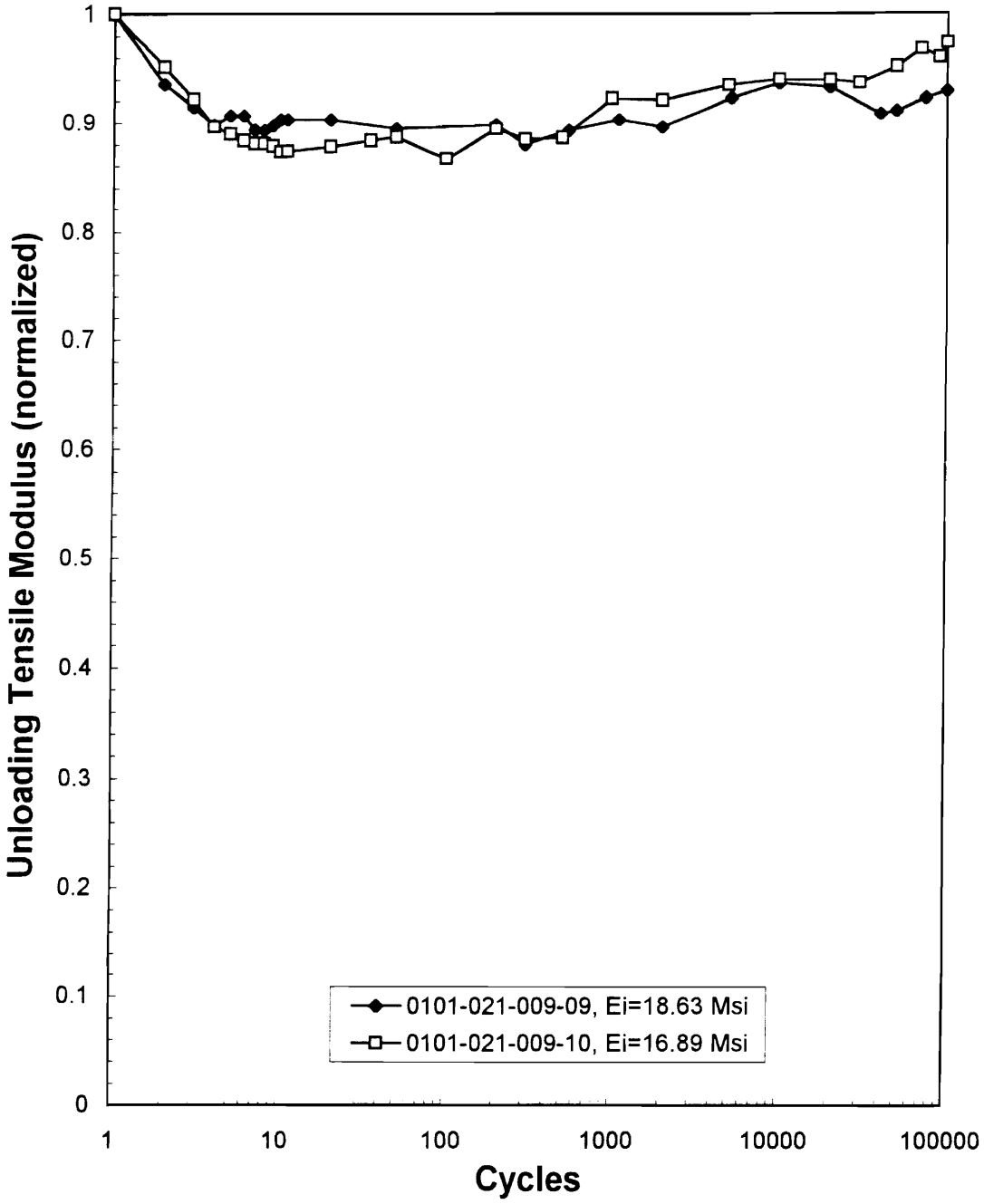

Figure 4.17: Stiffness degradation of a $[(0,90)/(+45,-45)]_{2s}$ laminate for σ_{max}=10 Ksi with R=-1, f=1 Hz, at 1800 F.

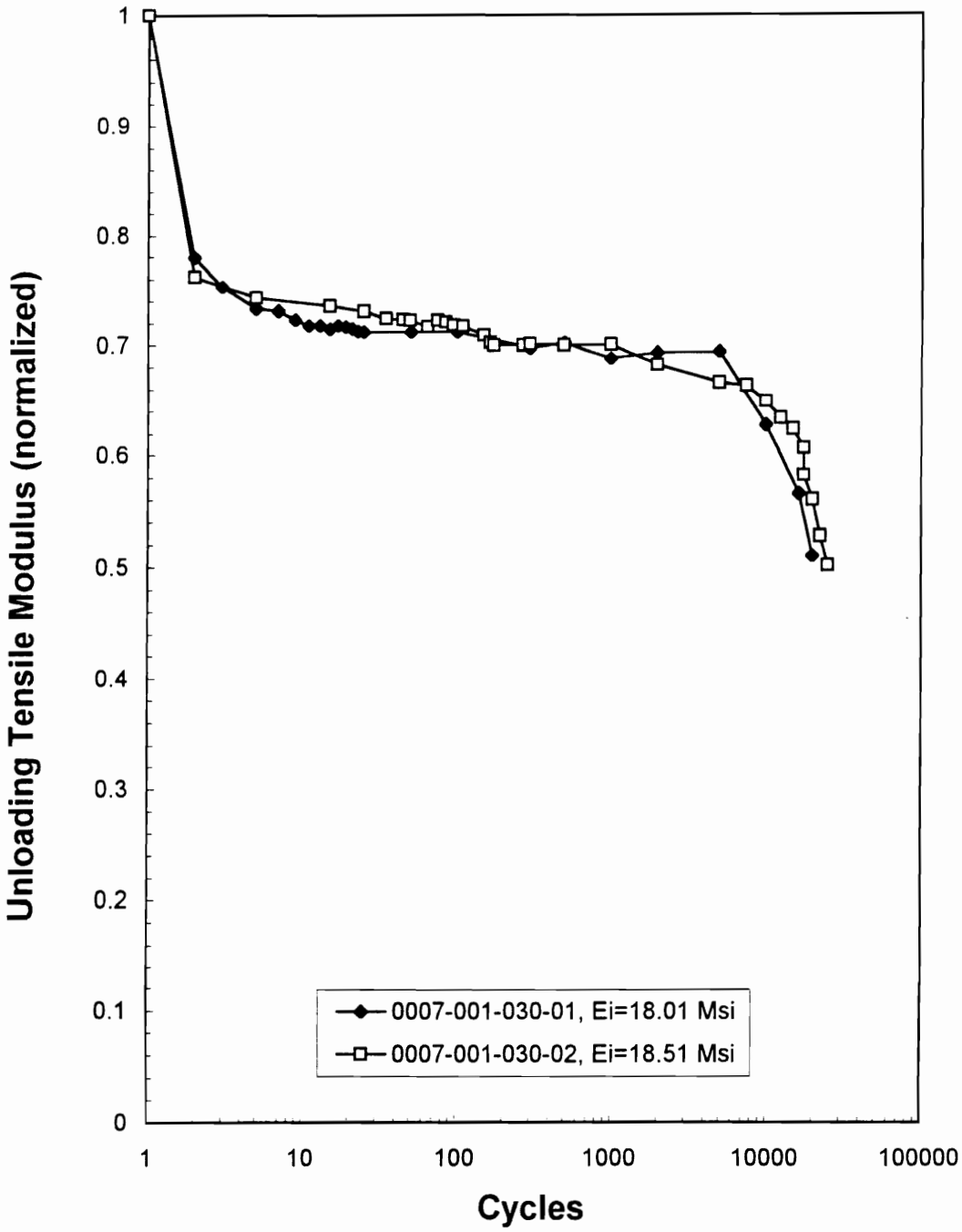

Figure 4.18: Stiffness degradation for a $[(0,90)/(+45,-45)]_{2s}$ for σ_{max}=13 Ksi with R=-1,f=1 Hz at 1800 F.

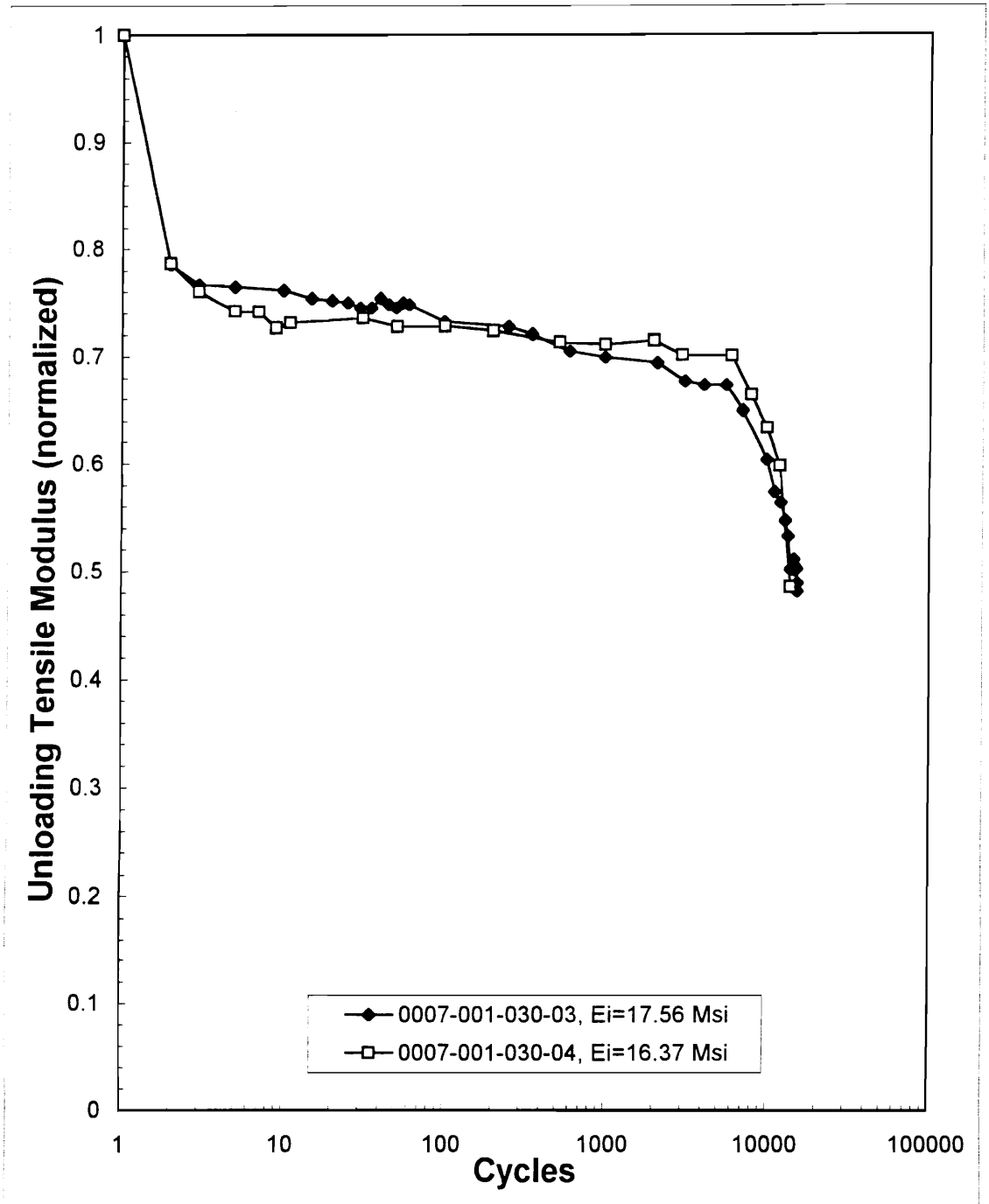

Figure 4.19: Stiffness degradation of $[(0,90)/(+45,-45)]_{2s}$ laminates for σ_{max}=15 Ksi with R=-1, f=1 Hz at 1800 F.

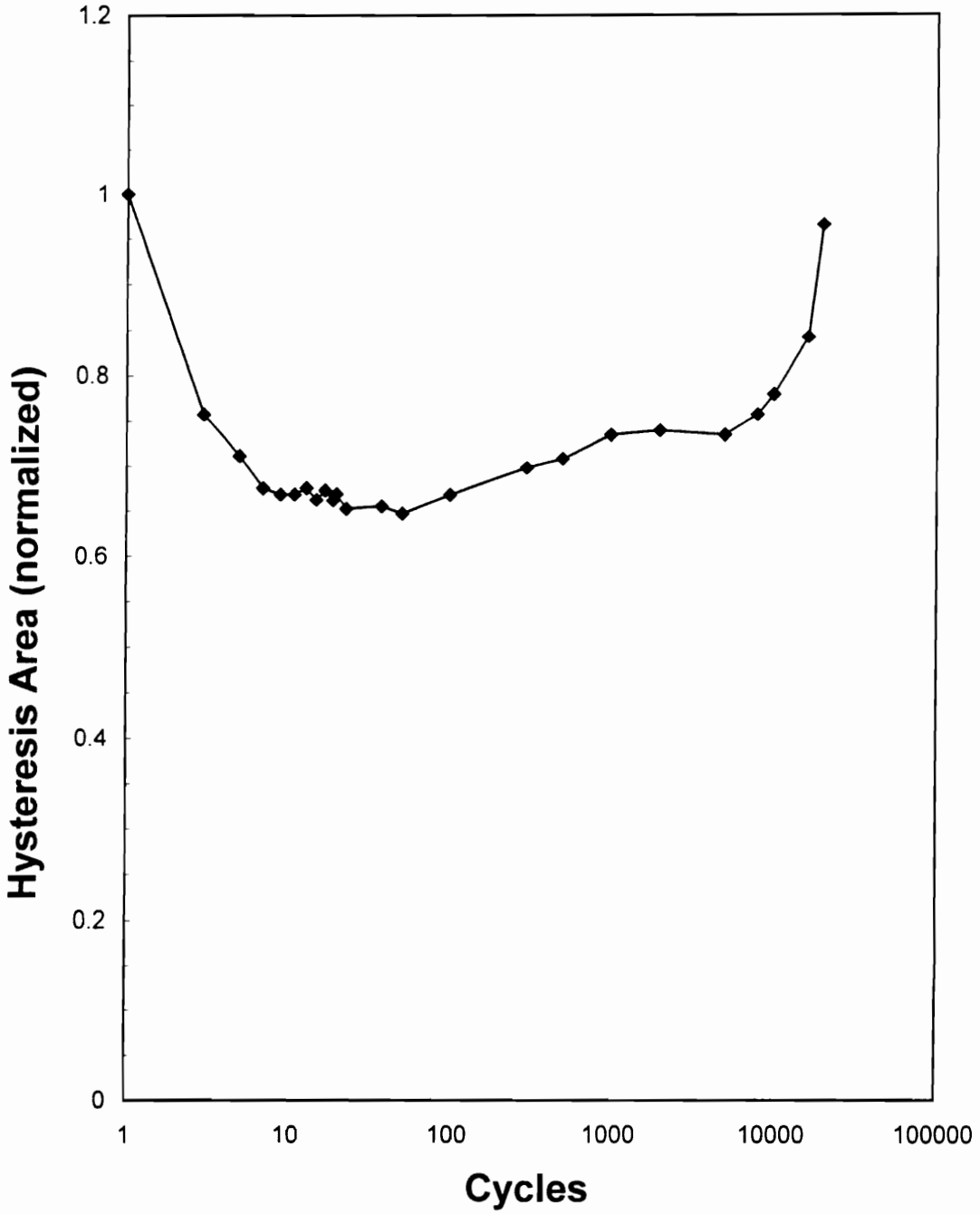

Figure 4.20:Evolution of hysteresis area for a [(0,90)/(45,-45)]$_{2s}$ laminate for σ_{max}=13 Ksi, R=-1, f=1 Hz at 1800 F.

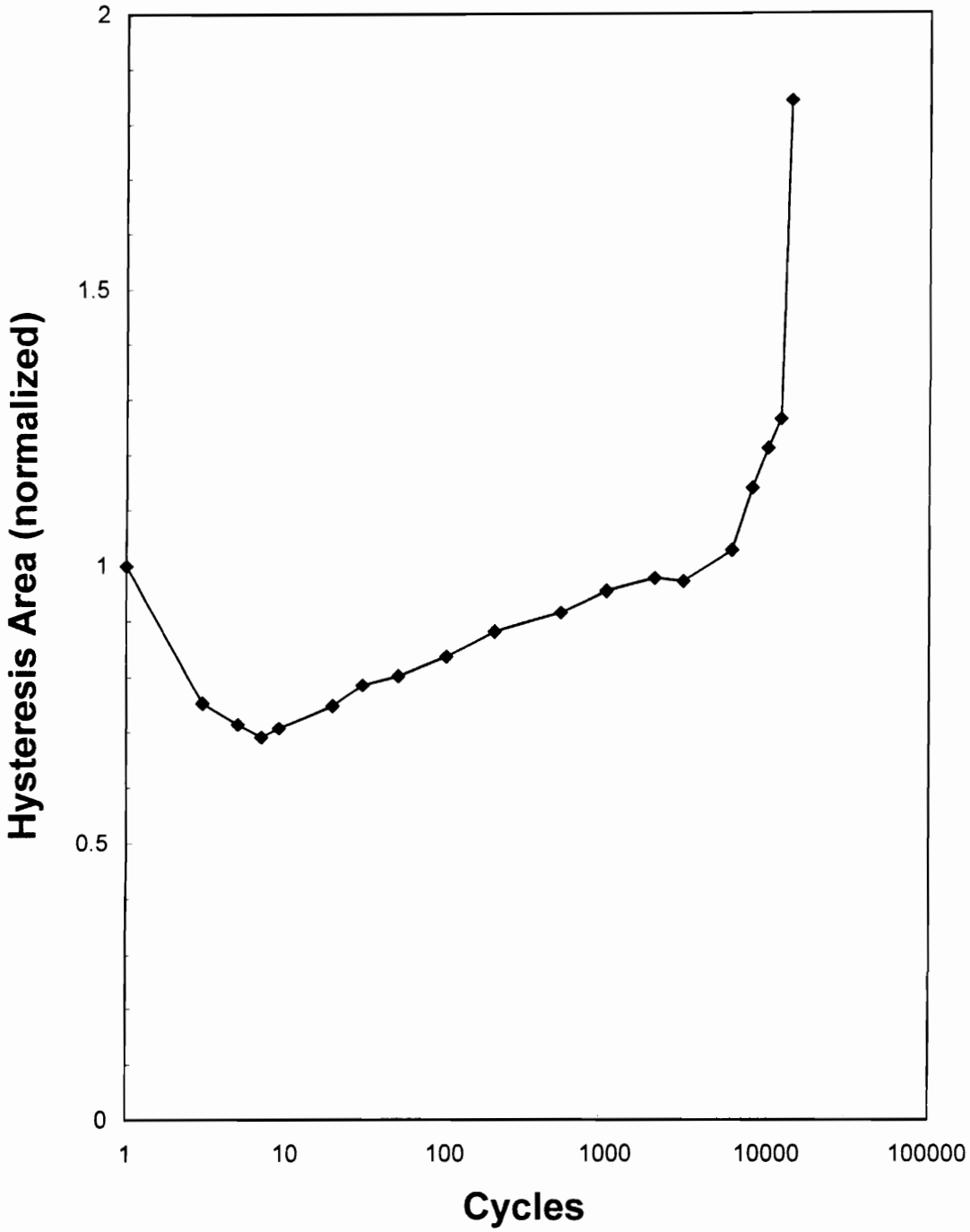

Figure 4.21:Evolution of hysteresis area for a [(0,90)/(45,-45)]$_{2s}$ laminate for σ_{max}=15 Ksi, R=-1, f=1 Hz at 1800 F.

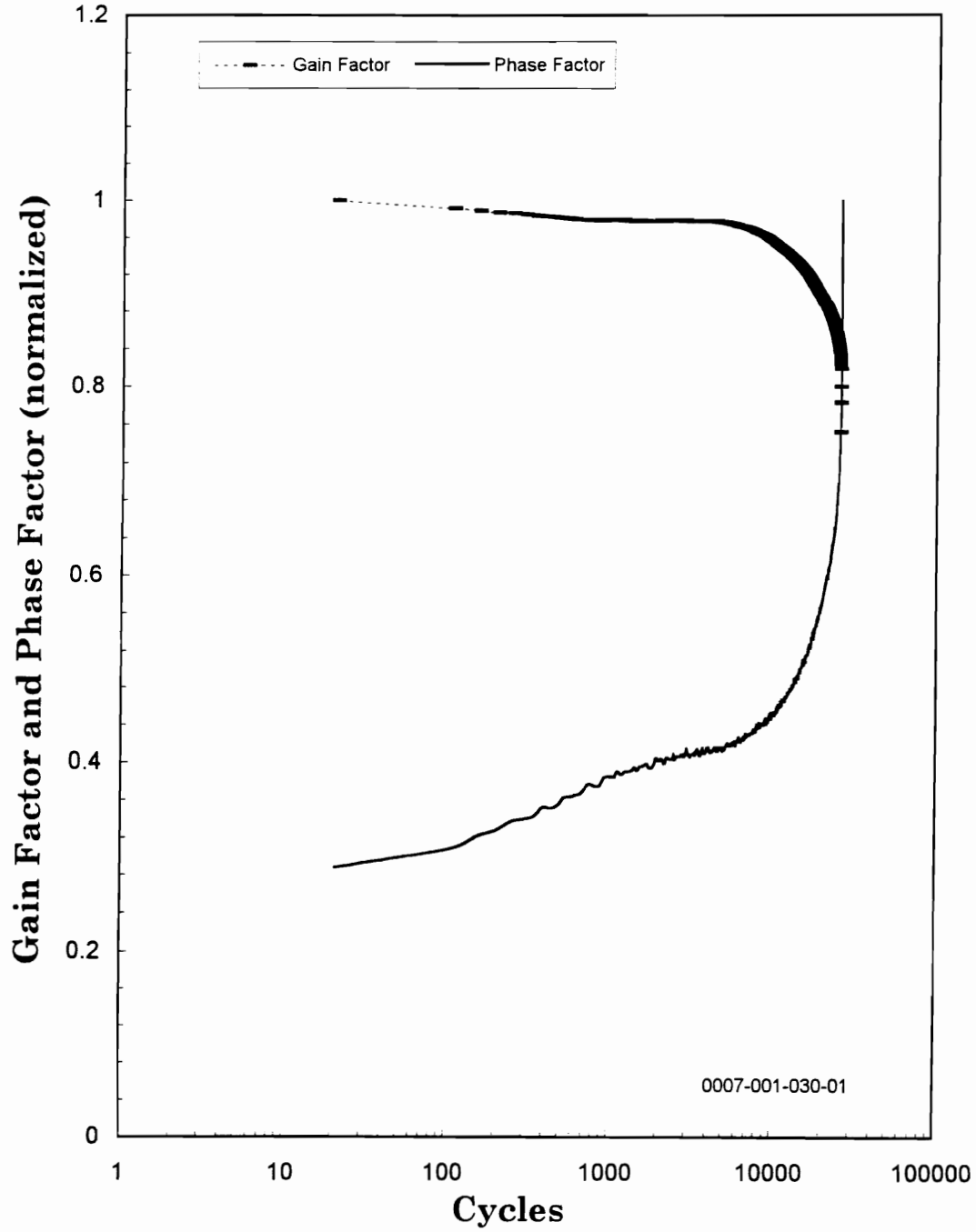

Figure 4.22:Dynamic response of a $[(0,90)/(+45,-45)]_{2s}$ laminate for σ_{max}=13 Ksi, R=-1, f=1 Hz at 1800 F.

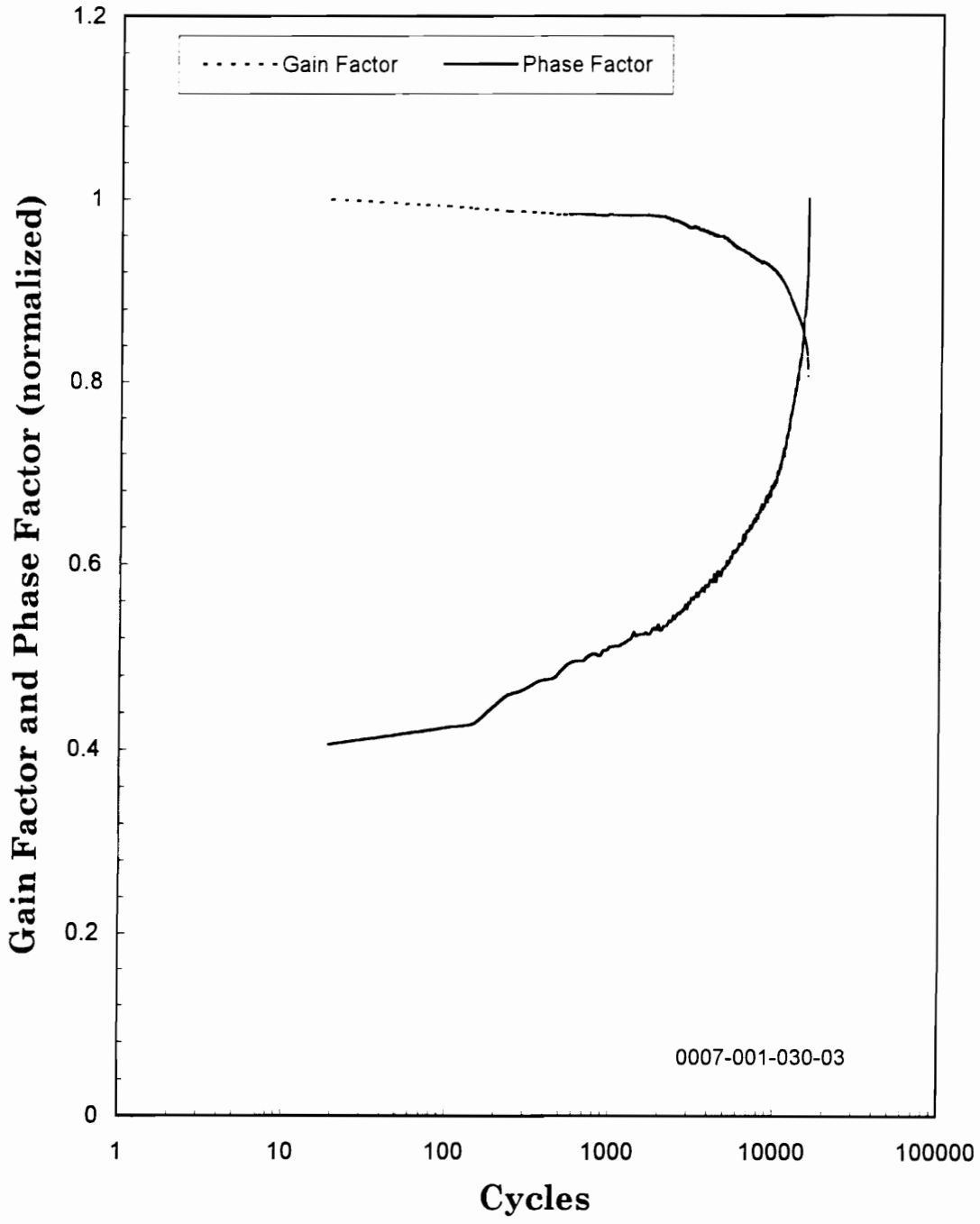

Figure 4.23: Dynamic response of a $[(0,90)/(+45,-45)]_{2s}$ laminate for σ_{max}=15 Ksi, R=-1, f=1 Hz at 1800 F.

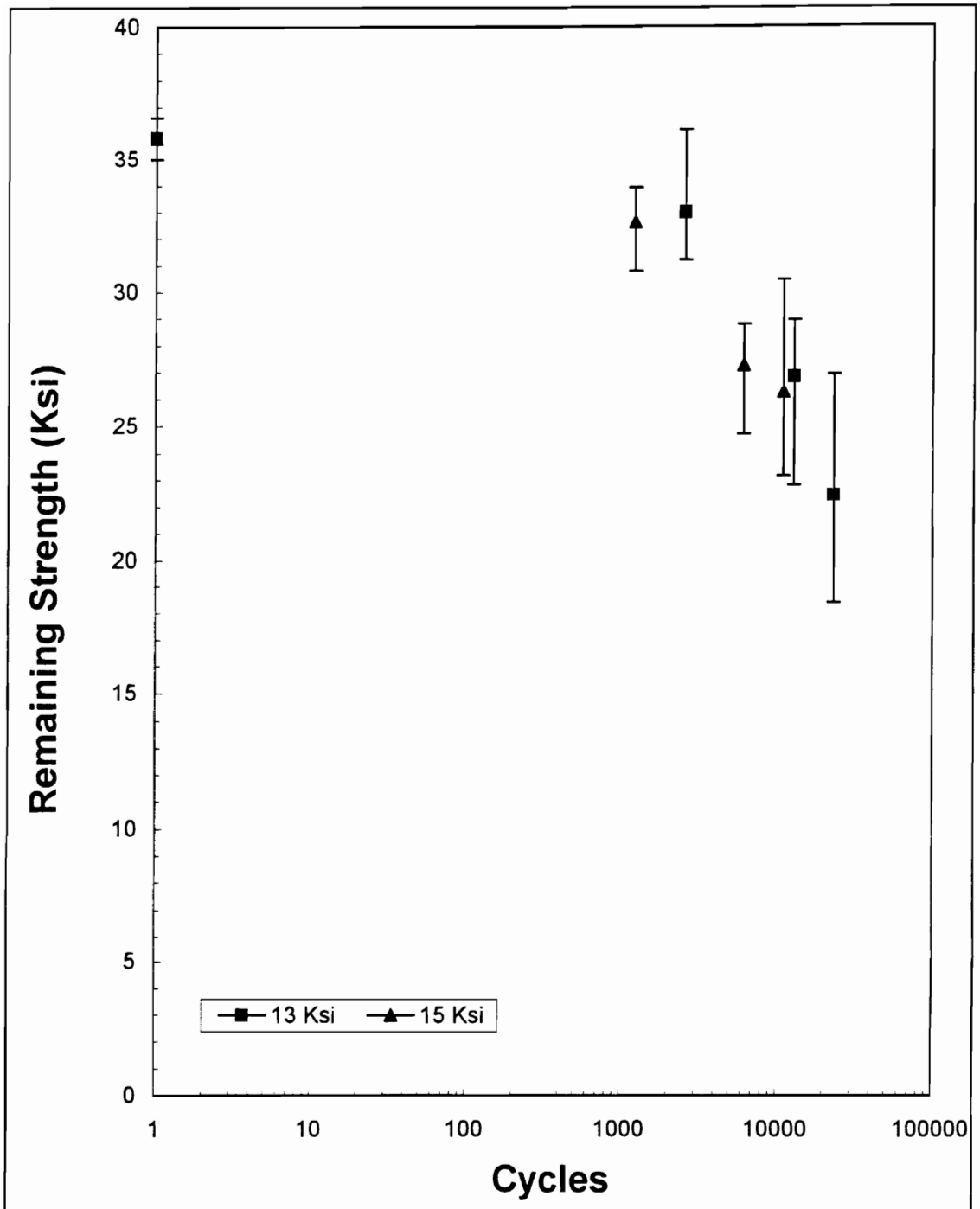

Figure 4.24: Remaining strength of $[(0,90)/(0/90)]_{2s}$ laminates for σ_{max}=13 Ksi, 15 Ksi, R=-1, f=1 Hz at 1800 F.

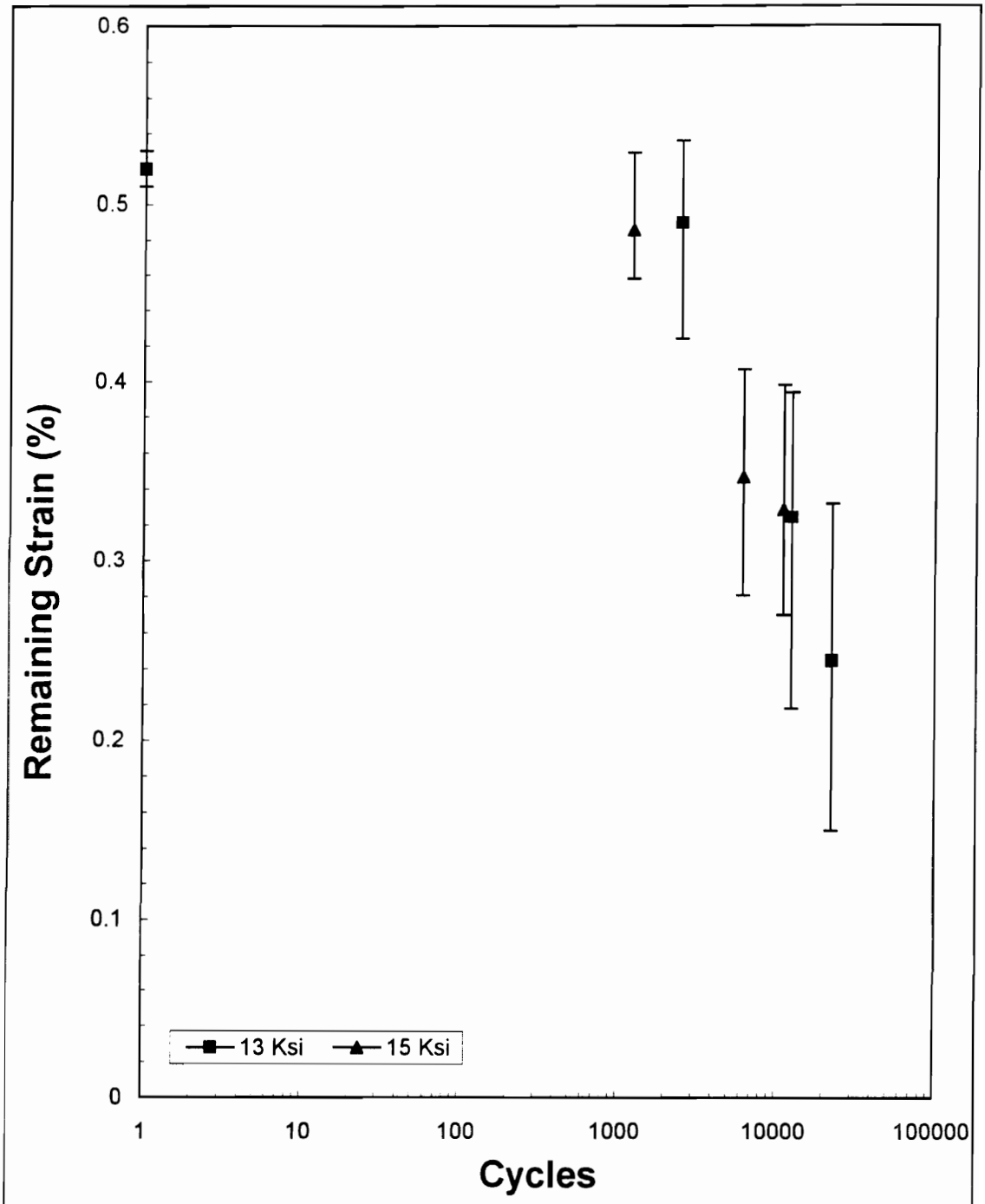

Figure 4.25: Remaining strain of $[(0,90)/(0/90)]_{2s}$ laminates for σ_{max}=13 Ksi and 15 Ksi with R=-1and f=1 Hz at 1800 F.

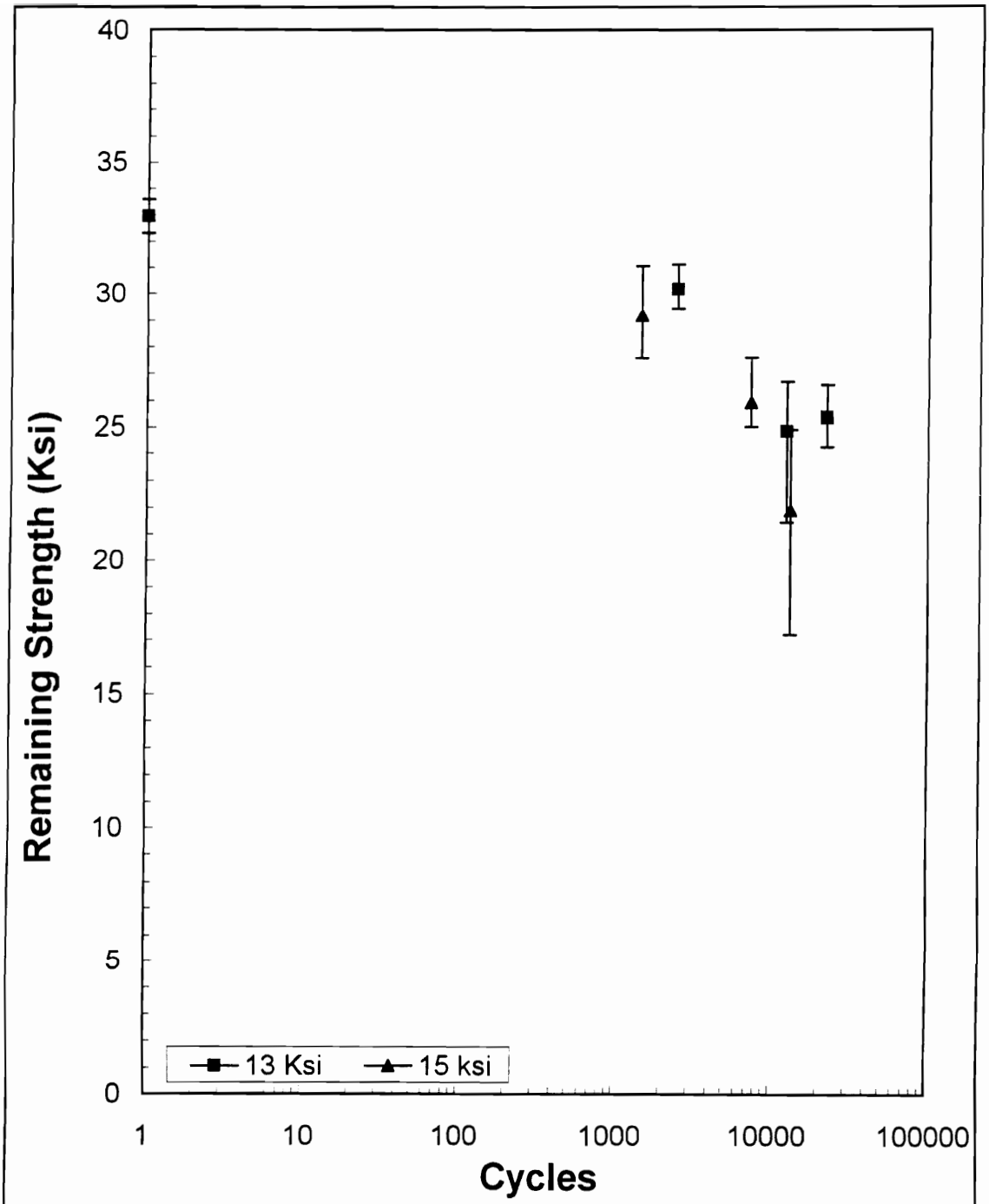

Figure 4.26: Remaining strength of $[(0,90)/(+45,-45)]_{2s}$ laminates for σ_{max}=13 Ksi, 15 Ksi, R=-1, f=1 Hz at 1800 F.

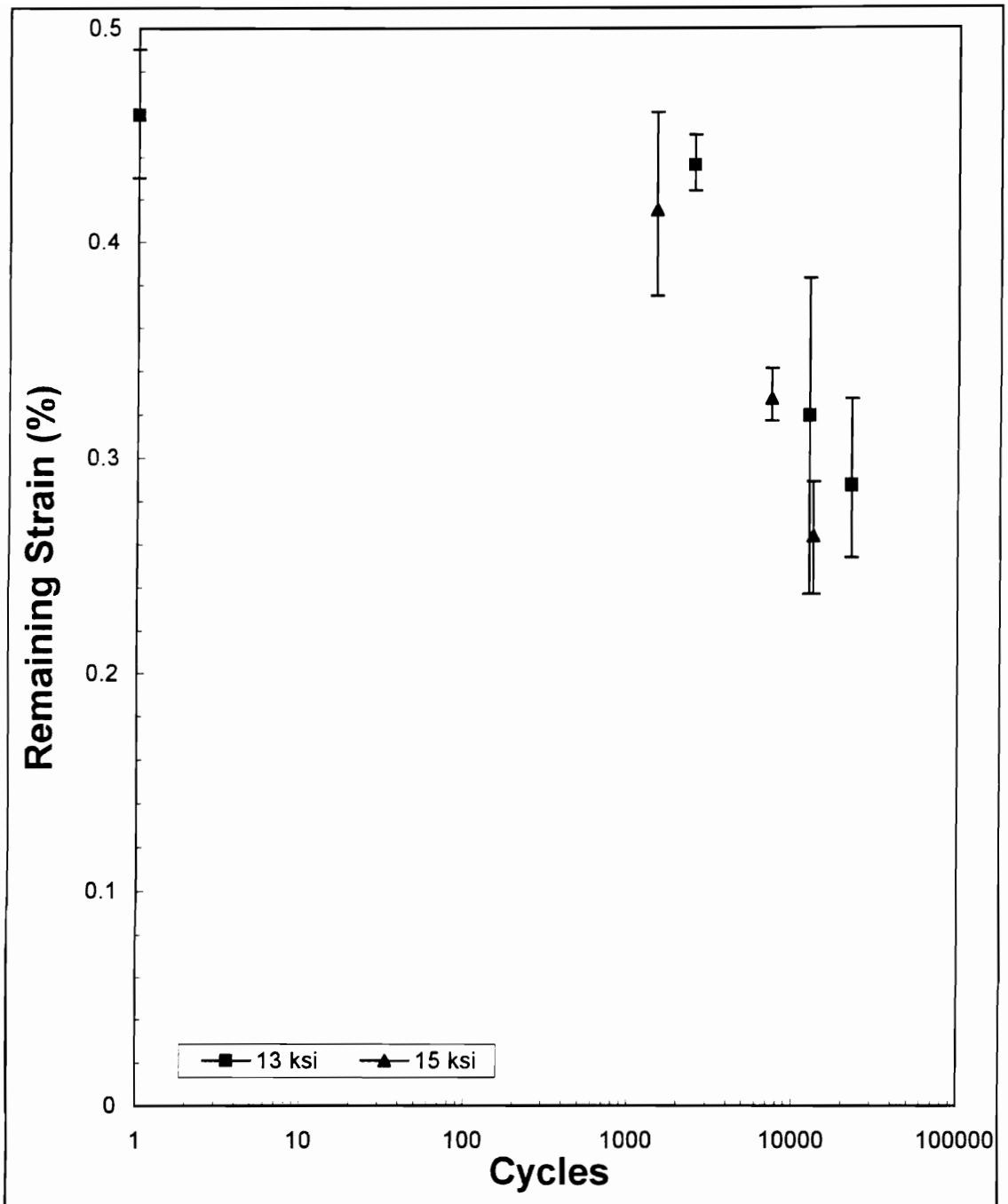

Figure 4.27: Remaining strain of $[(0,90)/(+45,-45)]_{2s}$ laminates for σ_{max}=13 Ksi and 15 Ksi, R=-1, f=1 Hz, 1800 F.

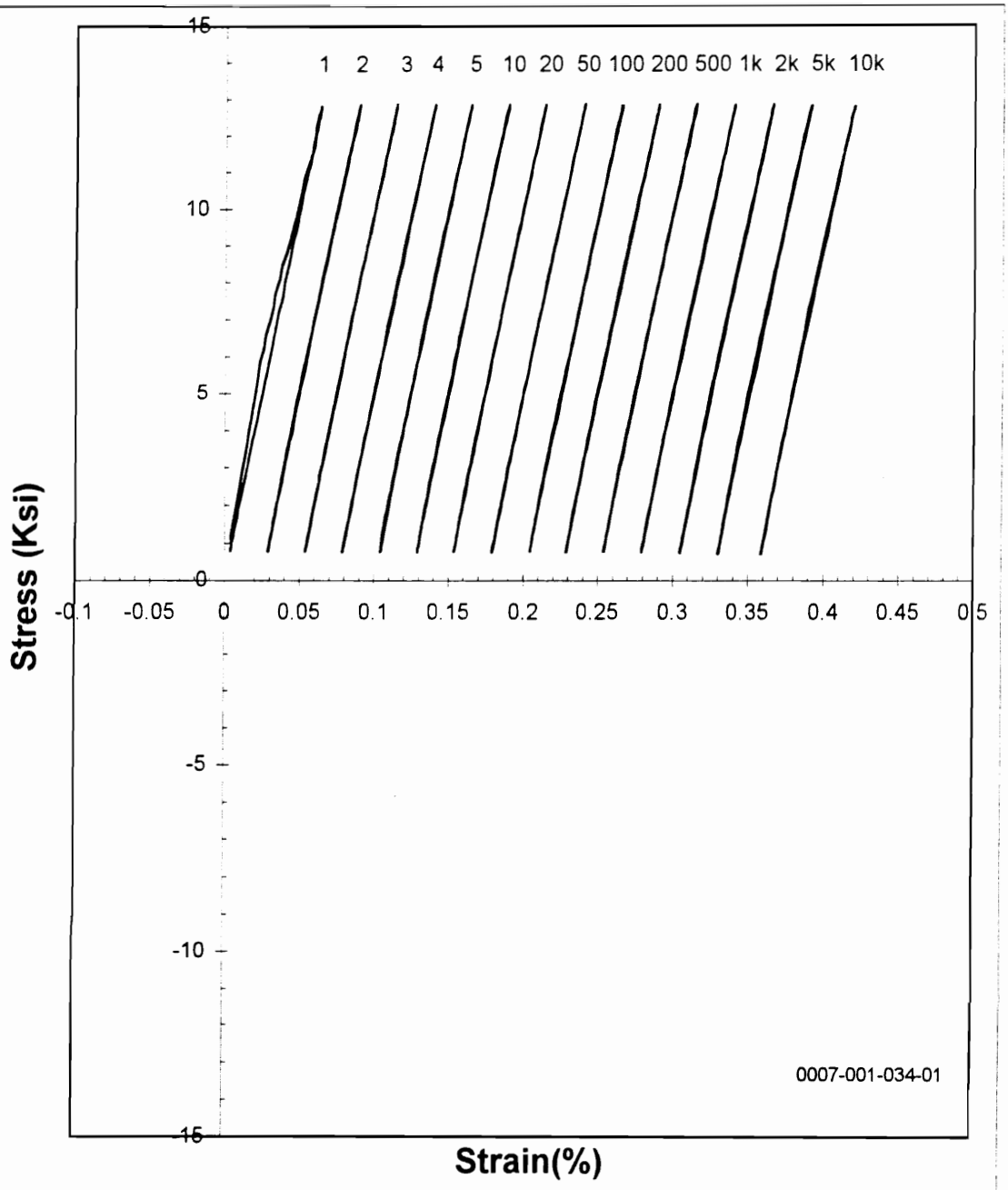

Figure 4.28: Stress-strain loops of a $[(0,90)/(+45,-45)]_{2s}$ laminate for σ_{max}=13 Ksi, R=0.05, and f=1 Hz at 1800 F.

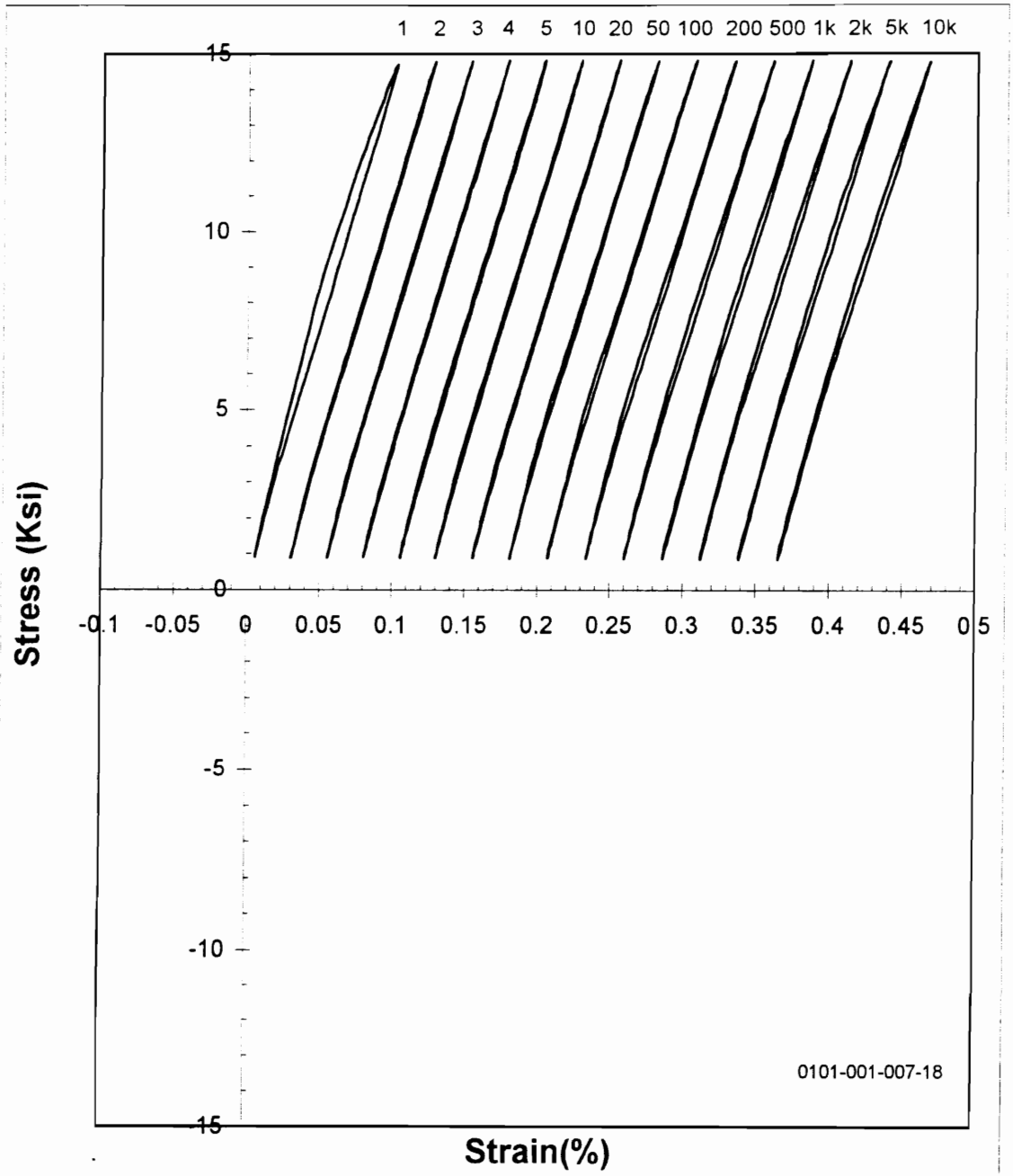

Figure 4.29: Stress-strain loops of a $[(0,90)/(+45,-45)]_{2s}$ laminate for σ_{max}=15 Ksi, R=0.05, f=1 Hz at 1800 F.

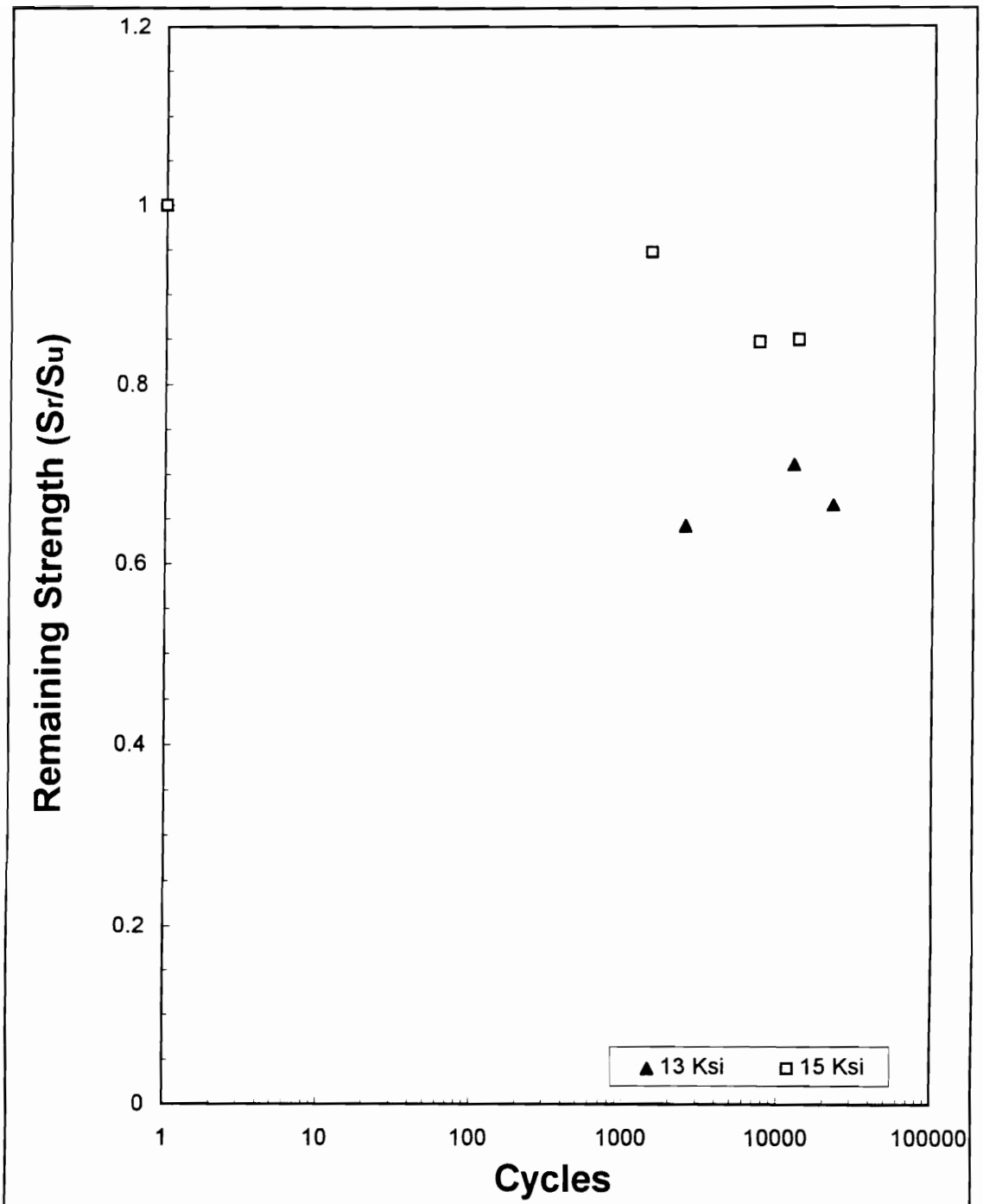

Figure 4.30: Remaining strength of $[(0,90)/(+45,-45)]_{2s}$ laminates for σ_{max}=13 Ksi, 15 Ksi, R=0.05, f=1 Hz at 1800 F.

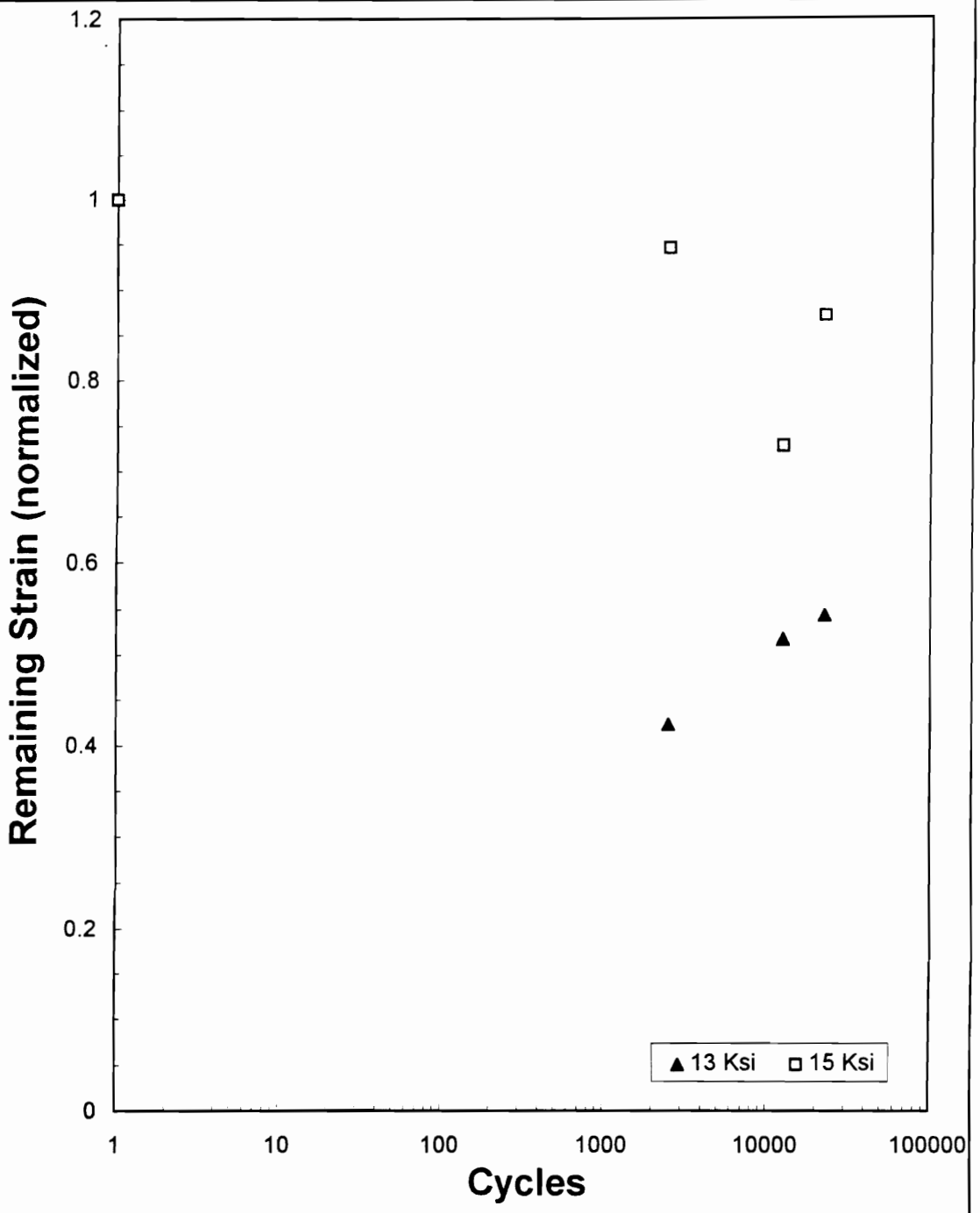

Figure 4.31: Remaining strain of $[(0,90)/(+45,-45)]_{2s}$ laminates for σ_{max}=13 Ksi,15 Ksi, R=0.05, f=1 Hz at 1800 F.

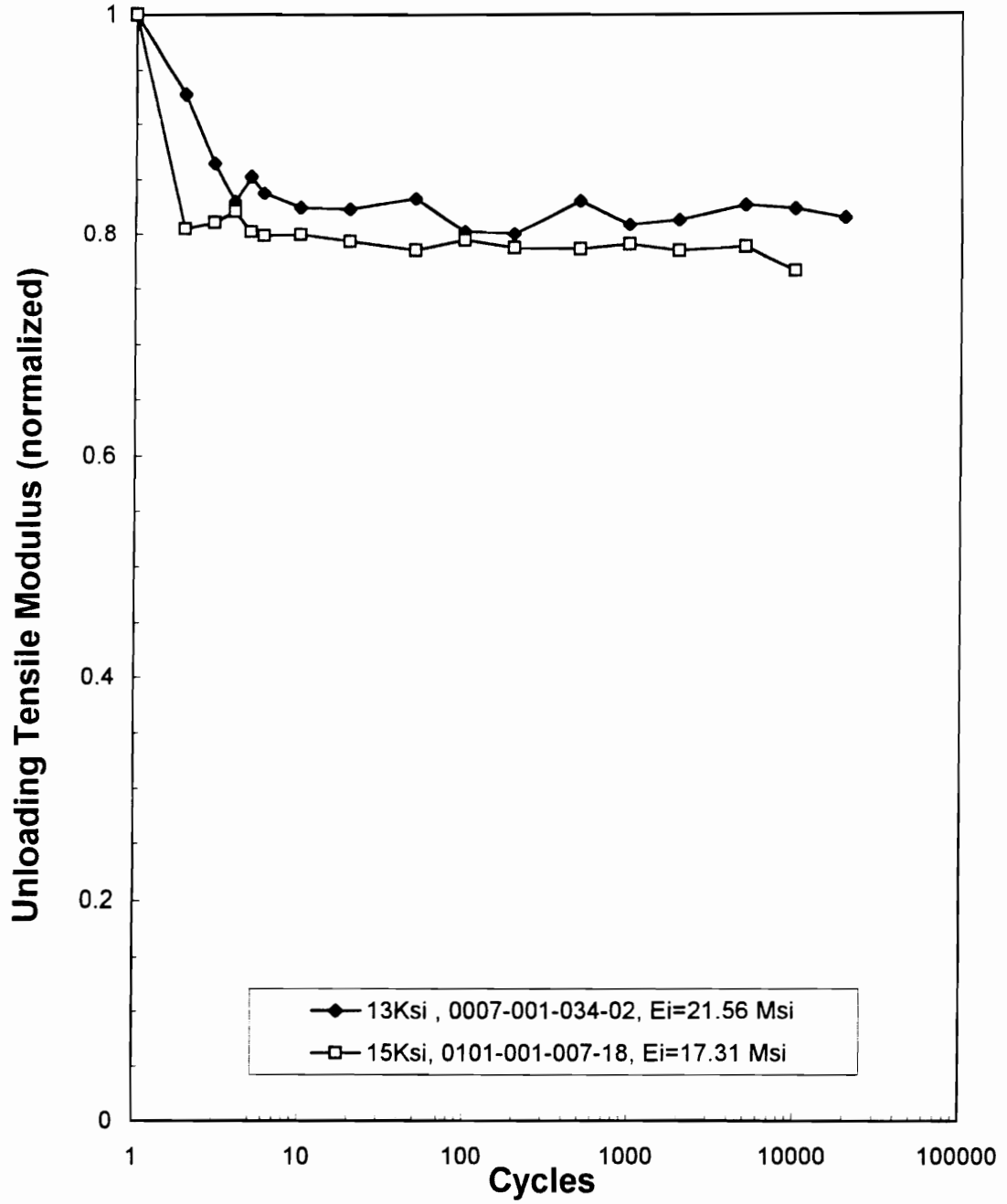

Figure 4.32: Stiffness degradation of $[(0,90)/(+45,-45)]_{2s}$ laminates for σ_{max}=13 Ksi,15 Ksi, R=0.05, f=1 Hz at 1800 F.

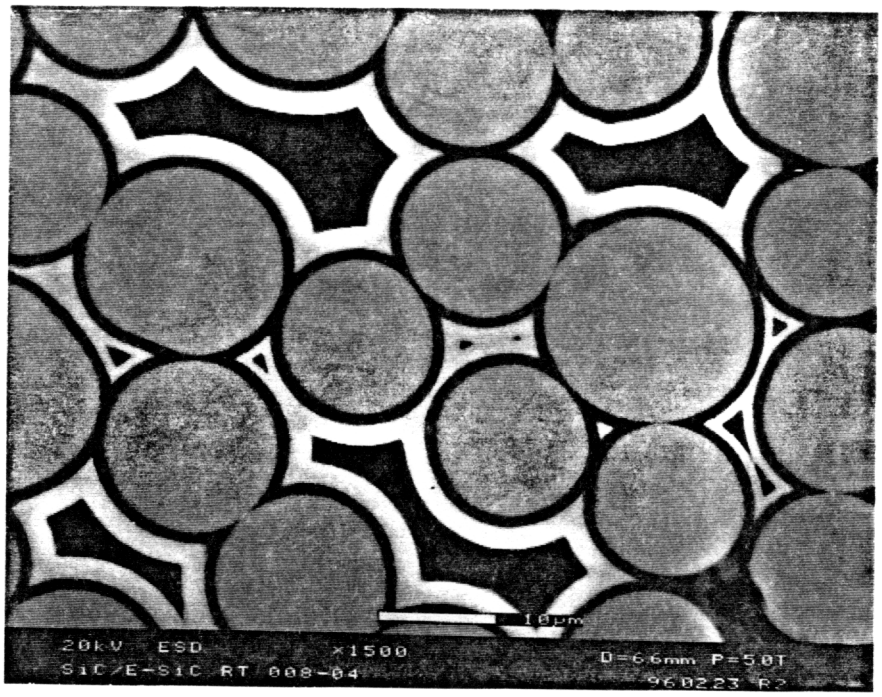

Figure 4.33: Cross-section of a 0 degree fiber bundle.

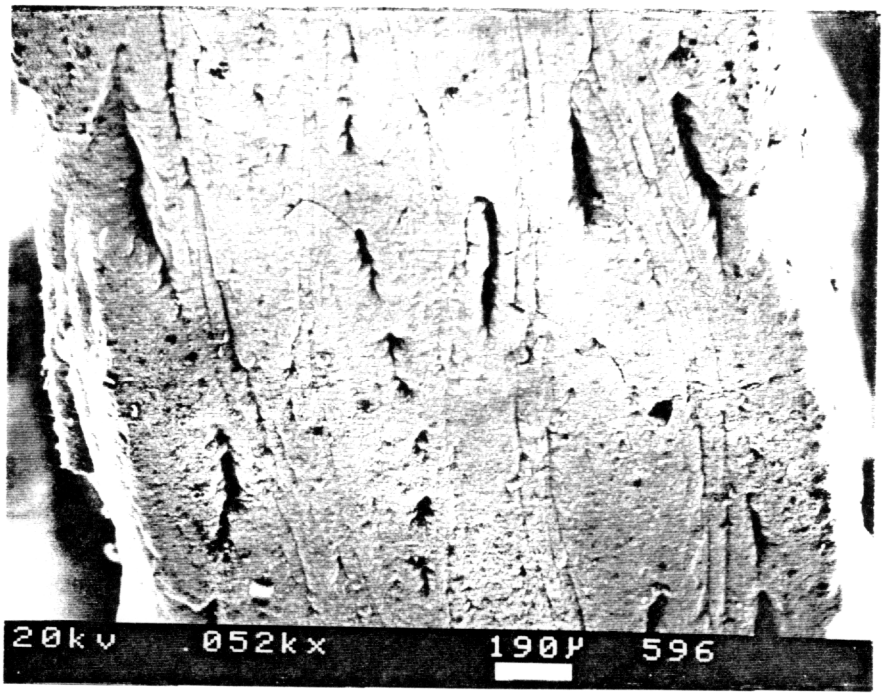

0/90,15,90

Figure 4.34: Cracking of protective SiC layer.

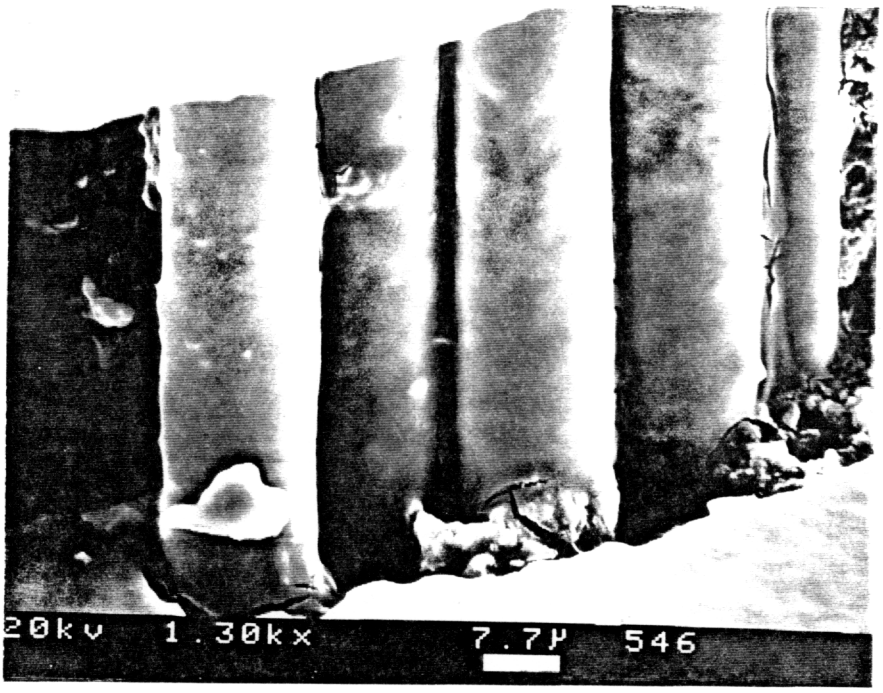

0/90.15.10

Figure 4.35: Seal coating of fibers at 1800 F.

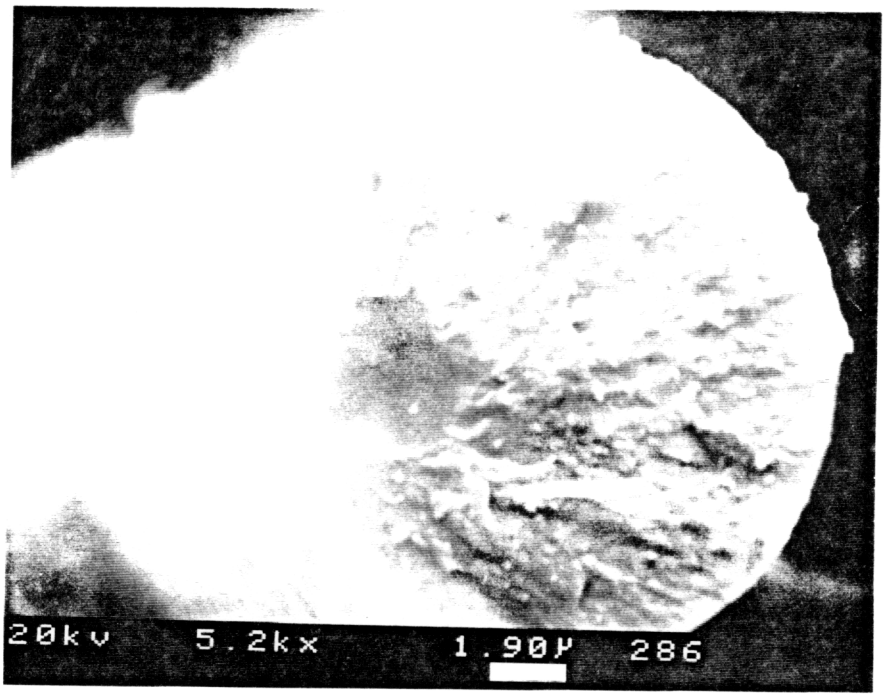

Figure 4.36: Fiber fracture originating from fiber imperfection.

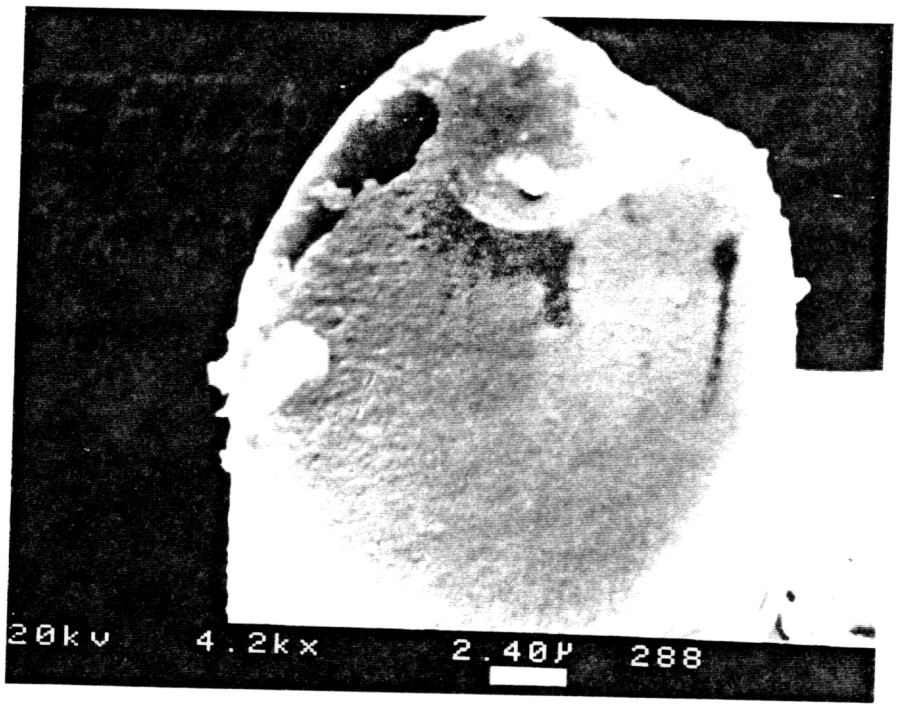

Figure 4.37: Porosity in Nicalon fibers.

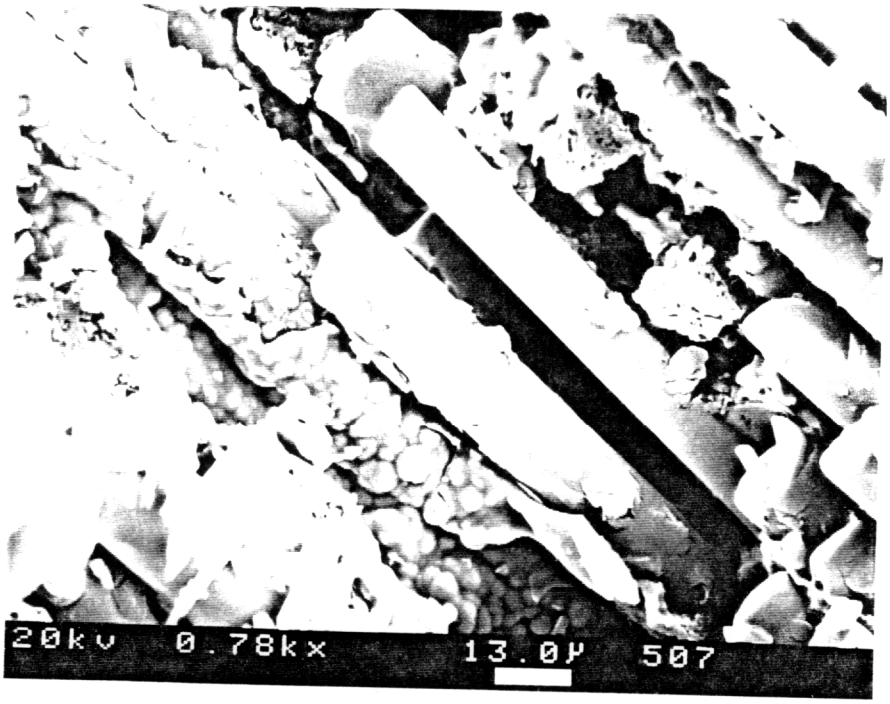

0/45.15.90

Figure 4.38: Cracking of glass coating of 45 degree fibers.

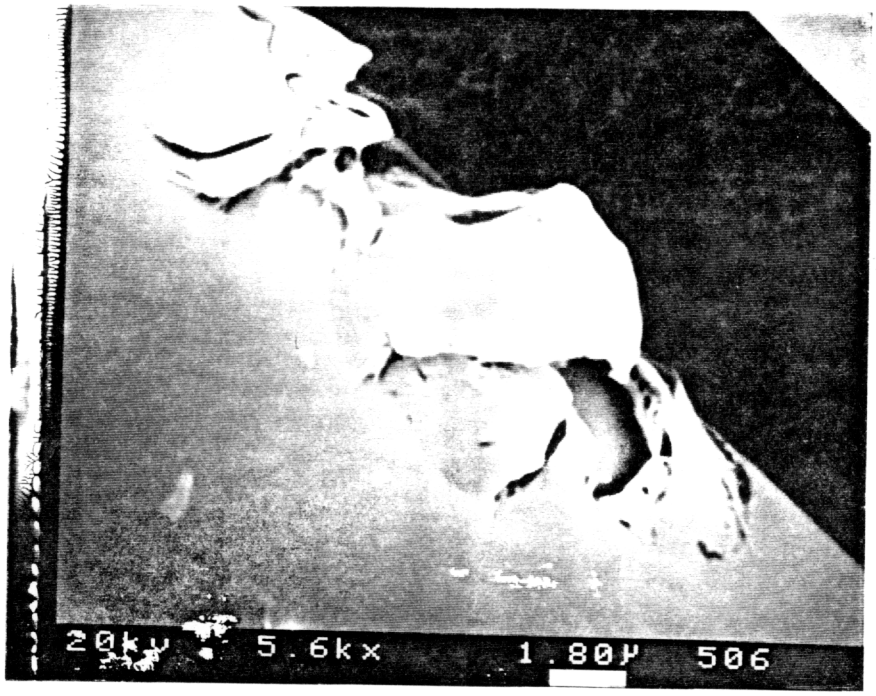

0/45.15.90

Figure 4.39: Cracking of seal coating around a fiber.

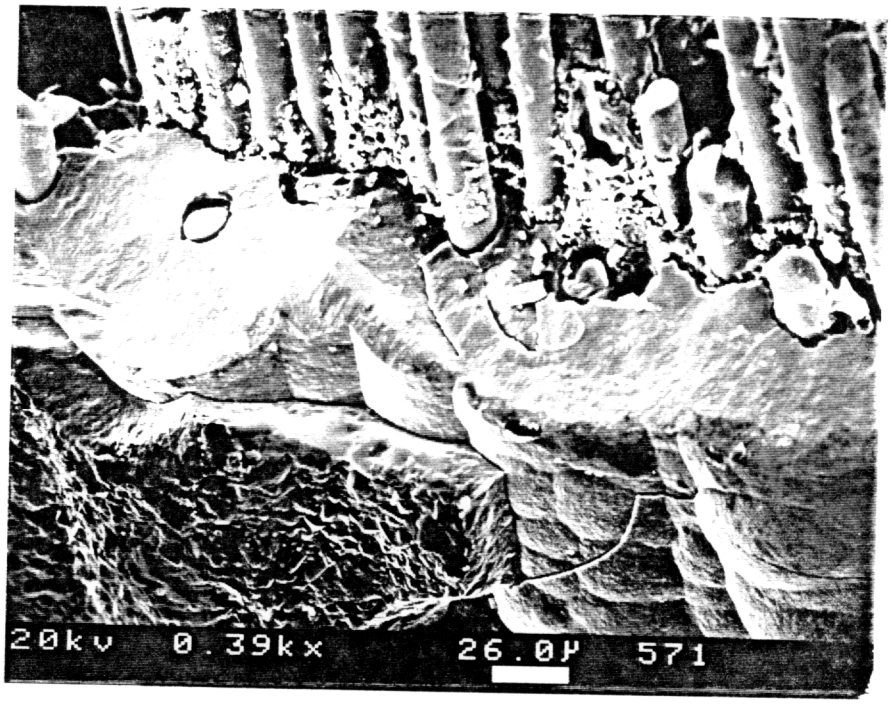

0/90.15.50

Figure 4.40: Various damage mechanisms in a fiber bundle.

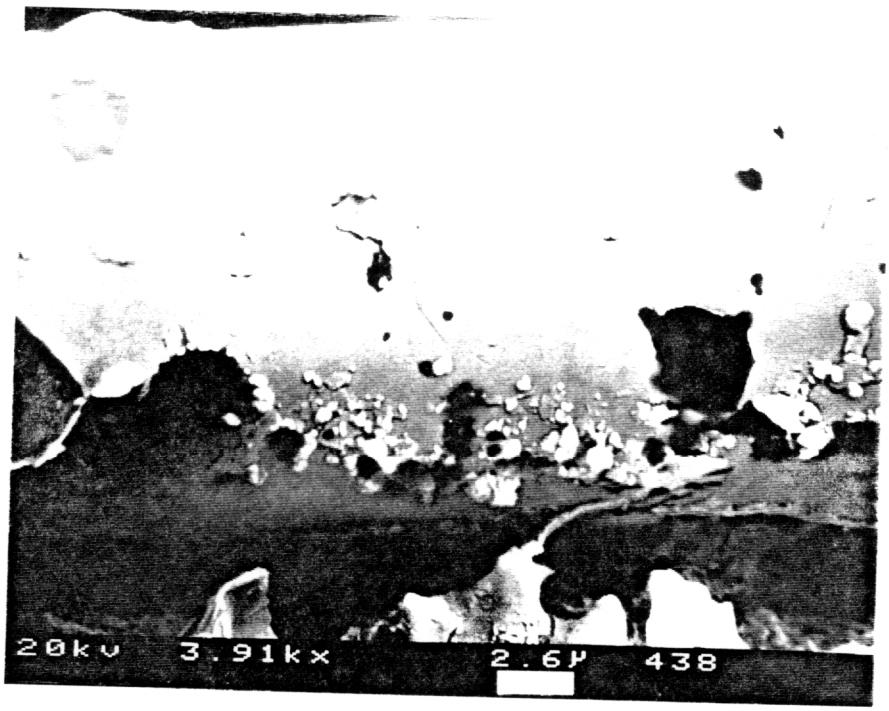

0/45.15.10

Figure 4.41: Damaged fiber due to oxidation and possibly frictional wear.

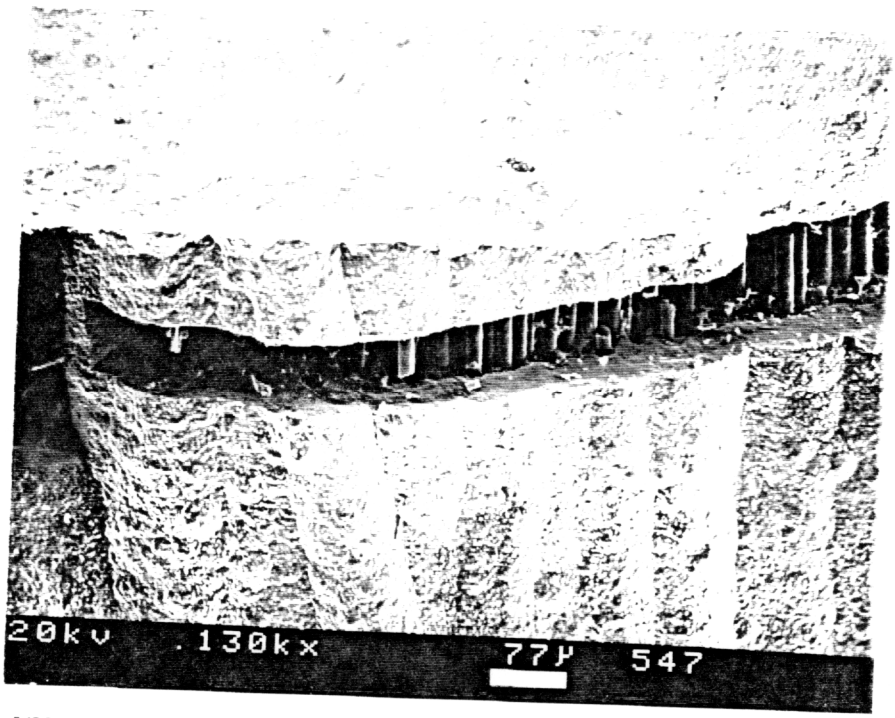

0/90.15.10

Figure 4.42: Fully cracked fiber bundle.

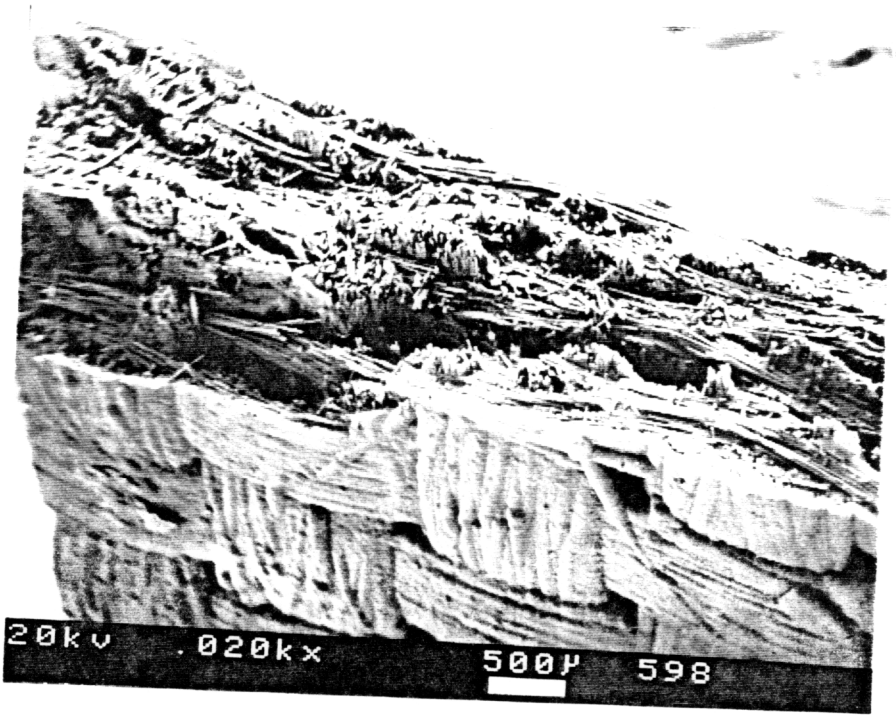

0/90.15.90

Figure 4.43: Fractured surface of a fatigued specimen.

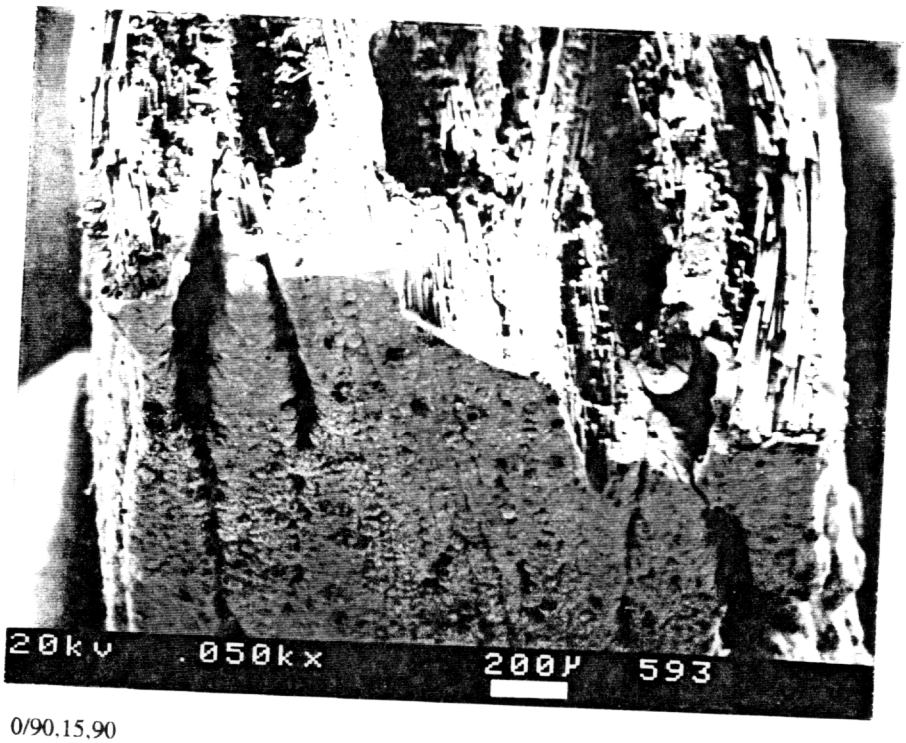

0/90.15.90

Figure 4.44: Fracture occurs at a high porosity location.

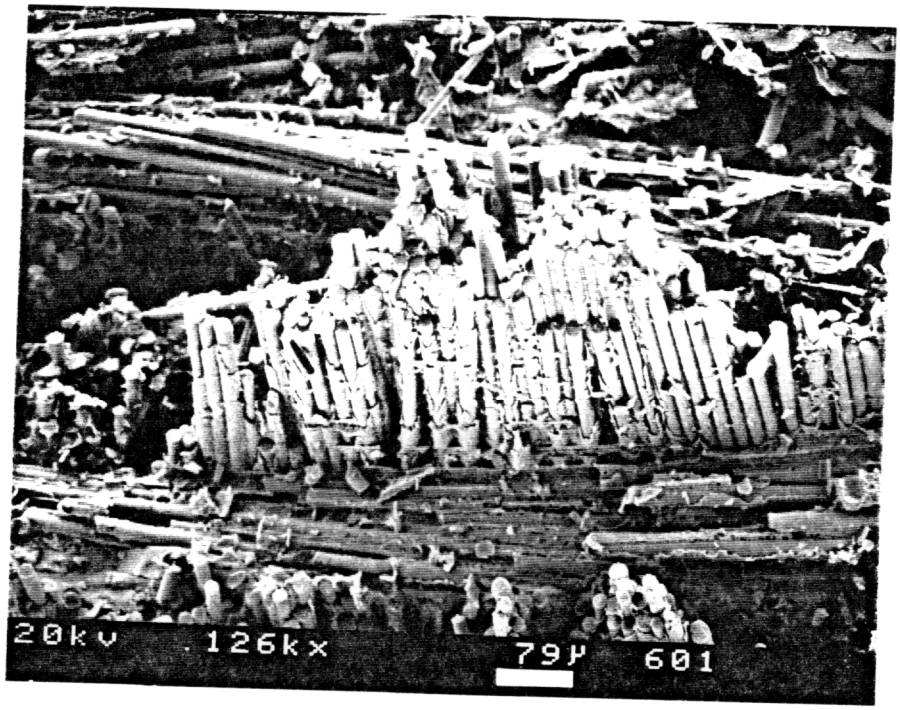

0/90.15.90

Figure 4.45: Wear and tear of fibers due to fatigue process for a $[(0,90)/(0,90)]_{2s}$ laminate at 1800 F.

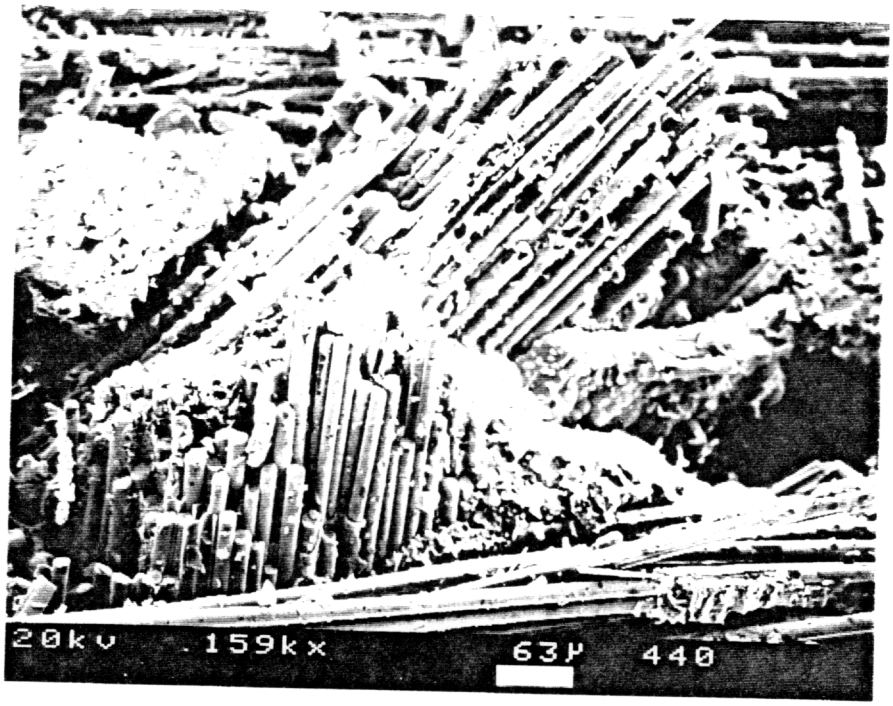

0/45.15.10

Figure 4.46: Wear and tear of fibers due to fatigue process for a $[(0,90)/(45,-45)]_{2s}$ laminate at 1800 F.

5. Remaining Strength and Life Predictions

To address issues such as damage tolerance and durability which are usually defined in terms of remaining strength and remaining life of a component, researchers have conducted many long-term experimental tests for a variety of conditions. In real life cost and time required to conduct such tests, have made it impossible to produce a complete phenomenological data base and extrapolation of data is often used. But, the insight obtained from a few fatigue tests can be used to predict performance of components exposed to actual in service environment. In this chapter a life and remaining strength prediction methodology which is based on a damage accumulation concept and uses remaining strength as a damage metric, is implemented to the cross-ply laminates of the material system in this investigation.

5.1 Performance Simulation Model

Employing damage accumulation concepts, almost a decade ago Reifsnider and Stinchcomb [88] proposed a critical element model to predict remaining strength and life in a cyclic fatigue test. This model is based on measurable parameters that can be used to characterize the damage development and the current state of damage in a composite laminate. This prediction methodology has evolved ever since by the Materials Response Group (MRG) at Virginia Tech and currently exists in form of a performance simulation code known as MRlife™. It has proven to be very successful with variety of material systems [89].

Prediction of remaining properties at any number of applied cycles requires knowledge of the state of stress and the state of material which keep on changing as the material's state of damage evolves. The philosophy

involved requires first, to establish the failure mode and damage mechanisms of materials under the loading environment. This requires us to conduct some mechanical testing and related NDE tests. Using the results along with laboratory experience a "representative" volume which is indicative of the testing material is identified [88]. For sake of simplicity consider a cross-ply laminate under cyclic tensile loading as an example. The representative volume naturally is any portion of the laminate that includes both 0 degree and 90 degree plies. Furthermore, this representative volume is divided into two sections known as "subcritical element" and "critical element" (figure 5.1). Experience tells us, failure of subcritical elements do not result in direct failure of component rather in redistribution of stresses throughout the component, therefore representing the state of stress. The nature and magnitude of this distribution in composite materials may be obtained from measured changes in local geometry and stiffness degradation (in general any measurable quantity will do such as crack length in fracture mechanics analysis of metals) respectively. Therefore, cracking of the 90 degree plies results in an increase in the load carried by the 0 degree plies rather than the failure of the laminate. Response of these elements are obtained using mechanistic analysis. On the other hand, Critical elements are those parts of the representative volume for which their failure will result in direct failure of the component, such as the 0 degree plies in the cross-ply laminate, therefore representing the state of the material. The response of these elements is obtained by constitutive equations and phenomenological information. Using the information regarding damage and their extent, damage analysis can be conducted to establish the state of stress in both the

critical and subcritical elements as a function life. By employing a failure criterion compatible with loading status and failure mode of the critical element, the state of material may be monitored as a function applied load Sa. Using this methodology along with a proper damage evolution integral, the remaining strength, Sr, and life may be evaluated as described by the flow chart of MRlife™ (figure 5.2). In general, remaining strength of a material, Sr, is nonlinear and takes various paths for various loading conditions. Failure of material is reached when remaining strength reaches the applied stress level Sa at time $\hat{\tau}$ (figure 5.3). Note that the stress level Sa_1 for a duration of t_1 reduces the remaining strength by the same amount as does the stress level Sa_2 lasting for a time of t_2. This feature is useful for block loading applications.

5.2 Theory

Following the general concept of damage mechanics, Reifsnider et al. assume that the strength of a composite system is defined by the accumulation of small variations in properties, geometry, arrangements fiber, matrix and the interface region between them. In case of general applied loading of critical element (3-D loading), material state variables Sa (from a failure criterion) and Sr (the damage metric) may be represented best in a more general non-dimensional form (i.e. normalized form with respect to material's ultimate tensile strength). This yields scalar quantities Fa and Fr which are referred to as failure function and remaining strength respectively. Therefore, remaining strength and life relationship may be represented as shown in figure 5.4. Next, a damage variable based on the

scalar quantity "continuity" Ψ which is a function of Fa is introduced [90]. For our argument we let function to be

$$\Psi = 1 - Fa \tag{5.1}$$

when $Fa = 0$ we have $\psi = 1$ representing the undamaged state of material. For a specific failure mode, kinetics may be defined by a specific damage accumulation processes with various rates. Considering a kinetic equation of the following form

$$\frac{\delta\Psi}{\delta\tau} = A\Psi j\tau^{j-1} \tag{5.2}$$

where j is the material constant and τ is a normalized generalize time variable defined as:

$$\tau = \frac{t}{\hat{\tau}} \tag{5.3}$$

Note that $\hat{\tau}$ is the characteristic time for any damage accumulation process. The characteristic time represents, a creep rupture life (having the above form) for a creep rupture process, or a fatigue life for a cyclic fatigue process, which may be expressed as

$$\tau = \frac{n}{N} \tag{5.4}$$

with n as the number of applied cycles and N is the number of cycles to failure. Integrating equation (5.2) yield

$$\int_{\Psi_1}^{\Psi_2} d\Psi = A\int_{\tau_1}^{\tau_2} \Psi(\tau) j\tau^{j-1} d\tau \tag{5.5}$$

Substituting for Ψ from equation (5.1), the right hand side (RHS) becomes

$$\int_{\Psi_1}^{\Psi_2} d\Psi = \Psi_2 - \Psi_1 = (Fa_o - Fa_2) - (Fa_o - Fa_1) = -\Delta Fa = Fr_2 - Fr_1 = \Delta Fr \tag{5.6}$$

For A=-1 the left hand side (LHS) becomes

$$A\int_{\tau_1}^{\tau_2}\Psi(\tau)j\tau^{j-1}d\tau = -\int_{\tau_1}^{\tau_2}(1-Fa)j\tau^{j-1}d\tau \qquad (5.7)$$

From equations (5.6) and (5.7), the change in remaining strength is

$$\Delta Fr = -\int_{\tau_1}^{\tau_2}(1-Fa(\tau))j\tau^{j-1}d\tau \qquad (5.8)$$

For $\tau_1 = 0$ we have $Fr_1 = 1$ and the remaining strength is

$$Fr = 1-\int_{0}^{\tau}(1-Fa(\tau))j\tau^{j-1}d\tau \qquad (5.9)$$

and for the special case when Fa is constant equation (5.9) becomes

$$Fr = 1-(1-Fa)\tau^{j} \qquad (5.10)$$

Equation (5.9) is suitable when $Fa(\tau)$ is continuous. For situations where block loading is applied, a modified version of the above is employed. Consider the block loading shown in figure 5.5 such that, load level of Fa_1 with a generalized time of τ_1, resulting in remaining strength of Fr_1, is followed by a load level Fa_2. To make the transition from Fa_1 at τ_1 to Fa_2, we need to evaluate the time required at load level Fa_2 in order to have the same amount damage (or change in remaining strength) as it does at load level Fa_1 for a duration of τ_1. This time is referred to as "pseudo-time" and is designated by τ_2^o [89]. Employing equation (5.10) along with requirement of equivalent damage state for these two load levels, we have

$$Fr\big|_{Fa_1,\tau_1} = 1-(1-Fa_1)\tau_1^{j} = 1-(1-Fa_2)(\tau_2^o)^{j} = Fr\big|_{Fa_2,\tau_2^o} \qquad (5.11)$$

The generalized time τ_2^o is then evaluated as

$$\tau_2^o = \left(\frac{1-Fr}{1-Fa_2}\right)^{\frac{1}{J}} \tag{5.12}$$

Using equation (5.8) the change in remaining strength during the time interval of τ_2^o to $\tau_2^o + \Delta t$ may be obtained as

$$\Delta Fr = -(1-Fa_2)\left[\left(\frac{\tau_2^o + \Delta t}{\hat{\tau}_2}\right)^J - \left(\frac{\tau_2^o}{\hat{\tau}_2}\right)^J\right] \tag{5.13}$$

The strength evolution is defined as, initial strength minus any incremental change in remaining strength as a result of any damage accumulation processes, and may be written as

$$Fr = 1 - \sum_{i=1}^{n} \Delta Fr_i \tag{5.14}$$

5.3 Cyclic Dependent Damage Accumulation

To account for fatigue, remaining strength can be may expressed in a cyclic domain as opposed to time domain. The adjustment for the "pseudo cycles" n_2^o is as following

$$n_2^o = N_2\tau_2^o = \left(\frac{1-Fr}{1-Fa_2}\right)^{\frac{1}{J}} N_2 \tag{5.15}$$

Accordingly, the change in remaining strength during the cycle interval of n_2^o to $n_2^o + \Delta n$ may be obtained as

$$\Delta Fr = -(1-Fa_2)\left[\left(\frac{n_2^o + \Delta n}{N_2}\right)^J - \left(\frac{n_2^o}{N_2}\right)^J\right] \tag{5.16}$$

To keep track of the number of cycles of any arbitrary applied loading, the slope of the loading profile is monitored constantly. When slope changes sign

the code takes it as a load reversal and adds 1/2 cycle to current number of cycles, Δn. In equation (5.15), Fa is taken as the maximum value of failure function over this one half cycle and code checks for failure using Fa>Fr relation.

Damage evolution due to cyclic loads can be represented by as a stiffness degradation curve. For $[(0,90)/(0,90)]_{2s}$ laminate (cross-ply), it is assumed that each (0,90) woven ply may be represented by a 0 degree fiber ply and a 90 degree matrix ply. We have also assumed any reduction in laminate stiffness is due to degradation of matrix stiffness only. Using results of previous chapter, stiffness degradation for 10 Ksi, 13 Ksi, and 15 Ksi stress level tests may best be represented by:

$$\frac{E(n)}{E_o} = b + m(\log n) \quad \text{where } (b,m) = \begin{cases} (0.926489, 0.000000) & for 10 Ksi \\ (0.683933, -0.00347) & for 13 Ksi \\ (0.680945, -0.01962) & for 15 Ksi \end{cases} \qquad (5.17)$$

where E_o is the initial stiffness of laminate (undamaged) and $E(n)$ is the laminate stiffness (damaged) which is a function of cycles. Using rule of mixtures the initial stiffness of laminate may be defined as:

$$E_o = v_f E_f + (1 - v_f) E_m^o \qquad (5.18)$$

where $v_f, E_f,$ *and* E_m^o are fill fraction (0.40), fiber stiffness (18.4 Msi), and initial stiffness of matrix (21.1 Msi) respectively. Similarly the laminate stiffness may be written as:

$$E(n) = v_f E_f + (1 - v_f) E_m(n) \qquad (5.19)$$

where $E_m(n)$ is the matrix stiffness as a function of cycles. Normalizing laminate stiffness by its initial stiffness we get:

$$\frac{E(n)}{E_o} = \frac{\nu_f E_f + (1-\nu_f) E_m(n)}{\nu_f E_f + (1-\nu_f) E_m^o} \tag{5.20}$$

By rearranging the above, cyclic dependent part of matrix, $E_m(n)$, may be obtained as following

$$E_m(n) = \frac{1}{(1-\nu_f)} \left\{ \frac{E(n)}{E_o} \left[\nu_f E_f + (1-\nu_f) E_m^o \right] - \nu_f E_f \right\} \tag{5.21}$$

In obtaining the failure function, maximum strain failure criteria is used as following

$$F_a = \frac{\varepsilon}{\varepsilon_c} \tag{5.22}$$

where ε *and* ε_c represent strain due to applied stress, σ, and strain to failure of composite respectively. In terms of stress we have

$$\varepsilon = \frac{\sigma}{\nu_f E_f + (1-\nu_f) E_m(n)} \tag{5.23}$$

and

$$\varepsilon_c = \frac{X_t}{\nu_f E_f + b(1-\nu_f) E_m^0} \tag{5.24}$$

where X_t is UTS of laminate (35.8 Ksi). Parameter b is used as a scaling factor because upon the application of first tensile loading, matrix cracks and its stiffness drops from E_m^o to bE_m^o.

The other cyclic dependent input should represent life of the critical element under constant stress state. A suitable representation is the S-N relationship for a unidirectional material under a constant load in fiber directions having the form

$$\frac{S_a(n)}{S_u(n)} = A_n + B_n(\log N)^{P_n} \tag{5.25}$$

where Sa is a function specifying the local stress state, Su is the corresponding function specifying the local strength state in the critical element. The rate of degradation associated with the unidirectional material under cyclic loading are expressed through the material constants An, Bn and Pn. The life of the element, N (to be entered into equations 5.15 and 5.16), is obtained from above equation as following

$$N = 10^{\left[\left(\frac{A_n - \frac{S_a(n)}{S_u(n)}}{B_n}\right)\right]^{\frac{1}{P_n}}} \tag{5.26}$$

where An=1.0, Bn=0.063, and Pn=1 based on the S-N diagram generated in chapter 4 for the cross-ply laminates.

5.4 Time Dependent Damage Accumulation

The influence of time-effect processes may be inputted into the code in the form of any available mathematical representation. The time-effect damage accumulation may be as a result of creep rupture or oxidation processes. The available rupture data at temperature are very limited (three data points at 1800 °F) and they include the oxidation effect as well. Rupture time $\hat{\tau}$ may be expressed in terms of parameters such as stress level σ, and test temperature T as following [91]:

$$Ln(\hat{\tau}) = \left[(A + B\sigma + C\sigma^2) + (D + ET_{red} + FT_{red}^2)\right] \tag{5.27}$$

where

$$T_{red} = \left| \frac{T - T_{pest}}{T_{pest}} \right| \quad and \begin{cases} A = 17.95038\ ,\ D = -0.611191 \\ B = -18.98970\ ,\ E = 0.7337560 \\ C = 0.0,\ T_{pest} = 1550F,\ F = 18.9449 \end{cases}$$

Measured and predicted rupture time for test temperatures of 1800 °F and 2010 °F are presented in figure 5.6. Testing by GE and P&W has indicated that among all strength reduction mechanisms, creep rupture behavior of this material system was the most dominant effect.

5.5 Iteration Process

A version of MRlife code known as CClife was used for the performance simulation. This code was developed to handle arbitrary loading conditions (mechanical and thermal) by using discrete values of the loading profile (figure 5.7a). It also utilizes an iteration procedure to evaluate the change in remaining strength for any incremental load increase. It keeps iterating until the difference in remaining strength obtained at j^{th} and $(j-1)^{th}$ iterations is less than some predefined tolerance. Consider the first two points of loading profile, (σ_0, T_0, t_0) and (σ_1, T_1, t_1), which are separated by time Δt (figure 5.7b). For the first run, failure functions due to σ_0 *and* σ_1 are obtained and averaged to get $\overline{Fa}(0,1) = \frac{Fa_o + Fa_1}{2}$. The remaining strength at node 1 is obtained as following

$$Fr^1 = Fr^0 + \Delta Fr^{0,1}\Big|_{\overline{Fa}(0,1),\Delta t} \qquad (5.28)$$

where $\Delta Fr^{0,1}$ is the change in remaining strength (equation 5.12) due to applied load of $\overline{Fa}(0,1)$, lasting for a duration of Δt, and Fr^0 is the remaining strength at node 0. For the first run there is no need for τ_2^o. For the second run, the Δt interval is divided into four equal segments (figure 5.7c). The remaining strength at node 1/2 may be obtained as following

$$Fr^{1/2} = Fr^0 + \Delta Fr^{0,1/2}\Big|_{\overline{Fa}(0,1/2),\Delta t/2} \tag{5.29}$$

where $\Delta Fr^{0,1/2}$ is the change in remaining strength due to applied load of $\overline{Fa}(0,1/2) = \frac{Fa_o + Fa_{1/2}}{2}$ *for* $\Delta t/2$ duration. Next The remaining strength at node 1 is obtained as following

$$Fr^1 = Fr^{1/2} + \Delta Fr^{1/2,1}\Big|_{\overline{Fa}(1/2,1),\Delta t/2} \tag{5.30}$$

where $\Delta Fr^{1/2,1}$ is obtained from equation (5.13) for $\tau_2^o = \left(\frac{1-Fr^{1/2}}{1-\overline{Fa}(1/2,1)}\right)^{\frac{1}{J}}$.

The new value and old values of Fr^1 (obtained from equations 5.31 and 5.29) are compared and the difference is checked against a tolerance. If tolerance is not satisfied the iteration continues by further dividing the time interval (t_o,t_1) into smaller segments. Once the tolerance is satisfied, the new value of Fr^1 is taken as the remaining strength at node 1 and the above procedure is applied to next load interval $\{(\sigma_1,T_1,t_1),(\sigma_2,T_2,t_2)\}$ with a time interval of $\Delta t = t_2 - t_1$.

5.6 Results and Discussions:

Using the performance simulation code, remaining strengths and life of laminates for 10 Ksi, 13 Ksi, and 15 Ksi tests were predicted. Predictions and measured values of remaining strengths for 10%, 50%, and 90% of life are presented in table 5.1. Results indicate close correlation especially for the 10 Ksi and 13 Ksi tests. Remaining strength and failure function values were normalized with respect to ultimate tensile strength and results were plotted as function of cycles (figures 5.8-5.10). The intersection point of these two curves represents the failure of the laminate. The number of cycles associated with this point is the life of laminate. Predicted fatigue-life diagrams along with measured values for 10 Ksi, 13 Ksi and 15 Ksi applied stresses are presented in figure 5.11. For the 10 Ksi test, life is predicted to be 235230 cycles. Because run-out was defined at 10^5 cycles, there are no experimental data available for comparison. For 13 Ksi test, a predicted life of 46719 cycles was obtained. This life is almost twice as high as the measured value (26000 cycles). A life of 12071 cycles was predicted for the 15 Ksi test which is very close to the measured value of 12350 cycles.

Table 5.1: Predicted and measured remaining strength for $[(0,90)/(0,90)]_{2s}$ laminates.

Applied Stress (Ksi)	%life (cycles)	Remaining Strength Prediction (Ksi)	Remaining Strength Experiment (Ksi)
10	(100000)	23.39	26.18
13	10 (2600)	33.38	33.00
13	50 (13000)	27.42	26.84
13	90 (23400)	22.58	22.46
15	10 (1235)	32.67	32.64
15	13 (6175)	24.64	27.25
15	15 (11115)	18.18	26.28

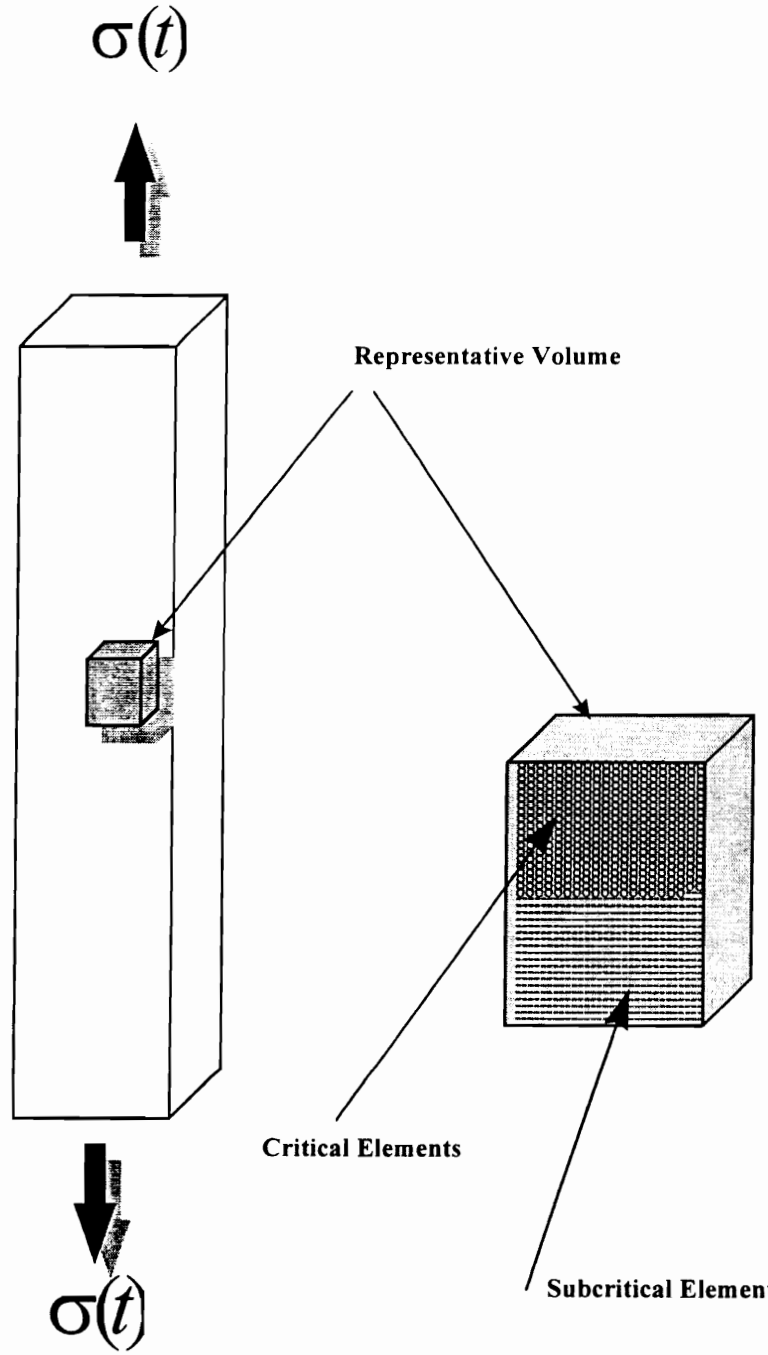

Figure 5.1: Schematic representation of representative volume.

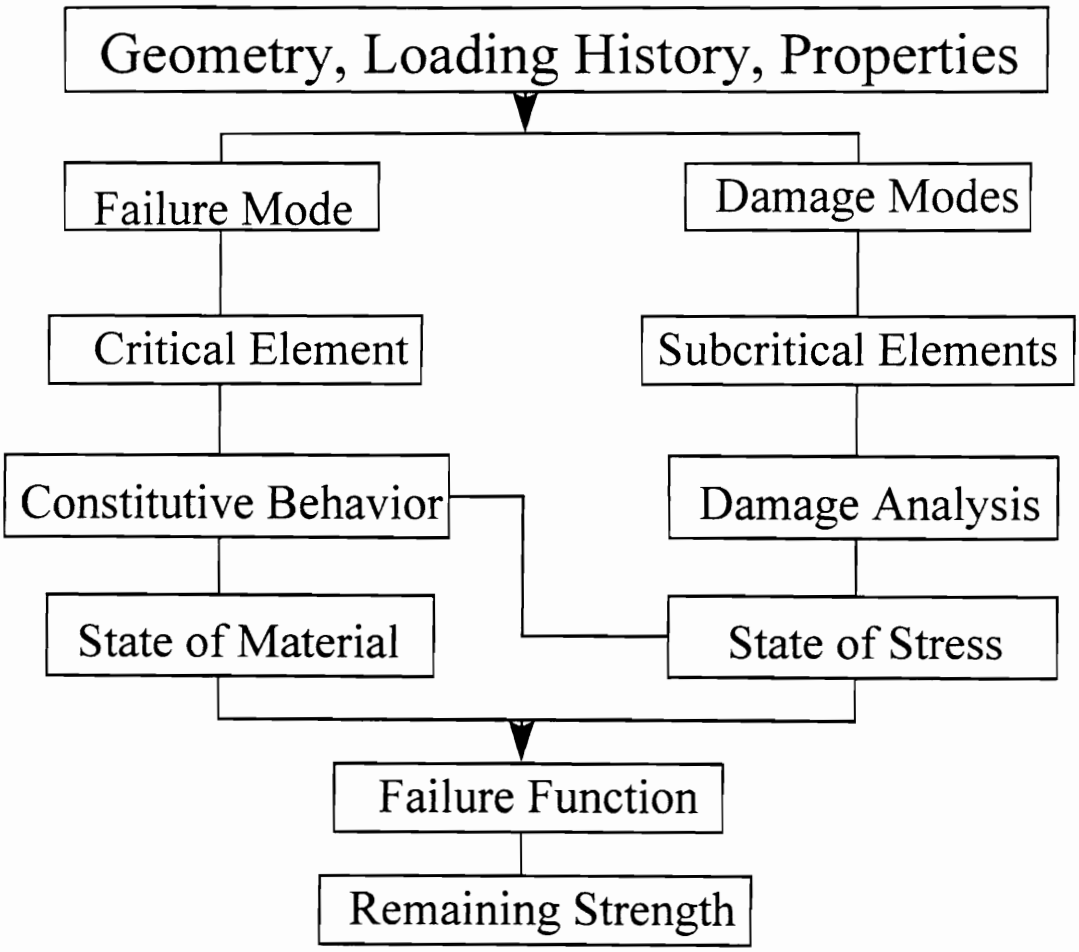

Figure 5.2: Flow chart representing the remaining strength prediction process.

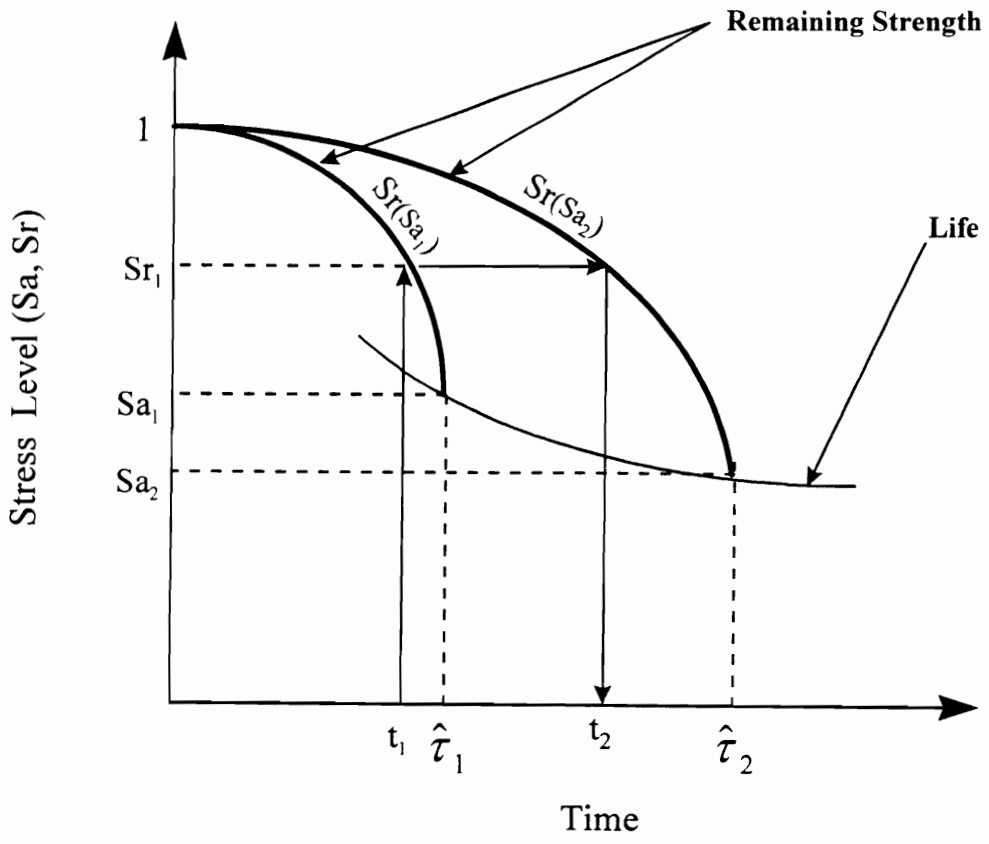

Figure 5.3: One-dimensional representation of relationship between remaining strength and applied stress.

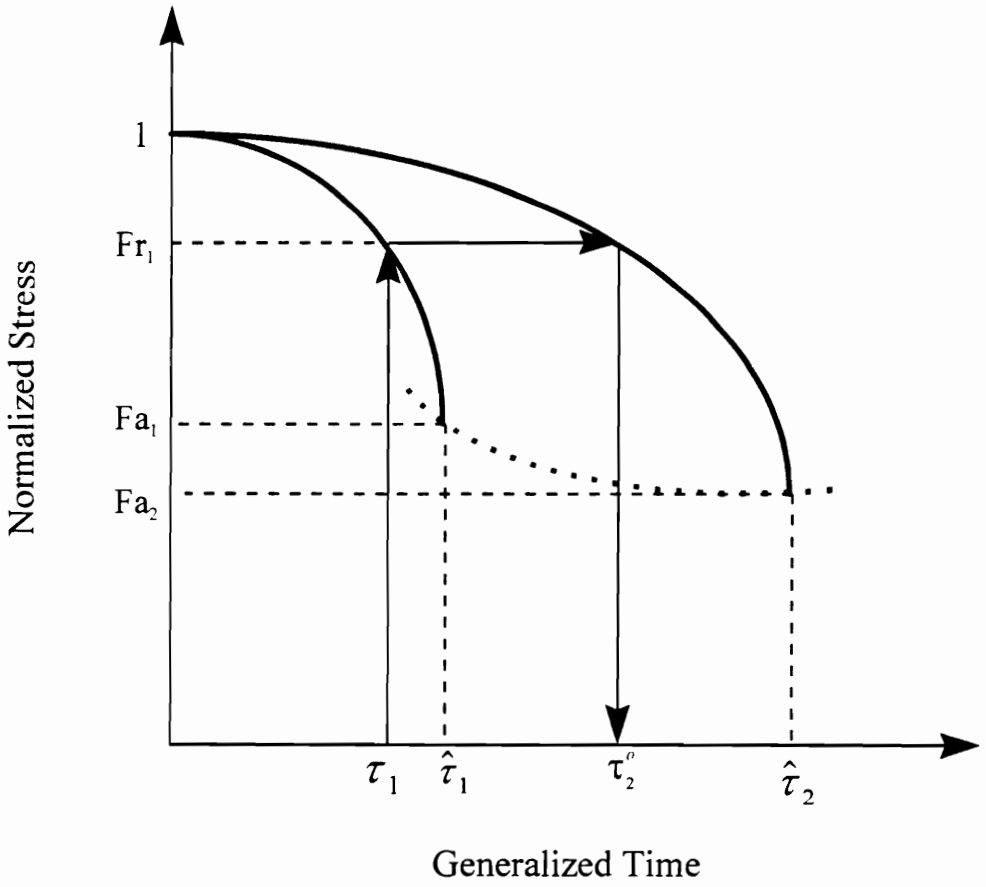

Figure 5.4: General representation of relationship between remaining strength and applied stress.

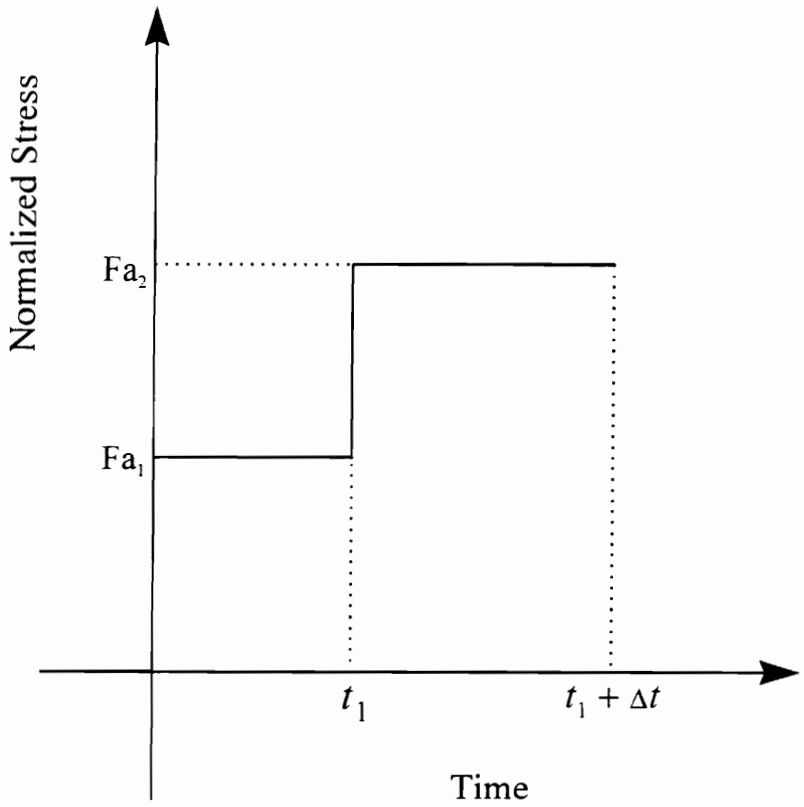

Figure 5.5: Representation of block loading in terms of failure function

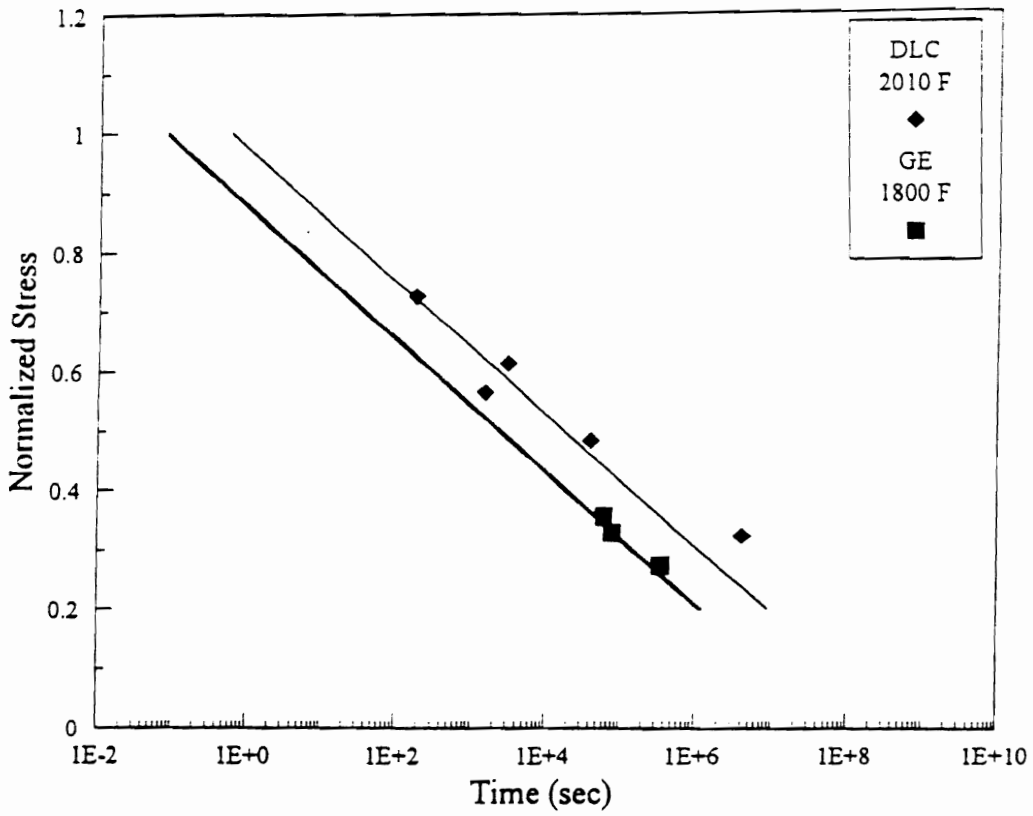

Figure 5.6: Stress-rupture behavior of 2-D woven Nicalon/E-SiC laminates (adapted from ref. 91)

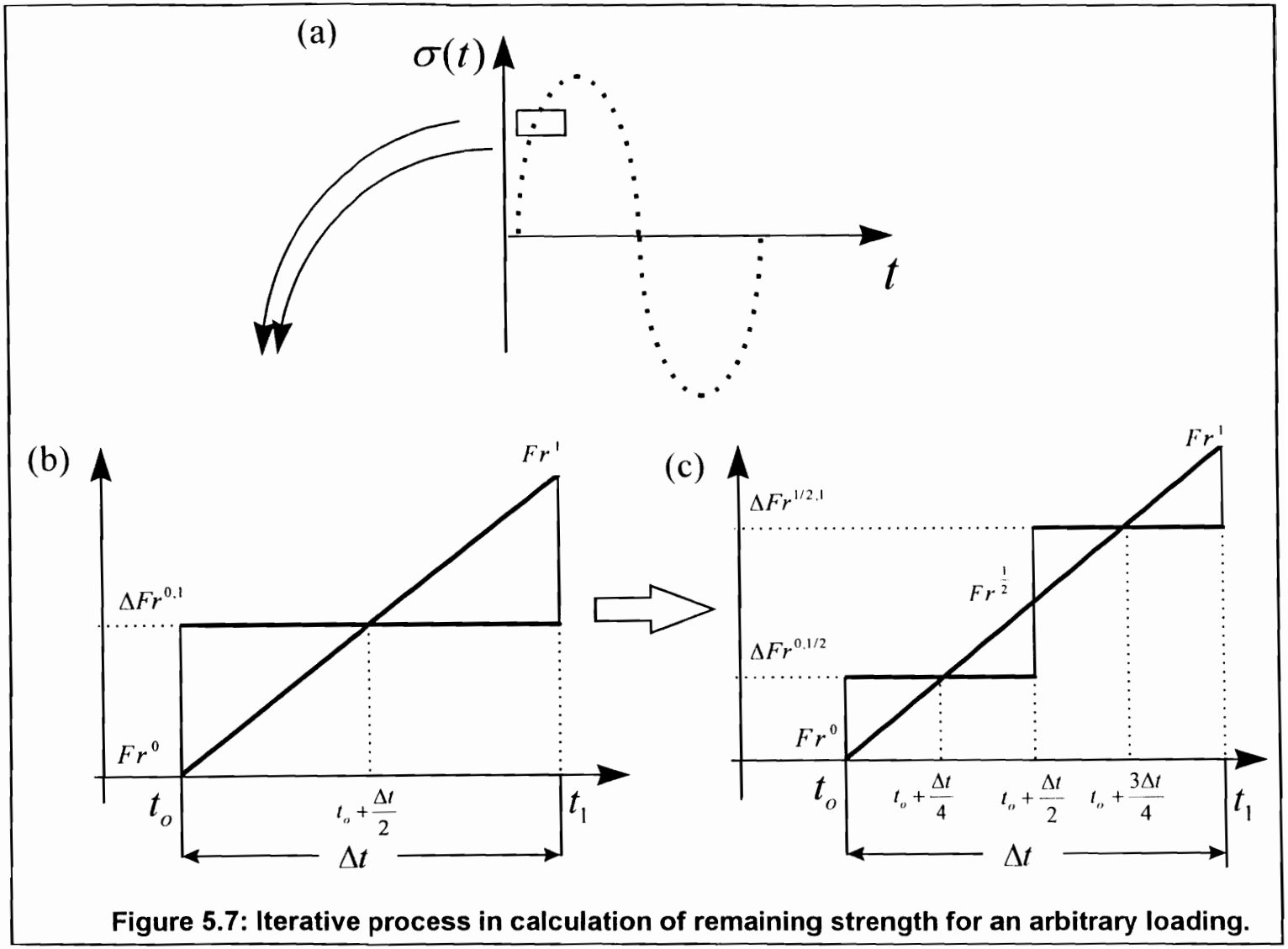

Figure 5.7: Iterative process in calculation of remaining strength for an arbitrary loading.

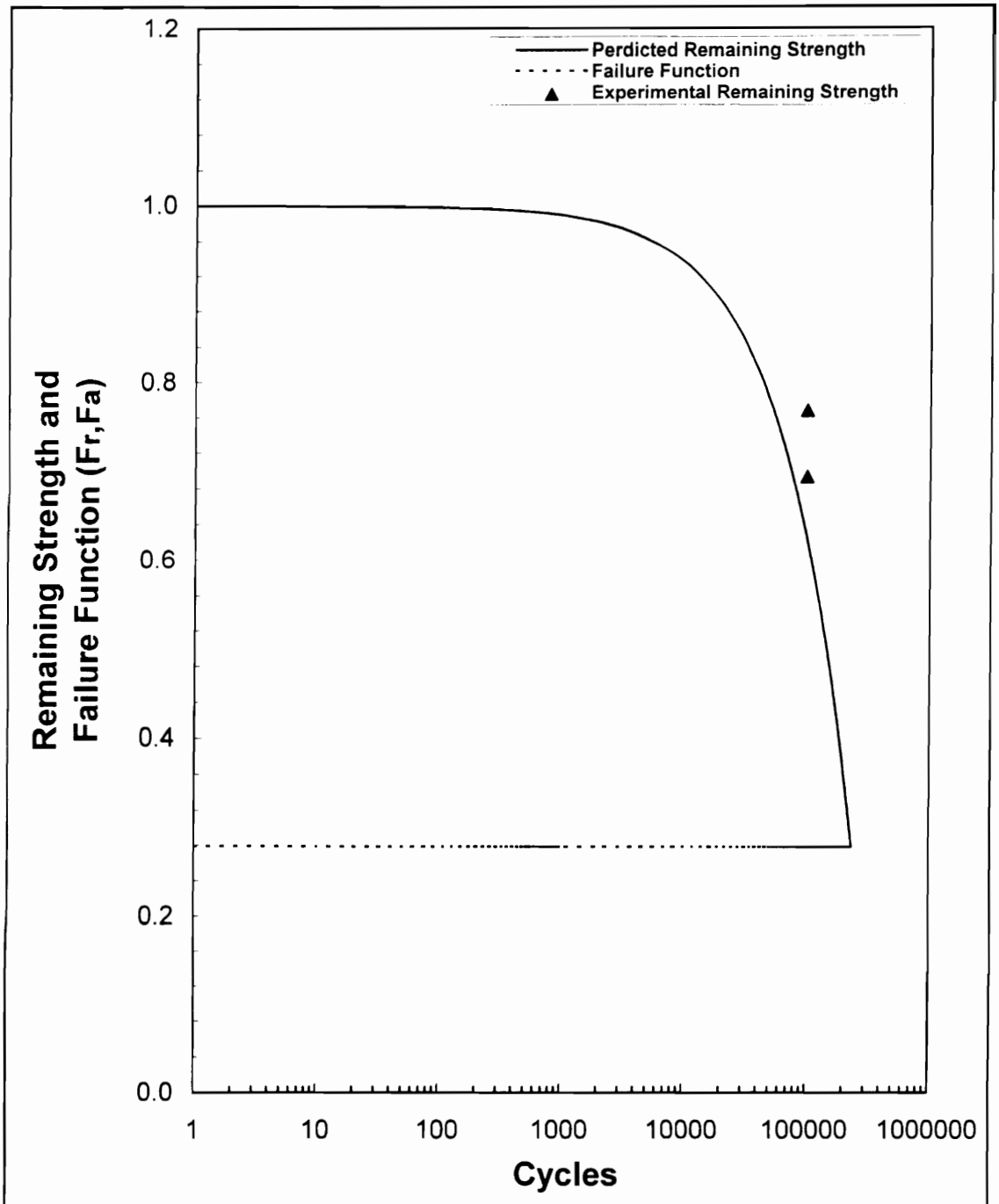

Figure 5.8: Comparison between experimental and predicted remaining strengths of $[(0,90)/(0,90)]_{2s}$ laminates for R=-1, σ_{max}=10 Ksi, f=1 Hz at 1800 F.

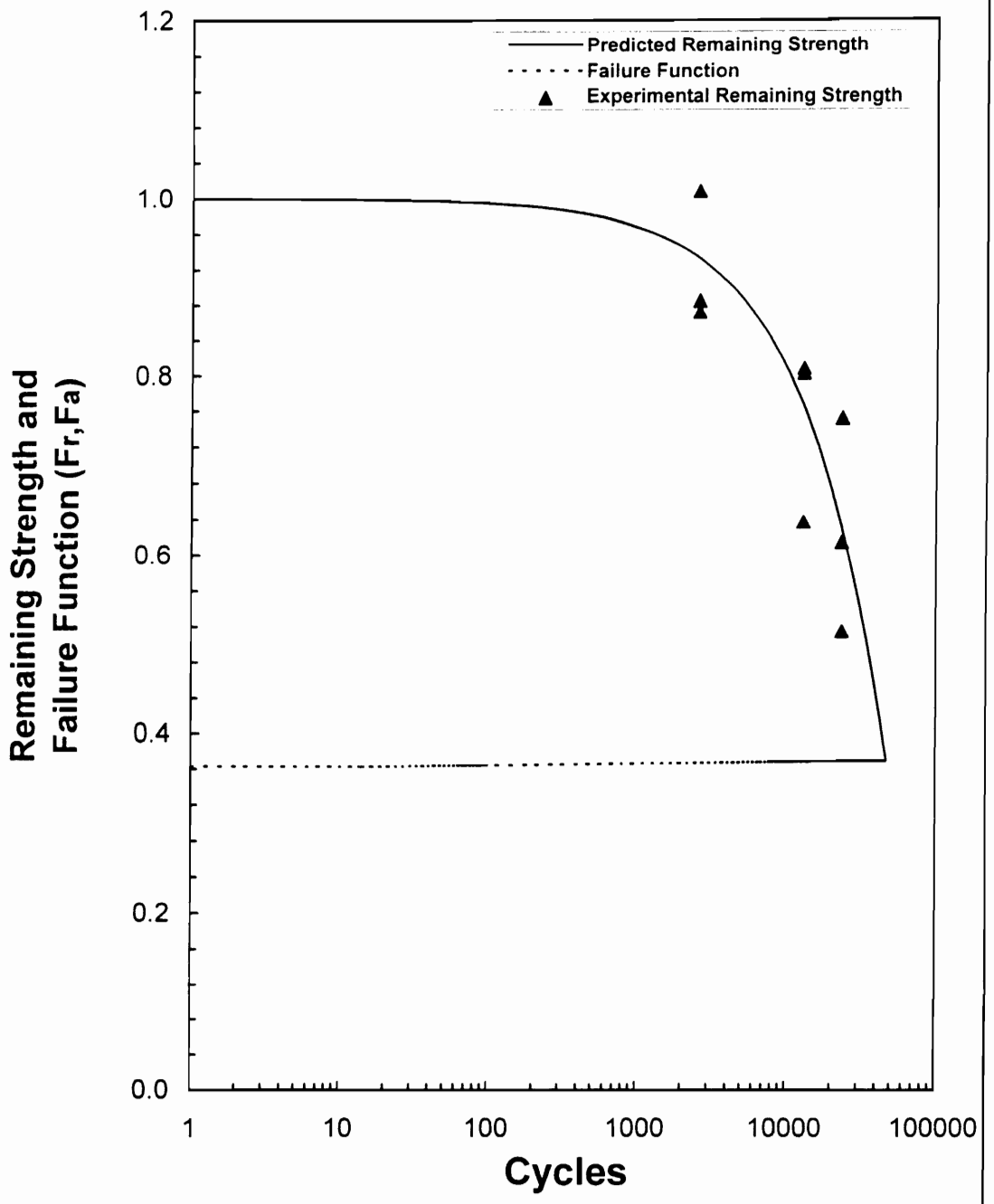

Figure 5.9: Comparison between experimental and predicted remaining strengths of $[(0,90)/(0,90)]_{2s}$ laminates for R=-1, σ_{max}=13 Ksi, f=1 Hz at 1800 F.

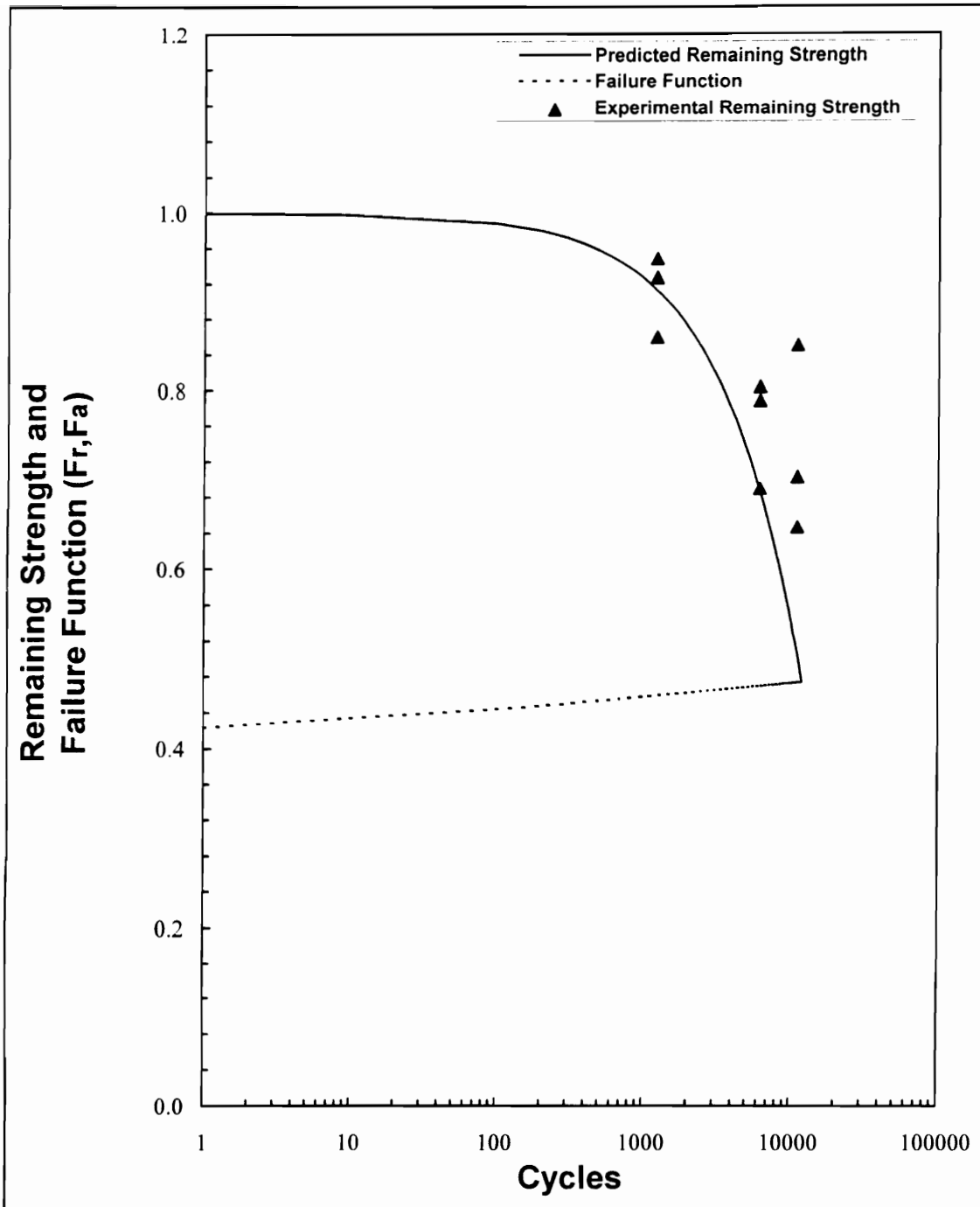

Figure 5.10: Comparison between experimental and predicted remaining strengths of $[(0,90)/(0,90)]_{2s}$ laminates for R=-1, σ_{max}=15 Ksi, f=1 Hz at 1800 F.

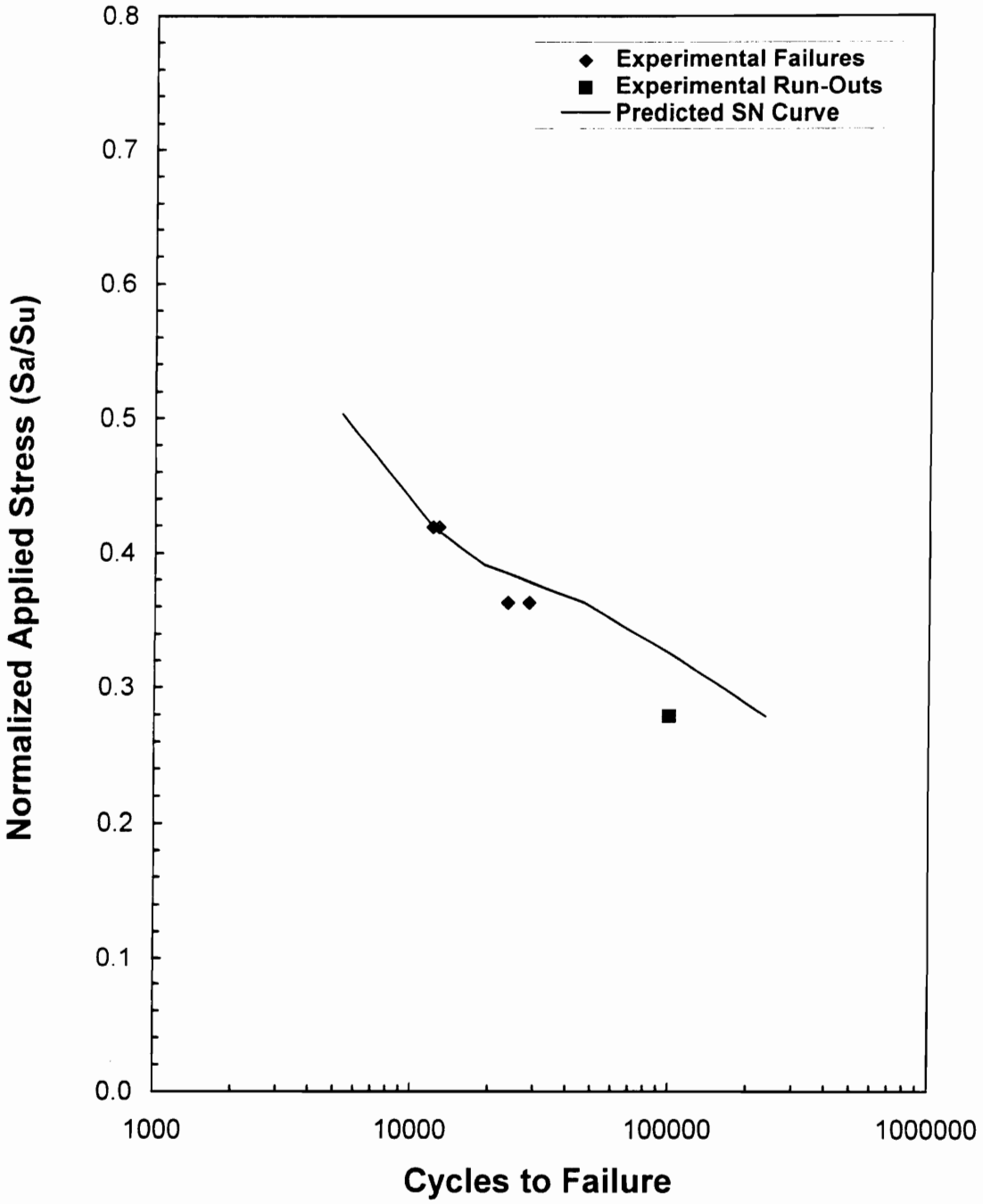

Figure 5.11: Comparison between experimental and predicted fatigue lives of $[(0,90)/(0,90)]_{2s}$ laminates for R=-1, and f=1 Hz at 1800 F.

6. Conclusions and Recommendations

Based on an extensive literature review and mechanical testing of CMC's at elevated temperatures, the following conclusions and recommendations are made to further improve the quality of testing methods and test data.

- Elevated temperature axial testing system using a cold gripping system is suitable for high temperature testing of CMCs. There is great need for standards on elevated temperature testing of ceramic composites.
- Tensile behavior of ceramic matrix composites is significantly influenced by the testing temperature and time at temperature. Depending on the constituents of composite, time and temperature may result in structural evolution of composite (i.e. 100 hours at 1800 °F for SiC/SiC system).
- For CVI processed Nicalon/SiC material system, susceptibility of Nicalon fibers to oxidation, and high degree of porosity, are two of the limiting factors in use of these material for man rated systems. Elastic modulus values show more scatter than the strength values.
- There is an opportunity to make quantitative measurement of porosity by measuring the amount of diffused gas into a specimen placed under vacuum originally.
- NDE results is most valuable when obtained in-situ or using a set up to mimic the in-situ condition (i.e. CMC's cracks tend to close up upon removal of load. A table-top screw driven loading fixture equipped with a load cell or a LVDT can be used to open up the cracks. This allows

application of many of the NDE techniques, such as x-ray, SAM, thermal conductivity measurements to the specimen under loading condition.

- There is great need for NDE techniques applicable to elevated temperature testing. SPATE system is the only known NDE technique at Virginia Tech that has the capability to be used with elevated temperature testing (≥2000 °F). Higher specimen temperature is reported to increase the infrared radiation photon emittance therefore enhancing the SPATE signal. Access to the specimen may be accomplished by providing a quartz window to the furnace.
- Temperature is found to enhance the ultimate tensile properties by relief of residual stresses. However, initial properties suffer.
- At room temperature, notches influence the ultimate properties of Nicalon/E-SiC significantly. Very similar room and elevated temperature tensile responses of notched specimens indicate, influence of notches on damage mechanism and failure mode is so great that temperature does not play a role.
- In fully-reversed cyclic fatigue tests, the compression part of loading in general does not influence the material response directly, but reduces by half the time that cracks stay open, exposing the fibers.
- Cross-ply and quasi-isotropic laminates indicate similar fatigue behavior, remaining strength, and life.
- The fatigue threshold stress, the level at which run-out occurs, is believed to be lower than the PLS. More tests are needed to determine the "Endurance Limit".
- Cyclic loading opens and closes the existing cracks causing relative fiber and matrix sliding against each other. This frictional sliding wears out

the fiber-matrix interface resulting in a reduction in interfacial shear stress and the remaining strength.

- A more sophisticated stress analysis formulation (possibly to include the woven fiber structure) is recommended for the performance simulation code.
- Remaining strength and life predictions compare well to the observed data.

7. References

1. Enabling Propulsion Materials Program, Quarterly Technical Progress Report, Vol.1 Task A-Combustor, FR 22043-7, Contract No. NAS3-26385.

2. R.W. Davidge, "Mechanical Behavior of Ceramics," Cambridge University Press, Cambridge,1979.

3. R.T. Bhatt, and D.R Behrendt,"Reaction-Bonded Si_3N_4 and SiC Matrix Composites, "Ceramics and Ceramic-Matrix Composites," Flight-Vehicle Materials, Structures, and Dynamics, Assessment and Future Directions, Vol. 3, A.K. Noor, S.L. Venneri.

4. E.L. Courtright, H.C. Graham, A.P. Katz, and R.J. Kerans, "Ultra High Temperature Assessment Study-Ceramic Matrix Composites," NASA Technical Report WL-TR-91-4061, Sep. 1992.

5. J. Aveston, and A. Kelly, "Theory of Multi Fracture of Fibrous Composites," J.Mat.Sci., 1973, (8).

6. J. Aveston, G.A. Cooper, and A. Kelly, "The Properties of Fiber Composites," Conference Proceedings, National Physical Laboratory ,IPC Science and Technology Press Ltd. 1971.

7. A.G. Evans, "Fracture Characteristics of Ceramic-Matrix Composites," Ceramics and Ceramic-Matrix Composites, Flight-Vehicle Materials, Structures, and Dynamics, Assessment and Future Directions, Vol. 3, A.K.Noor, S.L.Venneri.

8. R.J. Kerans, R.S. Hay, and N.J. Pagano, "The Role of The Fiber-Matrix Interface in Ceramic Composites," Ceram.Bull., 68[2], 429-442, 1989.

9. Literature Review of Damage Modes and Failure Mechanisms in Ceramic Matrix Composites, Investigation of Damage Accumulation in Model CMC's, Prepared by Material Response Group at ESM Dept. at Virginia Tech for HSCT initiative, Ref. RFQ 693-K959195, Aug, 1993 .

10. K.K. Chawla, "Composite Materials Science and Engineering" New York:Springer-Verlag, Inc., 1987, page 250.

11. L.C. Sawyer, M. Jamieson, D. Brikowski, M.I. Haider, and R.T. Chen, "Strength,Structure, and Fracture properties of Ceramic Fibers Produced from

Polymeric Precursors: I, Base-Line Studies," J.Am.Ceram.Soc., 70 [11] 798-810 (1987).

12. J. Sankar, A.D. Kelkar, and R. Vaidyanathan, "Investigation of Forced and Isothermal Chemical Vapor Infiltrated SiC/SiC Ceramic Matrix Composites," Final report, Prepared by NCA&T State University, Mechanical Engineering Department, for ORNL (ORNL/Sub/88-SC423/01), Sept. 1993.

13. P.J. Lamicq, G.A. Bernhart, M.M. Dauchier, and J.G. Mace, "SiC/SiC Composite Ceramics" Am.Ceram.Soc.Bull., 65[2], 336-338, 1986.

14. A. Chulya, J.Z. Gyekenyesi, and J.P. Gyekenyesi, "Failure Mechanisms of 3-D Woven SiC/SiC Composites Under Tensile and Flexural Loading at Room and Elevated Temperatures,"Ceram. Eng.Sci.Proc. , 13[7-8], 420-432,1992.

15. Du Pont Composites, Preliminary Engineering Data, Pencader Plant, P.O.Box 6100, Newark, Delaware 19714-6100

16. L. Heraud, and P. Spriet, "High Toughness C-SiC and SiC-SiC Composites in Heat Engines, "Whisker and Fiber Toughened Ceramics, Proceedings of an International Conference, Oak Ridge, T.N., U.S.A., 7-9 June 1988, Edited by R.A. Bradly, D.E.Clark, D.C.Larsen, J.O. Stiegler, 217-224.

17. J.M. Yang, W. Lin, C.J. Shih, W. Kai, S.M. Jeng, and C.V. Burkland, "Mechanical Behavior of Chemical Vapour Infiltration-Processed Two-and Three-Dimensional Nicalon/SiC Composites," J.Mat.Sci., 26, 2954-2960, 1991.

18. J. Sankar, A.D. Kelkar, and R. Vaidyanathan, "Mechanical Properties Testing of Ceramic Fiber-Ceramic Matrix Composites," Proceedings of the Sixth Annual Conference on Fossil Energy Materials, July 1992, 53-69.

19. M.Gomina, P.Fourvel, and M.H.Rouillon, " High Temperature Mechanical Behavior of an Uncoated SiC-SiC Composite Material," J.Mat.Sci., 26[7], 1891-1898,1991.

20. M.Bouquet, J.M.Birbis, and J.M.Quenisset,"Toughness Assessment of Ceramic Matrix Composites ," J.Comp.Sci.Tech., 37, 223-248, 1990.

21. G. Navarre, J.C. Rouais, and D. Rouby, "Observation of Crack Path in an SiC-SiC Fibre Composite by X-ray Radiography and SEM," J.Mat.Sci.Lett. 9,1990, 636-638.

22. J.M. Quenisset, "B6-K2 Damage Mechanisms in Ceramic Matrix Composites Reinforced by Continuous Fibers," Euro Mat, Advanced Structural Materials, Vol. 2, Proceedings of the 2nd European Conference on Advanced Materials and Processes, University of Cambridge, UK., 22-24 July 1991, 418-428.

23. J.M. Yang, J.C. Chou, and C.V. Burkland, "High Temperature/High Performance Composites," Materials Research Society, Pittsburgh, 1988, 163.

24. C.V. Burkland, W.E. Bustamante, R. Klacka, and J.M. Yang, "Whisker-and Fiber-Reinforced Ceramics," ASM International, Metals Park, 1988, 225.

25. F..K. Ko, "Preform Fiber Architecture for Ceramic-Matrix Composites," Ceram.Bull., 68[2],1989, 401-414.

26. P. Descamps, J. Tirlocq, and F. Cambier, "Ceramic Matrix Composites: Properties and Applications," Third European Symposium on Engineering Ceramics, Edited by F.L.Riley, 109-125.

27. E. Fitzer and R. Gadow, "Fiber-Reinforced Silicon Carbide," Ceram.Bull. 65[2] 1986, 326.

28. S.V. Nair, and Yu-Lin Wang, "Failure Behavior of a 2-D Woven SiC Fiber/SiC Matrix Composite at Ambient and Elevated Temperatures," Ceram. Eng. Sci. Proc., 13[7-8], 433-441, 1992.

29. H.C. Kim, K.J. Yoon, R. Pickering, and P.J. Sherwood, "Fracture Toughness of 2-D Carbon Fibre Reinforced Carbon Composites," J.Mater.Sci., 20, 1985, 3967-3975.

30. Y.M. Pan, M. Sakai, J.W. Warren, and R.C. Bradt, "Toughness Anisotropy of a SiC/SiC Laminar Composite," Materials Science Research, Vol.20, Tailoring Multiphase and Composite Ceramics, Edited by R.E.Tressler, G.L.Messing, C.G.Pantano, and R.E. Newnham.

31. F. Abbe, and J.L. Chermant, "Fiber-Matrix Bond-Strength Characterization of Silicon Carbide/Silicon Carbide Materials," J.Am.Ceram.Soc.,72[8], 2573-2575, 1990.28. R.W.Rice, "Mechanisms of Toughening in Ceramic Matrix Composites," Ceram.Eng.Sci.Proc . ,2 [7-12], 661-701,1981.

32. R.W. Rice, "Ceramic Matrix Composite Toughening Mechanisms: An Update," Ceram.Eng. Sci. Proc., 6 [7-8], 589-607,1985.

33. G. Bernhart, P. Lamicq, and J. Mace, Industrie Ceramique, 1/85, 1985, 790.

34. M. Dauchier, P. Lamicq, and J. Mace, "Thermomechanical Behavior of Ceramic-Ceramic Composites," Revue Internationale des Hautes Temperatures et des Refractaires 19, 1982, 285-299.

35. M.H. Headinger, D.H. Roach, and R.J. Carter, "Mechanical Property Design Database for Ceramic Matrix Composites," Du Pont CVI Ceramic Matrix Composites Preliminary Engineering Data, 1991.

36. T. Mah, N.L. Hecht, D.E. McCullum, J.R. Hoenigman, H.M. Kim, A.P. Katz, and H.Lipsitt, " Thermal Stability of SiC Fibers (Nicalon)," J.Mat.Sci., 19[4], 1984, 1191-1201.

37. D.J. Posher, K.C. Goretta, R.S. Hodder, Jr., and R.E. Tressler, "Strengths of Ceramic Fibers at Elevated Temperatures," J.Am.Ceram.Soc., 72[2], 284-288,1989.

38. M.A. Rigdon, and W.S. Hong, "Comparison of High-Temperature Tension Testing Results of Ceramic Fibers," Thermal and Mechanical Behavior of Metal Matrix and Ceramic Matrix Composites, ASTM STP 1080, J.M.Kennedy, H.H.Moeller, and W.S.Johnson, Eds., ASTM, Philadelphia, 1990, 116-123.

39. T.J. Clark, R.M. Arons, J.B. Stamatoff, and J. Rabe, "Thermal Degradation of Nicalon* SiC Fibers," Ceram.Eng.Sci.Proc., 7[7-8], 1985, 576-588.

40. T. Mah, M.G. Mendiratta, A.P. Katz, and K.S. Mazdiyasni, "Recent Developments in Fibre-Reinforced High Temperature Ceramic Composites," Am.Ceram.Soc.Bull. ,66[2],1987,304-308

41. J. Ayache, S. Bonnamy, X. Bourrat, A. Deurbergue, Y. Maniette, A. Oberlin, E. Bacque, M. Birot, J. Dunogues, and J.P. Pillot, "Characterization of some yrolysed Polycarbosilanes by Transmission Electron Microscopy," J.Mat.Sci.Lett., 7, 1988, 885-890.

42. T.J. Clark, M. Jaffe, J. Rabe, and N.R. Langley, "Thermal Stability Characterization of SiC Ceramic Fibers: I, Mechanical Property and Chemical Structure Effects," Ceram.Eng.Sci. Proc., 7[7-8], 1986.

43. Y. Maniette and A. Oberlin, "TEM Characterization of Some Crude or Air Heat-Treated Silicon Carbide Nicalon Fibers," J.Mat.Sci., 24[9],1989, 3361-3370.

44. L.C. Sawyer, R.T. Chen, F. Haimbach IV, P.J. Harget, E.R. Prack and M. Jaffe, " Thermal Stability Characterization of SiC Ceramic Fibers:II, Fractography and Structure," Ceram. Eng. Sci. Proc., 7[7-8], 1986, 914-930.

45. J.W. Hinze, and H.C. Graham, "The Active Oxidation of Si and SiC in the Viscous Gas-Flow Regime," Journal of the Electrochemical Society, Solid-State Science and Technology,Vol. 123, July 1976.

46. R.D. James, R.A. Lowden, and K.L. More, "The Effects of Oxidation and Combustion Environments on the Properties of Nicalon™/SiC Composites," Ceram.Trans., Vol.19, Advanced Composite Materials, Edited by D.Sacks, Westerville, Ohio 1991.

47. J.E. Amaral, and C.N. Pollock, "Machine Design Requirements For Uniaxial Testing of Ceramics Materials," Inter.J.High Tech.Ceram., 4, 1988, 143-160.

48. P. Pluvinage, L. Filipuzzi, and G. Camus, "Mechanical Behavior and Oxidation Resistance of a Unidirectional SiC/SiC Fibrous Composite," Ceram.Trans., Vol.19, 937-944, Edited by M.D. Sacks, The American Ceramic Society, OH., USA, 1991.

49. C.K.L. Davies, and S.K. Sinha Ray, "A Simple Apparatus For Carrying Out Tensile Creep Tests on Brittle Materials Up to Temperatures of 1750 °C," J.Physics E:Scientific Instruments, 4, 1971, 421-424.

50. G.E. Dieter, Mechanical Metallurgy, Second Edition, McGraw-Hill, New York, 1976, 561-67

51. R.A. Lowden, "Characterization and Control of the Fiber-Matrix Interface in Ceramic Matrix Composites," ORNL/TM-11039, Oak Ridge National Laboratory, Oak Ridge, TN. Mar.1989.

52. R.A. Lowden, and K.L. More, " The Effect of Fiber Coatings on Interfacial Shear Strength and the Mechanical Behavior of Ceramic Composites," MRS Symposium Proceedings,Vol.170, Tailoring Multiphase and Composite Ceramics, March 1989.

53. J.J. Bernan, "Interfacial Characterization of Glass and Glass-Ceramic Matrix /Nicalon SiC Fiber Composites," MRS Proceedings, Vol. 20, Tailoring Multiphase and Composite Ceramics," Ed. R.E.Tressler et al., Plenum Publishing Corp., 1986,549-560.

54. J.Y. Rossignol, J.M. Quenisset, and R. Naslain, "Mechanical Behavior of 2D-C-C /TIC Composites made from a 2D-C-C Preform Densified with TIC by CVI," Composites,18[2], 1987, 135-144.

55. A.J. Caputo, D.P. Stinton, R.A. Lowden, and T.M. Besmann," Fiber-Reinforced SiC Composites with Improved Mechanical Properties," Am.Ceram.Soc.Bull., 66[2], 1987, 368-372.

56. J.E. Hove, and W.C. Riley, "Graphite," Ceramics for Advanced Technologies, John Wiley and Sons, New York,NY., 1965, 14-76.

57. R.T. Bhatt, "Laminate Behavior for SiC Fiber-Reinforced Reaction Bonded Silicon Nitride Matrix Composites," NASA Technical Memorandum 101350, Oct.1988.

58. R.T. Bhatt, "Influence of Interfacial Shear Strength on The Mechanical Properties of SiC Fiber Reinforced Reaction-Bonded Silicon Nitride Matrix Composites," Ceram. Eng. Sci. Proc. , 11[7-8], 1990, 974-994.

59. K.J. Bowman, P.E. Reyes-Morel, I.W. Chen, "Reversible Transformation Plasticity in Uniaxial Tension-Compression Cycling of Mg-PSZ," Advanced Structural Ceramics, MRS Symposium Proceedings, Edited by P.F.Becher, M.V.Swain, and S.Somiya, Material Research Society, Pittsburgh, Penn. 1986.

60. S.M. Wiederhorn, "Creep and Creep Rupture of Ceramic-Matrix Composites," Ceramics and Ceramic-Matrix Composites, Flight-Vehicle Materials, Structures, and Dynamics, Assessment and Future Directions,Vol. 3, A.K.Noor, S.L.Venneri.

61. J.A. Dicarlo," Creep of Chemically Vapour Deposited SiC Fibers," J.Mat.Sci., 21, 1986,217-224

62. G. Simon and A.R. Bunsell, "The Creep of Silicon Carbide Fibers," J.Mater.Sci.Lett., 2, 1983, 80-83.

63. S. Yajima, "Special Heat-Resisting Materials from Organomettalic Polymers," Am.ceram.Soc. Bull., 62, 1983, 893-898.

64. F. Abbe, R. Cain, and J.L. Chermant, "Tensile and Compressive Creep Characteristics From Bending Tests: Application to SiC-SiC Composites," J.Euro.Ceram.Soc., 5[3], 1989, 201-205.

65. T.J. Chuang, "Estimation of Power-Law Creep Parameters From Bend Test Data," J.Mater. Sci., 21, 1986, 165-175.

66. I.A. Yavorskii, V.I. Elchin, and G.G. Gnesin, "Reactions of Silicon Carbide With Oxidizing Atmospheres," Soviet Powder Metallurgy and Metal Ceramics, 17, 1978, 542-545.

67. D.W. McKee, and D. Chatterji, "Corrosion of Silicon Carbide in Gases and Alkaline Melts," J.Am.Ceram.Soc., 59[9-10], 1976, 441-444.

68. S. Mall, and G.D. Tracy, "Characterization of Fatigue Behavior in Quasi-Isotropic Laminate of Ceramic Composite", Journal of Reinforced Plastics and Composites, Vol. 11, Mar 92, pp 243-250.

69. W.R. Moschelle, "Load Ratio Effects on the Fatigue Behavior of Silicon Carbide Fiber Reinforced Silicon Carbide", Ceram.Eng.Sci.Proc., Vol 15, [4], 1994, 13-22.

70. L.P. Zawada, J.J. Pernot, and L.B. Butkus," Fatigue Behavior of Several Ceramic Matrix Composites," Proceedings of the Fifth International Conference on Fatigue and Fatigue Thresholds, May 3-7,1993, Montreal Canada, Edited by J.P. Bailon and J.L. Dickson.

71. M.H. Headinger, D.H. Roach, and D.J. Landini, "High Temperature Fatigue of Ceramic Matrix Composites," Presented at AeroMat 1994.

72. Measurement of Test System Alignment Under Tensile Loading,HSR/EPM-TSS-001-93, GE Aircraft Engines, 1 Neumann Way, Mail Drop G-50, Cincinnati , OH. 45215-6301.

73. C.G. Larsen, L.E. Johnson, and L.G. Mosiman, "Gripping Techniques and Concerns for Mechanical Testing of Ultra-High Temperature Materials,"MTS Systems Corporation, Materials Testing Division,Eden Prairie,MN.55344 USA.

74. Monotonic Tensile Testing of Ceramic Matrix, Intermetalic Matrix and Metal Matrix Composite Materials, HSR/EPM-D-001-93 Consensus Standard, GE Aircraft Engines, 1 Neumann Way,Mail Drop G-50,Cincinnati, OH.45215-6301.

75. Tension-Tension Load Controlled Fatigue Testing of Ceramic Matrix, Intermetalic Matrix and Metal Matrix Composite Materials, HSR/EPM-D-002-93 Consensus Standard, GE Aircraft Engines, 1 Neumann Way, Mail Drop G-50, Cincinnati, OH. 45215-6301.

76.T.J. Dunyak, K.L. Reifsnider, and W.W. Stinchcomb, "An Examination of Selected NDE Methods for Ceramic Composite Tubes," Center for Composite Materials and Structures, Virginia Tech, Report no. CCMS-89-18, Dec. 1989.

77.M.Elahi, A. Razvan, K.L. Reifsnider, "Characterization of Composite Material's Dynamic Response using Load/Stroke Frequency Response Measurement," Composite Materials: Fatigue and Fracture, Fourth Volume, ASTM STP 1156, 1993, pp. 575-588.

78.J.S., Bendat, and A.G. Piersol, "Correlation and Spectral density Functions," Chapter 3, Engineering Applications of Correlation and Spectral Analysis, 1980, John Wiley & Son, Inc.

79.W.H. Press, S.A. Teukolsky, W.T. Vetterling, and B.P. Flannery, "Fast Fourier Transform" Chapter 12 of Numerical Recipes in Fortran: The art of scientific computing, 2nd edition, Cambridge University Press, Cambridge, U.K., 1992.

80.Fundamentals of signal analysis, Hewlett-Packard application note 243.

81.C.E. Bakis, "Fatigue Behavior of Notched Carbon Epoxy Laminates During Reversed Cyclic Loading," Ph.D. Dissertation, Virginia Tech, Aug 1988.

82.D.S. Fox, and Q.N. Nguyen, "Oxidation Kinetics of Enhanced SiC/SiC," Ceram. Eng. Sci. Proc., Vol. 16, No. 8, 1995, pp. 877-884.

83.P.Reynaud, D. Rouby, G. Fantozzi, F. Abbe, and P. Peres, "Cyclic Fatigue at High Temperatures of Ceramic-Matrix Composites," High-Temperature Ceramic-Matrix Composites I:Design, Durability, and Performance. Ceramic Transactions ,Vol. 57,pp.85-94.

84.A.G. Evans, and F.W. Zok, "The physics and mechanics of fibre-reinforced brittle matrix composites," Journal of Material Science 29 (1994) 3857-3896.

85.A.G. Evans, F.W. Zok, and R.M. McMeeking, "Fatigue of Ceramic Matrix Composites," Acta metall mater, vol 43, No 3, pp. 859-875, 1995.

86.D. Rouby, and P. Reynaud," Fatigue Behaviour Related to Interface Modification During Load Cycling in Ceramic-Matrix Fibre Composites," Composite Science and Technology 48 (1993) 109-118.

87.J. Lamon, F. Rebillat, and A.G. Evans, "Micro-composite Test Procedure for Evaluating The Interface Properties of ceramic Matrix Composites," J.Am.Ceram.Soc78(2) 401-405 (1995).

88.K.L. Reifsnider, and W.W. Stinchcomb, "A critical Element Model of the Residual Strength and Life of Fatigue-Loaded Composite Coupons," Composite Materials: Fatigue and Fracture, ASTM STP 907, Edited by H.T. Hahn, ASTM, Philadelphia (1986), 298-303.

89.S.W. Case, "Mechanics of Fiber-Controlled Behavior in Polymeric Composite Materials," Ph.D. Dissertation, Virginia Tech, June 1996.

90. L.M. Kachanov, 1986, "Introduction to Continuum Damage Mechanics," Martinus, Nijhoff, Boston.

91. K.L. Reifsnider, S. Case, N. Iyengar, "Recent Advances in Composite Damage Mechanics," Forthcoming.

8. Vita

Mehran Elahi was born on February 14, 1960 to Shayesteh Sharif and Rahim Elahi in Mahallat, Iran. He grew up in Tehran, the capital. After graduating from Azar High School, he went to United States and enrolled in Mississippi State University (MSU) in May 1979. He completed his B.S. degree in Mechanical Engineering in may 1982. After that, he entered the M.S. program and completed his degree in Mechanical Engineering in May of 1985. He worked for few years as a graduate teaching assistant at Physics Department at MSU before attending the Virginia Polytechnic Institute and State University to pursue his Ph.D. in Engineering Mechanics. Recently he has accepted a position in Mechanical and Aerospace Engineering Department at University of Tennessee in Knoxville.